



**HAL**  
open science

# Application of the microwave analogy to study the scattering properties of trees, atmospheric particles and microorganisms

Hassan Saleh

► **To cite this version:**

Hassan Saleh. Application of the microwave analogy to study the scattering properties of trees, atmospheric particles and microorganisms. Electromagnetism. Aix-Marseille Université, 2017. English. NNT: . tel-02456811

**HAL Id: tel-02456811**

**<https://hal.science/tel-02456811>**

Submitted on 27 Jan 2020

**HAL** is a multi-disciplinary open access archive for the deposit and dissemination of scientific research documents, whether they are published or not. The documents may come from teaching and research institutions in France or abroad, or from public or private research centers.

L'archive ouverte pluridisciplinaire **HAL**, est destinée au dépôt et à la diffusion de documents scientifiques de niveau recherche, publiés ou non, émanant des établissements d'enseignement et de recherche français ou étrangers, des laboratoires publics ou privés.

# THÈSE

Pour obtenir le grade universitaire de  
**Docteur d'Aix-Marseille Université**

Spécialité  
**Optique, photonique et traitement d'image**

Ecole doctorale Physique et Sciences de la Matière n°352

Présentée par

**Hassan SALEH**

Analogie microonde appliquée à l'étude de la diffraction par des arbres, par des particules atmosphériques et des micro-organismes

Application of the Microwave Analogy to Study the Scattering Properties of Trees, Atmospheric Particles and Microorganisms

Soutenue le 09/11/2017 devant le jury :

Mme Geneviève MAZE-MERCEUR	Directeur de recherche, CEA-CESTA	Rapporteur
M. Jean-Yves DAUVIGNAC	Professeur, LEAT, Université de Nice-Sophia Antipolis	Rapporteur
M. Philippe BESNIER	Directeur de recherche, IETR, CNRS	Examineur
M. Philippe PANNIER	Professeur, IM2NP, Aix-Marseille Université	Examineur
M. Francis BIQUARD	Professeur, Aix-Marseille Université	Invité
M. Jean-Michel GEFFRIN	Ingénieur de Recherche, Institut Fresnel, CNRS	Co-directeur de thèse
M. Hervé TORTEL	Maître de conférences (HDR), Institut Fresnel, Aix-Marseille Université	Directeur de thèse



---

---

*Dedicated to my late father Abed El Monem Saleh*

## ACKNOWLEDGMENTS

---

This thesis is the result of the three unforgettable years I spent as a PhD candidate at the Institut Fresnel in Marseille. First of all, I would like to express my gratitude to my adviser Jean-Michel Geffrin who has been helping me from the first day of my PhD work. Jean-Michel granted me long discussion times, especially at the beginning of this thesis and provided me a daily follow-up to guarantee an efficient and powerful work progress. He taught me the beautiful world of experimentation and helped me to understand the scientific meaning of each experiment I have made. I am particularly thankful for his guidance, valuable advises and constant encouragement that helped me achieve this work. I am profoundly grateful to my adviser Hervé Tortel. I am thankful for our discussions that improved my knowledge and for his scientific guidance and constructive advises during our regular meetings.

My sincere thanks are to my employer, the Centre Commun de Ressources en Microondes represented by Mr. Bernard Albouy and Mr. Francis Biquard, for funding my PhD and hiring me as a measurement engineer. I thank them for providing me the unlimited access to the experimental facility which allowed me to develop deep technical skills.

I would like to express my gratitude to the jury members for the time they devoted for reading this thesis and valuable comments and questions that helped enhancing the quality and readability of the manuscript.

I am thankful to Amélie Litman, chief of our group at Institut Fresnel for the quality and diversity of her scientific knowledge. Amélie was always available to receive me and answer my questions in her simple and clear way. I really don't know how to thank Christelle Eyraud for her kindness and her great help for me. I learned a lot from her previous experience as a former PhD student on the same experimental facility on which I have been working. I thank her for the long time she granted me for the analysis of some experimental results. I would like also to thank Pierre Sabouroux for his enthusiasm and delight.

I would like to thank all the collaborators with whom I have worked and from whom I have learned. I am thankful to the partners from: Institut Pascal (Clermont-Ferrand), Laboratoire d'Electronique et Electromagnétisme of the Sorbonne University (Paris), Laboratoire d'Energie Moléculaire et Macroscopique Combustion of Centrale Supélec (Paris).

## Acknowledgments

---

My sincere thanks are to Cécile Leroux and Arnaud Coudreuse from the Centre de Transfert et de Technologie du Mans (Le Mans). I have very special thanks to Angela Barreda and Fernando Moreno from the University of Cantabria (Santander, Spain) with whom the collaboration was a pleasant journey that ended up with a prestigious publication.

I am profoundly grateful to Rodolphe Vaillon from the Centre d’Energetique et de Thermique de Lyon. Rodolphe was always there, through direct and indirect discussions, to help my work progress with his knowledge and guidance.

Several colleagues, who quickly became friends, made the struggle a bit easier from the beginning. I have to start with my best friend in the Institute, Awoke Negash, with whom I have shared all the ups and downs during the PhD life. We have been leaving the work together every evening, talking about our work and our future, sometimes complaining and sometimes laughing. Thanks for my officemates Luisa, Nicolas, Thibaut and the unforgettable Anar, who “drinks separately and eats parallel”, for all the good time we had together. I will never forget, Mauricio, Emmanuelle, Ismail and Mahmoud and for our chats during our daily lunches.

I would like to thank my mother for her sacrifice, encouragement and support since the first day I decided to quit my home and come to France for pursuing my studies. I am glad to see you proud of me. Still, there is only one person with whom I have shared the joy of the successful achievement I made and who has bearded with me my difficult and frustrating moments. I owe it all to my soulmate, best friend and love, Dima.

Last but not least, I have to say that I loved from the bottom of my heart the beautiful Marseille city that I considered my hometown during the three years of stay. I really loved its landscaping, its weather and its people. I will be leaving Marseille in the coming months to discover a new adventure, but my memories are going unforgettable about “la cité phocéenne”.

*Marseille, September 2017*

## LIST OF ABBREVIATIONS

---

CW :	.....	Continuous Wave
DDA :	.....	Discrete Dipole Approximation
DFC :	.....	Digital Frequency Converter
$E_{sca, cal}^{mes}$ :	.....	Calibrated measured scattered field
$E_{sca, driftCorr}^{mes}$ :	.....	Drift corrected experimental scattered field
$E_{inc}^{mes}$ :	.....	Measured incident field
$E_{sca}^{mes}$ :	.....	Raw experimental scattered field
$E_{tot}^{mes}$ :	.....	Measured total field
IF :	.....	Intermediate Frequency
IFBW :	.....	Intermediate Frequency bandwidth
RCS :	.....	Radar Cross Section
SIR :	.....	Scale Invariance Rule
TUT :	.....	Target Under Test
VNA :	.....	Vector Network Analyzer

# CONTENTS

---

Acknowledgments.....	4
List of abbreviations.....	6
Contents .....	7
List of figures .....	12
Résumé français en version longue.....	24
Analogie microonde.....	24
Le système de mesures microondes su CCRM.....	25
Motivation de ce travail .....	26
Objectifs de cette thèse .....	26
Système de filtrage temporel « Hardgating ».....	27
Optimisation du paramétrage du système .....	28
Analogues ayant des propriétés contrôlées .....	29
Etudes bistatique des cibles faiblement diffractant.....	30
Mise en place d'un système de mesures quasi-monostatique.....	31
Conclusion .....	32
General Introduction .....	34
Background.....	34
Objectives.....	36
Layout .....	38
1 Microwave scattering measurement .....	39
1.1 Introduction .....	39
1.2 Microwave analogy .....	40
1.2.1 Microwave facility at State University of New York (SUNYA).....	45
1.2.2 Microwave facility at Ruhr University Bochum.....	45
1.2.3 Millimeter Facility at University of Florida.....	46
1.2.4 Conclusion .....	48
1.3 Microwave scattering measurement facilities .....	48
1.3.1 Cactus facility at CEA-CESTA (France).....	48
1.3.2 BIANCHA facility at INTA (Spain).....	49
1.3.3 Circular millimeter wave scattering measurements at LEAT (France) .....	50

## Contents

---

1.3.4	Spherical millimeter wave scattering measurements at LEAT (France) .....	52
1.3.5	BABI facility at ONERA (France).....	52
1.4	Experimental facility of the CCRM: Previous state.....	54
1.4.1	Anechoic chamber.....	54
1.4.2	Measurement setup: previous state .....	55
1.4.3	Geometrical configurations.....	56
1.4.4	Positioning systems and angles definition .....	60
1.4.5	Available antennas .....	63
1.4.6	Measurement of the scattered electric field .....	65
1.4.7	Targets alignment.....	66
1.4.8	Calibration.....	67
1.4.9	Post-processing .....	69
1.4.10	Previously measured targets examples .....	73
1.4.11	Conclusion .....	77
1.5	Scattering measurement at the CCRM: Characterization and optimization.....	77
1.5.1	CCRM measurement setup: current state.....	77
1.5.2	Measurement devices: frequency and power profile .....	78
1.5.3	Optimization possibility of the remote mixers based setup .....	80
1.5.4	Implementation of a quasi-monostatic configuration .....	82
1.6	stray signals filtering .....	84
1.6.1	Introduction.....	84
1.6.2	Stray signals in quasi-monostatic measurements.....	85
1.6.3	Stray signals in bistatic measurements.....	87
1.6.4	Soft gating post-processing.....	88
1.6.5	Measurement time vs Precision .....	89
1.6.6	Hard gating principle .....	90
1.6.7	Hardgating system in the CCRM setup.....	94
1.6.8	Some similar Hardgating systems.....	96
1.6.9	Performance validation of the Hardgating system.....	98
1.6.10	Conclusion .....	103
1.7	Random noise characterization and measurement accuracy improvement.....	105
1.7.1	Random error on the incident field .....	105

## Contents

---

1.7.2	Standard deviation, random error and measurement uncertainties .....	106
1.7.3	Random noise on the scattered field .....	107
1.7.4	Challenges in improving the measurement accuracy.....	110
1.7.5	Optimization of the setup configuration .....	113
1.7.6	Measurement of very low scattering objects in optimized configuration.....	116
1.7.7	Conclusion .....	117
1.8	Conclusion.....	120
2	Additive manufacturing of analogs with controlled permittivity .....	121
2.1	Introduction .....	121
2.2	Additive manufacturing in stereolithography.....	122
2.3	Relative complex permittivity of materials .....	124
2.4	Microwave applications using additive manufacturing.....	124
2.4.1	Ceramic additive manufacturing at Xlim Institute (France) .....	125
2.4.2	Additive manufacturing in University of Texas at El Paso (United States) .....	127
2.4.3	Ceramics/polymers manufacturing at the University of Oxford.....	128
2.5	Analog fabrication in stereolithography : collaboration with the Centre de transfert et de technologie du Mans .....	129
2.5.1	The used stereolithography 3D printer.....	129
2.6	Permittivity estimation from far field scattering measurement.....	130
2.6.1	Comparison criterion $F$ based on Root Mean Square Error calculation.....	130
2.6.2	Uncertainties on the permittivity value .....	131
2.7	Fabrication of porous objects with low permittivity ( $1 < \epsilon' < 3$ ).....	133
2.7.1	Parameters selection for on-demand permittivity .....	134
2.7.2	Measurement of low permittivity spheres in optimized configuration .....	136
2.8	Fabrication of objects with high permittivity ( $\epsilon' > 3$ ).....	146
2.8.1	Use of alumina ceramic.....	147
2.8.2	Use of barium titanate ceramic .....	149
2.9	Fabrication of lossy objects ( $\epsilon'' \neq 0$ ) .....	150
2.10	Conclusion .....	152
3	Microwave analog experiments in bistatic configuration.....	154



3.1	Spheroidal low scattering microalgae analogs .....	154
3.1.1	Introduction .....	154
3.1.2	Fabrication of spheroidal microalgae analogs .....	156
3.1.3	Measurement protocol.....	158
3.1.4	Numerical simulations .....	159
3.1.5	Scattering over the full angular range .....	161
3.1.6	Measurement uncertainties related to the random noise.....	163
3.1.7	Conclusion .....	167
3.2	High refractive index dimer .....	168
3.2.1	Introduction.....	168
3.2.2	Motivation and background .....	168
3.2.3	Dimer configuration and measurement protocol .....	170
3.2.4	Dipolar resonance .....	173
3.2.5	Linear polarization degree .....	175
3.2.6	Conclusion .....	180
3.3	soot aggregates .....	181
3.3.1	Introduction.....	181
3.3.2	Extinction and Optical theorem .....	183
3.3.3	Analogs fabrication .....	185
3.3.4	Numerical simulations .....	187
3.3.5	Measurement protocol.....	188
3.3.6	Extinction Cross Section Measurement .....	192
3.3.7	Conclusion .....	196
4	Microwave analog experiments in quasi-monostatic configuration.....	197
4.1	Introduction .....	197
4.2	Measurement procedure .....	197
4.3	Reference target: Squat metal cylinder .....	200
4.4	Single metal and dielectric targets.....	201
4.5	Metallic and dielectric targets .....	203
4.6	Forest scaled model: trees analogs with metal tank .....	207
4.7	Conclusion.....	211
	General conclusion and perspectives .....	212

## Contents

---

Publications.....	217
Peer-Reviewed Journals.....	217
International Conferences.....	217
National Conferences.....	217
References.....	218
Abstract.....	225
Résumé.....	226

## LIST OF FIGURES

Figure 1 Le principe de l'analogie microonde appliqué à l'étude de la diffraction par une particule de suie et par un arbre .....	25
Figure 2 Le dispositif de mesure dans la chambre anéchoïque du CCRM.....	26
Figure 3 Réponse impulsionnelle montrant l'amplitude en dB du champ diffracté brut mesuré par une sphère diélectrique de diamètre 50.75 mm, dans le domaine temporel et en fonction de l'angle monostatique et de la distance parcouru par le signal.....	27
Figure 4 Amplitude du champ mesuré diffracté par un palet métallique à 2 GHz en configuration bistatique .....	28
Figure 5 Comparaison entre la mesure et la simulation de l'amplitude du champ diffracté par une sphère de 35 mm de diamètre et de permittivité $\varepsilon = 1.02 + 0j$ , dans un cas non-optimisé et un cas optimisé.....	29
Figure 6 Les étapes de la technique proposé pour créer une faible permittivité à partir du matériau de base.....	30
Figure 7 Photos et valeurs de permittivités de quelques sphères de faible permittivité fabriquées selon la technique de maillage proposée .....	30
Figure 8 Photos des analogues étudiés en configuration bistatique. (a) Analogues de micro-algues sphéroïdaux. (b) Analogue d'une particule de suie. (c) Dimer analogue de particules de silicium ..	31
Figure 9 Photo du système de mesure dans une configuration quasi-monostatique.....	32
Figure 10 Comparaison en amplitude (gauche) et phase (droite) entre mesure et simulation du champ diffracté par un palet métallique, à 11 GHz, en configuration quasi-monostatique dans les deux cas de polarisations $\varphi\varphi$ et $\theta\theta$ .....	32
Figure 0.1 Scheme showing the principle of the microwave analogy applied to the scattering of electromagnetic waves by soot particles and a forest environment (tree) .....	35
Figure 1.1 Examples of nanometric and micrometric particles of interest in electromagnetic scattering studies. (a) A soot aggregate [15]. (b) A gold particle [16]. (c) A dry sea-salt particle [17]. (d) A desert soil particle [18]. (e) An ice crystal particle [19].....	41
Figure 1.2 GOA and T-Matrix computation results for monodisperse, randomly oriented circular cylinders with surface-equivalent-sphere size-parameters $xs = 40, 80, 120$ and 180 [26].....	43
Figure 1.3 Principle on the microwave analog experiment. (a) Scale extension. (b) Scale reduction .....	44
Figure 1.4 The microwave facility at SUNYA[29].....	45
Figure 1.5 The microwave facility of the Ruhr university [29] .....	46

## List of figures

---

Figure 1.6 The experimental setup at the University of Florida [29] .....	47
Figure 1.7 CACTUS facility at CEA-CESTA in France [43].....	49
Figure 1.8 The experimental setup at INTA in Spain [46] .....	49
Figure 1.9 Results of the measurement of a metal cube at 5.8 GHz [45] .....	50
Figure 1.10 The millimeter measurement setup at LEAT [47].....	51
Figure 1.11 Amplitude and phase of the measured and calculated scattered field by a 20mm metal cylinder [47].....	51
Figure 1.12 The recent spherical millimeter wave setup at LEAT [48] .....	52
Figure 1.13 The BABI at ONERA in France [49] .....	53
Figure 1.14 Measured RCS of the cylinders compared to simulations. (a) VV polarization, (b) HV polarization, (c) VH polarization and (d) HH polarization [49] .....	53
Figure 1.15 Photography of the anechoic chamber of the CCRM.....	54
Figure 1.16 The measurement setup in its previous state [51].....	55
Figure 1.17 Position of the sources (a) and the receivers (b) in the spherical configuration and definitions of the polarizations.....	56
Figure 1.18 Schematic showing the spherical configuration of the CCRM and the possible displacements on the source the receiver and the TUT .....	58
Figure 1.19 Azimuthal circular configuration of the CCRM showing the possible displacements of the receiver and the TUT. The source is at a fixed position .....	59
Figure 1.20 Vertical circular configuration. The source and the receiver are on the vertical arch....	59
Figure 1.21 The displacement of the superior and inferior wagons holding the antennas on the vertical arch (in red).....	61
Figure 1.22 The displacement of the azimuthal arm carrying the receiving antenna (in green).....	62
Figure 1.23 rotating mast carrying the TUT (in blue).....	63
Figure 1.24 photo of some of the used antennas.....	64
Figure 1.25 A schematic showing the measurement of the (a) total field and the (b) incident field...	65
Figure 1.26 Total, incident and scattered field obtained with a 35 mm metal sphere measured at 10 GHz in the VV polarization .....	66
Figure 1.27 The alignment of the sphere using the laser diode .....	67
Figure 1.28 A photo of a polystyrene holder made especially to the alignment of a soot aggregate analog of complex shape. The dielectric spheres and the black absorbing pieces are removed after the alignment is accomplished.....	67
Figure 1.29 Calibrated experimental and simulated scattered fields by a dielectric sphere at 11 GHz in HH polarization as a function of the receiving angle [22].....	68

## List of figures

---

Figure 1.30 Raw measured and simulated scattered fields by a dielectric sphere at 11 GHz in HH polarization as a function of the receiving angle. (a) amplitude, (b) phase [51] .....	69
Figure 1.31 Angular spectrum of the measured (without drift correction) and simulated scattered fields by a dielectric sphere at 11 GHz in HH polarization as a function of the angular frequency [51] .....	70
Figure 1.32 Angular spectrum of the measured scattered field by a dielectric sphere at 11 GHz in HH polarization as a function of the angular frequency with and without drift correction [22] .....	71
Figure 1.33 Raw measured, drift corrected and simulated scattered fields by a dielectric sphere at 11 GHz in HH polarization as a function of the receiving angle. (a) amplitude, (b) phase [22] .....	72
Figure 1.34 Angular lowpass filtering of a 35 mm diameter metal sphere at 10 GHz. The figure shows the scattered field spectrum before the filtering, after the filtering and the cutoff frequency .....	73
Figure 1.35 Front (a) and side (b) views of the aggregate analog placed on its polystyrene support. The plexyglass spheres are used to align to aggregate in the measurement setup and are removed after the alignment is done [54] .....	74
Figure 1.36 Amplitude and phase of the experimental scattered field compared to the simulations obtained with different numerical methods for $\varphi_s=90^\circ$ and at 20 GHz in HH polarization (a, c) and in VV polarization (b, d) [54] .....	75
Figure 1.37 (a) A photo showing the positioning of the trees analogs on the aluminum plate, of the transmitting antenna and of the receiving antenna. (b) a schematic on the tree analog [11] .....	76
Figure 1.38 Comparison between experimental and theoretical results of the fields scattered by the trees samples in HH polarization and at $F=4.2$ GHz [11] .....	76
Figure 1.39 Synoptic of the measurement configuration using external mixers, synthesizers and Vector Network Analyzer .....	78
Figure 1.40 The configuration summary sheet, made on Microsoft Excel .....	81
Figure 1.41 Definition of the quasi-monostatic in Theta and in Phi .....	82
Figure 1.42 Quasi-monostatic in Theta and in Phi .....	83
Figure 1.43 A schematic of the modified and optimized quasi-monostatic configuration with the source antenna, the receiving antenna and the mixers fixed on the same wagon .....	84
Figure 1.44 Stray signals identification in quasi-monostatic configuration. (a) Schematic of the measurement showing the potential sources of stray signals. (b) Impulse response representation by means of Inverse Fourier transform of the measured and simulated field scattered by a 50.75 mm dielectric sphere .....	86
Figure 1.45 Stray signals identification in azimuthal bistatic configuration. (a) Schematic of the measurement. (b), (c) and (d) are the time domain analysis by means of Inverse Fourier transform of	

the raw measured scattered field, drift corrected scattered field and simulated scattered field respectively obtained with a 35 mm metal sphere .....	87
Figure 1.46 Raw and soft gated measured field scattered by the dielectric sphere in quasi-monostatic configuration at the monostatic angle $9^\circ$ . (a) Representation in the frequency domain. (a) Representation in the distance domain showing the tapered Hanning window.....	89
Figure 1.47 holograms showing the stray signals filtering using soft gating in quasi-monostatic configuration for the dielectric sphere. (a) Raw measured scattered field. (a) Simulated scattered field. (c) Soft gated measured scattered field .....	89
Figure 1.48 Characteristics of pulsed signals in time and frequency domains .....	91
Figure 1.49 Narrowband mode in Hardgating measurement.....	92
Figure 1.50 Wideband mode in Hardgating measurement .....	93
Figure 1.51 The parameters of the Hardgating system of the CCRM .....	95
Figure 1.52 A schematic of the Hardgating setup of the CCRM used in bistatic configuration .....	96
Figure 1.53 StingRay gated CW radar architecture [67] .....	97
Figure 1.54 Compact Range measurements facility of EADS [69].....	98
Figure 1.55 The Plexiglas sphere (left) and the squat metal cylinder (left).....	99
Figure 1.56 Amplitudes of fields scattered by the squat metal cylinder in HH polarization at 2 GHz, 4 GHz, 6 GHz and 8 GHz. Comparison between simulation, non-gated, soft-gated and hard-gated measurements.....	100
Figure 1.57 Holograms of the relative Equivalent Scatterer ( $ESdB_{relative}$ ) as a function of the frequency and the receiving angle for the three measurement cases of the squat metal cylinder: (a) Non-gated measurement. (b) Soft-gated measurement. (c) Hard-gated measurement.....	101
Figure 1.58 Mean deviation of the DR criterion for the measurements of the squat metal cylinder .....	101
Figure 1.59 Amplitudes of fields scattered by the dielectric sphere in HH polarization at 12 GHz, 14 GHz, 16 GHz and 18 GHz. Comparison between simulation, non-filtered, soft-gated and hard-gated measurements.....	102
Figure 1.60 Holograms of the relative Equivalent Scatterer ( $ESdB_{relative}$ ) as a function and the receiving angle for the three measurement cases of the dielectric sphere: (a) Non-gated measurement. (b) Soft-gated measurement. (c) Hard-gated measurement .....	103
Figure 1.61 Mean deviation of the DR criterion for the measurements of the dielectric sphere.....	103
Figure 1.62 (a) Real part and (b) imaginary part of the 500 acquisitions of the incident field at 18 GHz for $\theta_r = -120^\circ$ with the K-band horn antennas .....	105

Figure 1.63 Amplitude in dB of the 500 acquisitions of the incident field at 18 GHz at the receiving angles  $-120^\circ$  and  $0^\circ$  ..... 106

Figure 1.64 (a) Random noise (standard deviations) and (b) measurement uncertainties (relative standard deviation) on the real and imaginary parts of the incident field as a function of the amplitude of the incident field at 18 GHz with the K-band horn antennas ..... 107

Figure 1.65 Total, incident and raw scattered field of a 35 mm metal sphere at 16 GHz with the DRG horn antennas ..... 108

Figure 1.66 (a) Random noise (standard deviations) and (b) measurement uncertainties (relative standard deviation) on the real and imaginary part of the incident field as a function of the amplitude of the incident field at 16 GHz with the DRG horn antennas ..... 108

Figure 1.67 Variation of the standard deviation on the real and imaginary parts of the incident, total and scattered fields as a function of the receiving angles for the 35 mm diameter sphere at 16 GHz using the DRG horn antennas ..... 109

Figure 1.68 Amplitude and phase of the calibrated measured scattered field by a 35mm sphere at 16 GHz with the DRG horn antennas showing the associated uncertainties with comparison to simulation ..... 110

Figure 1.69 Real and imaginary parts on the 500 acquisitions and the corresponding quantiles diagrams at 16 GHz with the DRG horn antennas and at  $\theta_r = -120^\circ$  (Gaussian distribution)..... 112

Figure 1.70 Real and imaginary parts on the 500 acquisitions and the corresponding quantiles diagrams at 16 GHz with the DRG horn antennas and at  $\theta_r = 0^\circ$ (Non-Gaussian distribution)..... 112

Figure 1.71 A schematic explaining the decomposition of the receiving excursion into three different zones, with different power profiles ..... 113

Figure 1.72 Amplitude levels of  $b_2$ ,  $a_1$  and  $b_2/a_1$  total signals in non-optimized and optimized (with zones decomposition) configurations in the case of the measurement of the 35 mm sphere with the DRG antennas at 16 GHz..... 115

Figure 1.73 Amplitude measurement uncertainties in (dB) corresponding to the three power profiles at 16 GHz with the DRG horn antennas (obtained from repetitive measurements in each configuration)..... 115

Figure 1.74 Comparison between the amplitudes of the calibrated fields scattered by the 35 mm metal sphere at 16 GHz in non-optimized and optimized configuration ..... 116

Figure 1.75 Amplitude of experimental scattered field by a 35 mm sphere with real part of relative permittivity of 1.02 in (left) non-optimized configuration and (right) optimized configuration..... 118

Figure 1.76 Phase of experimental scattered field by a 35 mm sphere with real part of relative permittivity of 1.02 in (left) non-optimized configuration and (right) optimized configuration ..... 119

Figure 2.1 Principle of the stereolithography process utilizing a vat of liquid photopolymer resin	123
Figure 2.2 Ceramic stereolithography setup used at Xlim [82] .....	126
Figure 2.3 RF microwave components fabricated at Xlim using the developed ceramic stereolithography technique. (a) Large bandpass monolithic waveguide operating at 26 GHz located in a woodpile made out of Zirconia [83]. (b) 60 GHz integrated lens antenna of 3 cm width made out of Alumina [82]. Zirconia plate used as input/output access to a narrow Ka bandpass filter operating at 33 GHz [84]. (d) Alumina resonant structure working at 12.57 GHz dedicated to RF filtering applications composed of a main structure containing the dielectric resonator and a surrounding cavity [85] .....	126
Figure 2.4 (a) Spatially variant self-collimating lattice [87]. (b) Anisotropic metamaterials [88] ..	127
Figure 2.5 Chess rook fabricated in stereolithography from epoxy/carbon nanotubes mixture [89] .....	128
Figure 2.6 The Real part of the relative permittivity of 3D parts for various loading fractions of BaTiO <sub>3</sub> between 0 wt% and 70 wt% at 15 GHz [90] .....	128
Figure 2.7 3D-printed polymer composite parts. (a) Rod-connected diamond photonic crystal structures printed in ABS polymer (left, $\epsilon' = 2.57$ ) and 50 wt% BaTiO <sub>3</sub> /ABS polymer composite (right, $\epsilon' = 4.95$ ). (b) 1D, 2D, band 3D periodic structures and a 1D graded structure printed using a combination of ABS polymer and 50 wt% BaTiO <sub>3</sub> in ABS polymer composite [90] .....	129
Figure 2.8 (a) The acrylate sphere. (b) Map in dB of the criterion $F_{minnoise}$ for $\epsilon' \in [1, 6]$ and $\epsilon'' \in [0, 1]$ at 18 GHz .....	132
Figure 2.9 Definition of the uncertainty on the determined relative permittivity from the variation of the criterion $F_{noise}$ of 3dB around $F_{minnoise}$ .....	132
Figure 2.10 Estimated real and imaginary parts of permittivity and the associated uncertainty of a 35mm diameter sphere of acrylate material fabricated in additive manufacturing with respect to the frequency .....	133
Figure 2.11 Porosity control using meshed geometry .....	134
Figure 2.12 Procedure of the meshing parameters prediction for a chosen permittivity estimation Spheres samples and permittivity determination .....	135
Figure 2.13 Photography of the meshed sphere <i>Acrylate6.61</i> showing the sphere diameter (35 mm), the mesh size (6.6 mm) and the cylinders diameter (1 mm) .....	136
Figure 2.14 Real part of the relative permittivity of the sphere <i>Acrylate1.40.35</i> determined at the four orientations ( $\theta_0 = -90^\circ, 0^\circ, 90^\circ$ and $180^\circ$ ) as a function of the frequency .....	137
Figure 2.15 Amplitude and phase of the measured scattered fields by the meshed 35 mm diameter sphere <i>Acrylate1.40.35</i> with comparison to the Mie simulation of equivalent homogeneous sphere.	



The relative permittivity value corresponding to each frequency is shown on the amplitude figures ..... 139

Figure 2.16 Photos and properties of the manufactured dielectric meshed spheres.  $\lambda_{min}$  corresponds to the highest frequency 18 GHz and  $\lambda_{max}$  corresponds to the lowest frequency 2 GHz. The values of the measured  $\epsilon'$  are obtained from an average over all the frequencies ..... 140

Figure 2.17 Real part of relative permittivity for the 5 meshed spheres presented in (Figure 2.16) as a function of the frequency. For each sphere, 4 permittivity determination are made, corresponding to the 4 orientations of the sphere. The names of each sphere is written at the right hand side of the figure ..... 141

Figure 2.18 Amplitude and phase of the measured scattered fields by the meshed 35 mm diameter sphere *Acrylate*6.62.5 with comparison to the Mie simulation of equivalent homogeneous sphere. The relative permittivity value corresponding to each frequency is shown. The presented measured fields result from an average over the 4 orientations ..... 142

Figure 2.19 Amplitude and phase of the measured scattered fields by the meshed 35 mm diameter sphere *Acrylate*6.61 with comparison to the Mie simulation of equivalent homogeneous sphere. The relative permittivity value corresponding to each frequency is shown. The presented measured fields result from an average over the 4 orientations ..... 143

Figure 2.20 Amplitude and phase of the measured scattered fields by the meshed 35 mm diameter sphere *Acrylate*4.70.56 with comparison to the Mie simulation of equivalent homogeneous sphere. The relative permittivity value corresponding to each frequency is shown. The presented measured fields result from an average over the 4 orientations ..... 145

Figure 2.21 Amplitude and phase of the measured scattered fields by the meshed 35 mm diameter sphere *Acrylate*4.70.2 with comparison to the Mie simulation of equivalent homogeneous sphere. The relative permittivity value corresponding to each frequency is shown. The presented measured fields result from an average over the 4 orientations ..... 146

Figure 2.22 Some of the acrylate/alumina 35 mm diameter meshed spheres ..... 148

Figure 2.23 Real part of relative permittivity  $\epsilon'$  of the 2 full acrylate/alumina spheres a function of the frequency. For each sphere, 4 permittivity determination are made, corresponding to the 4 orientations of the sphere. (a) Acrylate+10% alumina. (b) Acrylate+20% alumina ..... 149

Figure 2.24 The 35 mm diameter acrylate/20% alumina. The cracks on the body of the sphere are indicated by the arrows ..... 149

Figure 2.25 Photos and properties of the manufactured meshed spheres with carbon and zinc oxide ..... 151

Figure 2.26 Relative permittivities of the spheres acrylate+0.5 % carbon, acrylate+0.5 % ZnO10 and Acrylate as a function of the frequency. The represented values for each sphere is an average of the permittivity over the 4 orientations. (a) Real part. (b) Imaginary part..... 151

Figure 2.27 A failed attempt to manufacture a full acrylate with carbon spheres. Only a quart of the sphere was manufactured ..... 152

Figure 3.1 A photo of the photobioreactor "DiCoFluV" developed at Institut Pascal in France. The incident solar radiations are captured and concentrated using Fresnel lenses shown on the upper side of (a). They are then driven to a reactor (b) using a huge number of fiber optics (c) [96] ..... 155

Figure 3.2 Diversity of photosynthetic microorganisms with different complexity in term of shape and refractive index.(a) A photosynthetic bacteria having three different refractive indices over the central part, the coat and the nucleous.(b) A cyanobacteria containing many cellular features with shap heterogeneity. (c) A microalgae with two nucleous and many other cellular features [20]..... 156

Figure 3.3 Photography of the machined spheroidal analogs ..... 158

Figure 3.4 Measurement of the spheroidal analogs in azimuthal bistatic configuration ..... 159

Figure 3.5 Schematics of the scattering configurations seen from the top showing the three studied orientations on the spheroids..... 159

Figure 3.6 Schematic showing the settings of the measurement setup for the measurement of the microalgae spheroidal analogs. Measurements are made in Hardgating mode with the K-band antennas..... 160

Figure 3.7 Experimental and simulated scattered fields from Laurel<sub>1,29</sub> and Hardy<sub>1,29</sub> as a function of the receiving angles at  $\theta_{or} = 45^\circ$  in VV polarization. (a) Amplitude of the field scattered by Laurel<sub>1,29</sub> in dB. (b) Phase of the field scattered by Laurel<sub>1,29</sub> in radian. (c) Amplitude of the field scattered by Hardy<sub>1,29</sub> in dB. (d) Phase of the field scattered by Hardy<sub>1,29</sub> in radian ..... 162

Figure 3.8 Experimental and simulated scattered fields from Laurel<sub>1,29</sub> and Hardy<sub>1,29</sub> as a function of the receiving angles at  $\theta_{or} = 0^\circ$  and  $\theta_{or} = 90^\circ$  in VV polarization. (a), (c) Amplitude of the fields scattered by Laurel<sub>1,29</sub> in dB at  $\theta_{or} = 0^\circ$  and  $\theta_{or} = 90^\circ$  respectively. (b), (d) Phase of the fields scattered by Laurel<sub>1,29</sub> in radian at  $\theta_{or} = 0^\circ$  and  $\theta_{or} = 90^\circ$  respectively ..... 163

Figure 3.9 Experimental scattered fields from Hardy<sub>1,29</sub> in VV polarization at  $\theta_{or} = 90^\circ$  with respect to the amplitudes of the incident and total field..... 164

Figure 3.10 Comparison between experimental scattered fields from Laurel<sub>1,29</sub> in VV and HH polarizations at  $\theta_{or} = 90^\circ$  with respect to the amplitudes of the incident and total field. (a) Amplitudes of the incident, total and scattered fields in VV. (b) Amplitudes of the incident, total and scattered fields in HH. (c) Phase of the scattered field in VV. (d) Phase of the scattered field in HH. The incident and total field are compensated by the same calibration coefficient applied on the scattered field 165

Figure 3.11 Uncertainties on the measurement of the electric field (incident and total) for Laure1<sub>1.29</sub> and Hardy1<sub>1.29</sub> in VV and HH polarizations as a function of the amplitude ..... 166

Figure 3.12 Intensity of the Far-field scattering pattern under Kerker conditions of a 9 mm sphere with  $\epsilon = 16.5 + 0j$ . The illumination direction is indicated by the yellow arrow. (a) zero-backward condition ( $\lambda = 84 \text{ mm}$ ). (b) minimum-forward condition ( $\lambda = 69 \text{ mm}$ )[12] ..... 169

Figure 3.13 Scattering configuration: a homogeneous sphere dimer with the same radius is illuminated by a monochromatic plane wave propagating along the z axis and linearly polarized either parallel to the dimer connecting axis. (a) Longitudinal configuration (P). (b) Transverse configuration (S).  $\theta$  is the scattering angle ..... 170

Figure 3.14 The measurement procedure of the field scattered by the dimer in azimuthal bistatic configuration. In this configuration, the HRI spheres are placed in their specific polystyrene holder, one next to the other as shown in the inset ..... 171

Figure 3.15 Schematic showing the settings of the measurement setup for the measurement of the dimer analog. Measurements are made in Hardgating mode with the DRG horn antennas ..... 172

Figure 3.16 Scattering coefficient  $Q_{sca}$  and its first four multipolar contributions for a sphere with  $\epsilon = 15.7 + 0.2j$  and radius 9 mm. The partial electric and magnetic dipolar and quadrupolar contributions are indicated by the vertical dashed lines ..... 174

Figure 3.17 Orientation of the induced dipoles in (a) longitudinal configuration and (b) transverse configuration. The red vectors represent the electric quantities, while the blue vectors represent the magnetic ones.  $E_0$  corresponds to the polarization of the electrical incident field and  $H_0$  corresponds to the polarization of the magnetic incident field. Both correspond to a plane wave with incidence direction  $k$ . They generate an electric dipole  $p$  and a magnetic dipole  $m$  in each sphere. The interaction between the two spheres (each of radius  $R$ ) generates a non-null Z-component for the electric dipole or for the magnetic dipole. This depends on both the orientation of the dimers and the polarization of the impinging wave.  $d$  corresponds to the gap distance between the two spheres ..... 175

Figure 3.18 Linear polarization degree  $P_L$  and scattered intensities from experiments and simulations at  $90^\circ$  for the sphere dimer as a function of the size-parameter  $q$  with (a)  $d_0=2$  and (b)  $d_0=1/3$ . The exciting field is linearly polarized and the electric field is either perpendicular ( $I_s$ ) or parallel ( $I_p$ ) to the scattering plane (see Figure 3.13). (MD=Magnetic dipole resonance, ED=Electric dipole resonance). The low (OFF)/high (ON) states are indicated with 0/1 and black arrows. (c) and (d) are zoomed details for  $I_s$  of plots (a) and (b) respectively..... 177

Figure 3.19 Polar plots showing the angular variations of the intensities  $I_s$  and  $I_p$  of the scattered fields around the switching frequency for  $q$  between 0.76 and 0.81 in large gap ( $d_0=1/3$ ) and ( $d_0=2$ ) cases ..... 178

## List of figures

---

Figure 3.20 (a) Experimental setup with directive C-band parabolic antennas. (b) Raw measured scattered fields for $\theta r = \pm 90^\circ$ . (c) Raw measured incident fields. (d) Raw measured total fields. These measurements have been made 3 times for three different dimers selected from a set of four identical spheres (all of them have diameter of 18 mm and $\epsilon r = 15.7 + 0.2j$ .....	179
Figure 3.21 Tomography of the soot particle collected from a propane-air flame [117] .....	182
Figure 3.22 TEM images of combustion generated soot aggregates showing the effects of (a) necking and (b) overlapping [76] .....	183
Figure 3.23 effect of extinction explained with an incident electromagnetic illumination and a receiver. (a) with absence on particle. (b) with the presence of a particle [118] .....	184
Figure 3.24 The corresponding configuration to the measurement of the Extinction Cross Section .....	185
Figure 3.25 The initial soot aggregate particle from propane-air flame and its corresponding analog <i>AGSEM</i> manufactured in stereolithography at the CTTM. The particle dimensions and the working wavelengths are multiplied by 66666 .....	186
Figure 3.26 Illustration of a set of 9 virtual aggregates with different degrees of necking and overlapping. The three aggregates we chose for microwave analog experiments are indicated by the red dashed rectangle.....	186
Figure 3.27 The initial numerically generated soot aggregate particles with three degrees of necking ( $\alpha = 0.005, 0.5$ and $1$ ) and their corresponding analogs ( <i>AG005</i> , <i>AG05</i> and <i>AG1</i> ) manufactured in stereolithography at the CTTM. The particles dimensions and the working wavelengths are multiplied by 154450.....	187
Figure 3.28 The three different discretization of the aggregate <i>AGSEM</i> of realistic morphology ..	188
Figure 3.29 The alignment procedure showing the aggregate <i>AG005</i> on the expanded polystyrene holder with the dielectric alignment spheres.....	189
Figure 3.30 Schematics of the scattering configurations seen from the top showing the four studied orientations on the aggregates analogs.....	189
Figure 3.31 A schematic explaining the used optimized configuration based on decomposition of the receiving excursion into three different zones, and the selected power profiles in each zone .....	189
Figure 3.32 Schematic showing the settings of the measurement setup for the measurement of the soot analogs. Measurements are made in Softgating mode with the DRG horn antennas .....	190
Figure 3.33 Amplitudes of scattered fields from experiments, DDA 50 and MOM 50 by the aggregate of realistic morphology in (left) non-optimized configuration and (right) optimized configuration at 4 GHz, 10 GHz and 16 GHz .....	191

Figure 3.34 Amplitude in dB of the incident and total fields corresponding to the measurement of *AGSEM* as a function of the size-parameter ..... 193

Figure 3.35 *Cext* from experiment, three DDA simulations and three MOM simulations for the aggregate *AGSEM* as a function of the size-parameter. (a) Experiment and DDA simulations in *m2*. (b) Experiment and DDA simulations in *dBm2*. (c) Experiment and MOM simulations in *m2*. (d) Experiment and MOM simulations in *dBm2* ..... 194

Figure 3.36 Schematic showing the orientation of the aggregates *AG005* and *AG1* at  $\theta_o = 0^\circ$  and  $\theta_o = 90^\circ$  ..... 195

Figure 3.37 *Cext* from experiment and MOM simulation in *dBm2* for the two aggregates *AG005* and *AG1* as a function of the size-parameter in two orientations (a)  $\theta_o = 0^\circ$  and (b)  $\theta_o = 90^\circ$  ..... 195

Figure 4.1 Photography of the quasi-monostatic measurement showing the transmitting and receiving antennas on the wagon, the metal plate and the quasi-monostatic angle ..... 198

Figure 4.2 Schematic explaining the quasi-monostatic measurement and the polarizations definition ..... 198

Figure 4.3 Schematic showing the settings of the setup for the quasi-monostatic measurement of the forest scaled model. Measurements are made in Hardgating mode with the X-band antennas..... 199

Figure 4.4 Comparison between experimental and simulated fields scattered by the squat metal cylinder. (a) Amplitudes at 9 GHz. (b) Phases at 9 GHz. (c) Amplitudes at 11 GHz. (d) Phases at 11 GHz ..... 200

Figure 4.5 (a) The Plexiglas cylinder. (b) The metal cylinder ..... 201

Figure 4.6 Schematic showing the placement of the Plexiglas cylinder and the metal L during the measurement ..... 201

Figure 4.7 Comparison between experimental and simulated fields scattered by dielectric Plexiglas square cylinder in both  $\varphi\varphi$  and  $\theta\theta$  polarizations. (a) Amplitudes at 9 GHz. (b) Phases at 9 GHz. (c) Amplitudes at 11 GHz. (d) Phases at 11 GHz..... 202

Figure 4.8 Comparison between experimental and simulated fields scattered by metal L in both  $\varphi\varphi$  and  $\theta\theta$  polarizations. (a) Amplitudes at 9 GHz. (b) Phases at 9 GHz. (c) Amplitudes at 11 GHz. (d) Phases at 11 GHz ..... 203

Figure 4.9 Variation of the real and imaginary parts of permittivity of the prepared liquid as a function of the frequency ..... 204

Figure 4.10 Schematic showing the positions of the dielectric cylinders and the metal L in the three studied cases..... 204

## List of figures

---

Figure 4.11 Photography of the combinations of the dielectric cylinder and metal L placed in their polystyrene holder. (a) L alone. (b) L + dielectric behind. (c) L + dielectric ahead. (d) L + dielectric beside .....	205
Figure 4.12 Variation of the scattered field in amplitude and phase from experiments and DEMOS simulation at 8 GHz in $\varphi\varphi$ polarization for the case of dielectric is behind the metal L .....	206
Figure 4.13 Variation of the scattered field in amplitude and phase from experiment and simulation at 11 GHz in $\varphi\varphi$ polarization for the case of dielectric is ahead the metal L.....	206
Figure 4.14 Variation of the scattered field in amplitude and phase from experiments and DEMOS simulation at 11 GHz in $\varphi\varphi$ polarization for the case of dielectric is beside the metal L.....	206
Figure 4.15 Holograms of the amplitudes of the experimental scattered fields obtained with (a) metal L. (b) metal L+ dielectric behind. (c) L + dielectric ahead. (d) L + dielectric beside .....	207
Figure 4.16 Pictures of the trees and tank analogs. (a) Tank analog alone. (b) The complete scene composed by the five trees analogs and the tank at the middle, all of the place at the center of the specific polystyrene holder .....	208
Figure 4.17 The four investigated orientations of the scene composed of the five trees analogs and the tank analog .....	208
Figure 4.18 Experimental scattered fields by the tank, trees and tank + trees at 11 GHz in $\varphi\varphi$ polarization in amplitude and phase.....	209
Figure 4.19 amplitude of the fields scattered by the components on the scene. (a) Tank + trees in $\varphi\varphi$ . (b) Tank + trees in $\theta\theta$ . (c) Trees in $\varphi\varphi$ . (d) Trees in $\theta\theta$ . (e) Tank in $\varphi\varphi$ . (f) Tank in in $\theta\theta$ .....	210

## RESUME EN FRANÇAIS (VERSION LONGUE)

---

### ANALOGIE MICROONDE

Quand une onde électromagnétique de longueur d'onde  $\lambda$  illumine un objet dont les dimensions sont de l'ordre de grandeur de  $\lambda$ , son énergie se disperse dans l'entourage de l'objet. La dispersion de cette énergie dans l'espace ainsi que son amplitude dépendent non seulement de la fréquence et de l'angle d'incidence de l'onde, mais aussi de la géométrie et de la composition matérielle de l'objet. Ce phénomène de dispersion d'énergie s'appelle « la diffraction électromagnétique ». La diffraction électromagnétique est à la base d'une large variété de technologies profitant de certains signaux diffractés afin de localiser et/ou obtenir des informations concernant la nature et la structure d'une cible. Il existe, dans le domaine de microondes plusieurs possibilités d'application de ce phénomène qui peuvent être en rapport avec la télédétection, l'imagerie non-destructive, ainsi qu'avec la détection radar des avions, des missiles, des fusées, des bateaux destinés à des usages militaires et civils [1]. D'autres applications peuvent se trouver dans le domaine de l'optique, telles que la microscopie par diffraction optique, la tomographie optique, et le diagnostic de certaines propriétés physiques de particules, etc [2].

Les expériences de laboratoire sont souvent vues sous un angle de complémentarité avec les approches théoriques de l'examen du problème de la diffraction dans le but de développer des instruments qui leurs sont associées. Contrairement aux mesures *in situ*, ces expériences de laboratoire procurent un environnement quasi-idéal permettant d'entreprendre des études dans des conditions parfaitement contrôlées, où l'on maîtrise la connaissance de la composition exacte de la cible, sa position, son éclairage, etc. Une chambre anéchoïque représente l'environnement le plus proche de l'espace libre pour réaliser des expériences de diffraction avec des fréquences microondes, souvent utilisées pour des applications radar.

L'analogie microonde consiste à réaliser une translation d'échelle d'un problème de diffraction électromagnétique, par exemple de la bande du visible vers la bande des microondes ou dans l'autre sens de la bande UHF vers la bande des microondes, en gardant le même rapport entre la longueur d'onde et les dimensions de l'objet tout en conservant ses caractéristiques diélectriques et magnétiques. Le principe de l'analogie microonde est illustré en Figure 1. Les objets cibles ici sont une particule de suie étudiée dans la bande du visible et un arbre étudié dans les bandes UHF/VHF. Dans les deux cas, la translation d'échelle par un

facteur  $k$  et la conservation des propriétés électromagnétiques ont permis d'obtenir des analogues microondes qui remplacent les objets initiaux pour réaliser des expériences de diffraction.

Comme exemple de mesures faites en utilisant le principe d'analogie microonde, si l'on ne met en œuvre que les parties métalliques, nous pouvons mentionner les mesures de la Surface Equivalent Radar (SER) des avions, des missiles et d'autres cibles aux dimensions énormes, parce qu'elles permettent d'éviter les lourdes dépenses sur les installations pour créer des environnements larges [3]–[5]. Elle est également pratique dans l'étude de la diffraction dans les bandes du visible et du proche infrarouge par des particules aux dimensions micrométriques, échelle à laquelle les mesures souffrent de la difficulté d'un contrôle précis des paramètres expérimentaux tels que la forme de la particule, sa position et son orientation, ses propriétés électromagnétiques et son éclairage [6].

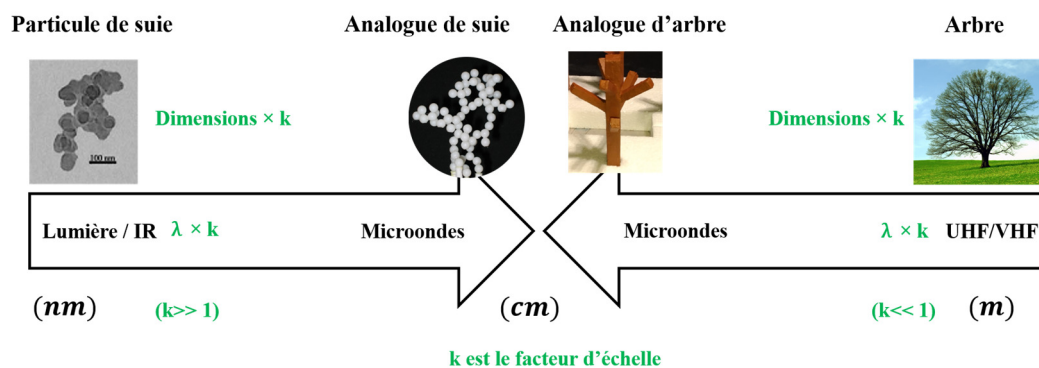


Figure 1 Le principe de l'analogie microonde appliqué à l'étude de la diffraction par une particule de suie et par un arbre

## LE SYSTEME DE MESURES MICROONDES SU CCRM

Dans cette thèse, des études d'analogie microonde sont réalisées dans la chambre anéchoïque du Centre Commun de Ressources en Microondes (CCRM). Cette chambre a été construite en 1996 pour des finalités de caractérisation d'antennes, de mesure de diffraction et de mesure de compatibilité électromagnétique. Elle a été utilisée pour des études de diffraction sur des cibles bidimensionnelles et tridimensionnelles dont les mesures ont été mises à la disposition de la communauté scientifique pour permettre de tester des algorithmes d'inversion avec des données réelles. Ces mesures sont connues en tant que « Fresnel Database » [7]–[9]. Le progrès accomplis dans le développement d'un système de mesures robustes et d'outils dédiés au post-traitement ont motivé des chercheurs pour étudier les problèmes complexes de diffraction à travers des expériences d'analogie microonde dans la bande de fréquences entre 2 GHz et 18 GHz (Figure 2). Par exemple, l'analogie microonde a été utilisée



pour étudier la diffraction par des analogues des agrégats de suie de géométrie complexe, par des modèles de forêts à échelle réduite et par des sphères de permittivité élevée que l'on souhaite utiliser dans le domaine visible [10]–[12].

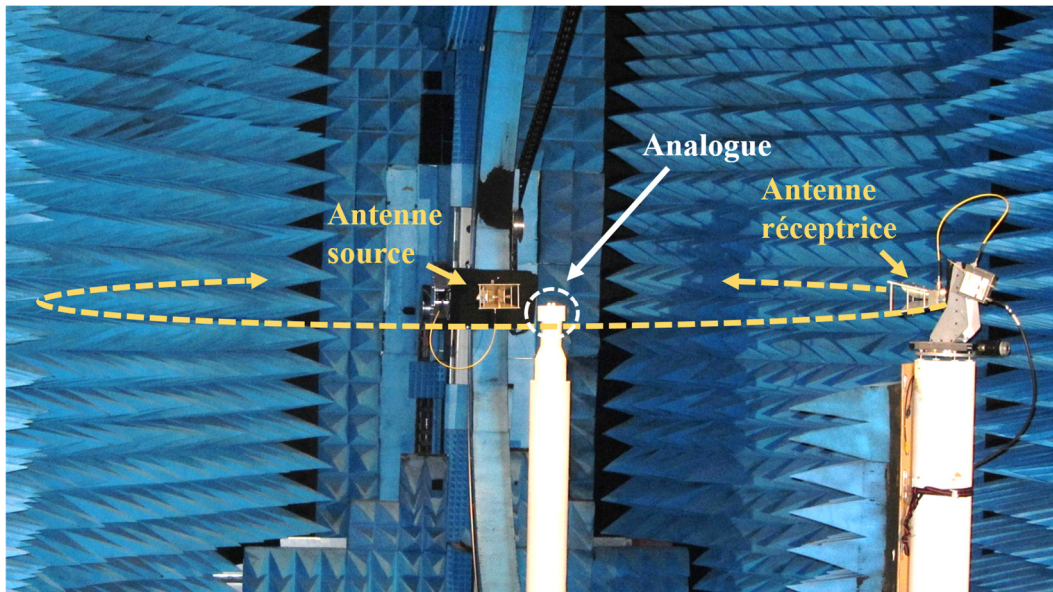


Figure 2 Le dispositif de mesure dans la chambre anéchoïque du CCRM

## MOTIVATION DE CE TRAVAIL

Afin de mieux combler les besoins de la communauté de recherche, il est vital non seulement d'avoir à disposition un système de mesure polyvalent capable de fournir des mesures fiables, mais aussi de posséder les outils de fabrication pour obtenir des analogues ayant les propriétés électromagnétiques et géométriques requises. Cependant, toutes les mesures de diffraction effectuées par le passé ont été obtenues à partir d'équipements de mesures relativement anciens, ayant des caractéristiques qui ont atteint leurs limites au fil du temps. De plus, la plupart des cibles mesurées étaient fabriquées au moyen de techniques classiques, ce qui limite notre capacité de contrôler leurs propriétés. La fabrication additive avait été utilisée pour contrôler la géométrie des cibles mais pas leurs permittivités.

## OBJECTIFS DE CETTE THESE

Le premier objectif de cette thèse est d'accroître les capacités expérimentales des équipements du CCRM à travers l'optimisation du système de mesures, la caractérisation du bruit aléatoire et des signaux parasites, et la proposition des solutions pour réduire leurs influences sur les mesures. La motivation de ce travail est l'étude d'objets faiblement diffractant dont la mesure était imprécise dans le passé. Ce qui fait la faiblesse de leur pouvoir de diffraction est soit leur faible permittivité, soit leur dimension considérée petite par rapport à la longueur

d'onde. L'étude d'objets faiblement diffractant introduit certaines difficultés car les niveaux des champs mesurés sont très faibles et sensibles à toute sorte d'erreurs expérimentales. Le deuxième objectif est de permettre un meilleur contrôle des propriétés géométriques et électromagnétiques des cibles en développant de nouvelles procédures de fabrication.

### SYSTEME DE FILTRAGE TEMPOREL « HARDGATING »

Nous nous sommes intéressés à étudier les signaux parasites qui interviennent lors d'une mesure de diffraction, comme le couplage entre les antennes et les différentes réflexions indésirables dans la chambre (Figure 3). Le moyen le plus commun pour isoler la réponse de la cible des signaux parasites est le Softgating basé sur l'application d'une Transformée de Fourier qui permet un fenêtrage temporel des signaux. L'inconvénient de cette technique est la longue durée de mesure nécessaire pour acquérir un grand nombre de fréquence permettant une bonne représentation temporelle du signal. Pendant cette thèse j'ai mis en place un système de mesure Hardgating qui permet de faire des mesures en mode pulsé en hachant les signaux continus. Le Hardgating permet de faire un filtrage en temps réel en utilisant un switch d'émission, un switch de réception créé par un générateur de fonction. L'efficacité du système a été validée à partir de comparaison de mesures en Hardgating et en Softgating avec les mêmes cibles. Des résultats comparables ont été obtenus avec les deux techniques (Figure 4). Ce système a été ensuite utilisé dans plusieurs études pendant cette thèse et il a permis de réduire significativement la durée de mesure.

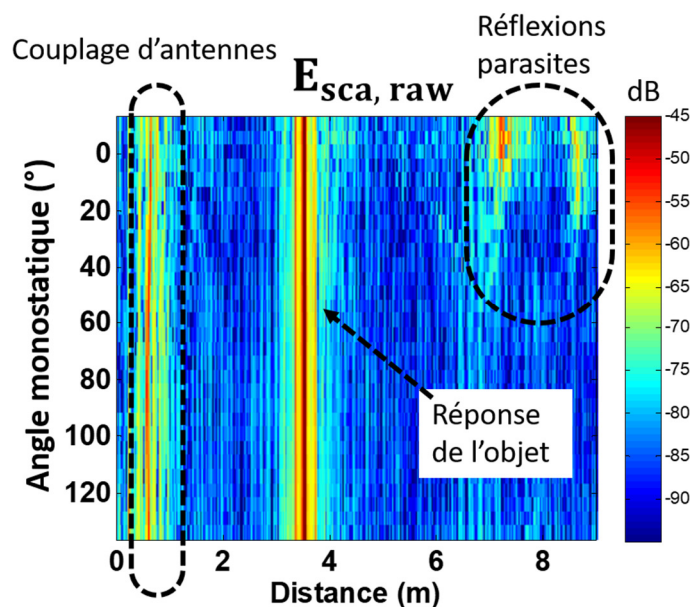


Figure 3 Réponse impulsionnelle montrant l'amplitude en dB du champ diffracté brut mesuré par une sphère diélectrique de diamètre 50.75 mm, dans le domaine temporel et en fonction de l'angle monostatique et de la distance parcourue par le signal

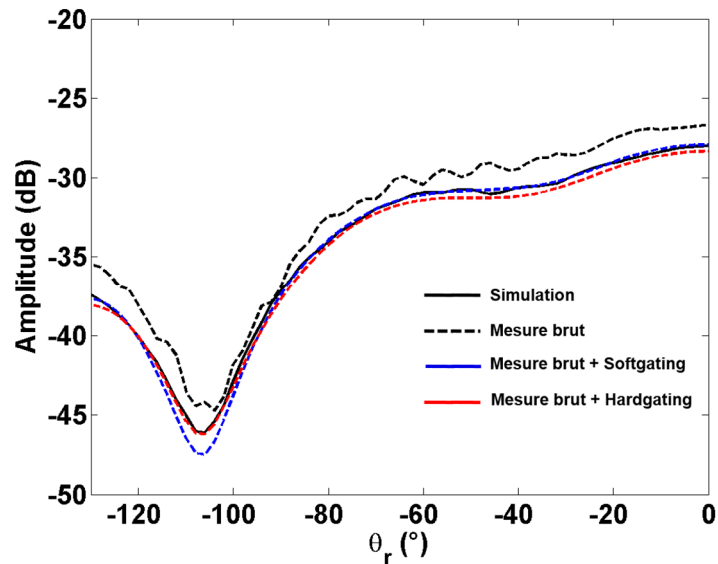


Figure 4 Amplitude du champ mesuré diffracté par un palet métallique à 2 GHz en configuration bistatique

## OPTIMISATION DU PARAMETRAGE DU SYSTEME

Une étude exhaustive de la caractérisation des nouveaux équipements de mesure a été effectuée et le bruit aléatoire a été caractérisé dans une configuration bistatique. A partir de la caractérisation du bruit aléatoire sur la partie réelle et la partie imaginaire des champs mesurés, il est possible de déterminer les incertitudes associées à chaque point de mesure. J'ai montré que la précision de mesure est proportionnelle à l'amplitude du champ mesuré. Avec les objets que nous étudions, en configuration bistatique, le niveau du champ mesuré est élevé dans la direction de diffraction avant et faible dans la direction de diffraction arrière. Aussi, afin d'optimiser la précision des mesures, j'ai proposé une technique qui consiste à décomposer l'excursion angulaire du déplacement du récepteur en différentes zones. Un paramétrage spécifique est appliqué dans chaque zone qui permet d'augmenter le niveau du champ tout en évitant les comportements non-linéaires des appareils de mesures. Le réglage du niveau de signal est obtenu à l'aide de deux paramètres : la puissance du synthétiseur de référence et le réglage de l'atténuateur interne de l'Analyseur de Réseaux sur la voie du signal test ( $b_2$ ). La mesure du champ diffracté par une sphère de diamètre 35 mm et de très faible permittivité ( $\epsilon = 1.02 + 0j$ ) est présenté en Figure 5. Elle est comparée avec un paramétrage non-optimisé et un paramétrage optimisé. Nous pouvons aisément constater que la technique d'optimisation proposée a permis d'avoir une bonne réduction du bruit sur le champ diffracté, notamment en diffraction arrière.

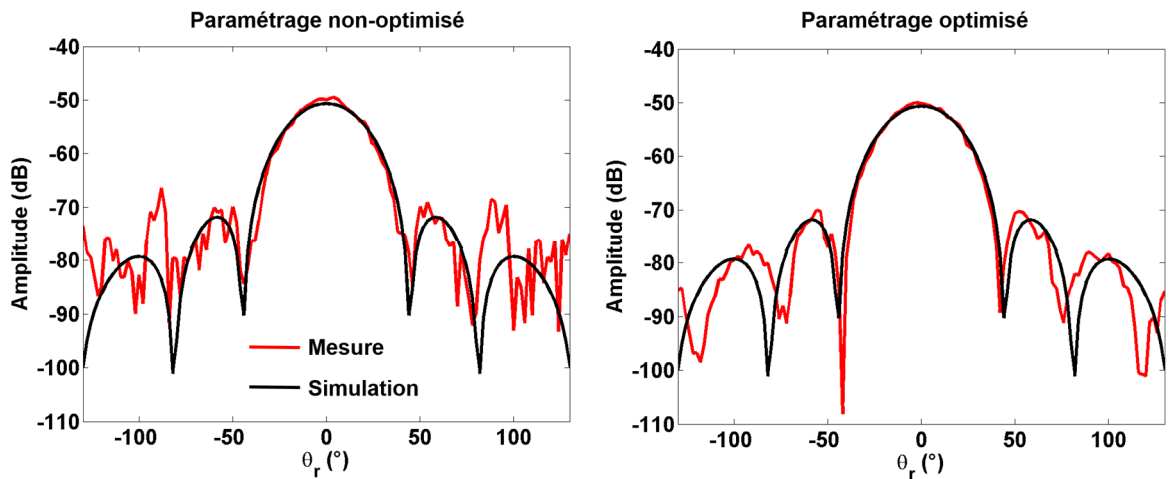


Figure 5 Comparaison entre la mesure et la simulation de l'amplitude du champ diffracté par une sphère de 35 mm de diamètre et de permittivité  $\varepsilon = 1.02 + 0j$ , dans un cas non-optimisé (à gauche) et un cas optimisé (à droite)

## ANALOGUES AYANT DES PROPRIETES CONTROLEES

Le contrôle des propriétés diélectriques des analogues a été étudié dans le cadre d'une collaboration établie avec le "Centre de Transfert et de Technologie du Mans" (CTTM). Des analogues de géométries complexes ont été fabriqués par stéréolithographie et une nouvelle technique a été proposée pour obtenir des analogues ayant des valeurs de permittivité complexe « à la demande ». Trois catégories de permittivité relative ont été étudiées en partant de la permittivité relative complexe du matériau de base qui est  $\varepsilon = 2.9 + 0.08j$ . i) Des objets de faible partie réelle de permittivité ( $1 < \varepsilon' < 2.9$ ), ii) des objets de partie réelle de permittivité élevée ( $\varepsilon' > 2.9$ ) et iii) des objets avec une partie imaginaire de permittivité non-nulle ( $\varepsilon'' \neq 0$ ). Un progrès considérable a été obtenu pour les objets de faible permittivité. La technique proposée pour atteindre cet objectif consiste à créer des porosités aléatoires dans les objets à partir des structures maillées. La géométrie voulue est d'abord créée ou importée à l'aide du logiciel gratuit « Gmsh » [13], puis transformée en structure maillée. Ensuite, le fichier « .msh » généré est envoyé à nos collègues du CTTM qui génèrent des cylindres qui remplacent les lignes qui relient les nœuds des mailles en utilisant le logiciel commercial « CATIA » [14]. Après avoir créé des cylindres, le fichier CAO est généré et envoyé à l'imprimante 3D (Figure 6). Les deux paramètres qui permettent le contrôle de la porosité, en par conséquent la permittivité, dans le volume de la sphère sont les longueurs et les diamètres des cylindres. Quelques résultats obtenus sur des sphères de faibles permittivités sont présentées en Figure 7.

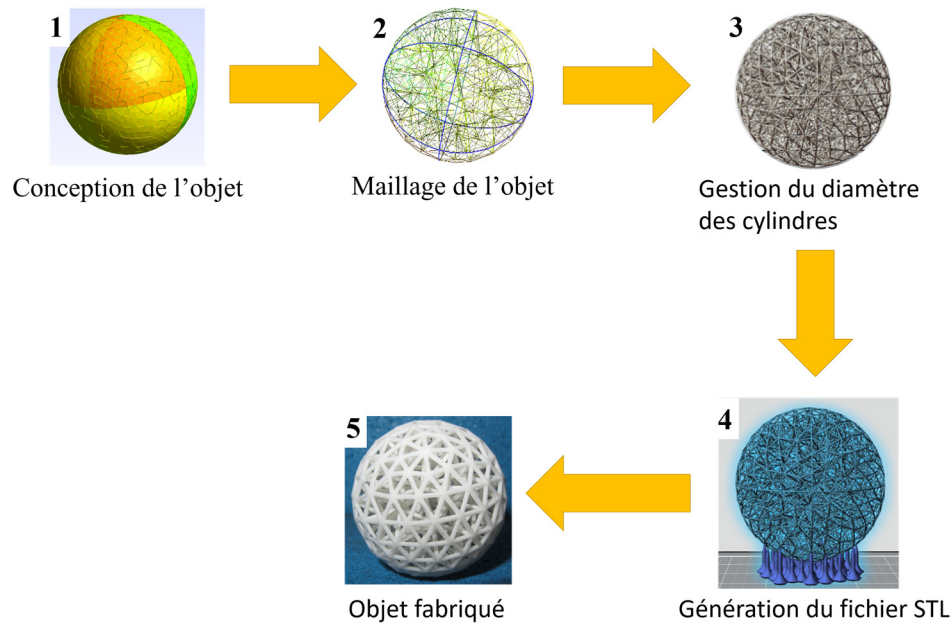


Figure 6 Les étapes de la technique proposé pour créer une faible permittivité à partir du matériau de base

Nom	Acrylate $_{6,6}^{2,5}$	Acrylate $_{6,6}^1$	Acrylate $_{4,7}^{0,56}$	Acrylate $_{4,7}^{0,2}$	Acrylate $_{1,4}^{0,35}$
Pourcentage d'air en volume	3 %	83 %	90 %	98 %	73 %
Longueurs des cylindres (mm)	6,6	6,6	4,7	4,7	1,4
diamètres des cylindres	2,5	1	0,56	0,2	0,35
Valeur mesurée de $\epsilon'$	2,3	1,25	1,15	1,02	1,4
Valeur estimée de $\epsilon'$ (Maxwell-Garnett)	2,8	1,21	1,13	1,02	1,35

Figure 7 Photos et valeurs de permittivités de quelques sphères de faible permittivité fabriquées selon la technique de maillage proposée

## ÉTUDES BISTATIQUE DES CIBLES FAIBLEMENT DIFFRACTANTES

L'analogie microonde a été utilisée dans une configuration bistatique pour étudier la diffraction par trois types d'objets :

1. Des objets sphéroïdaux de faible permittivité ( $\epsilon' < 1.5$ ), analogues de micro-algues photosynthétiques. L'application de cette étude est dans le développement de la technologie des photobioreactors. La fabrication de ces analogues a été faite par usinage de mousse de polyuréthane de faible densité (Figure 8-a). Ces analogues ont été mesurés à une seule fréquence 18 GHz en configuration Hardgating.



2. Des agrégats de suie de formes complexes. Deux types d'analogues d'agrégats ont été mesurés : i) un agrégat de morphologie réaliste déterminé à partir d'une tomographie réalisée avec des mesures faites avec un Microscope à Balayage Electronique et ii) des agrégats avec différentes épaisseurs de couches de matière couvrant les particules. Les analogues ont été fabriqués par stéréolithographie dans le cadre de notre collaboration avec le CCTM. Dans le cas de cette étude nous nous sommes intéressés au champ diffracté par les analogues mais aussi à la mesure de la section efficace d'extension des particules (Figure 8-b).
3. Des sphères, analogues de particules de silicium dans la bande du visible ou du proche infrarouge, de permittivité  $\varepsilon = 15.7 + 0.2j$ . Dans cette étude nous proposons de réaliser les fonctions de switch et de séparateur de faisceau en utilisant une paire de sphères. Nous nous sommes particulièrement intéressés par l'observation du champ diffracté par le dimer, à  $90^\circ$  du faisceau incident, en fonction de la polarisation de l'onde incidente (Figure 8-c).

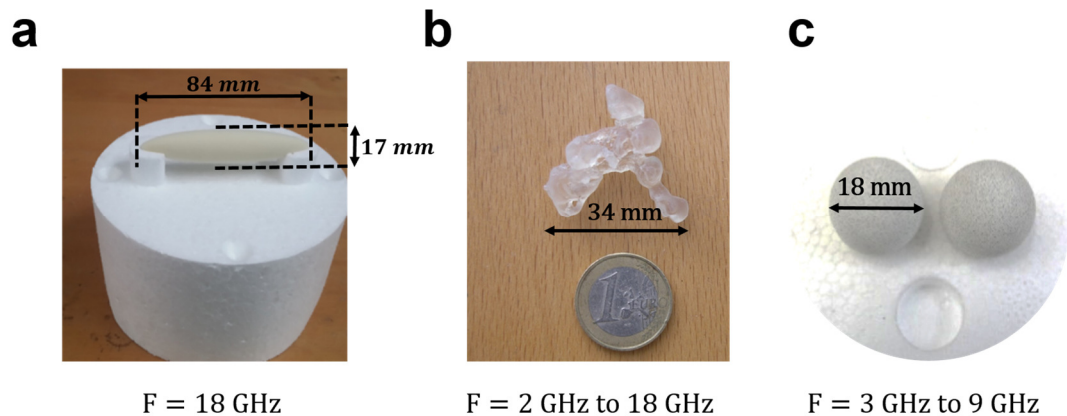


Figure 8 Photos des analogues étudiés en configuration bistatique. (a) Analogues de micro-algues sphéroïdaux. (b) Analogue d'une particule de suie. (c) Dimer analogue de particules de silicium

## MISE EN PLACE D'UN SYSTEME DE MESURES QUASI-MONOSTATIQUE

Une nouvelle configuration de mesures quasi-monostatique a été également ajoutée au dispositif de mesure pendant cette thèse. Une antenne émettrice et une antenne réceptrice peuvent désormais être positionnées sur le même chariot sur l'arche verticale avec un angle de quasi-monostatisme qui peut descendre jusqu'à  $12^\circ$  (Figure 9). Les mélangeurs d'émission et de réception qui étaient à plusieurs mètres des antennes ont aussi été fixés sur le même chariot afin d'éviter la propagation des signaux RF dans des longues câbles et éviter les potentiels problèmes d'atténuation et de déphasage de signaux. L'efficacité de la configuration a été validée par des mesures quasi-monostatique avec des objets diélectriques et métalliques. Elle

a été ensuite utilisée pour des études de diffraction sur des scènes de forêts composées d'analogues d'arbres associés au véhicule métallique. Un exemple de mesure quasi-monostatique avec un palet métallique comme cible est présenté en (Figure 10). Les résultats expérimentaux sont comparés aux simulations en amplitude et phase dans les deux cas de co-polarisations.

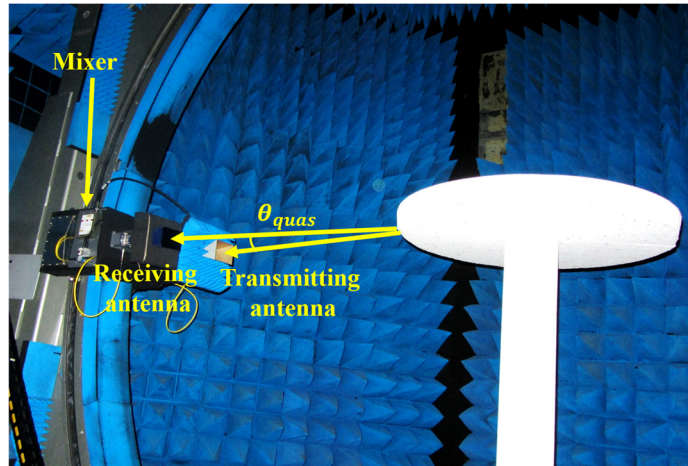


Figure 9 Photo du système de mesure dans une configuration quasi-monostatique

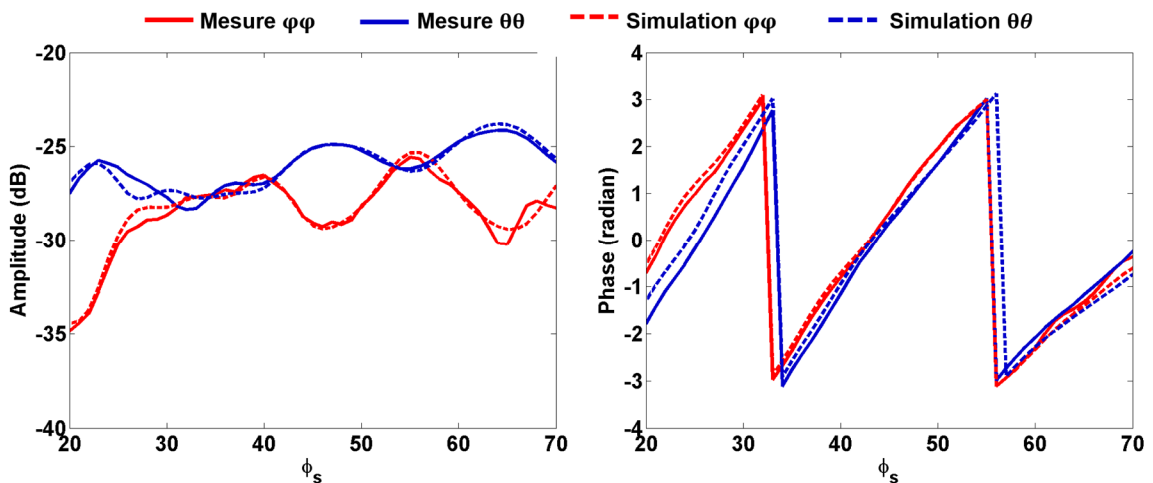


Figure 10 Comparaison en amplitude (gauche) et phase (droite) entre mesure et simulation du champ diffracté par un palet métallique, à 11 GHz, en configuration quasi-monostatique dans les deux cas de polarisations  $\varphi\varphi$  et  $\theta\theta$

## CONCLUSION

L'analogie microonde est un moyen efficace pour étudier expérimentalement la diffraction électromagnétique par des objets de dimensions micrométriques (particules, microorganismes, etc.) ou de dimensions métriques (véhicules, arbres, comètes, etc.). Une transposition vers l'échelle microonde est donc réalisée en conservant le même rapport entre les di-

mensions de l'objet et la longueur d'onde, ainsi que les propriétés diélectriques (et magnétiques) de l'objet. Cette thèse a eu pour objectif d'étendre le potentiel des applications de l'analogie microonde, i) par l'implication des techniques de fabrication additive dans le contrôle de la géométrie et de la permittivité complexe des analogues, ii) par l'optimisation de l'instrumentation du système de mesure. Les expériences d'analogie microondes ont été réalisées dans la chambre anéchoïque du CCRM. Un intérêt particulier a été porté aux objets faiblement diffractant. Les réflexions parasites dans la chambre anéchoïque ont été étudiées et identifiées, et leur filtrage a été rendu possible par la mise en place d'un système de filtrage temporel « Hardgating ». Le bruit aléatoire perturbant les mesures a été également caractérisé. A la suite, une nouvelle technique d'optimisation du paramétrage des appareils de mesure, qui tient compte de la nature des objets étudiés, a pu être proposée. Cette technique consiste à utiliser un réglage polyvalent de la chaîne de mesure en fonction de la position angulaire de l'antenne réceptrice en configuration bistatique. Les bénéfices de ces diverses optimisations des paramètres de mesure ont été démontrés et ils ont permis de mesurer des niveaux de section efficace radar aussi faible que  $-60 \text{ dBm}^2$ . Des sphéroïdes de faible permittivité, analogues de micro-algues, des analogues d'agrégats des suies de formes complexes et des sphères de haute permittivité, analogues de particules de silicium ont été mesurés en configuration bistatique. De même, des scènes forestières composées d'analogues d'arbres et de véhicules ont été mesurés en configuration quasi-monostatique.

L'axe principal sur lequel j'ai travaillé pour élargir le champ des applications de l'analogie microonde est l'adaptation des techniques de fabrication des analogues pour créer des objets de caractéristiques diélectriques (et magnétiques) choisies et de géométries contrôlées. La fabrication additive par stéréolithographie est désormais impliquée dans ce but dans le cadre d'une collaboration avec le Centre de Transfer et de Technologies du Mans (CTTM). Nous avons proposé une nouvelle technique qui permet, en créant des structures poreuses, de baisser la permittivité d'un analogue à partir du matériau de base. Les avancées sur le contrôle de la permittivité permettent de réaliser des analogues de géométrie maîtrisée avec des permittivités à la carte dans la gamme de 1 à 3. Les problèmes d'analogues de permittivité élevée et d'analogues avec une partie imaginaire de permittivité non-nulle ont également été étudié mais les investigations méritent d'être poursuivies dans ces direction pour élargir encore les possibilités.



## GENERAL INTRODUCTION

---

### BACKGROUND

When an electromagnetic wave illuminates a certain target, the carried energy by the wave is dispersed in all the surrounding directions. The spatial distribution of the energy and its strength depends upon the frequency and the angle of incidence of the wave, but also depends on the size, shape and material composition of the target. This energy dispersion is called electromagnetic scattering, and the target is called a scatterer. Electromagnetic scattering is at the core of a wide variety of engineering technologies that use a scattered signal to localize and/or retrieve structural information about the scatterer. Many applications exist in the radiofrequency bands which are mostly related to remote sensing, non-destructive imaging, and radar identification of aircraft, missiles, rockets, ships and other objects for military and civil purposes [1]. Other applications operate at the optical band, such as optical diffraction microscopy, optical tomography, *in situ* remote diagnostics of certain physical properties of particles and many others [2].

Laboratory experiments are best viewed as complementary to other theoretical approaches of investigating the scattering problem for the development of the associated technologies. Unlike the measurements in the “real world”, they provide the ideal environment to make a study in well controlled conditions, such as the knowledge of the target’s composition, its position, its illumination, etc. They allow to highlight the sensibility of the scattered signal with respect to the experimental error, to validate the post-processing methods, to clarify the optimal measurement conditions and to make a cross-validation with theoretical solutions of the problem. Thus, if the laboratory experiments are sufficiently controlled and accurate, they can be used as experimental simulations of the real situations that may be difficult to control, as it is for instance in astronomy when observing comets with radio waves or in optics at microscale when the scatterers are of nanometric dimension, and thus difficult to accurately known. Anechoic chambers represent a good free-space environment for laboratory scattering experiments at the radiofrequencies and hyperfrequencies, mostly used for radar applications.

According to Maxwell’s equations, the basic principle of electromagnetic theory, a linear electromagnetic system can be up-scaled or down-scaled in frequency, with the dimensions scaled in proportion to the wavelength. This law of electromagnetic similitude, known by the Scale Invariance Rule (SIR), states that an electromagnetic system will give equivalent results at any frequency if all geometrical dimensions of the system are scaled in proportion

to the wavelength, while keeping the dielectric and magnetic characteristics constant (and being far enough from the atomic scale). For example, the scattering pattern of a real radar target having a maximum dimension of 40 m and measured at 1 GHz, can be identically retrieved from a constructed scaled analog having a maximum dimension of 1 m and measured at 40 GHz, under the condition of conserving the same initial permittivity and permeability. Microwave analogy describes the situation when a laboratory electromagnetic scattering problem is up-scaled to the microwave wavelengths from visible and terahertz bands, or down-scaled to the microwave from radiofrequency bands. Microwave analogy is useful in Radar Cross Section (RCS) measurements on aircrafts, missiles and other huge dimensions targets, when the measurements at the real scale are cost-intensive [3], or when the effect of a design variation on the RCS is needed to be determined before choosing the final design [4] or even to allow well-controlled experiments in a small environment [5]. Microwave analogy is also very helpful for investigating the scattering by micrometer-sized particles at the visible and near-visible wavelengths. In fact in the optical scale, the real scattering targets, the wavelengths, the permittivity and permeability are “as they are”. Therefore difficulties may appear when precise and controlled experiments are needed. The main origin of the difficulties may be with building a scattering object with the required size, shape, morphology and composition. Another origin of difficulty may be the limitation in sensitivity of the optical device or the difficulty of measuring the phase of the signal.

In order to show the great potential of this approach and illustrate it, I present the example in Figure 0.1. The real targets of interest here are a soot nanoparticle and a tree, which are proposed for study in terms of their scattering, at visible and UHF/VHF bands respectively. In the former case, the soot particles have complex shapes and in the former case, the trees are also complex in terms of both morphology and composition. In both cases, a twofold change of scale makes it possible to obtain analog scale models on the centimeter scale and to replace the initial optical/radio waves by microwaves in order to measure the characteristics of electromagnetic radiation interacting with the analog targets.

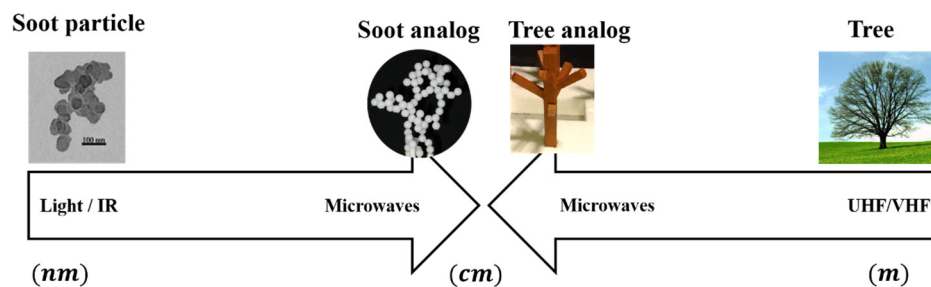


Figure 0.1 Scheme showing the principle of the microwave analogy applied to the scattering of electromagnetic waves by soot particles and a forest environment (tree)

In this thesis the microwave scattering measurements are made in the facility of the anechoic chamber of the Centre Commun de Ressources en Microondes (CCRM). The facility was built in 1996 to be used in antennas characterization, scattering measurements and electromagnetic compatibility. It was used in scattering studies on bi-dimensional targets and the measurements were made available for the scientific community for them to test their reconstruction algorithms on real data. They are known under the name the “Fresnel database” first published in 2001 [7] then in 2005 on inhomogeneous targets [8]. Later, experiments on three-dimensional targets such as spheres, cylinders and aggregate of spheres were performed and were diffused as the Fresnel database 2009 [9]. The achieved advances on developing a robust measurement setup and dedicated post-processing tools, in addition to the particular features of the setup allowing to make spherical measurements, have motivated researchers to take profit of the capacity of the facility to investigate complex scattering problems through microwave analogy in the frequency band between 2 GHz and 18 GHz. For instance, scattering measurements on complex shaped aggregates, scaled model of a forest and small spheres were successfully performed [10]–[12].

In order to further response the demands of the research community, it is crucial to have a versatile setup providing accurate measurements, but it is also necessary to possess the fabrication tools to satisfy the required electromagnetic properties of the targets. However, most of the scattering measurements made before my thesis were obtained with an “old” measurement setup having acceptable but limited features. The possibilities offered by the new acquired measurement chain were only overviewed and I had to deeply explore them. In addition, most of the measured targets were fabricated using classical machining techniques. The additive manufacturing was used for the fabrication of soot analogs [10] but the control of the permittivity of analogs was not investigated yet.

## **OBJECTIVES**

The first objective of my PhD thesis was to widen the capacity of the experimental setup of the CCRM through optimizing the settings of the measurement, characterizing the noise and propose the solution to reduce its impact on the measurement. I aimed to move forward the utilization of the setup to its limits, to identify its current limits and propose the possible ways of evolution. The motivation behind this work is the aim for investigating lower scattering analogs, with electromagnetic signature weaker than what was measured in the pre-

vious state of the setup. The targets have weak signature either because they have low permittivity contrasts, or because their dimensions are small compared to the wavelength. In fact, the study of low scattering targets introduces particular difficulties. The levels of the measured scattered fields are very low and they are sensitive to all kinds of experimental errors.

The second objective is to allow a control of the geometric and electromagnetic properties of targets by developing new manufacturing processes. Previously, most of the studied targets were obtained using classical machining techniques with distinguished difficulties for obtaining complex shaped targets and lack of accurate control of their complex permittivities. The recent progresses in the development of fast prototyping methods helped to obtain, before this thesis, promising results on 3D printed soot analogs [10], and have highly encouraged making an extensive study for investigating the most appropriate fabrication techniques for developing scaled models, which can be completely analogs to real-life counterparts in term of their morphological and permittivity properties.

Therefore, an extensive study on the characterization of the new measurement setup was made and the measurement uncertainties related to the random error were characterized in a bistatic configuration. I proposed a novel optimization technique that uses, for each measurement case, the best parameters of the setup devices according to the antennas and the target under study. The undesired reflections within the anechoic chamber were also investigated and a noise filtering system utilizing pulsed signals measurement was installed. A new quasi-monostatic measurement configuration was also added to the measurement setup.

I investigated the control of the targets properties within an established collaboration with the “Centre de Transfert et de Technologie du Mans” (CTTM). Complex shaped targets were manufactured in stereolithography and a novel technique was proposed to obtain targets with “on-demand” value of their complex permittivity. The manufactured targets were characterized from the scattering measurements.

Since the aforementioned studies aimed at widening the applicability of the microwave analogy, the achieved progress was evaluated through four applications: (i) low permittivity spheroids, analogs of photosynthetic microalgae, (ii) dimer of high permittivity spheres, analogs of silicon particles, (iii) soot aggregates analogs with complex shape, and (iv) scaled forest scene models composed of tree analogs with some metal vehicle analogs, but thanks to those progresses, there are probably a lot of scattering studies that could benefit from the microwave analogy.

## LAYOUT

This manuscript is organized in four chapters.

In the first chapter, I present the principle and the history and of the microwave analogy and I discuss the state of art of the experimental setup of the CCRM. I detail the geometrical configuration, the previously defined post-processing tools and some examples of microwave analog experiments that were made in the past. The rest of the chapter is dedicated for explaining the contribution of my PhD work in the enhancement of the measurement accuracy through optimization of the setup settings and the implementation of noise reduction Hardgating setup.

In the second chapter, I discuss my work on the implication of the additive manufacturing for controlling the complex permittivities and the shapes of analogs, within the established collaboration with the CCTM. The main novelty brought by this work is the ability to obtain analogs with “on-demand” values of real part of relative permittivity between 1 and 3. Manufactured samples are presented and the results are discussed.

In the third chapter, I present the performed bistatic scattering experiments throughout this PhD. Experiments are made to investigate scattering by microalgae analogs, silicon spheres analogs and soot particles analogs. All of them are dielectrics and with dimensions of the order of the wavelength. For each analog case, the specificity of the measurement is reviewed, correspondent optimization is shown and the experiments accuracy is assessed through comparisons to numerical simulations.

In the fourth chapter, I present the new introduced quasi-monostatic configuration in the experimental facility. A study is performed on a scaled forest scene composed of tree analogs with some metal vehicle analogs. The encountered experimental difficulties are reported and the configuration efficiency is evaluated.

# 1 MICROWAVE SCATTERING MEASUREMENT

---

## 1.1 INTRODUCTION

We previously mentioned two main pre-requisites for realizing microwave analog experiments: (i) the ability to build controlled analogs in morphology and electromagnetic properties and (ii) the ability to measure a scattered energy issued from the interaction of the analog with an impinging electromagnetic wave. The measurement of a scattered field within a space is obtained using different microwave devices that constitute the measurement setup. The features offered by that setup together with different mechanical devices allow to obtain a scattered field at different positions in the space surrounding the target.

At the next level, it is important to talk about the accuracy of a measurement. The measurement accuracy depends upon many criteria, some of them are the settings of their measurement devices, the influence of perturbation signals, and the properties of the target under test itself. Improving the measurement accuracy against the well-defined perturbation sources can be achieved through:

1. Use of dedicated post-processing tools
2. Development of adapted noise filtering techniques
3. Characterization of the noise affecting the measurement and optimization of the measurement setup.

These topics are at the core of this chapter. First, the principle and history of the microwave analogy is presented. An overview is given on some national and international microwave scattering measurement facilities that have similarities with the facility of the CCRM and that could be utilized to carry out microwave analog experiments.

The rest of the chapter is dedicated to explain the measurement setup of the CCRM that is used along this thesis. The state before this thesis of the setup is presented with an introduction to the measurement devices, the geometrical configurations and quasi monostatic measurements, the principle of the measurement of an experimental scattered field and the previously defined post-processing tools. Next, a focus is made on the contribution of this thesis to the improvement of the measurement accuracy through noise filtering and noise reduction techniques.

## 1.2 MICROWAVE ANALOGY

When an electromagnetic wave of certain wavelength encounters an isolated particle matter, the incoming wave scatters in the medium and an electromagnetic scattering phenomenon takes place. The way the scattering behaves depends upon the ratio of the wavelength over the particle's size, its electromagnetic properties and its shape. The investigation of the scattered signal allow to retrieve useful information about the scatterer.

Electromagnetic scattering phenomenon by particles and particle groups is an omnipresent interaction in many engineering and science fields. Hereunder I give some application examples:

- In researches related to combustion, engines performance as well as in researches related to global warming and health, the electromagnetic interaction with soot aggregates is a main focus. Those soot aggregates originate from the agglomeration of carbon nanospheres of diameter between 10 and 100 nm in the process of fuel combustion [15] (Figure 1.1-a).
- In medical and biological research the colloidal gold nanoparticles can be used to label the cells in solid-phase immunoassay when studying microbial and mutant strains and this procedure requires the calculation of the extinction cross section of the gold particles as a function of the used wavelengths in the labeling process [16] (Figure 1.1-b).
- Earth's climate changes studies focus on the atmospheric aerosols such as sea-salt aerosols which cause a direct radiation through absorption and scattering of the solar spectrum and counteract global warming. Accurate electromagnetic models and measurements are needed to quantify the radiative forcing and the optical properties of those aerosols [17] (Figure 1.1-c).
- Dust storms in desert areas represent a significant source of coarse mode particles (particles with diameter greater than 1  $\mu\text{m}$ ). Those particles scatter and partially absorb solar radiation and they have the potential to alter the outgoing terrestrial radiation flux. The dust influences the atmospheric heating rates and the formation of ice clouds. The study of their radiative properties through electromagnetic modelling is crucial in atmospheric science [18] (Figure 1.1-d).
- Global climate models, weather prediction and remote sensing algorithms rely on the parametrization of the cloud microphysics. In the atmosphere, the clouds properties depend upon the moisture of ice particles that are produced from the cooled air. The

small ice crystals can affect the cloud's radiative properties and therefore the quantification of the absorption and extinction coefficients of ice crystals is required through electromagnetic modeling and/or measurement [19] (Figure 1.1-e).

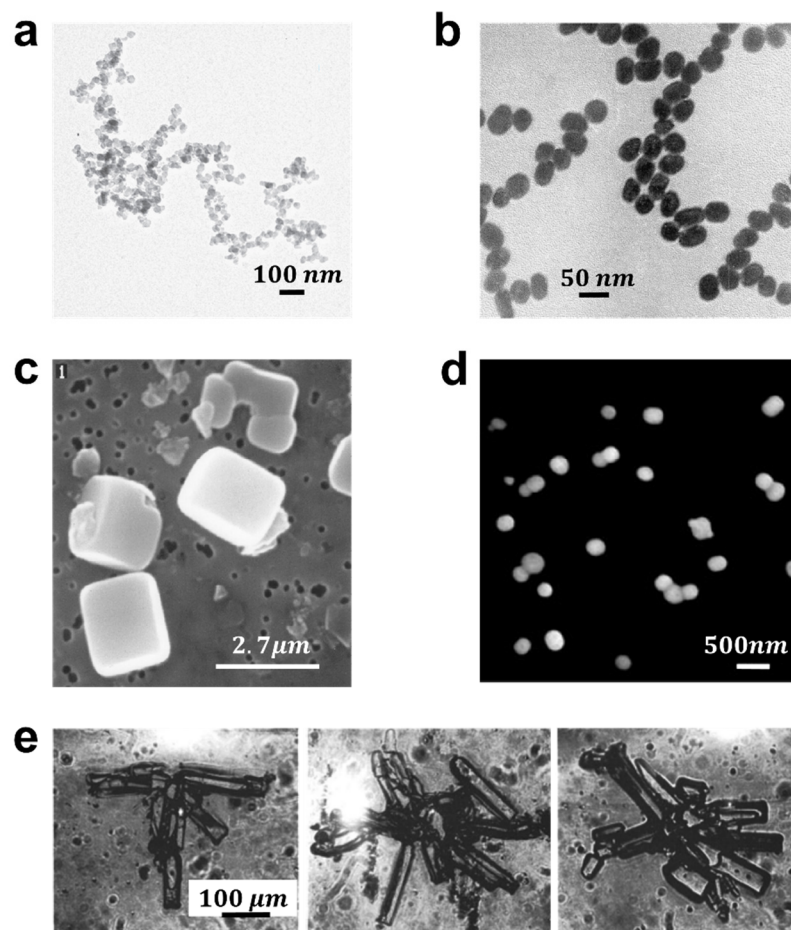


Figure 1.1 Examples of nanometric and micrometric particles of interest in electromagnetic scattering studies. (a) A soot aggregate [15]. (b) A gold particle [16]. (c) A dry sea-salt particle [17]. (d) A desert soil particle [18]. (e) An ice crystal particle [19]

In order to solve the problem of electromagnetic interaction with particles one should resolve the Maxwell equations for the given particle's characteristics, incident wavelength, medium properties, etc. However, the analytical solutions can only be obtained for a limited range of problems. There are many numerical exact methods to calculate the electromagnetic field scattered by a finite object composed of one or several particles using a direct computer solver. One can cite the Lorenz-Mie Theory, the Finite Element Method (FEM), the Point-Matching Method (PMM), T-Matrix and Finite Difference Time Domain Method (FDTD), and also for example the Method of Moment (MOM) and the Discrete Dipole approximation (DDA). However, all of these methods have certain practical limitations in term of size-to-wavelength ratio and refractive indices and the resolution of Maxwell equations becomes



cumbersome and time and memory consuming especially in the case of multi-particles object such as, for example, particle suspensions in photobioreactors engineering [20], [21] atmospheric clouds [9, 10], and interstellar dust particles [23], [24].

The distinguished limitations of the numerical methods and the needs to extend the range of applications have motivated the development of well-characterized approximate approaches which do not require huge computer resources but provide accurate results. As examples of approximate methods we cite Rayleigh approximation, Rayleigh-Gans approximation, Anomalous Diffraction Approximation (ADA) and Geometrical Optics Approximation (GOA). The use of approximations is useful in the case of objects of large size compared to the wavelength, complex morphology and especially with particle groups. Every approximate model is based upon some assumptions. For instance ADA allows to obtain the scattering properties under the assumption of having low refractive index. The GOA is based on the assumption of large object size and its accuracy improves as the object's size-parameter increases [25]. However, it is necessary to characterize the limitations of the approximate methods and to define the limits beyond which the initial assumptions become no more valid. In [26] the authors present, among other cases, the computation using GOA and T-Matrix of the scattering phase function for monodisperse randomly oriented circular cylinders with diameter-to-length ratio of unity, refractive index of 1.311, and surface-equivalent sphere size-parameters  $x_s$  from 40 to 180. The T-Matrix computation aims to validate the limitations of GOA for this type of cylindrical objects. The associated results are shown in Figure 1.2. The authors comment on this as follow: "It is clear that although the main geometrical optics features can be qualitatively reproduced by particles with size-parameters less than 100, obtaining good quantitative accuracy in GOA computations of the scattering matrix for nonspherical particles still requires parameters exceeding a few hundred". Therefore, approximate methods assessment is only obtained with comparison to an exact reference solution. However, in many target cases no reference solutions are existing in order to evaluate the error made using the approximate methods. Comparison to results obtained with Lorenz-Mie method, under the assumption of representing the initial particles by equivalent spheres, is usually made.

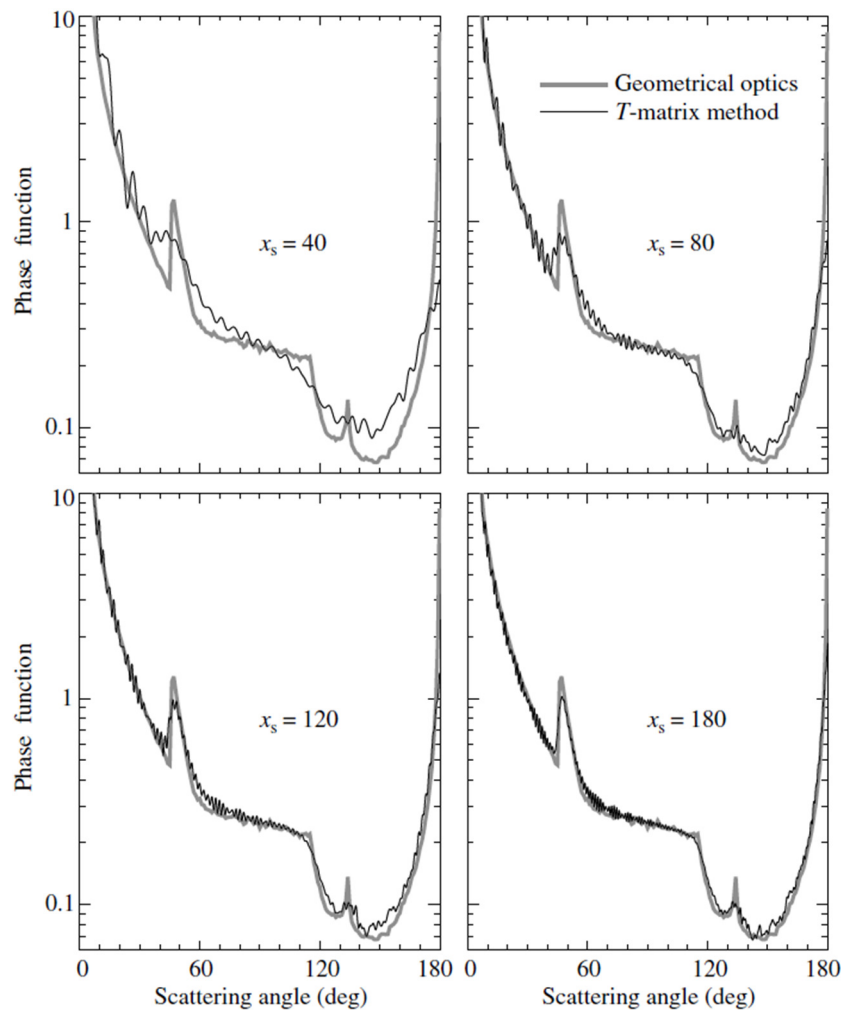


Figure 1.2 GOA and T-Matrix computation results for monodisperse, randomly oriented circular cylinders with surface-equivalent-sphere size-parameters  $x_s = 40, 80, 120$  and  $180$  [26]

When no reference numerical solution is available, the use of specialized laboratory experiments appear as a promising way to characterize the limitations of the approximate methods and to define the limits beyond which the initial assumptions become no more valid. One possibility is to use the measurement of visible and infrared light scattering by the particles of interest which may have sizes ranging from hundredths of a micron to hundred microns. This type of measurement takes advantage of the availability of sensitive detectors and intense laser source power, as well as of high-quality optical elements [6], [27], [28]. However, the measurement of light scattering by micrometer-sized suffers from the difficulty to precisely control the experimental parameters such as the particle's shape, its position and orientation, its refractive index, the angle of incidence of the laser, etc [25]. Therefore, the use of the microwave analogy to carry out the measurement in the microwave domain on centimetric objects is a promising way to obtain a better control of the experiment parameters.

The Microwave analogy, also called microwave analog experiments, is an insight gained from the Scale Invariance Rule (SIR): a fundamental property of Maxwell's theory. It states the following: if one multiplies both the dimensions of the particle and the associated incident wavelength  $\lambda$  by the same factor  $k$  so that the ratio between them is kept constant, and keeps fixed the shape, the morphology and the electromagnetic properties of the initial particle, then the same scattering behavior will be generated with the particle's analog. In the same context, the microwave analogy can also be used to study the scattering by large targets (meter-sized) through reduction of the incident wavelength and of the target's size (Figure 1.3).

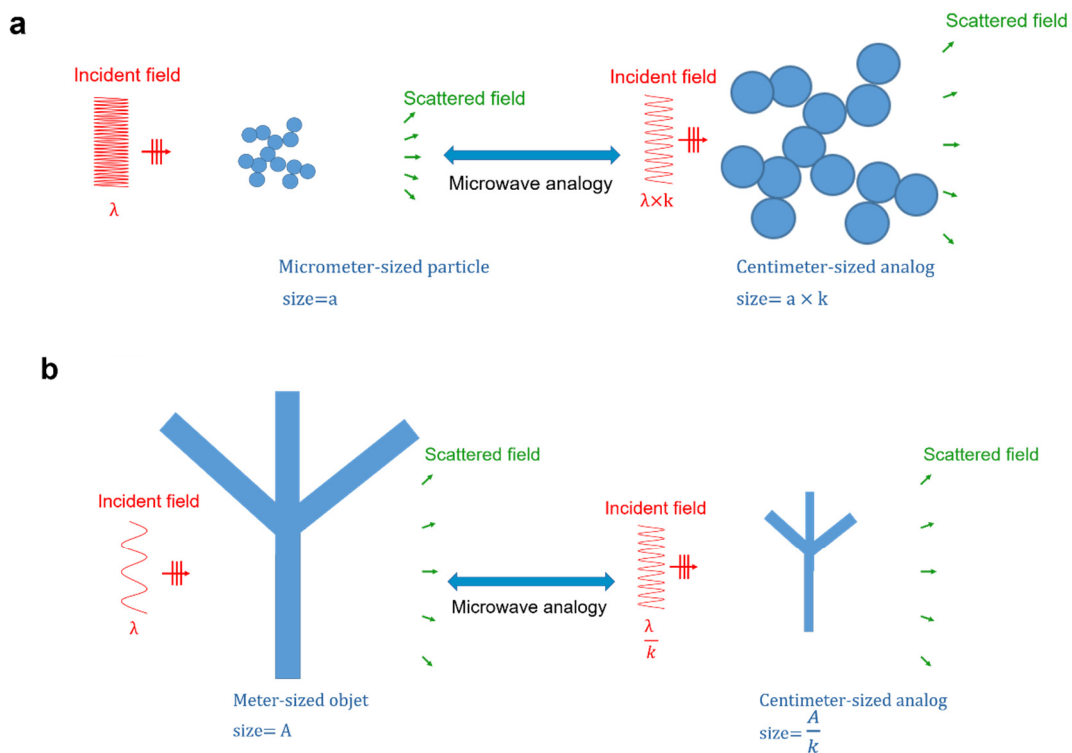


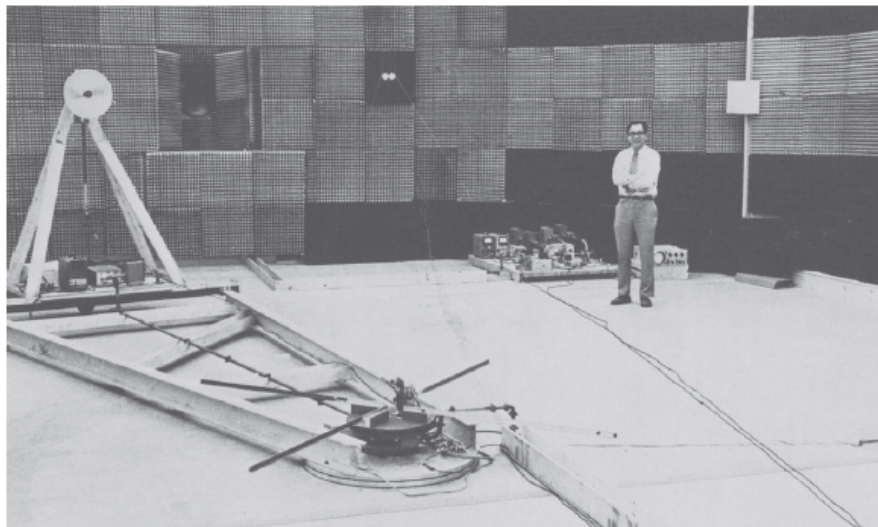
Figure 1.3 Principle on the microwave analog experiment. (a) Scale extension. (b) Scale reduction

The first microwave analog experiment was motivated by the theoretical limitation on the study of scattering by non-spherical objects: Mie theory had been known for providing an analytical solution to the electromagnetic scattering by homogeneous sphere but solutions for non-spherical particles were rather limited [29]. J. Mayo Greenberg et al. took advantage of the emergence of precise microwave instrumentations and carried out the first microwave analogy experiment for application in astrophysics at the State University of New York at Albany (SUNYA) [30].

### 1.2.1 Microwave facility at State University of New York (SUNYA)

The first microwave analog experiment was carried out at SUNYA by Greenberg in 1960 for applications in astrophysics, in order to study the scattering of starlight by micrometer and submicrometer-sized silicate and ice interstellar grains [30] of non-spherical shapes. At that era, numerical resolution of this scattering problem failed because the interstellar grains are in order of the wavelength (size-parameter  $x^1=1$ ). The grain analogs were fabricated from plastic with sizes between 1 and 5 centimeters and were measured in the X-band (8 - 12 GHz). The layout of the SUNYA facility is shown in (Figure 1.4). The setup allowed to obtain the forward and backward scattering by particles analogs in four polarization combinations, allowing the constitution of the entire S-Matrix components.

Sherman, Wang and Gustafson followed Greenberg in running the setup which was used in microwave analog experiments until the early 1990s and many experiments were realized such as scattering by arbitrary shaped spheroids to validate a computer code expanded from the method of Asano and Yamamoto [31], scattering by aggregates of small silicate cylinders to mimic the scattering observed from interstellar and interplanetary dust [32], and a study on the effect of particle shape and orientation on the scattering using cylinders, prolate and oblate spheroids, spheres and disks.

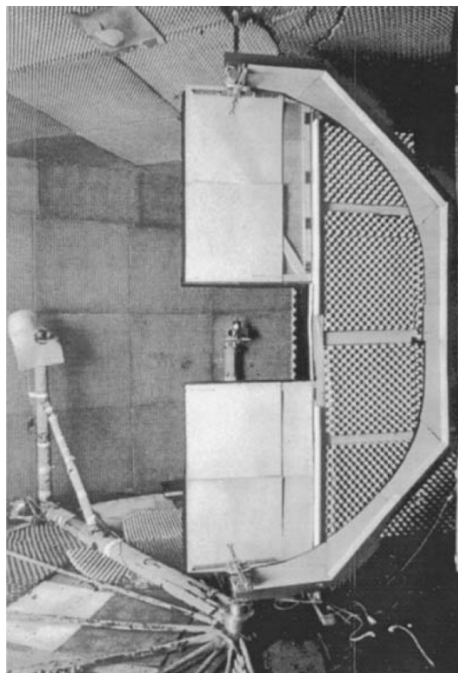


*Figure 1.4 The microwave facility at SUNYA[29]*

### 1.2.2 Microwave facility at Ruhr University Bochum

When Greenberg was initiating the microwave analog experiments at the facility of SUNYA, Giese et al. were also performing similar experiments at the facility of the Eberhard Karls University and later at the Ruhr University Bochum until 1990 [33]. In addition to the presence of a measurements setup operating in the optical spectrum, the introduction of a

microwave facility to perform scaled measurements in the microwave spectrum allowed more flexibility and provided the comfortable conditions to investigate particles of sizes between 0.5 and 10 times the wavelength [34]. The facility ran at 35 GHz with a wavelength around 8 millimeters and the measurements used a transmitting and a receiving horn antennas with a bistatic angle between 0 and 175 degrees (Figure 1.5). Therefore, the determination of the extinction cross section and the angular scattering was possible. The setup operated in the far field condition and allowed the manipulation of relatively large objects of size-parameter  $x$  up to 40, which corresponds to a particle diameter between 5 and 8 micrometer at the visual spectrum [29]. The main interest was focused on understanding the scattering by interplanetary particles and on validating the approximations in theoretical models. Special attention was paid to particles of non-spherical shapes [35]. Samples such as cubes, convex and concave particles were investigated and their scattering was compared to that of spheres of equivalent volumes obtained with Mie theory. In addition, it allowed to experimentally test the accuracy of the equivalent sphere approximation in the case of an aggregate of identical spheres on which successive layers of an absorbing mantle were added [36].



*Figure 1.5 The microwave facility of the Ruhr university [29]*

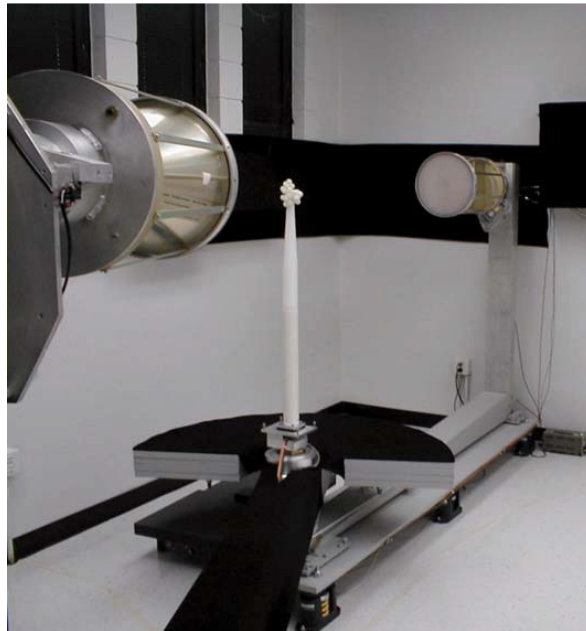
### **1.2.3 Millimeter Facility at University of Florida**

The facility of university of Florida became functional in 1995. Its main feature compared to the SUNYA facility is the higher accuracy and repeatability, the high degree of automation, the operation at millimeter wavelength (75 to 110 GHz) and the higher angular range with bistatic angles from 12 to 180 degrees. The aim of the development of this setup

was to assess approximations in electromagnetic theoretical solutions especially for compact and fluffy aggregate particles of complex internal structure.

Among other works, the facility was used to experimentally validate the numerical values given by the solution on the Cruzan formulation for vector translation through scattering measurement on aggregates of 2, 8 and 27 identical spheres [5]. In [38] the microwave experiments on an aggregate of two spheres were compared to calculations obtained with Discrete Dipole Approximation (DDA) and results showed that the DDA method was efficient for small volume structures but it deviates from the correct solution for larger structures. A scattering model based on the Geometrical Theory of Diffractions (GTD) was also experimentally validated on transparent plates with arbitrary refractive index and with width-to-thickness ratios of moderate to large value [39]. Other works include assessing the effective medium theory approximations for inhomogeneous particles [40], investigating the scattering by titan's aerosols [41] and cometary dust [42].

Figure 1.6 is a photo of the millimeter wave facility at the University of Florida during the measurement of scaled analog of an aggregate of spheres. The target is mounted on a vertical mast at the center of the setup and is illuminated with a transmitting antenna mounted on the top of an aluminum and titanium support. The transmitting and the receiving antennas are identical.



*Figure 1.6 The experimental setup at the University of Florida [29]*

#### 1.2.4 Conclusion

The microwave analogy is inspired from Maxwell equation and it allows to scale the scattering measurements from the optical domain to the microwave domain or from the radio-waves to the microwaves. In this section I presented the definition of the microwave analogy and its initiation. In microwave analog experiments the reproduction of the target's properties is a keystone to mimic the scattering phenomenon in the optical domain but other important requirements are the possibility to generate signals at the required wavelength, the possibility to illuminate the target with many angles of incidence and to measure the scattering in many directions in the space. The ideal environment to carry out such scattering measurement are the bistatic Radar Cross Section (RCS) facilities which are often embedded inside anechoic chambers. First, the anechoicity allows to create the closest medium to the free space conditions. Second, such bistatic facilities are equipped to control the frequency, the incidence angles, the scattering angles, and the position of the target. The microwave analog experiments carried out in this thesis are performed in the anechoic chamber on the Center Commun de Ressources en Microondes (CCRM) which is described in sections 1.4 and 1.5. In the next section I present some national and international bistatic microwave facilities that have similar features to the facility used along this thesis, and that have the required features to be used in microwave analog experiments.

### 1.3 MICROWAVE SCATTERING MEASUREMENT FACILITIES

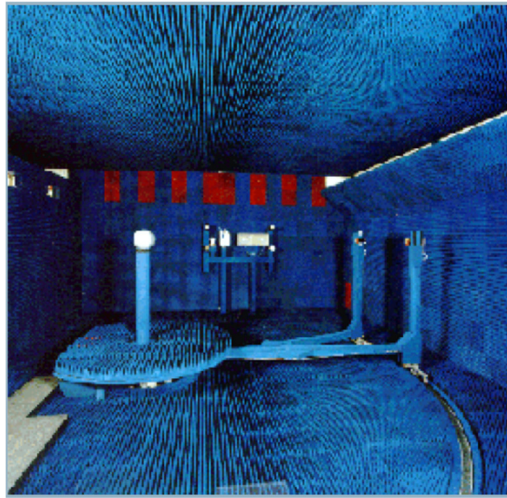
In this section, we present some national and international electromagnetic scattering measurement facilities. The presented facilities allow to make bistatic (and some of them also quasi-monostatic) measurements, in a similar way to the configuration used along my PhD thesis. The cited facilities are mainly used for RCS measurements. They are housed inside full/semi anechoic environments to recreate the conditions of free space and they have either circular or spherical configurations.

#### 1.3.1 Cactus facility at CEA-CESTA (France)

The Centre d'Etudes Scientifiques et Techniques d'Aquitaine CESTA has an indoor Radar Cross Section (RCS) measurement facility called CACTUS embedded inside an anechoic chamber ( $9 \times 12 \times 6 \text{ m}^3$ ). The facility is used for RCS and antennas measurements in spherical monostatic and bistatic configurations and it operates from 1 GHz to 18 GHz (Figure 1.7). The distance between the antennas and the target is about 6 meters and the bistatic angles



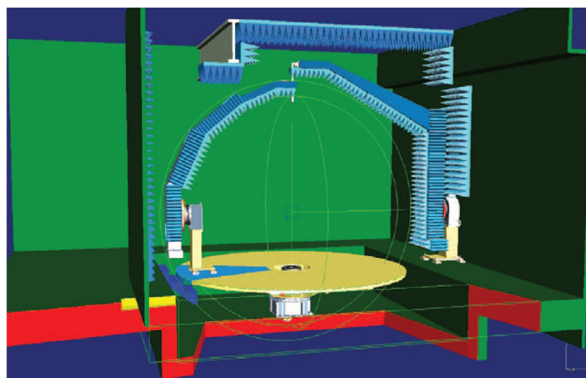
are between few degrees up to 180 degrees [43]. Most of the developed measurements are in relation with military applications.



*Figure 1.7 CACTUS facility at CEA-CESTA in France [43]*

### 1.3.2 BIANCHA facility at INTA (Spain)

The National Institute of Aerospace Technique (INTA) in Madrid developed in 2010 a versatile spherical indoor facility called BIANCHA for electromagnetic tests: RCS measurements, antennas measurements, estimation of materials properties, etc [44]. The setup is housed inside an anechoic chamber of  $5.5 \times 6.0 \times 3.7 \text{ m}^3$ . It consists of two arms on which the emitting and the receiving antennas are mounted and of an azimuthal turntable (Figure 1.8). Each of the arms has an elevation positioner and an azimuth positioner. Furthermore, one of the arms is fixed on the ground and the other is fixed on the turntable. This set of mechanical movements allows the positioning of the emitting and the receiving antennas at any point on an imaginary hemisphere of 1.7 m radius, at the center of which the target is placed. The functional frequencies are from 1 GHz to 26 GHz [44]–[46]. The setup allows bistatic and monostatic 3D measurements



*Figure 1.8 The experimental setup at INTA in Spain [46]*



Among other targets, a 12 cm metal cube was measured in a far field bistatic configuration in different polarization cases. The measurements are post-processed with software gating techniques and are calibrated using a metallic sphere. The measurement results at 5.8 GHz are presented in (Figure 1.9) with comparison to simulations obtained with two commercial softwares: HFSS and MONURBS. The measurements present good agreement with simulations.

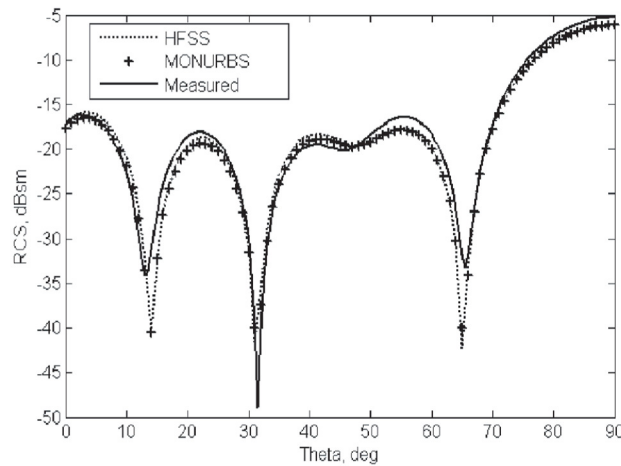


Figure 1.9 Results of the measurement of a metal cube at 5.8 GHz [45]

### 1.3.3 Circular millimeter wave scattering measurements at LEAT (France)

The Laboratoire d'Electronique, Antennes et Télécommunications LEAT at the university of Nice has conceived a scattering measurement setup that works in the W band (75 – 110 GHz). The setup has the advantage of being easily removable since, when first developed, it was placed inside an anechoic chamber basically used for antenna measurements. Later, the setup was installed in semi anechoic environment. The target under test is placed at the center of circular motorized rails. It is illuminated with a fixed position horn antenna 40 cm away from the target to satisfy the far field condition, as the wavelength is between 2.7 mm and 4 mm (Figure 1.10). The target and the receiving antenna are placed on a tower which is driven by a rotational positioner.

The great challenge with such short wavelength systems is the high sensitivity of measurements to the positioning errors. Therefore, the system is designed to reduce as possible the displacements. The mm-wave heads are directly attached to the antennas. The transmitting antenna is chosen to be a low directivity antenna (an open-ended waveguide) to provide the target a constant illumination and overcome the misalignment errors. The receiving antenna, however, is chosen to be a high directive antenna because this latter is fixed with the target on the same support and therefore the misalignment between them is constant.

The circular displacement of the receiving antenna insures a back and forward scattering (bi-static angle between 30 and 330 degrees, with an angular step of 0.2 degree).

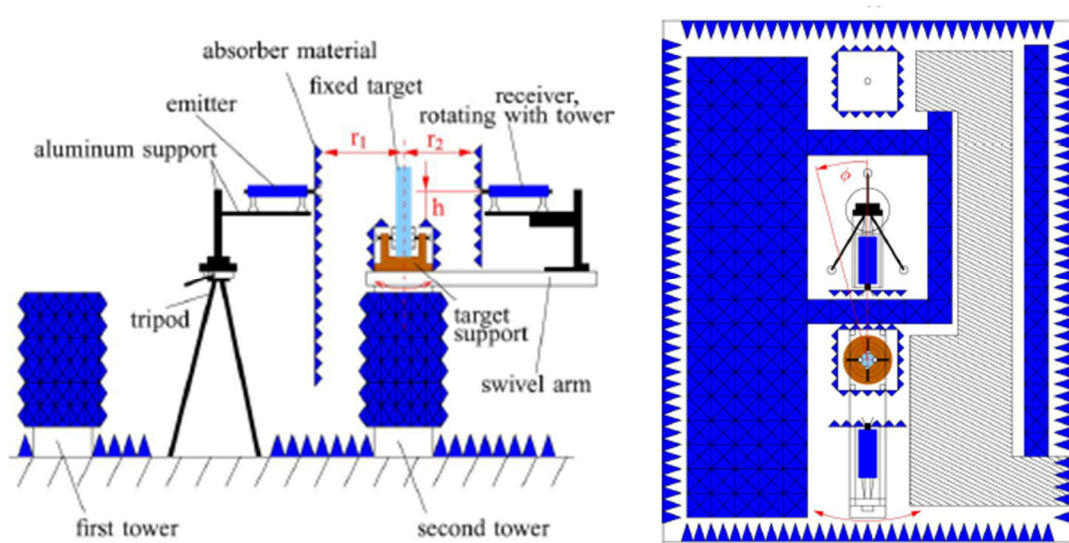


Figure 1.10 The millimeter measurement setup at LEAT [47]

The accuracy of the measurement setup was evaluated through measurements of two Perfect Electric Conductor (PEC) cylinders of 8 mm and 20 mm diameter. The scattering measurement of the 20 mm cylinder is used to calibrate that of 8 mm. The measured scattered fields are post-processed by a misalignment correction that doesn't require a prior knowledge of the target. Results in amplitude and phase at 92.5 GHz for the 20mm cylinder are shown in (Figure 1.11) and are compared to analytical calculation. The good agreement with calculation, especially in phase at such small wavelength proves a rather good overcome of the alignment errors and open perspectives to measure more complex targets.

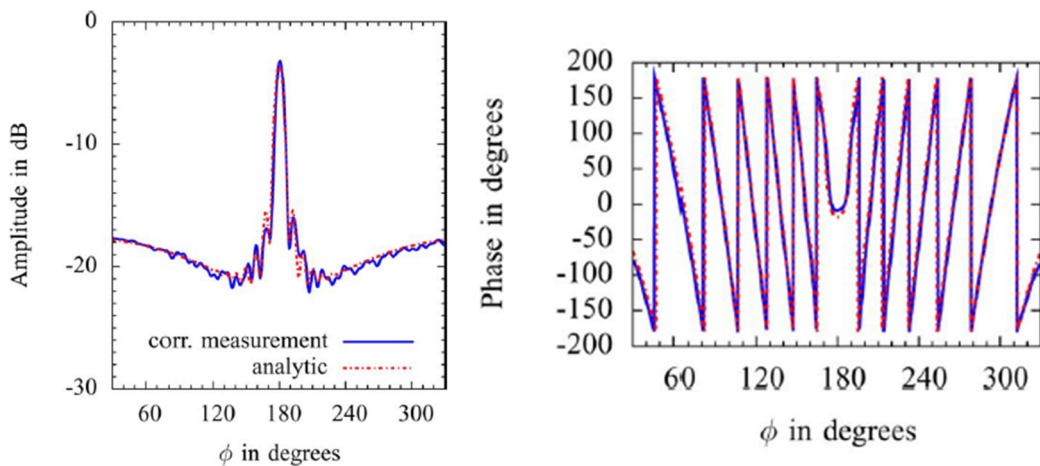


Figure 1.11 Amplitude and phase of the measured and calculated scattered field by a 20mm metal cylinder [47]

### 1.3.4 Spherical millimeter wave scattering measurements at LEAT (France)

The LEAT laboratory has recently installed a new spherical millimeter wave scattering setup (Figure 1.12). The target is placed on a support at the center of the setup and the source is placed at 380 mm from the center of the support (the distance is 380 mm in vertical polarization and 334 mm in horizontal polarization). The receiver is placed on a swinging arm at a distance of 585 mm from the center of the support. The movement of the arm allows to place the receiver on a good part of a sphere surrounding the target. The setup operates in the W band (75 GHz – 110 GHz). The maximal dimension of the studied targets is 20 mm and according to the distances between the target and the antennas the measurements are made in the far-field region [48].

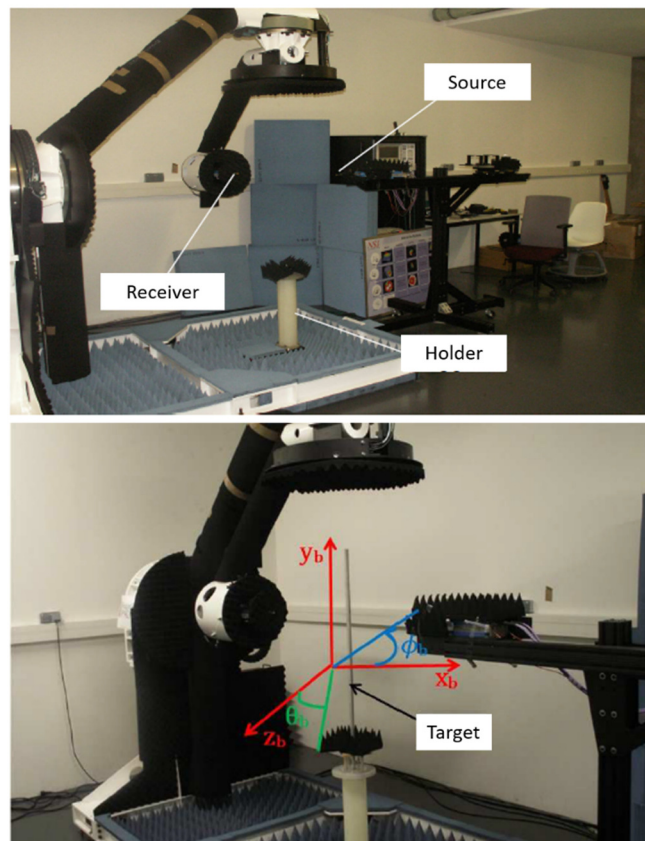


Figure 1.12 The recent spherical millimeter wave setup at LEAT [48]

Although it is not working at the same frequency band, this measurement system has a similarity with the setup of the CCRM used along this thesis (described in sections 1.4 and 1.5) in term of using external remote mixers, an LO/IF distribution unit.

### 1.3.5 BABI facility at ONERA (France)

The French Center for Aerospace Research ONERA has an indoor RCS facility called BABI which operates between 500 MHz and 40 GHz [49], [50]. The facility is rather similar

## Microwave scattering measurement

to that of CEA-CESTA (section 1.3.1) but is placed in a semi-anechoic environment. It consists of a circular rail on which one transmitting and one receiving antennas can move circularly around the target at 5.5 meters away. The antennas are at 2.5 meters' height where the target under test is placed at the center on a polyfoam mast of adjustable height (Figure 1.13). The facility is mainly used for military applications (scattering measurements on aircrafts, missiles, etc.). The angle between the antennas can be set between 4 and 190 degrees, providing the possibility to make quasi-monostatic as well as bistatic measurements.



Figure 1.13 The BABI at ONERA in France [49]

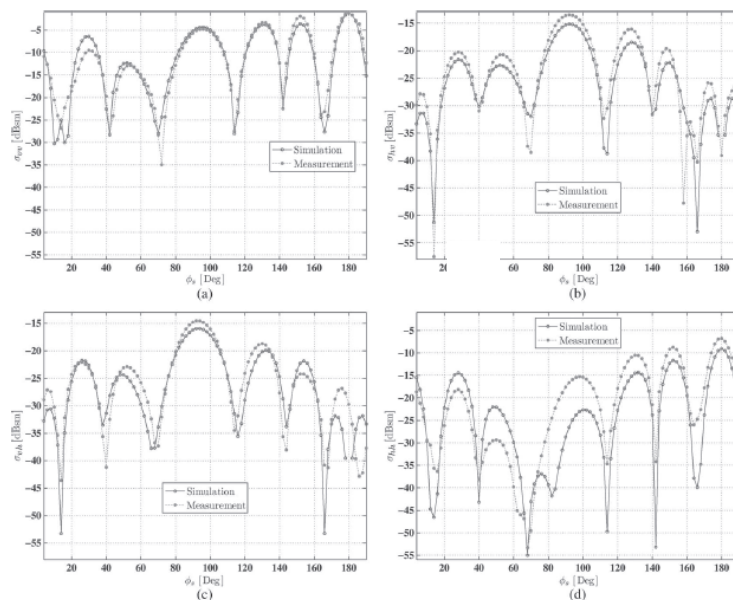


Figure 1.14 Measured RCS of the cylinders compared to simulations. (a) VV polarization, (b) HV polarization, (c) VH polarization and (d) HH polarization [49]



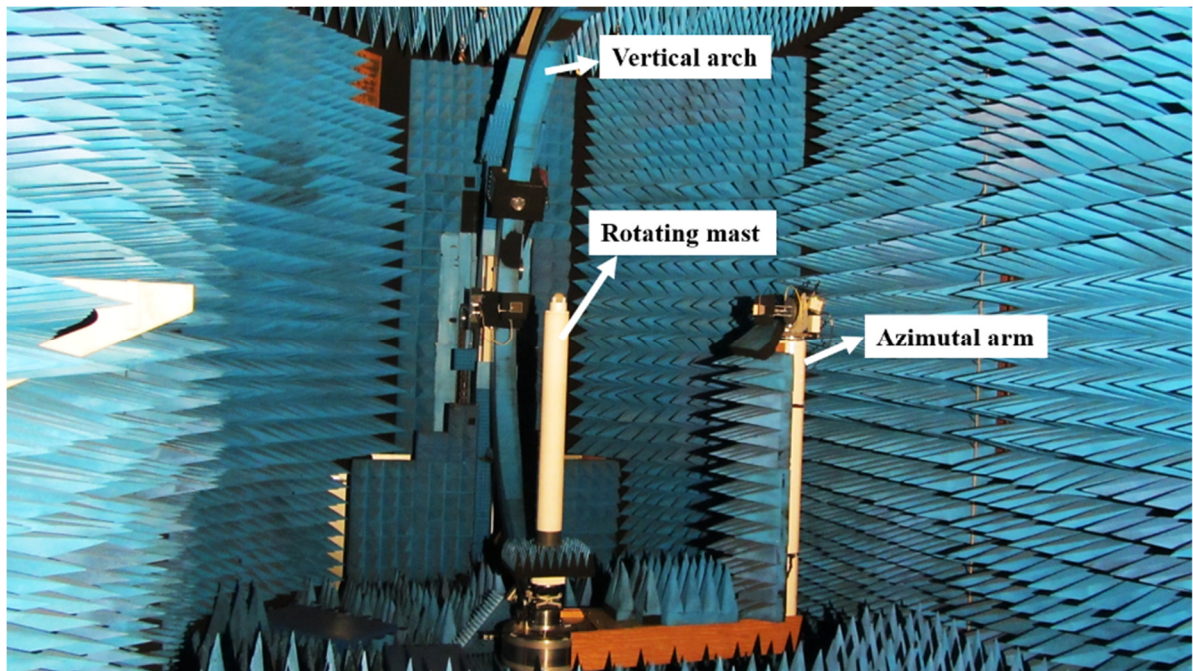
As an example, Figure 1.14, presents the RCS measurements compared to calculations on a group of dielectric vertical and tilted square cross-sectional cylinders placed on a metal circular plate in VV, VH, HV and HH polarizations.

## 1.4 EXPERIMENTAL FACILITY OF THE CCRM: PREVIOUS STATE

The used experimental setup along this thesis belongs to the Centre Commun de Ressources en Microondes (CCRM) in Marseille. It consists of an anechoic chamber in a Faraday cage containing different mobile supports and a chain of microwave devices allowing the generation, the transmission and the reception of microwave signals. This assembly was historically conceived to make antennas and scattering measurements in a spherical configuration. In this section I precise the state of the setup before the beginning of this thesis. A state of art on the geometrical and mechanical features of the setup, the different existing antennas, the previously developed post-processing tools and an overview on some early explored targets are given.

### 1.4.1 Anechoic chamber

The chamber is enclosed into a Faraday cage of dimensions  $(14.5 \times 6.5 \times 6.5) \text{ m}^3$  to isolate the interior structure from any perturbation source in the external environment (Figure 1.15). The anechoicity of the chamber is insured by pyramidal absorbing foams (Siepel APM 45 and APM 66) providing an attenuation of at least 40 dB for frequencies above 1 GHz.



*Figure 1.15 Photography of the anechoic chamber of the CCRM*

### 1.4.2 Measurement setup: previous state

In this section I review the state of the measurement setup before the beginning of my thesis. The setup is described in Figure 1.16. The measurement of the microwave signals is obtained through external remote mixers (*HP 85320*) and using an *HP 8510 C* Vector Network Analyzer as a simple 20 MHz receiver.

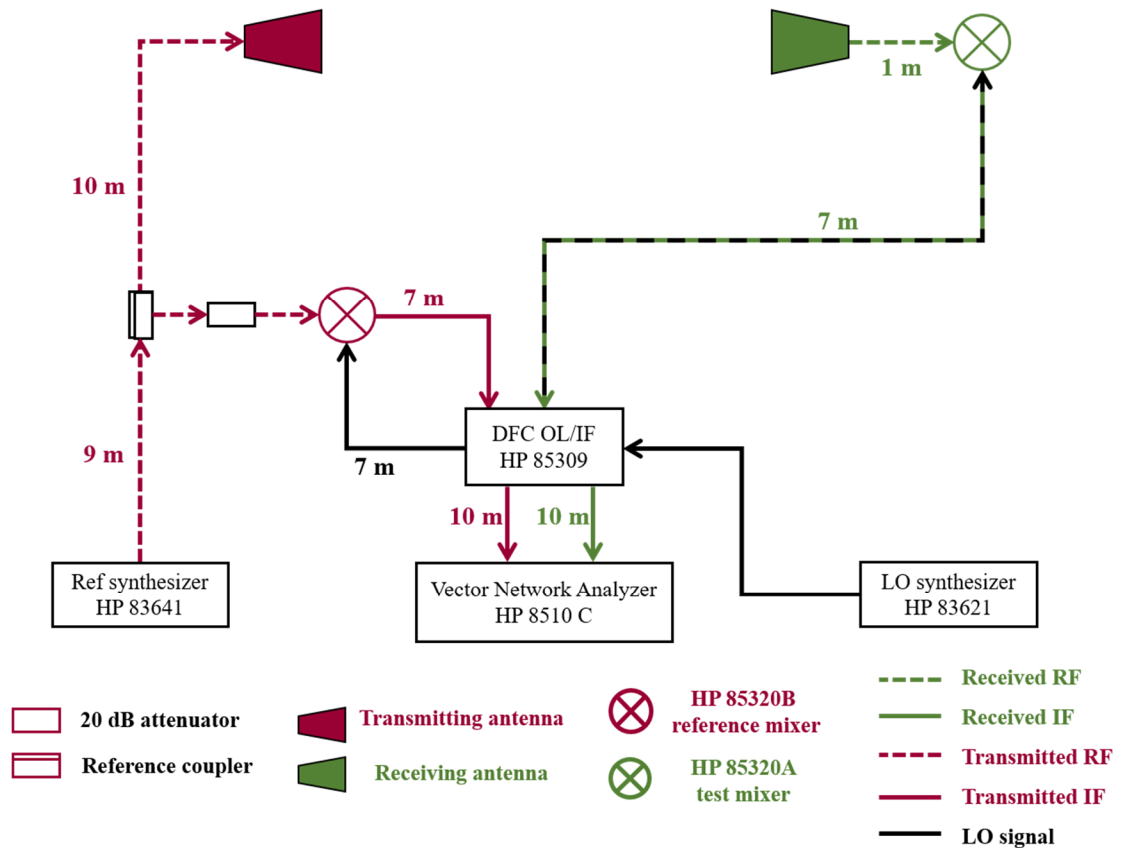


Figure 1.16 The measurement setup in its previous state [51]

The first reason of using remote mixers is to reduce the losses due to the propagation of the RF signals and their sensitivity to noises and perturbations in long cables. The second reason is to keep a multipurpose setup that can be modified upon need. A reference synthesizer (*HP 83641*) generates a Continuous Wave (CW) signal of a frequency  $F_B$  between 1 and 18 GHz, which is the frequency band of the system. This signal propagates in a 19 meters long coaxial cable towards the transmitting antenna. At 9 meters away from the synthesizer's output a reference coupler is used to deliver the transmitted signal at its direct output and the reference signal at its 20 dB reference output. The signal at the output of the 20 dB reference output is fed to a 20 dB reference attenuator and then delivered to the reference mixer. The coupler and the attenuator ensure an attenuation of 40 dB at the input of the reference mixer

to avoid feeding this latter by high amplitude signals which may exceed its operational dynamic range. The reference mixer scales the reference RF signal from microwaves to an Intermediate Frequency (IF) of 20 MHz using a local oscillation frequency  $F_{LO} = F_B - 20\text{MHz}$ . A 20 dB attenuator is placed at the entrance of the mixer. The  $F_{LO}$  signal is generated by an LO synthesizer (HP 83621) and delivered to the reference mixer through a Digital Frequency Converter (DFC) (HP 85309). Therefore, the  $a_1$  IF signal generated by the transmitting mixer is forwarded to the VNA through the DFC.

At the receiving side, the signal captured by the receiving antenna propagates in a short coaxial cable of almost one-meter length and is guided to the test mixer. The receiving mixer receives the  $F_B$  signal from the antenna and the  $F_{OL}$  signal from the DFC and translates the received signal to an IF signal of 20 MHz, in a similar way to the function of the transmitting antenna. The IF received signal constitutes the test signal  $b_2$  that is sent to the VNA. The final measured quantity by the VNA is the ratio  $\frac{b_2}{a_1}$  in amplitude and phase.

### 1.4.3 Geometrical configurations

The facility allows to do measurements in different geometrical configurations thanks to different geometrical movements. Spherical, circular and quasi-monostatic measurements are possible. Considering a referential frame linked to the target under test (TUT), the whole configuration can be seen as positions on a sphere with radius of 1.7 meter (distance from the center of the sphere to the aperture of the antenna), at the center of which the TUT can be placed. The sources are located all around the target at positions defined by  $\theta$  and  $\varphi$  (Figure 1.17).

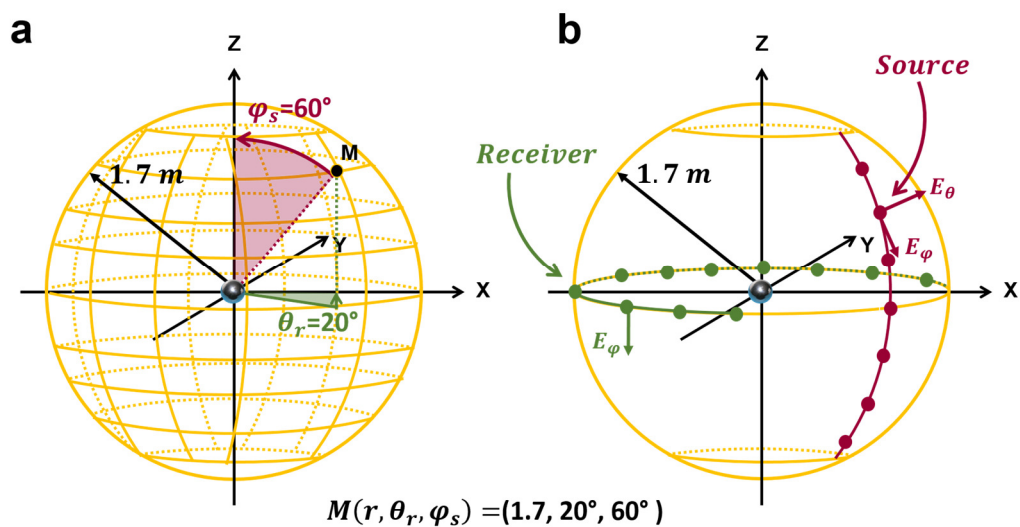


Figure 1.17 Position of the sources (a) and the receivers (b) in the spherical configuration and definitions of the polarizations

Considering a referential frame linked to the measurement setup (which is the real case), the source can move on a vertical trajectory and the receiver on an azimuthal trajectory (Figure 1.17-b). The equivalent combination of all the source positions shown in (Figure 1.17-a) can be obtained through axial rotation of the target around the z axis.

#### 1.4.3.1 Spherical configuration and polarizations

In the geometrical configuration of the setup, a source antenna is fixed on a wagon on a vertical arch, a receiving antenna is fixed on the azimuthal arm and the TUT is placed on a central rotating mast at the origin O (Figure 1.18). The transmitting and the receiving antennas can therefore move on circular trajectories in two orthogonal planes. The displacement of the transmitting antenna circularly around the TUT both with the rotation of the TUT around itself allow to generate angles of incidence almost all over the sphere surrounding the TUT. The positioning systems are individually described in section 1.4.4.

Throughout this thesis the positions of the antennas and of the TUT are defined as following:

- The position of the source antenna is referred to the angle  $\varphi_s$  defined in the xOz plane from the Z axis. The values of  $\varphi_s$  are between  $-11^\circ$  and  $169^\circ$ .
- The position of the receiving antenna is referred to the angle  $\theta_r$  defined in the xOy plane from the X axis. The values of  $\theta_r$  are between  $-130^\circ$  and  $130^\circ$ .
- The position of the TUT is referred to the angle  $\theta_o$  defined in the xOy plane from the X axis. The values of  $\theta_o$  are between  $-180^\circ$  and  $180^\circ$ .

The polarizations of antennas (source and receiver) are defined using the unity vectors  $E_\theta$  and  $E_\varphi$  of the spherical coordinate system. The polarization is noted  $\theta$  (respectively  $\varphi$ ) if the antenna is polarized along  $E_\theta$  (respectively along  $E_\varphi$ ):

- The polarization  $\theta\theta$  corresponds to the case where the two antennas are polarized along  $E_\theta$ .
- The polarization  $\varphi\varphi$  corresponds to the case where the two antennas are polarized along  $E_\varphi$ .
- The polarization  $\theta\varphi$  corresponds to the case where the source antenna is polarized along  $E_\theta$  and the receiving antenna is polarized along  $E_\varphi$ .
- The polarization  $\varphi\theta$  corresponds to the case where the source antenna is polarized along  $E_\varphi$  and the receiving antenna is polarized along  $E_\theta$ .

In the case of measurements in the azimuthal circular configuration (section 1.4.3.2) where the source, the TUT center and the receiver are included in the same horizontal plane,



the polarizations  $\theta\theta$ ,  $\varphi\varphi$ ,  $\theta\varphi$ ,  $\varphi\theta$  are called HH, VV, HV, and VH respectively. Where H means horizontal polarization and the V means vertical polarization.

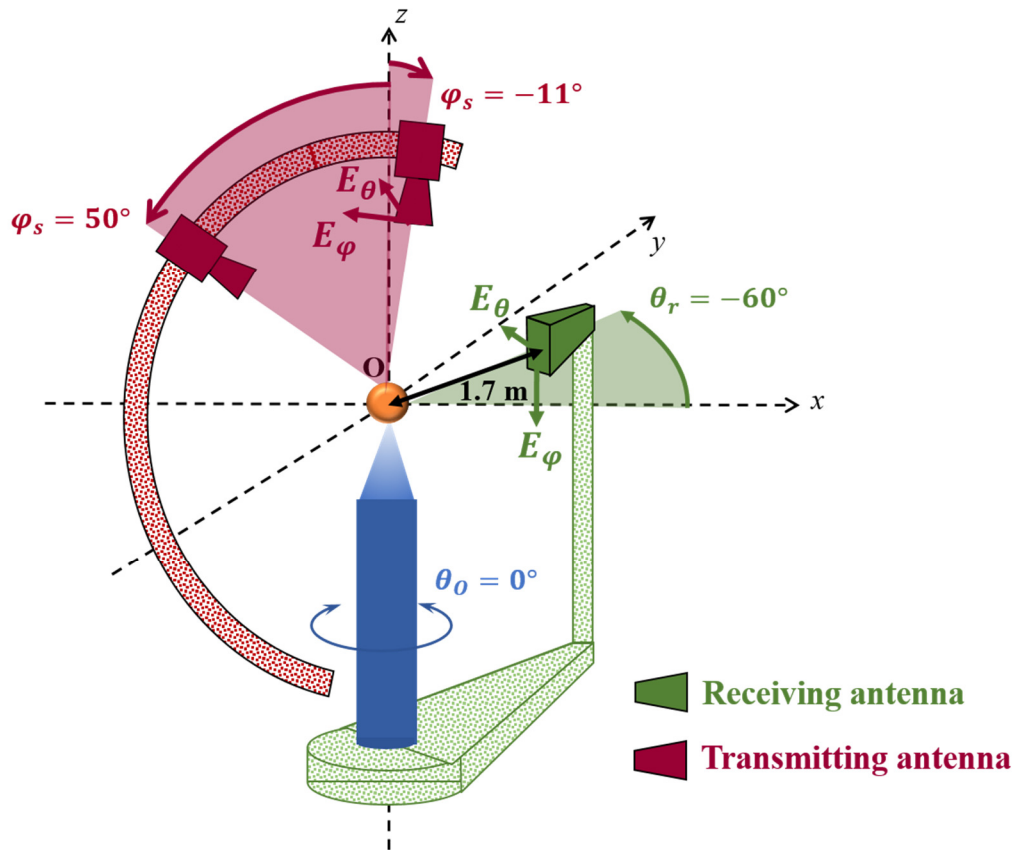


Figure 1.18 Schematic showing the spherical configuration of the CCRM and the possible displacements on the source the receiver and the TUT

### 1.4.3.2 Azimuthal circular configuration

This configuration is a special case of the spherical one, where the transmitting antenna is fixed at  $\varphi_s = 90^\circ$ . The source, the receiver and the TUT are all included in the same azimuthal plane (Figure 1.19). The displacement of the receiver in the horizontal plane allows the scattering measurement of bistatic angles between  $50^\circ$  and  $310^\circ$  (the bistatic angle represents the angle between the source and the receiver but the positions of the turntable are referred to the  $\theta_r$  angle as shown in figure 1.18). Along this thesis, most of the measurements are made in this configuration.

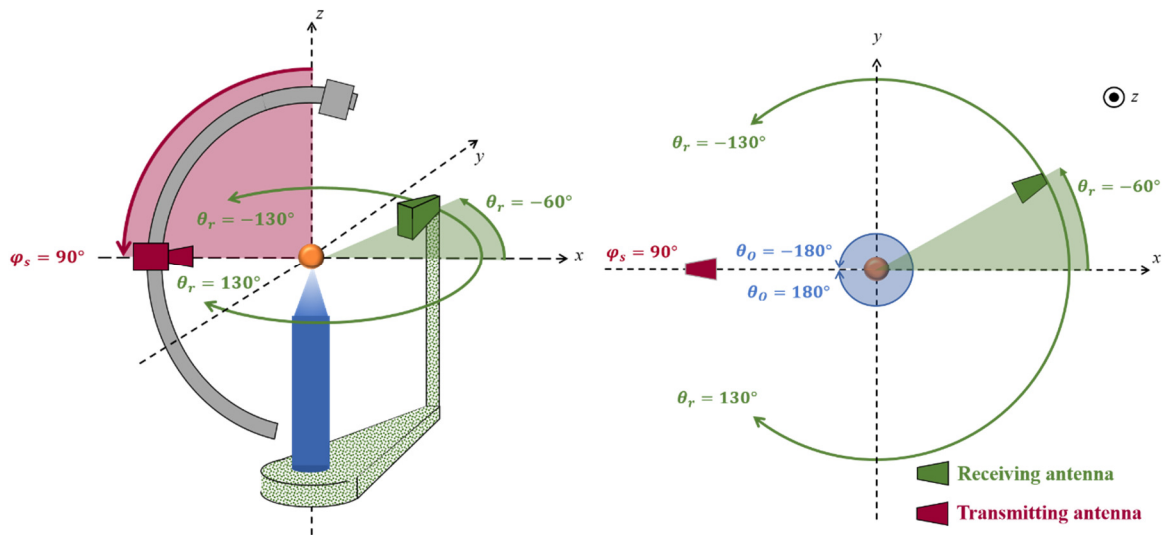


Figure 1.19 Azimuthal circular configuration of the CCRM showing the possible displacements of the receiver and the TUT. The source is at a fixed position

### 1.4.3.3 Vertical circular configuration

This configuration uses the antennas on the vertical arch. The azimuthal arm is not utilized. One of the antennas on the arch is used as a source and the other as a receiver. They move on a trajectory which is centered on the TUT. It is mainly used to measure the backscattering for small bistatic angles below  $50^\circ$ , which is not possible with the azimuthal circular configuration (Figure 1.20).

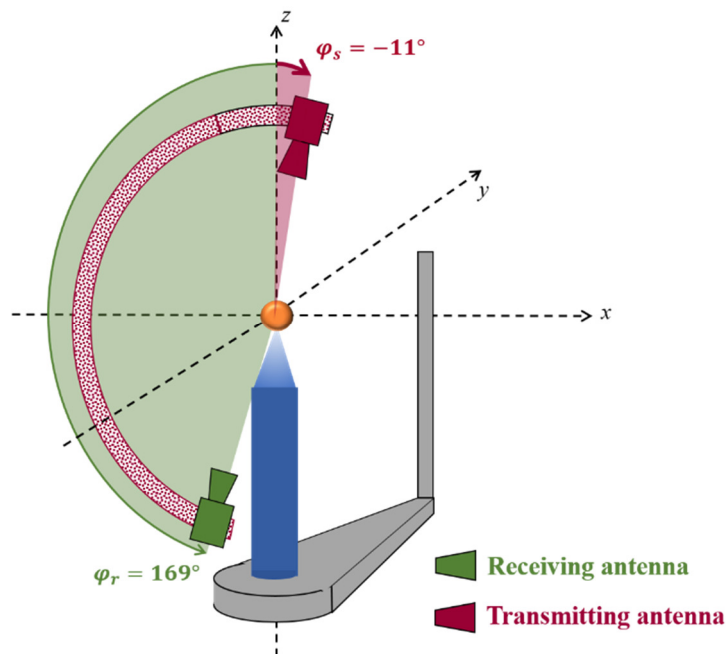


Figure 1.20 Vertical circular configuration. The source and the receiver are on the vertical arch

#### 1.4.3.4 Configurations summary

A summary of the aforementioned configurations is presented in Table 1.1.

	$\varphi_s$	$\theta_r$	$\varphi_r$
Spherical configuration	-11° to 169°	-130° to 130°	-
Azimuthal circular configuration	90°	-130° to 130°	-
Vertical circular configuration	-11° to 157°	-	1° to 169°

Table 1.1 Summary of the definition of the angles  $\varphi_s$ ,  $\theta_r$  and  $\varphi_r$  for each configuration case

#### 1.4.4 Positioning systems and angles definition

The positioning of the antennas and of the target under test (TUT) is achieved through mechanical trajectories of different supports inside the chamber: vertical circular trajectory on a vertical arch, azimuthal circular trajectory using an azimuthal arm and an axial.

##### (i) Vertical arch

Two antennas wagons  $W_s$  (superior wagon) and  $W_i$  (inferior wagon) can move along a circular vertical arch of 4 meters diameter, each of them can carry one antenna (or two in the quasi-monostatic configuration described in section 1.5.4). The circular trajectory of the antennas is centered at the origin  $O$  of the system, which is often also the position of the target's center. The maximal angular excursion of the arch is 180°, from -11° to 169°, 0° being the zenith. The smallest reachable angular excursion between the antennas on the wagons is of 12° which corresponds to closest position of the wagons to each other.

The positions of the emitting antennas on the arch are defined in the  $xOz$  plane with  $\varphi_s$  being the angle of the antenna to the  $z$  axis. The angle  $\varphi_s$  varies from -11° to 157° for the antenna on the superior wagon and from 1° to 169° for the antenna on the inferior wagon (Figure 1.21). Within the framework of this thesis, the full spherical configuration (two sources on the arch and one receiver on the azimuthal arm) is only used for measurements for inverse problem purposes.

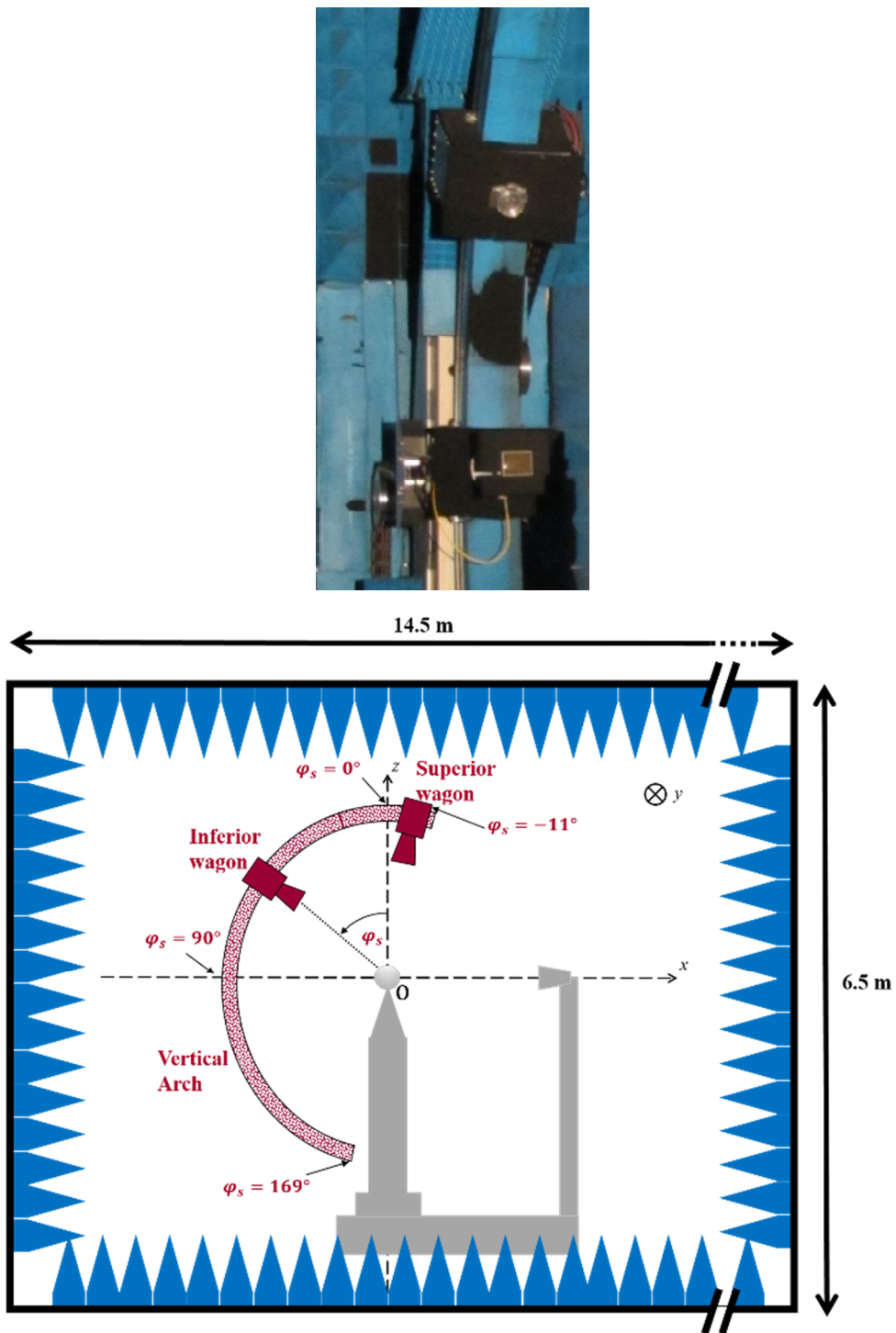


Figure 1.21 The displacement of the superior and inferior wagons holding the antennas on the vertical arch (in red)

**(ii) Azimuthal arm**

An antenna (transmitting or receiving) can be fixed on top of a metallic mast which is placed on the extremity of an azimuthal arm of 2 meters length. The arm by itself is fixed on a turntable (Newport RTM 660) whose rotation axis is the z axis. This rotational movement of the motor allows a circular displacement of the receiving antenna around the center O in

## Microwave scattering measurement

the  $xOy$  horizontal plane (Figure 1.22). The position of the receiving antenna is in the  $xOy$  plane with  $\theta_r$  being the angle of the antenna position to the  $x$  axis. The values of  $\theta_r$  are within  $-130^\circ$  and  $+130^\circ$ , angles beyond  $-130^\circ$  and  $130^\circ$  are unreachable due to mechanical constraints. This configuration is used in bistatic azimuthal measurements (see chapter 2).

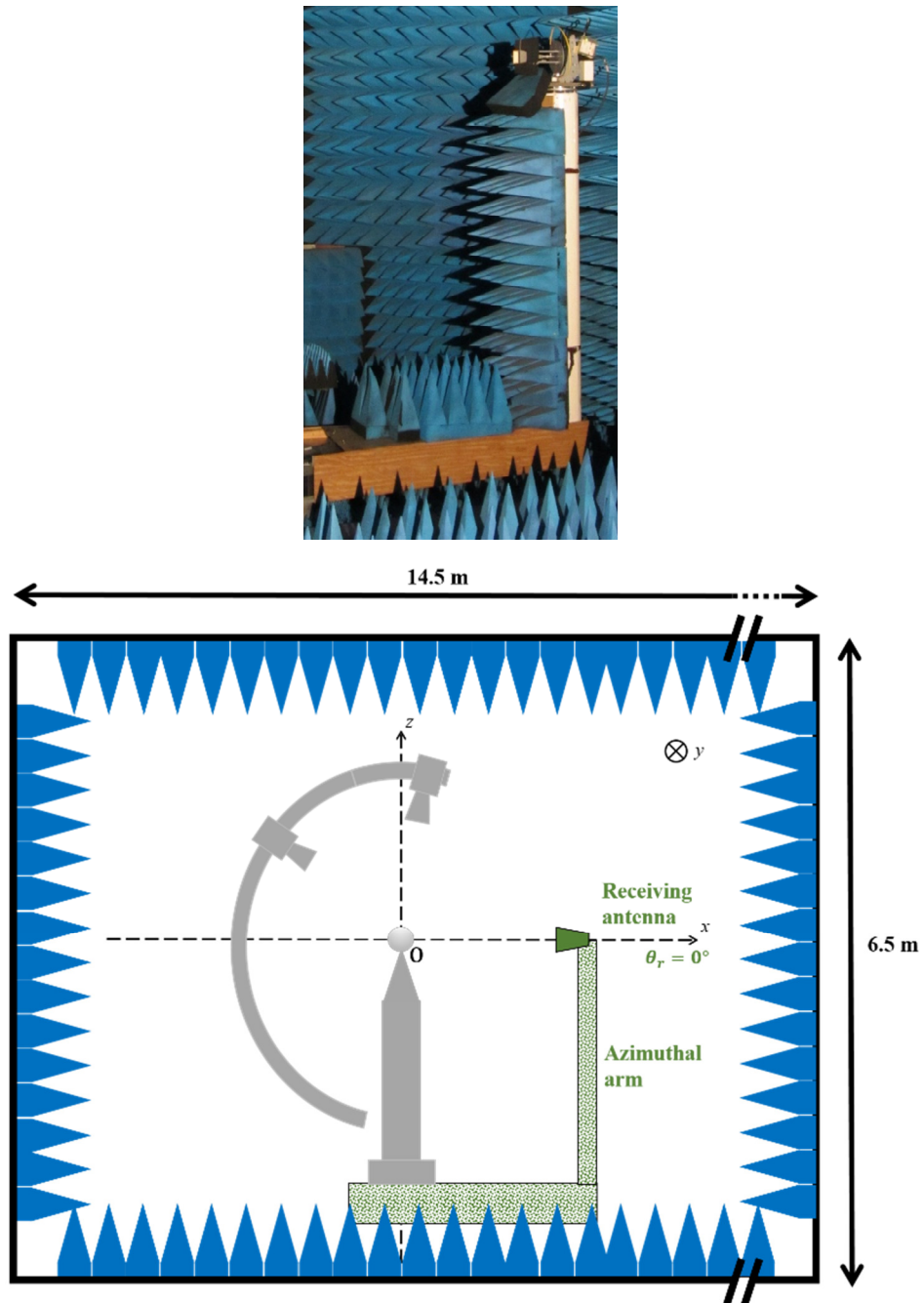


Figure 1.22 The displacement of the azimuthal arm carrying the receiving antenna (in green)

**(iii) Central rotating mast**

At the center of the setup, a vertical mast made of expanded polystyrene is fixed on top of a rotating motor (Newport RV240CCHL). This mast is used as a support to hold the TUT, and it is made of expanded polystyrene, commonly used in anechoic chambers for being almost transparent to microwaves. The mast can therefore make a rotation of  $360^\circ$  around the z axis, allowing all the possible orientations around the z axis of the TUT. The angle  $\theta_o$  describing the rotation of the TUT around the Oz axis is defined according to the Ox axis. The values of  $\theta_o$  are chosen between  $-180^\circ$  and  $180^\circ$  (Figure 1.23).

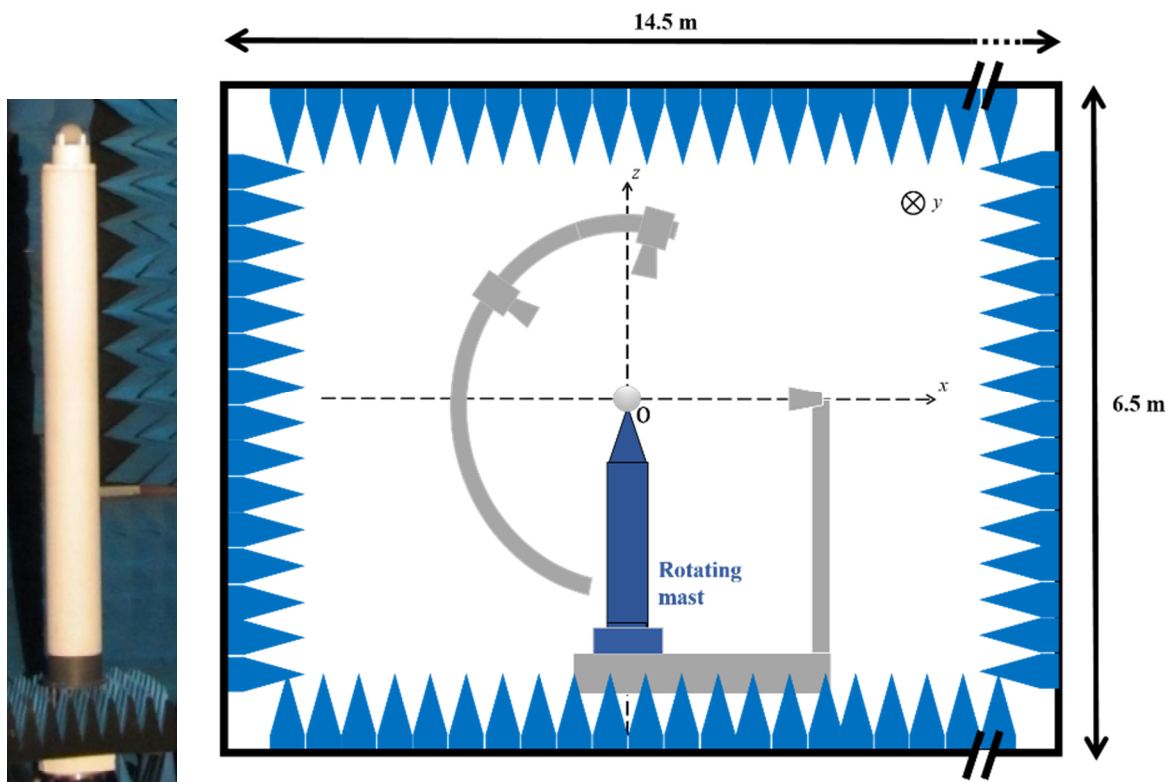


Figure 1.23 rotating mast carrying the TUT (in blue)

**1.4.5 Available antennas**

In this section we present the different types of antennas used along this thesis. Five different types of antennas have been used and the choice of one of them in every case of study depends mainly on the frequency band in interest and on its directivity. All of them are linearly polarized, therefore the change of polarization whether at the emitting side or at the receiving side is achieved through a rotation of the antenna around its axis. The used antennas are listed hereunder and their figures are shown in Figure 1.24.

**1. Wideband DRG horn antennas with logarithmic profile [2 – 18 GHz]**

The advantage of these antennas is that they operate on a wide band of frequency from 2 to 18 GHz. however, they have low directivity. Their 3dB bandwidth is between 20° and 35° in the E and H plane depending on the frequencies.

**2. C-band Parabolic antennas [4-8 GHz]**

The parabolic reflectors (HYPTRA NE5256) are used with a wideband source between 4 GHz and 8 GHz. They are used when high directivity is needed for measurement in the C-band. Their 3 dB bandwidth is around 5° in the E and H plane.

**3. X-band horn antennas [8-12 GHz]**

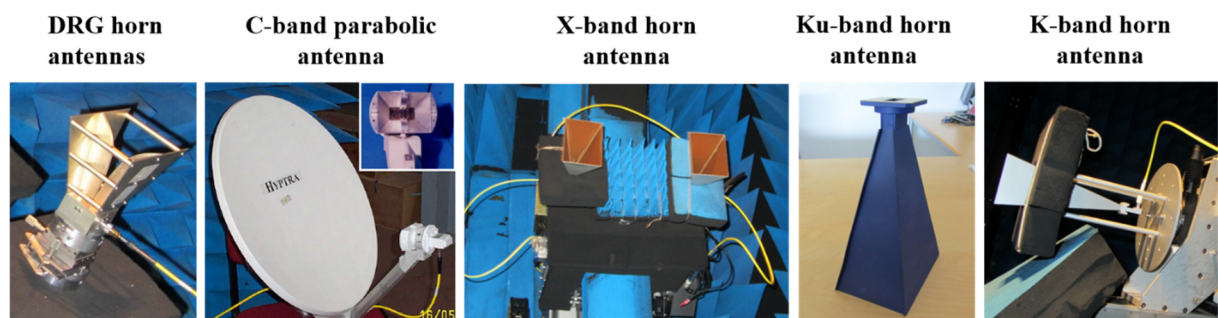
These X-band horn antennas were used for the measurements in a quasi-monostatic configuration (see chapter 4). They have a gain between 19 dB and 21 dB over the frequency band.

**4. Ku-band horn antennas [12-18 GHz]**

These antennas were used for some of the bistatic scattering measurements. They have a gain of 20 dB.

**5. K-band horn antennas [18-26.5 GHz]**

These antennas have high directivity and they are used for measurement at a single frequency of 18 GHz, which is the highest reachable frequency with the measurement setup. They have been used in this thesis for the measurements in section 3 and section 3.1. Their gain is 21 dB at 18 GHz.



*Figure 1.24 photo of some of the used antennas*



### 1.4.6 Measurement of the scattered electric field

The measurement of the field scattered by a TUT is not obtained in a unique step. When the TUT is illuminated with an electromagnetic wave generated from the emitting antenna, the signal measured by the receiving antenna is the summation of two fields: the incident field  $E_{inc}^{mes}$  and the scattered field  $E_{sca}^{mes}$ . This signal is called the total field  $E_{tot}^{mes}$ . The determination of the scattered field requires the complex subtraction of the incident field to total field. These two fields are obtained through two separated measurements, the first with the presence of the TUT and it allows to obtain  $E_{tot}^{mes}$ , and the second without the TUT and it allows to obtain the incident field  $E_{inc}^{mes}$ . The scattered field is therefore deduced from the complex subtraction of those two fields (Figure 1.25). In the case of targets of the order of the wavelength, the total and incident fields are quite similar because the target's contribution is small (Figure 1.26).

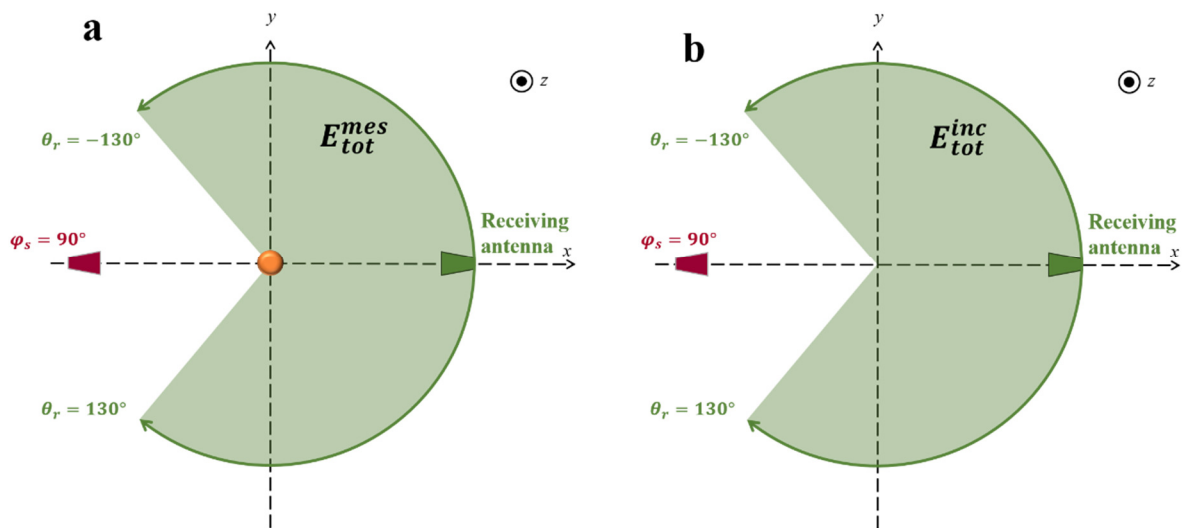


Figure 1.25 A schematic showing the measurement of the (a) total field and the (b) incident field

Here I emphasize that the measured signal at the VNA is not a referenced electric field but the ratio  $b_2/a_1$  which represents the  $S_{12}$  parameter. The quantitative estimation of the electric field, whether the scattered incident or total field, is obtained from the  $b_2/a_1$  ratio after applying the calibration process that refers in our case, using a reference target, the amplitude of the incident signal to an amplitude of 1 V/m at the center of the TUT and a null phase at the same location (see section 1.4.8).



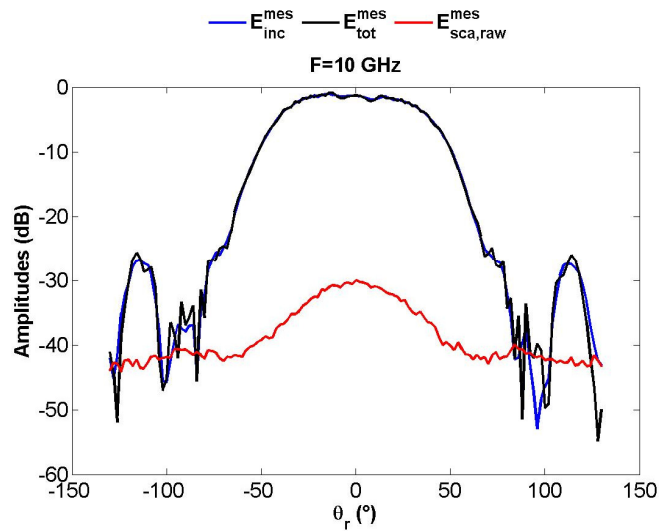


Figure 1.26 Total, incident and scattered field obtained with a 35 mm metal sphere measured at 10 GHz in the VV polarization

#### 1.4.7 Targets alignment

This setup is designed so that the rotation axis, along  $z$ , of the receiving antenna in the  $xOy$  plane and that of the transmitting antenna on the arch, along  $y$ , in the  $xOz$  plane intersect both at the position  $O$ , the origin of the coordinate system. A laser diode had been positioned in the chamber, fixed on the wall orthogonal to the  $Ox$  axis, and its illumination direction was aligned to coincide with the  $Ox$  axis. The alignment of the targets through this laser illumination accuracy was characterized at 0.1 mm. Every time a target needs to be measured it should be aligned. Unless otherwise specified, the targets are aligned to have their center coincide with the origin  $O$  of the coordinate system.

We can distinguish between two types of targets in term of alignment:

- (i) The first type is the metal and dielectric spheres. In this case the sphere is placed on the top of the polystyrene mast which is fixed on the rotational motor RV240CCHL (paragraph (iii)). A specific white board with a hole is placed between the sphere and the diode, and one keep visualize the appearance of reflected laser beam by the sphere's interface on that board. In order to place the sphere at  $O$ , its manual displacement is possible in the  $Oz$  axis using the elevation of the mast, and in the  $xOy$  plane using the translation sliding system at the bottom of the mast. Therefore, rotations of the sphere around the  $Oz$  axis are made using the RTN 240 motor, and once the laser beam reflection is invariant as a function of the rotation of the RTN 240 motor, the sphere is correctly placed at  $O$  due to its symmetry (Figure 1.27).

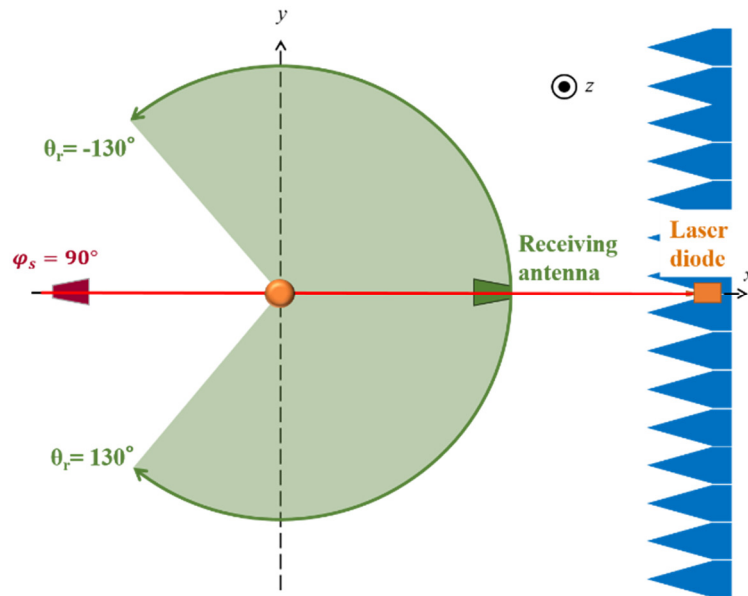


Figure 1.27 The alignment of the sphere using the laser diode

- (ii) The second type is the non-spherical targets. In this case a specific expanded polystyrene holder is fabricated to align the target. The holder consists of four hemispherical holes making the four corners of a square, at the center of which relies the target. The four holes are made to hold four identical dielectric spheres of 16 mm diameters. Therefore, the alignment of the polystyrene holder at the origin O is possible using the reflection of the laser beams by the spheres on the white board and through the rotation of the RTN 240 motor, in a similar approach to the spherical targets (Figure 1.28).



Figure 1.28 A photo of a polystyrene holder made especially to the alignment of a soot aggregate analog of complex shape. The dielectric spheres and the black absorbing pieces are removed after the alignment is accomplished

#### 1.4.8 Calibration

To compare quantitatively the experimental scattered fields with the simulated scattered field of the TUT, it is important to calibrate the experimental one. The calibration procedure uses the measurement as well as the simulation of the field scattered by a reference

target  $TUT_{ref}$ . The typical chosen reference target is a highly conductor sphere to be considered as Perfect Electric Conductor (PEC) and this is for three reasons: first, it is simple to calculate analytically the field scattered by sphere thanks to Mie theory. Second, the PEC sphere which removes any doubt on its permittivity in the simulation. Finally, it is easy to be precisely aligned in the measurement setup due to its symmetry.

The calibration coefficient  $C^{coef}$  is determined through a comparison between the simulated field  $E_{sca, ref}^{sim}$  and the experimental field  $E_{sca, ref}^{mes}$  of the reference sphere. One calibration coefficient per frequency and per polarization is determined through minimization of the difference between experimental and simulated fields. For a given frequency,  $C^{coef}$  should be the same whichever is the emitting angle  $\varphi_s$ , the receiving angle  $\theta_r$  and the target rotation angle  $\theta_o$ . For the measurement of  $E_{sca, ref}^{mes}$  with  $\varphi_s = 90^\circ$ ,  $C^{coef}$  is calculated as following:

$$C^{coef} = \frac{\sum_{\theta_r} E_{sca, ref}^{sim} \overline{E_{sca, ref}^{mes}}}{\sum_{\theta_r} |E_{sca, ref}^{mes}|^2} \quad (1.1)$$

Once the calibration coefficient is obtained it will be applied to the experimental scattered field by the TUT to obtain the calibrated scattered field  $E_{sca, cal}^{mes}$ .

$$E_{sca, cal}^{mes} = E_{sca}^{mes} \times C^{coef} \quad (1.2)$$

This calibration procedure is made to refer the experimental incident field to an amplitude equal 1V/m and a null phase at the center of the TUT (Figure 1.29).

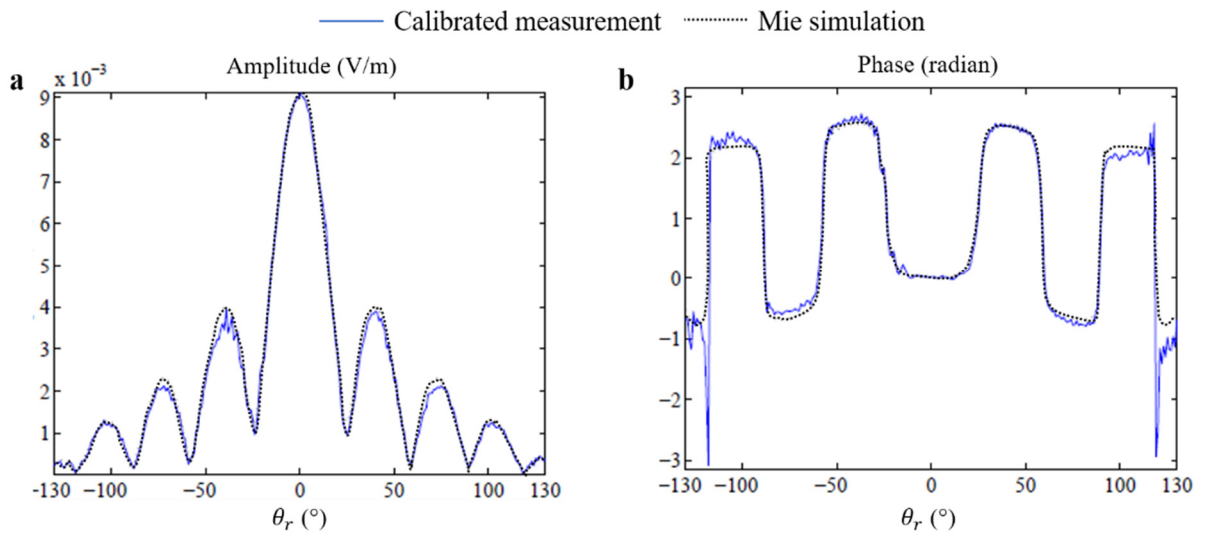


Figure 1.29 Calibrated experimental and simulated scattered fields by a dielectric sphere at 11 GHz in HH polarization as a function of the receiving angle [22]

## 1.4.9 Post-processing

### 1.4.9.1 Drift correction

The measurement of the electric field scattered by a target cannot be obtained in a unique step, but it is rather obtained through the complex subtraction of two electric fields: the total field  $E_t$  measured at the time  $t_t$  and the incident field  $E_i$  measured at the time  $t_i$

$$E_{sca}^{mes} = E_{tot}^{mes}(t_t) - E_{inc}^{mes}(t_i) \quad (1.3)$$

The total field is the signal measured with the presence of the TUT in the chamber, where the incident field is the signal measured with the absence of the TUT in the chamber (background measurement). The required time to accomplish those two measurements may last from 40 minutes up to several hours in some cases, depending on the number of frequencies and the different mechanical displacements. That time delay creates a variation in the measurement conditions, for example in temperature, which creates drifts in the amplitude and/or the phase of the signal propagating in the RF cables, in the VNA, in the RF mixers, etc. The impact of that drift error is observed as fast spatial fluctuations on the amplitude and phase of the scattered field [22]. For instance, for a measurement time of 10 hours, a variation around 1% on the amplitude and around 0.01 radian on the phase was noticed [51], [52].

An example showing the effects of the drift on the scattered field is presented in Figure 1.30. The example presents the measured and simulated scattered fields by a dielectric sphere at 11 GHz in HH polarization. It is apparent that the measured scattered field undergoes fast parasitic variations which do not exist on the simulated one.

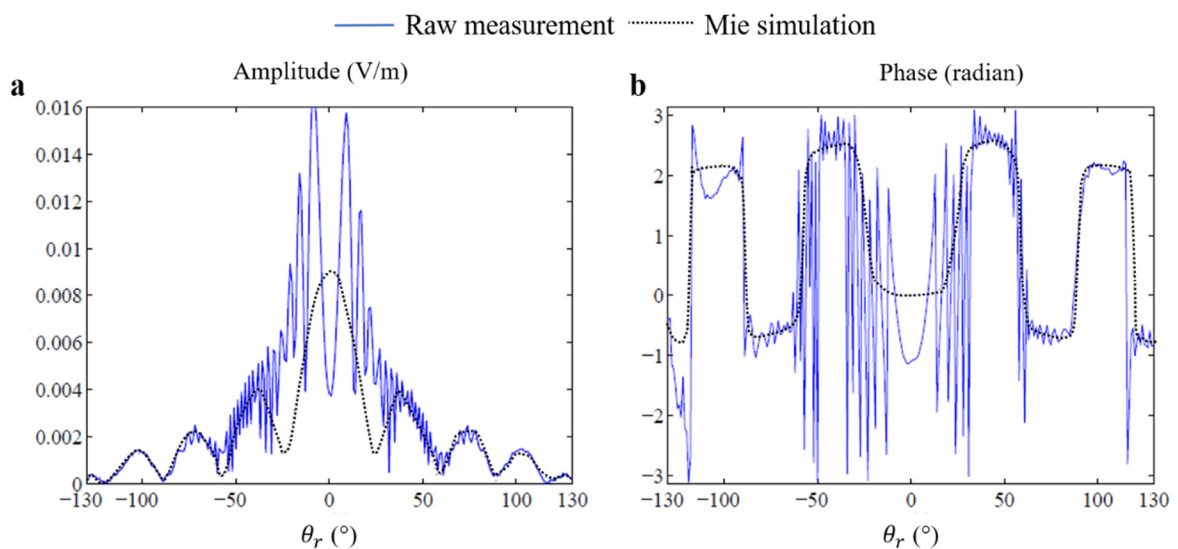


Figure 1.30 Raw measured and simulated scattered fields by a dielectric sphere at 11 GHz in HH polarization as a function of the receiving angle. (a) amplitude, (b) phase [51]

A processing on the spectral band of the scattered signal is performed to correct the drift error. This drift correction technique is based on the fact that the scattered field is spatially bandlimited as it was theoretically demonstrated in [53].

At each frequency, and for a given source position and a given target position, a Fourier transform is applied on the scattered signal as a function of the receiving angles:

$$\hat{E}(k_r) = \int_0^{2\pi} E(\varphi_r) e^{-j2\pi\varphi_r k_r} d\varphi_r \quad (1.4)$$

$\hat{E}$  is called the angular spectrum and  $k_r$  is the associated angular frequency. The comparison between the angular spectrum of the measured and simulated scattered fields of the same dielectric sphere are presented in Figure 1.31. The angular spectrum of the measured scattered field has a low frequency component in a similar way to that of the simulated scattered field, but has also high angular frequency components of lower amplitudes which do not exist in the simulation spectrum. These high angular frequencies are nothing but the spatial fluctuations due to the drift error.

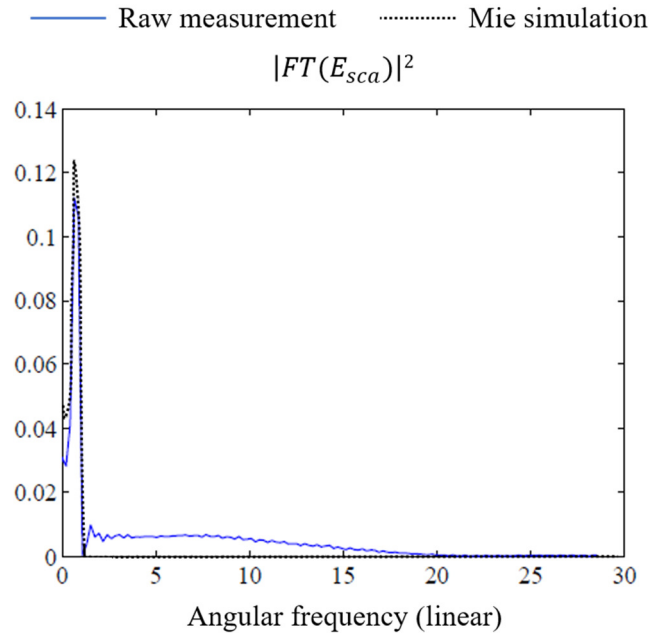


Figure 1.31 Angular spectrum of the measured (without drift correction) and simulated scattered fields by a dielectric sphere at 11 GHz in HH polarization as a function of the angular frequency [51]

In order to filter out the high frequency components, a drift correction procedure based on the properties of limited spatial bandwidth of the scattered field was previously developed and is being processed on the bistatic measurements [51], [52]. The drift correction procedure is summarized in the following.

During the movement of the receiver in the horizontal plane between  $-130^\circ$  and  $+130^\circ$ , the evolution of the drift error is considered null. For a given source position, a given target position, and a given polarization, the drift error affecting the scattered field at each of the receiving angles is the same. Since the incident field is independent of the target, the correction coefficient is applied to the total field. Therefore, the concerned drift correction method aims to find only one complex correction coefficient  $a \cdot e^{j\varphi}$  to be applied to the total field before subtraction of incident field:

$$E_{sca, driftCorr}^{mes} = a \cdot e^{j\varphi} \cdot E_{tot}^{mes}(t_t) - E_{inc}^{mes}(t_i) \quad (1.5)$$

Where  $E_{sca, driftCorr}^{mes}$  is the measured scattered field after drift correction. The values of the amplitude coefficient  $a$  and the phase coefficient  $\varphi$  are calculated through the minimization of the spatial bandwidth  $\widehat{E_{sca, driftCorr}^{mes}}$  of the drift corrected experimental scattered field:

$$\min_{a, \varphi} \frac{\int k_r^2 |\widehat{E_{sca, driftCorr}^{mes}}(k_r)|^2 dk_r}{\int |\widehat{E_{sca, driftCorr}^{mes}}(k_r)|^2 dk_r} \quad (1.6)$$

The angular spectrum of the drift corrected scattered field is presented in Figure 1.32 and scattered fields in amplitude and phase are presented in Figure 1.33. It can be seen that the high frequency components have been removed but also the low frequency components have been smoothed.

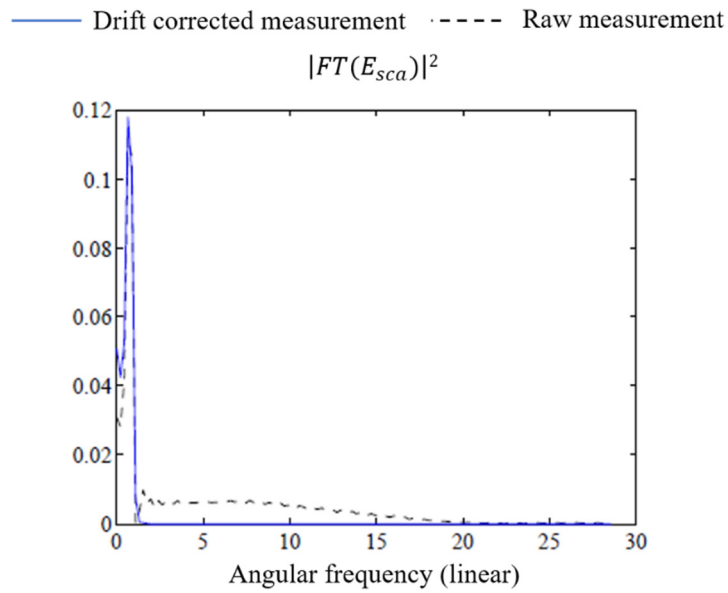


Figure 1.32 Angular spectrum of the measured scattered field by a dielectric sphere at 11 GHz in HH polarization as a function of the angular frequency with and without drift correction [22]

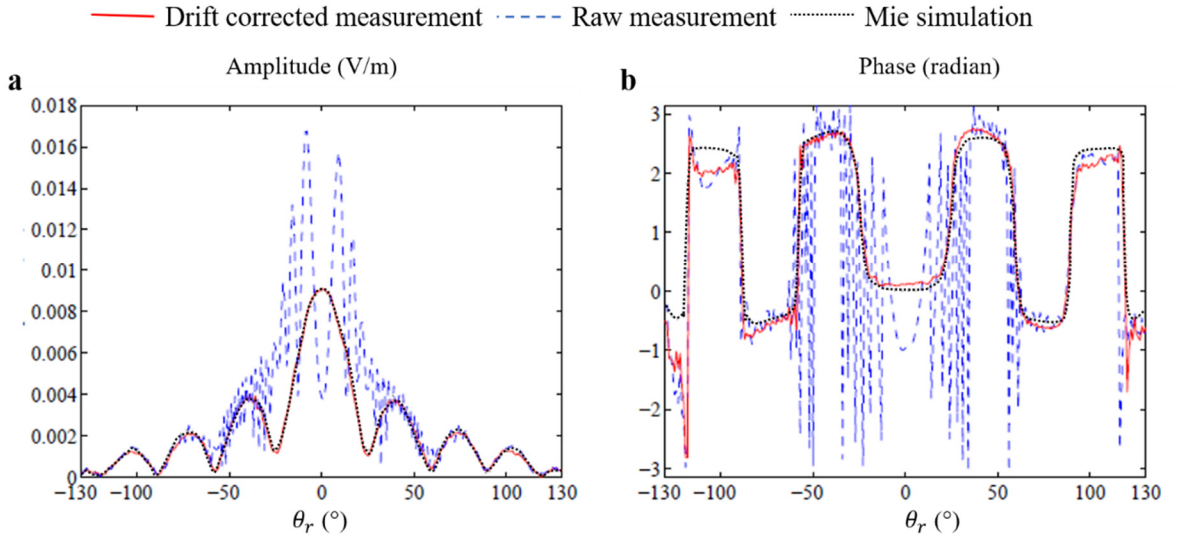


Figure 1.33 Raw measured, drift corrected and simulated scattered fields by a dielectric sphere at 11 GHz in HH polarization as a function of the receiving angle. (a) amplitude, (b) phase [22]

This drift correction procedure was used along this work to enhance the raw measurements and, except specification, was applied in all the bistatic measurements.

#### 1.4.9.2 Angular Lowpass filter

After the drift correction of the scattered field, an angular lowpass filtering is applied. This filtering is based on the fact that the scattered field has a limited spatial bandwidth that has been proved in [53]. It states that any scattered field is characterized by a spatial bandwidth which depends only on the overall dimension of the target. The spatial frequency of the scattered field is limited by the term  $2ka_{maxi}$ , where  $k$  is the wave vector ( $k = \frac{2\pi}{\lambda}$ ) and  $a_{maxi}$  is the radius of the virtual sphere in which the target can be included. Therefore, all the spectral frequencies that are greater than  $2ka_{maxi}$  can be considered as noise and are filtered out.

For instance, considering a measurement in circular azimuthal configuration of a 35 mm diameter metal sphere where the source is at  $\varphi_s=90^\circ$  and  $\theta_r=[-130^\circ$  to  $130^\circ]$ , then at every frequency, the spatial spectrum is obtained through Fast Fourier Transform (FFT) of the scattered field over all the  $\theta_r$  values. The result of this FFT is in black in (Figure 1.34). Next, the cutoff frequency  $2ka_{maxi}$  is defined and the components with frequencies above the cutoff are filtered out (red line of the figure).

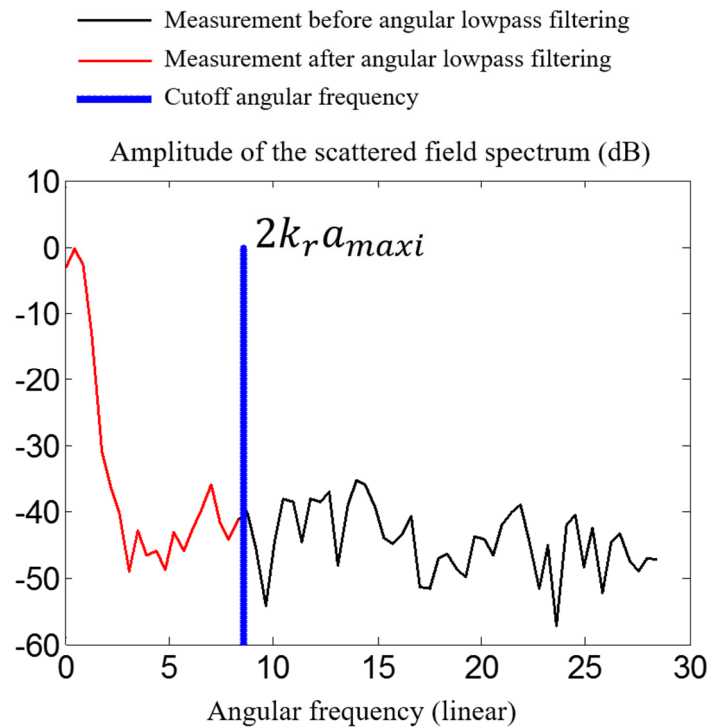


Figure 1.34 Angular lowpass filtering of a 35 mm diameter metal sphere at 10 GHz. The figure shows the scattered field spectrum before the filtering, after the filtering and the cutoff frequency

#### 1.4.10 Previously measured targets examples

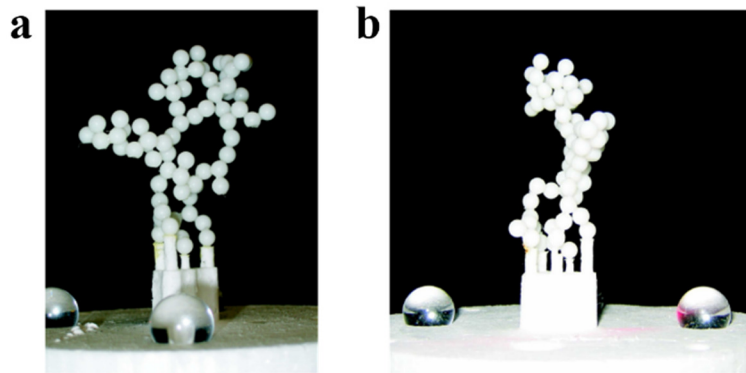
The features of the measurement setup such as the possible mechanical displacements of the antennas and the TUT in addition to alignment, drift correction and calibration procedures, allowed over the last decade to perform accurate microwave analog experiments on targets of diversity of shape and permittivity: soot aggregate analogs of complex shapes ( $\epsilon' = 2.8$ ) [54], analog-to-silicon spheres with high permittivity ( $\epsilon' = 16$ ) [12], [55], and inversely through a scale reduction, trees analogs mimicking forests ( $\epsilon' = 9$ ). In this section I briefly review a set of targets which have been measured in the experimental facility of the CCRM as well as some of the associated experimental results.

##### 1.4.10.1 Analog of a soot aggregate particle

Microwave analog scattering experiments had been made on a complex aggregate of spheres with well determined electromagnetic and geometrical properties and to compare the experimental results to calculations obtained with different computational methods. The aim is to scale to the microwave domain the scattering phenomenon by the carbonaceous soot particles with a form of aggregation. Such soot particles are produced in combustion processes, e.g. in the engines of cars, aircrafts, factories. In the case of this soot aggregate and more generally with “newborn” aggregates, the monomers of the aggregate are considered as



spheres with diameters below 0.1  $\mu\text{m}$  and they are investigated in the visible and infrared ranges. Therefore, an analog with monomers of 5mm diameter and with real part of permittivity of 2.8 was fabricated and measured at the frequency band between 15 and 20 GHz [54]. The aggregate analog was fabricated using a 3D micro milling machine adapted to manipulate spheres of 5 mm in diameter, then the spheres were stuck together with glue. The fabricated aggregate is shown in Figure 1.35. The scattering measurements have been made on this aggregate in a spherical configuration, where the transmitter is either in the plane containing the aggregate and the receiver ( $\varphi_s=90^\circ$ ) or outside that plane ( $\varphi<90^\circ, \varphi_s>90^\circ$ ) and different orientations of the target were investigated using the rotation of the polystyrene mast around the  $oz$  axis ( $\theta_o=-90^\circ, -45^\circ, 0^\circ, 45^\circ$  and  $90^\circ$ ).



*Figure 1.35 Front (a) and side (b) views of the aggregate analog placed on its polystyrene support. The plexyglass spheres are used to align to aggregate in the measurement setup and are removed after the alignment is done [54]*

The experimental results were confronted to numerical simulations obtained with four different codes:

- (i) `ddscat7.0` code based on the Discrete Dipole Approximation (DDA) [56].
- (ii) A homemade Method of Moment (MoM) Code [57].
- (iii) A T-Matrix code developed by Mackowski and Mishchenko [58].
- (iv) A T-Matrix code developed by Stout and Auger [59].

The first two methods are based on 3D volume integral formulation, where the third and the fourth are of the multiple Mie sphere solution type which are referred to as T-Matrix method.

The experimental results obtained at 20 GHz, for  $\varphi_s=90^\circ$  in VV and HH polarizations, together with the simulation results obtained with the four aforementioned codes are presented

in Figure 1.36. The experimental results showed good agreement with the simulations in amplitude and phase.

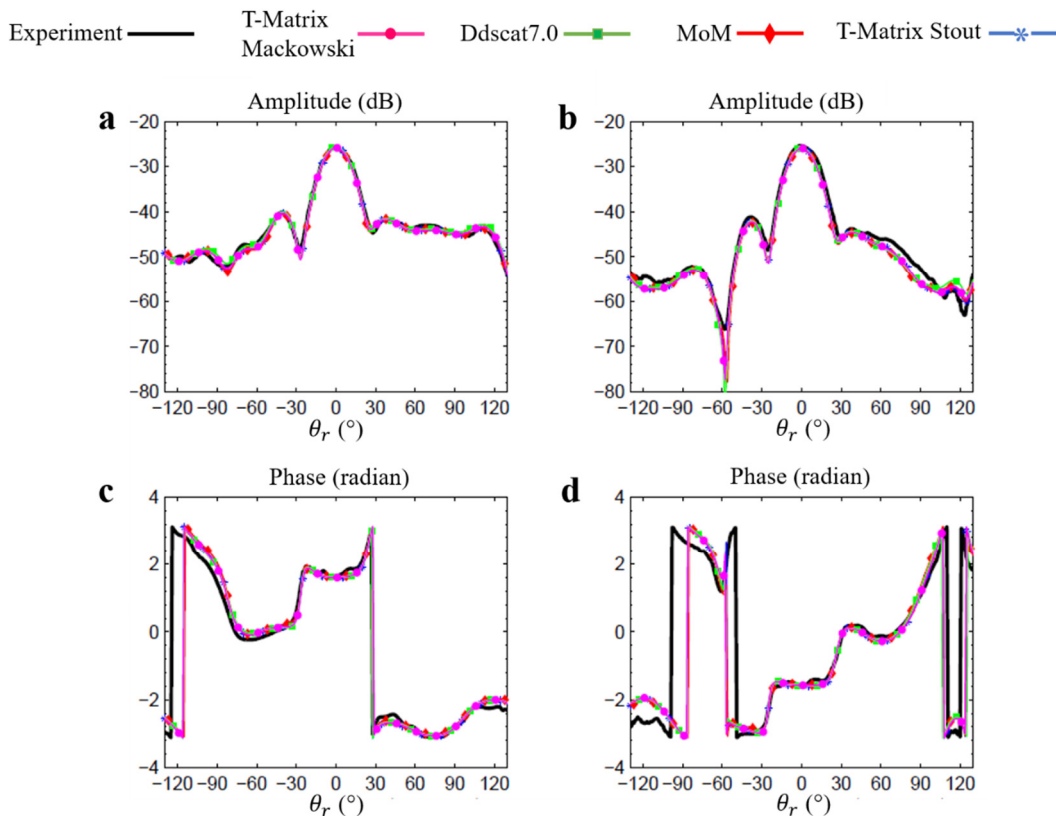


Figure 1.36 Amplitude and phase of the experimental scattered field compared to the simulations obtained with different numerical methods for  $\varphi_s=90^\circ$  and at 20 GHz in HH polarization (a, c) and in VV polarization (b, d) [54]

#### 1.4.10.2 Analogs of trees in forest environment

A theoretical model based on the Volume Integral Formulation have been developed by researchers from the “Laboratoire d’Electronique et Electromagnétisme” (L2E) at Université de Pierre et Marie Curie to investigate the scattering phenomenon in forested areas, to support the design of bistatic radar systems for military and civil applications. Due to the complexity of outdoor experimental validation and its cumbersome costs, the microwave analogy provided an efficient solution to carry out indoor experimental validation of the proposed model [49].

A forest imaging radar is preferred to operate at VHF and UHF. Regarding the trees in the model, the trunks are 3 meters high, the branches are 1 meter long and their permittivity is  $\varepsilon = 9 + 0.001j$ . The leaves were not represented because their contribution is considered negligible. A reduction factor  $k = 40$  was applied to scale the experimental situation to the microwave domain. Therefore, the scattering experiments were carried out at frequencies between 4 and 12 GHz on centimetric trees analogs. The trees analogs were made of vertical

and tilted dielectric parallelepipeds of  $\epsilon = 9 + 0.001j$ . The soil was mimicked by an aluminum circular plate. Figure 1.37-a shows the experimental configuration and the positions of the source antenna, receiving antenna and the aluminum plate on the surface of which the trees analogs are glued. Different configurations were investigated regarding the incidence angles, the receiving angles and the number and the form of the analogs. For instance, we present here the case of the measurement of the field scattered by a tree analog with 8 horizontally tilted branches (Figure 1.37-b).

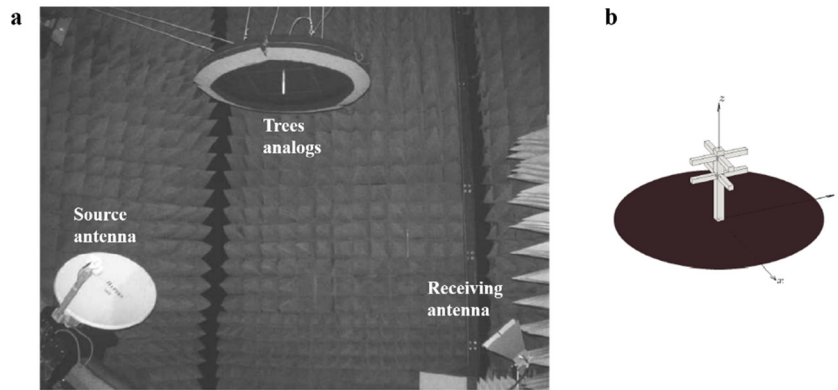


Figure 1.37 (a) A photo showing the positioning of the trees analogs on the aluminum plate, of the transmitting antenna and of the receiving antenna. (b) a schematic on the tree analog [11]

In this case the source antenna is fixed and the arm on which the receiving antenna is fixed rotates in azimuth around the z axis from  $-130^\circ$  to  $130^\circ$ . An example of the experimental results is presented in Figure 1.38. They showed good agreement with theoretical results especially on the amplitudes, where the phases showed some discrepancies, probably due to some alignments errors.

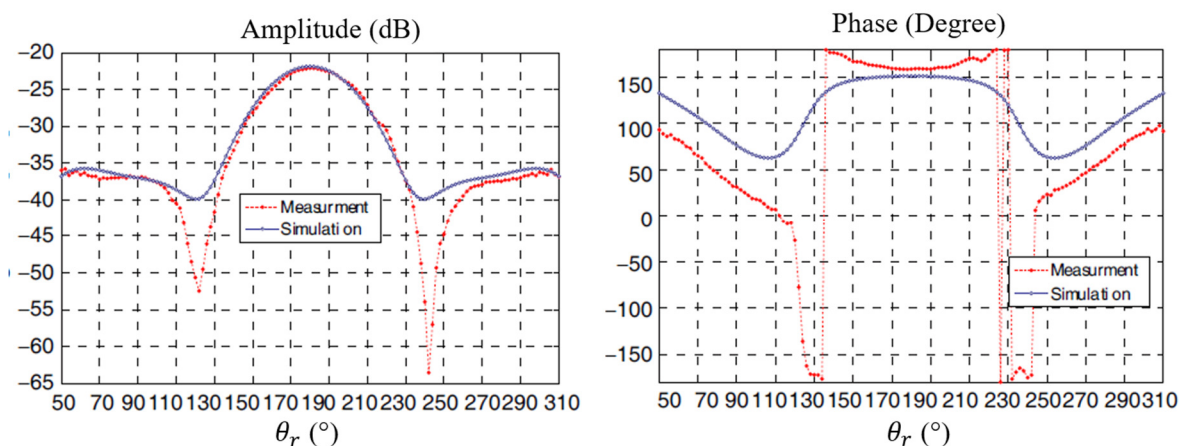


Figure 1.38 Comparison between experimental and theoretical results of the fields scattered by the trees samples in HH polarization and at  $F=4.2$  GHz [11]

### 1.4.11 Conclusion

In this section, we reviewed the basic features of the measurement setup and its state before the beginning of this thesis. The previously used devices were presented, the geometrical configuration and alignment procedure, as well as the post processing tools such as the drift correction and the calibration. I took benefit from these previous achievements and I utilized them along this thesis. Nevertheless, two remarks should be made here. First, the previous state of the microwave setup utilizing *Agilent HP* devices has been changed a while before this thesis started and the actual system is discussed in the next section. Second, the measurements were made in the past with a non-optimized state of the devices parameters. A complete and consistent study of the influence of the configuration parameters on the measurement accuracy is crucial especially for the study of small and low scattering targets. In the remaining section of this chapter the optimization of the setup configuration is investigated.

## 1.5 SCATTERING MEASUREMENT AT THE CCRM: CHARACTERIZATION AND OPTIMIZATION

### 1.5.1 CCRM measurement setup: current state

As mentioned previously, the equipment of the setup was changed a while before the beginning of this thesis. With the current setup, the measurement of the electric field is obtained through external mixers using a *Rohde & Schwarz* Vector Network Analyzer (*R&Z ZNB4*) as a simple 20 MHz receiver, two remote mixers (*Near Field Inc, NSI-RF-5945*) and two RF synthesizers (*R&S SMB110A*) as shown on the schematic in (Figure 1.39). With this setup, the IF signal circulating from the transmitting mixer toward the Digital Frequency Converter (DFC) and the  $F_{OL}$  signal circulating from the DFC toward the mixer propagate both in the same coaxial cable. The reference  $a_1$  IF signal is generated by the reference mixer and forwarded to the VNA through the DFC. At the receiving side, the test mixer receives the  $F_B$  signal from the antenna and the  $F_{OL}$  signal from the DFC and translates the received signal to an IF signal of 20 MHz. The IF received signal constitutes the test signal  $b_2$  that is sent to the VNA. The final measured quantity by the VNA is the ratio  $\frac{b_2}{a_1}$  in amplitude and phase. The aforementioned measurement devices, in addition to the employed cables and connectors (of type N and 3.5mm), all provide an operation frequency range between 2 GHz and 18 GHz. It is also possible to work at higher frequencies until 40 GHz using the third harmonic mode of the devices.

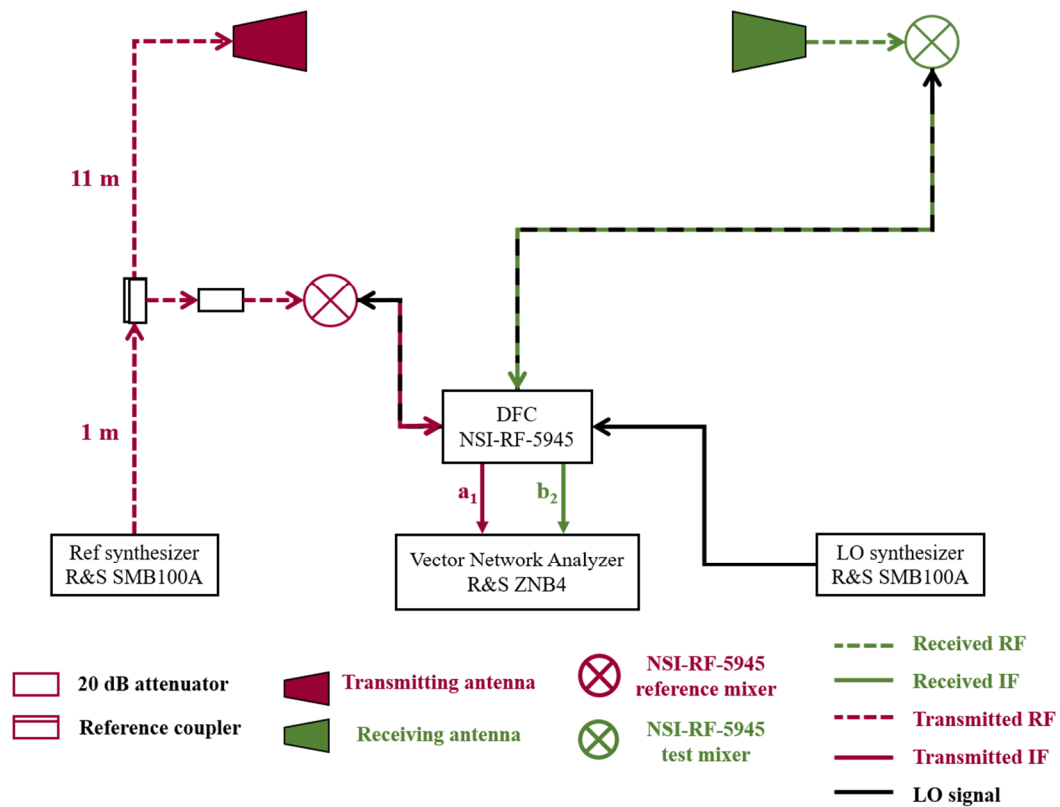


Figure 1.39 Synoptic of the measurement configuration using external mixers, synthesizers and Vector Network Analyzer

## 1.5.2 Measurement devices: frequency and power profile

### (i) Reference synthesizer (Rohde & Schwarz SMB100A-40GHz)

The reference synthesizer operates between 100 kHz and 40 GHz. Its maximal output is 15 dBm on the frequency range of interest (between 2 GHz and 18 GHz) and its minimal output power is 0 dBm.

### (ii) Local oscillator synthesizer (Rohde & Schwarz SMB100A-20GHz)

The local oscillator synthesizer operates between 100 kHz and 20 GHz. Its output power is always fixed at 5 dBm for an optimal operation of the DFC.

### (iii) RF to IF mixers (Near Field Inc. NSI-RF-5945)

The mixers operate from 1 to 40 GHz (with fundamental mixing for frequencies from 1 to 20 GHz and with third harmonic mixing for frequencies from 20 GHz to 40 GHz). The signals detection sensitivity is -117 dBm and the 0.1 dB compression point is at -26 dBm. This value is very important because it will contribute to the choice on the parameters for each measurement. The  $b_2$  or  $a_1$  signal at the input of the receiving or the transmitting mixer should be maintained below -26 dBm to avoid a nonlinear behavior at the mixer.

**(iv) Digital Frequency Converter (DFC)**

The DFC receives the LO signal from the LO synthesizer and forwards it to the reference and test mixers. In the other direction, it also receives the reference and test IF signals from the mixers and forwards them toward the VNA. The DFC adjusts the signals levels and amplifies the IF signals with a gain of 13 dB. Like the mixers, it operates from 1 to 40 GHz (with fundamental mixing for frequencies from 1 to 20 GHz and with third harmonic mixing for frequencies from 20 GHz to 40 GHz).

**(v) Vector Network Analyzer (VNA) (*Rohde & Schwarz R&Z ZNB4*)**

The VNA is used only as a receiver since the  $a_1$  signal is generated by the reference synthesizer and the RF-IF frequency translation is made with the remote mixers. The  $a_1$  and  $b_2$  signals are set at 20 MHz at the input of the VNA. The 0.1 dB compression point for  $a_1$  and  $b_2$  is at 10 dBm.

Moreover, two more parameters are involved in the configuration of the VNA: the IF filter bandwidth and the average on the real and imaginary part of the measured electric field. These two parameters intervene in the measurement of every frequency during a frequency sweep, where the sweep represents one measurement point.

The bandwidth of the IF filter can be set between 1 MHz and 1 Hz. A narrow bandwidth allows to filter adjacent signals which are separated by a small frequency spacing but it also requires a longer sweep time, because the sweep time  $\approx \frac{1}{IF \text{ bandwidth}}$ . During the experiments presented in this thesis the IF filter bandwidth has been generally set to 100 Hz, in a way to compromise between the measurement accuracy and the measurement time.

The average of the real and imaginary part option allows to select a time, called “Meas. Time”, during which each point of the sweep will be repeated N times. Therefore, the VNA collects all the valid results among the N measurement and yields their complex arithmetic mean value. This averaging allows to remove statistical fluctuations, such as noise contribution, from the measured signal. During the experiments presented in this thesis the “Meas. Time” has been generally set to 200 ms, except in the case of the inverse problem experiments where it has been set to 40 ms to economize the measurement time. For instance, with an averaging of 200 ms and an IF filter bandwidth of 100 Hz the average is calculated over 20 repetitions.

Finally, one important parameter in the VNA is the internal power attenuator. This VNA processes internal attenuators which allows to attenuate the  $a_1$  and/or the  $b_2$  signals by 10 dB, 20 dB or 30 dB when a power adjustment is needed on the receiver.

**(vi) IF Amplifier (MITEQ AM-1663)**

An IF signal amplifier is occasionally used, depending on the configuration case per case, to amplify the signal power at the input of the VNA. It is placed in the measurement chain between the DFC and the VNA. It has a power gain of 35 dB and its 1 dB compression point is at -14.5 dBm.

**1.5.3 Optimization possibility of the remote mixers based setup**

Based on the foregoing, the power level at each stage of the measurement setup, at the transmission and the receiving side, should be adjusted to have the most appropriate power level at the input of each device to insure a good measurement accuracy but also prevent falling into non-linear behavior (due to a high-power level exceeding the compression point or due to a low power level of small signal to noise ratio). The power configuration cannot be the same for all the measurement cases, since the signals power for each experiment depend upon the working frequency, the gain and the radiation pattern of the used antennas, the polarization of the incident and received signal, etc. A configuration summary sheet, which takes into account all the setup parameters, has been prepared to help choosing the optimal power configuration for each experimental case (Figure 1.40). The configuration optimization is discussed in detail in section 1.7.

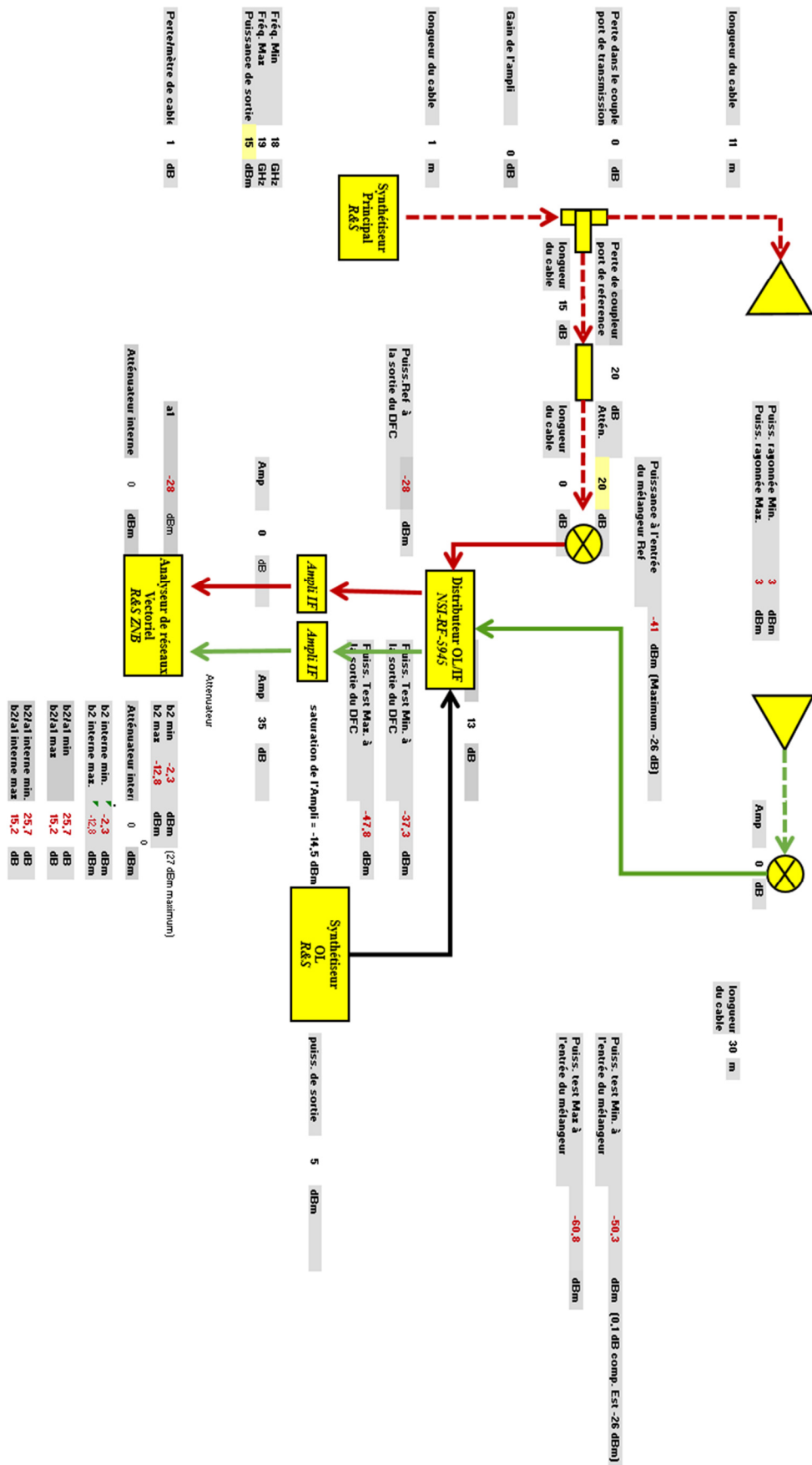


Figure 1.40 The configuration summary sheet, made on Microsoft Excel



### 1.5.4 Implementation of a quasi-monostatic configuration

So far the presented setup configurations allowed to carry out bistatic scattering measurements: in a spherical configuration (section 1.4.3.1), in a circular configuration for forward scattering measurement (section 1.4.3.2) and in a circular configuration for backward scattering measurement (section 1.4.3.3). Quasi-monostatic measurement might be feasible by using the two wagons on the vertical arch, the first carrying a transmitting antenna and the second carrying a receiving one, and through a simultaneous vertical displacement of both antennas. This configuration suffers from some weaknesses:

- (i) The quasi-monostatic angle between the transmitter and the receiver is restricted by the mechanical conditions of the wagons and the smallest achievable angle is  $12^\circ$ .
- (ii) Only quasi-monostatism in  $\varphi$  would be achievable. The quasi-monostatisme in  $\theta$  would be impossible (Figure 1.41).
- (iii) In this configuration, the cables in which propagate the transmitted and the received RF signals are displaced at every wagon movement and are undergoing consecutive position changes. The instability of the propagation conditions in such many meters long cables is quite likely to suffer from uncontrollable noise (phase shift, amplitude attenuation variations, etc.). This may create differences in the conditions between the measurement of the total field and that of the incident field, or even with the calibration measurement.

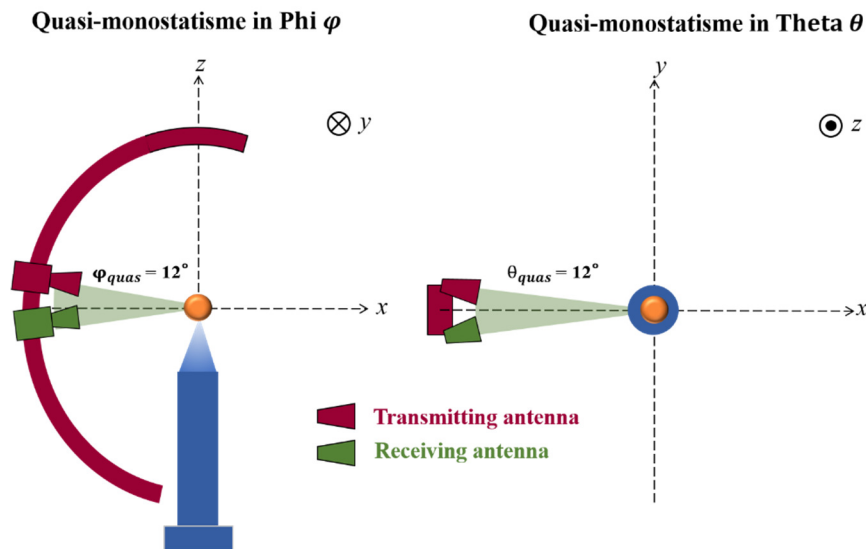


Figure 1.41 Definition of the quasi-monostatisme in Theta and in Phi

In order to overcome the aforementioned weaknesses and allow versatile quasi-monostatic measurements, I have modified this configuration to place two antennas on the same wagon:

- (i) A special lightweight rectangular plate has been machined to be fixed on the wagon and hold both transmitting and receiving antennas. Different gaps between the antennas are possible on the plate, allowing to have quasi-monostatic angles between  $1^\circ$  (if the antennas are small enough) and  $12^\circ$  for the given distance of 1.7 m between each of the antennas and the origin O of the coordinate system. This mounting advantageously allows to make experiments in both theta and phi quasi-monostatism and allows as well to have small quasi-monostatic angles down to  $1^\circ$  (Figure 1.42).
- (ii) In order to eliminate the perturbations created by the propagation of RF signals in long and moving cables, it is better to perform the frequencies translation from RF to IF as close as possible to the antennas. The propagation of the  $a_1$  and  $b_2$  signals at IF (20 MHz) is less likely to undergo losses, amplitude and phase errors. The solution I have proposed is to move the RF-IF mixers, which have been so far placed at the backside of the vertical arch, at the proximity of the antennas. A schematic of quasi-monostatic configuration is shown in (Figure 1.43). The two RF-IF mixers, the 20 dB reference coupler and the 20 dB attenuator are fixed on the superior wagon on the arch. Two new cables of around 10 meters long have been passed through the drag chain to guide the  $a_1$  and  $b_2$  signals from the mixers to the DFC (solid red line and solid green line on Figure 1.43).

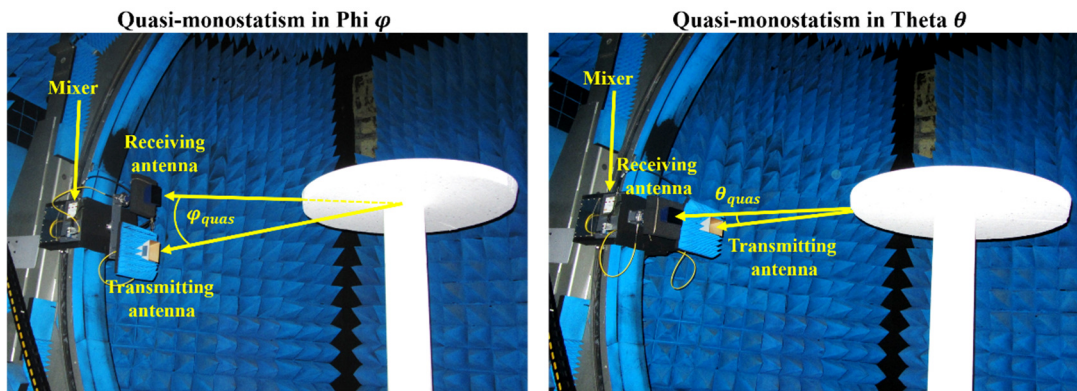


Figure 1.42 Quasi-monostatism in Theta and in Phi

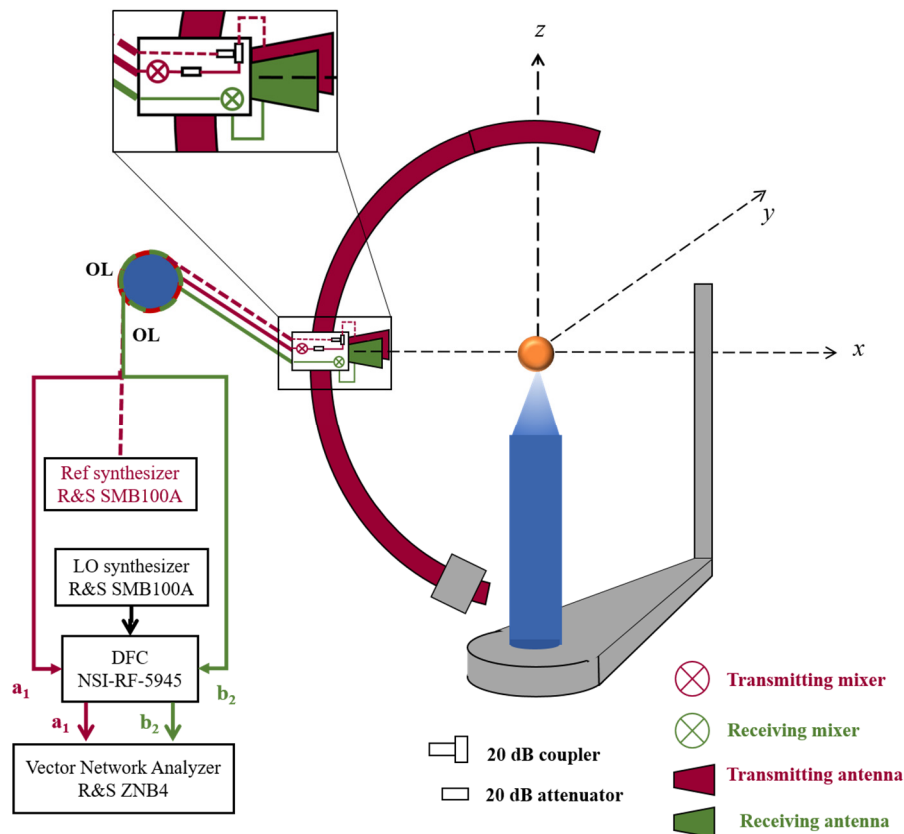


Figure 1.43 A schematic of the modified and optimized quasi-monostatic configuration with the source antenna, the receiving antenna and the mixers fixed on the same wagon

## 1.6 STRAY SIGNALS FILTERING

### 1.6.1 Introduction

One of the encountered challenges in indoor scattering measurements is the isolation of the target's response from stray signals. The anechoicity of the chamber allows to significantly attenuate the multipath propagations but these latter may not be totally cancelled. For instance, undesired reflections from the absorbers in the chamber can still exist especially at low frequencies, where the RAM (Radar Absorbing Materials) which are based on carbon filled polyurethane foams don't perfectly absorb the electromagnetic radiations. Other noise sources are the leakage between the antennas and the reflections from the metal parts of the positioning systems.

In the experimental facility of the CCRM, the investigation of low scattering targets with dimensions in the order of the wavelength, and more delicate with low permittivity, has a great interest (chapters 2 and 3). Such kind of targets are error prone with respect to multipath propagations inside the anechoic chamber. The main identified sources of stray signals in the chamber are classified in the following and I distinguish between the quasi-monostatic

and the bistatic configurations. Whether the measurement configuration is quasi-monostatic or bistatic, it has been noticed that background subtraction with the incident field does not totally compensate the coupling, because the energy distribution in the chamber may not be exactly reproduced between the measurements of the incident and total fields due to the time delay.

### 1.6.2 Stray signals in quasi-monostatic measurements

In quasi-monostatic configuration, the transmitting and receiving antennas are near each other, not more than 12 cm away in our case. The undesired direct coupling between them can therefore be high, even if they are quite directive. In Figure 1.44, we show in (a) a schematic of a quasi-monostatic scattering experiment with a dielectric sphere of 50.75 mm diameter with an indication to the potential stray signals sources, and in (b) the time domain analysis of the experimental scattered field compared to simulation obtained with Mie theory. The measurement was made between 1.5 GHz and 12.5 GHz with the DRG horn antennas. To make easier the interpretation, the scattered fields are presented as a function of the distance rather than time. On the holograms, we can easily identify the target's response at a propagation distance of 3.4 m, which is the source-target-receiver distance. Since the target is axisymmetric, its time response keeps the same whichever is the monostatic angle. Two other important types of echoes can be distinguished on the measurement but not on the simulation. The first one represents the coupling or leakage from the source to the receiver. Since the distance between the antennas is the same over all the monostatic angles, this echo has always a travel distance of around 0.4 m. The second type of echo is a bunch of stray signals appearing at small monostatic angles corresponding to the antennas at the upper side of the vertical arch. They have propagation distances between 7 m and 8.5 m. Their signals are likely to be the reflections by the RTN660 turntable and its large metal arm. Their amplitudes are high for monostatic angle around 0 and lower when the antennas descend on the arch, and they vanish at monostatic angles above 50°.

The amplitudes of stray signals are very comparable to that of the sphere's response (only 10 dB lower). We can expect that for lower scattering targets the noise may become even higher than the target's response and degrades the measurement accuracy.

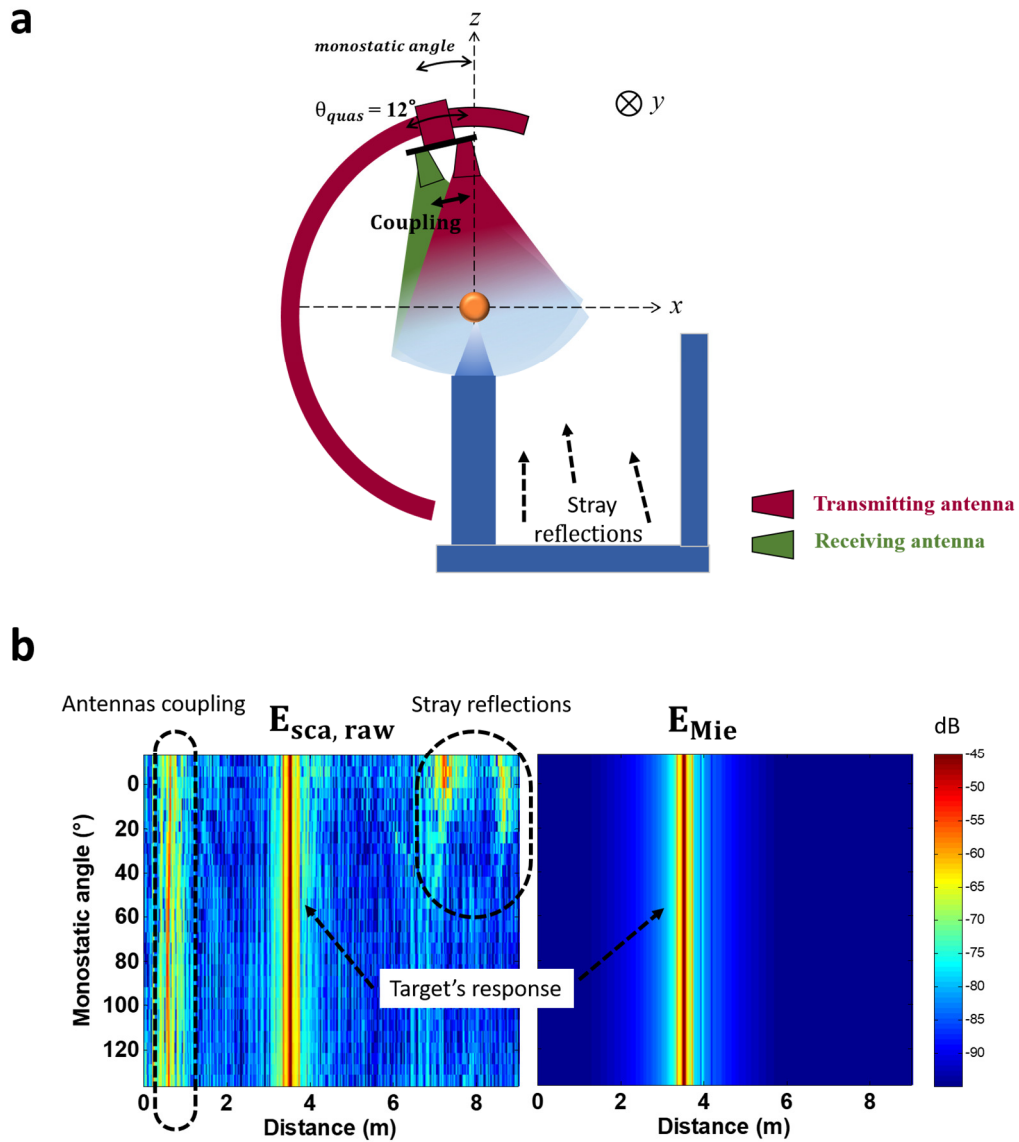


Figure 1.44 Stray signals identification in quasi-monostatic configuration. (a) Schematic of the measurement showing the potential sources of stray signals. (b) Impulse response representation by means of Inverse Fourier transform of the measured and simulated field scattered by a 50.75 mm dielectric sphere

We should emphasize that basically the calibrated measurement and the simulation are referred to an incident field with phase origin at the center of the target. This calibration should make the time domain response of the target (here the sphere) appears at a propagation distance around 1.7 m, which is nothing but the distance between the target's center and the receiver. However, in order to make clearer the time sequence of the different echoes in the time domain representation, the measured and simulated fields in Figure 1.44-b were multiplied by an artificial phase coefficient so that the phase origin is referred to the source antenna, hence the sphere's response is appearing at a traveling distance of 3.4 m (which is the scattering round trip).

### 1.6.3 Stray signals in bistatic measurements

In bistatic measurements the distance between the antennas is much larger and with our setup it varies from 1.7 m to 3.4 m when the receiving antenna moves from  $\theta_r = \pm 130^\circ$  to  $\theta_r = 0^\circ$ . Although the coupling in this case is lower than in quasi-monostatic configuration, it still can be distinguished on the scattered field. The coupling is seen as a residual energy on the time domain representation of the scattered field. In Figure 1.45 we show in (a) a schematic of a bistatic scattering experiment on a metal sphere of 35 mm diameter with an indication to the potential stray signals sources and in (b, c and d) the time domain analysis of the experimental scattered field compared to simulation obtained with Mie by means of Inverse Fourier Transform.

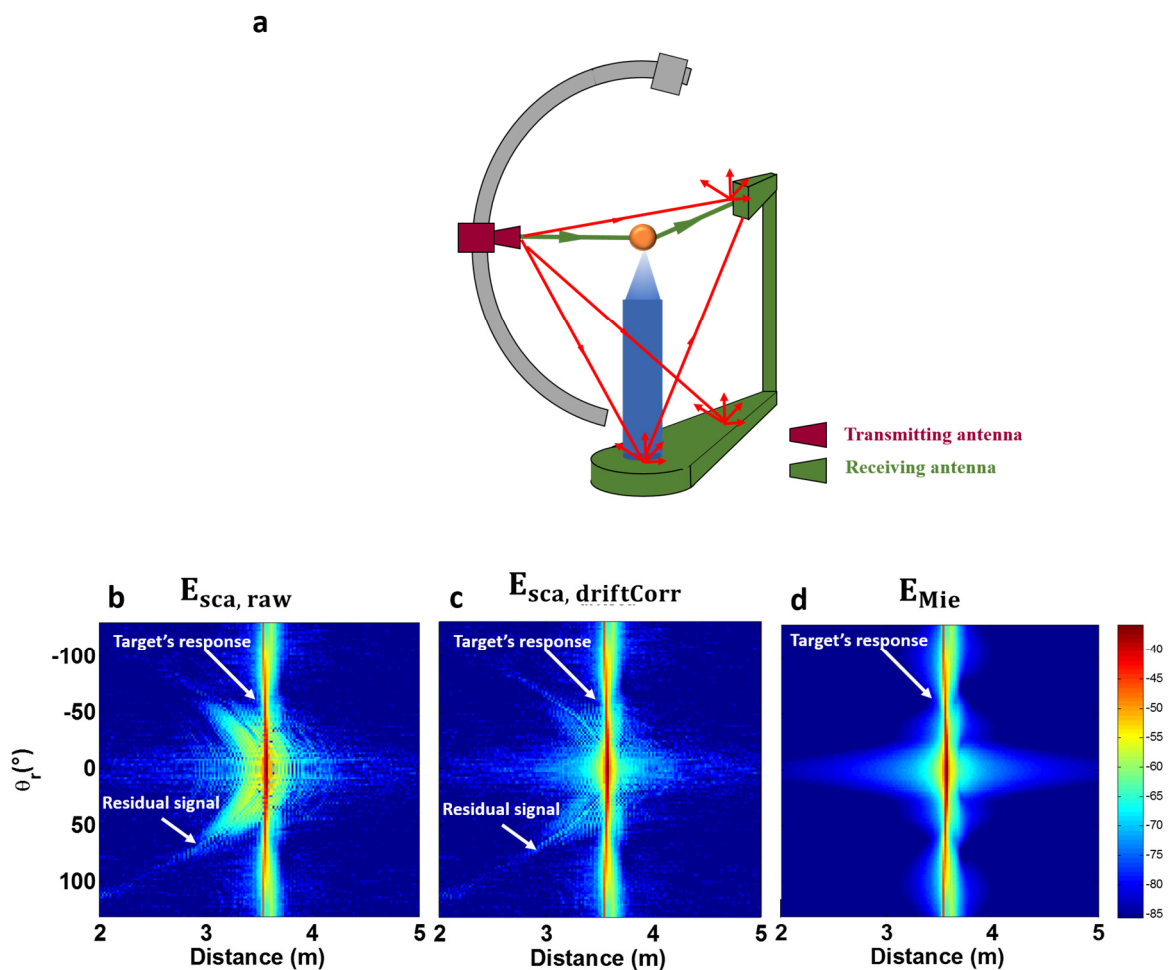


Figure 1.45 Stray signals identification in azimuthal bistatic configuration. (a) Schematic of the measurement. (b), (c) and (d) are the time domain analysis by means of Inverse Fourier transform of the raw measured scattered field, drift corrected scattered field and simulated scattered field respectively obtained with a 35 mm metal sphere

The measurement was made between 2 GHz and 18 GHz in azimuthal bistatic configuration using the DRG horn antennas. On the time domain representation of the raw scattered

field  $E_{rawsac}$  in Figure 1.45-b, we can distinguish the vertical impulse corresponding to the signal scattered by the metal sphere. Whichever is the position of the receiver  $\theta_r$ , that signal has the same travel distance of around 3.4 m which is nothing but the distance between the sphere and the receiver. The residual signal from the subtraction of the total and incident field is also shown on the same figure. It has a curved shape corresponding to the positions of the receiver with respect to the emitter. The amplitude of this signal is low at the near backward scattering for  $\theta_r$  around  $\pm 130^\circ$  and it becomes stronger in the forward scattering angles for  $\theta_r$  around  $0^\circ$ . It is worthy to notice that the drift correction post processing allows to attenuate that residual signal but it does not filter it out completely, as shown on the time domain representation of the drift corrected scattered field  $E_{sca, driftCorr}$ .

According to the distance/time propagation along different paths in the chamber, the stray signals contributions have different delays. To filter out the multipath stray signals and only maintain the target's response, specific time gating techniques are usually applied. We can distinguish between two gating approaches: Softgating and Hardgating. The choice of the one or the other is a performance trade off in term of filtering efficiency, system complexity, measurement time and cost.

#### 1.6.4 Soft gating post-processing

The soft gating principle is the most commonly applied time gating technique [60]. The measurement is made in CW mode and it is not restricted to the frequencies of interest but rather extended to a larger frequency band with a relative narrow frequency step. A posterior processing is later applied by means of discrete Fourier-transformation (DFT) to recover the time domain components. The choice of the overall frequency bandwidth  $B$  determines the time step  $\Delta t$  between adjacent samples in the time domain ( $\Delta t = \frac{1}{B}$ ), whereas the sampling frequency interval  $\Delta f$  determines the unambiguous time interval  $T$  in time domain ( $T = \frac{1}{\Delta f}$ ). The multipath stray signals which have been received before or after the target's response can be filtered out by applying a time gate. This gate or window should have a smooth amplitude tapering in order to avoid leakage effects in the frequency domain.

As example, we show in Figure 1.46 the application of soft gating on the measured scattered field of same dielectric sphere presented in section 1.6.2 in quasi-monostatic configuration. The frequency bandwidth is 10 GHz, from 1.5 GHz to 12.5 GHz and the frequency sampling interval  $\Delta f$  is 20 MHz. The DFT is applied and the time representation of the raw measurement is shown in Figure 1.46-b. A Hanning window centered on the target's response is applied and the undesired signals are removed away. The importance of the filtering is



clearly seen on Figure 1.46-a where the very noisy signal became smooth. The effect of the filtering is also shown on the holograms in Figure 1.47 showing a comparison between the raw measurement, the Mie simulation and the soft gated measurement.

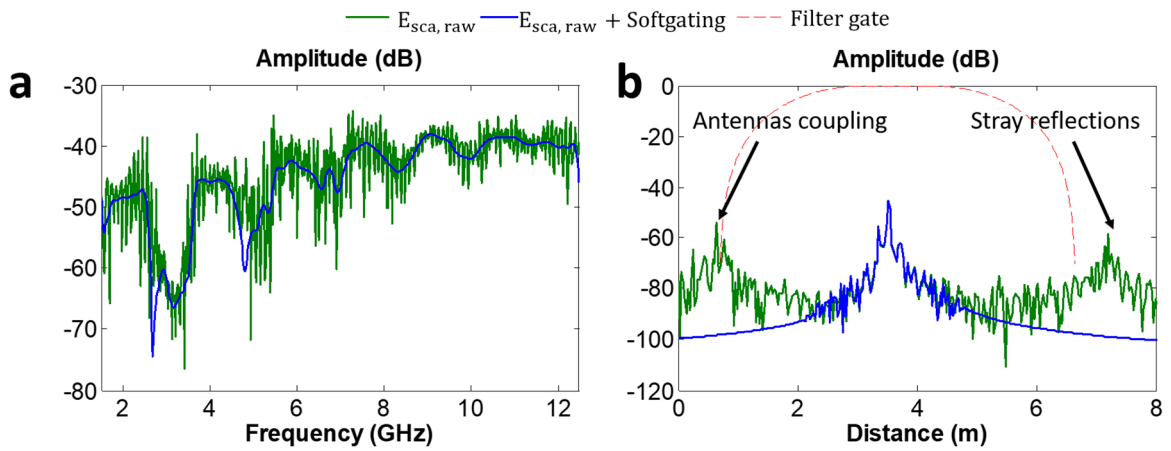


Figure 1.46 Raw and soft gated measured field scattered by the dielectric sphere in quasi-monostatic configuration at the monostatic angle  $9^\circ$ . (a) Representation in the frequency domain. (a) Representation in the distance domain showing the tapered Hanning window

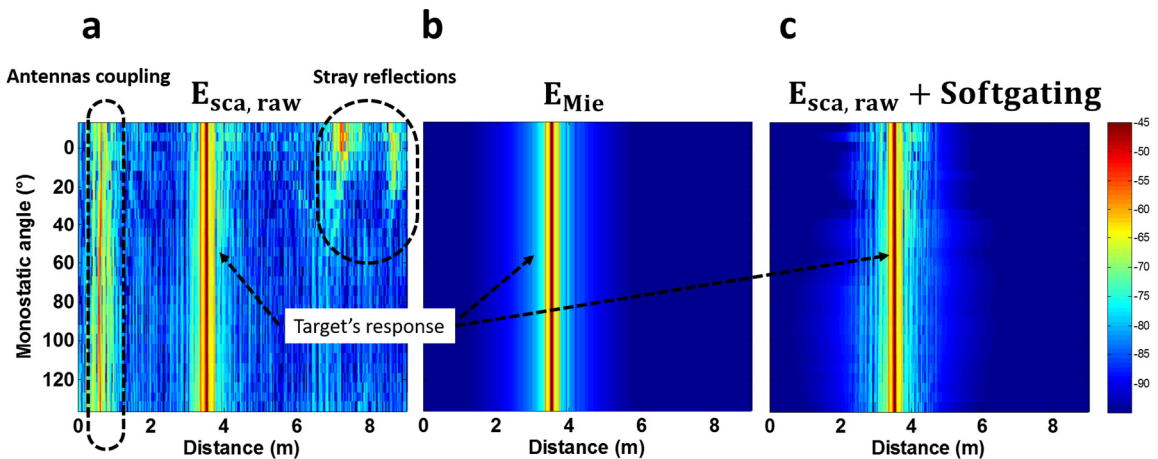


Figure 1.47 holograms showing the stray signals filtering using soft gating in quasi-monostatic configuration for the dielectric sphere. (a) Raw measured scattered field. (a) Simulated scattered field. (c) Soft gated measured scattered field

### 1.6.5 Measurement time vs Precision

Softgating insures that stray signals are filtered out because it forces their amplitudes to be null. It also provides a flexibility with filter design. The width and sharpness of the time window can be adjusted. However, the main disadvantage of this techniques is the long measurement time due to the huge requirement in frequency sampling. For instance, in the example presented in section 1.6.2, the measurement has been done with 496 frequencies in the working band between 2 GHz and 18 GHz. this sweep was obviously applied at each set of position



of the target and the receiver. For a single source position and a single target position, around three hours were needed to acquire both the incident and total fields. One can imagine that for measurement with many target orientations and/or many angles of incidence at the source the measurement time becomes extremely long. A typical case is the inverse problem imaging where the measurement time, with only one frequency, lasts few days due to numerous mechanical movements of the source, target, and receiver as well as in different polarization cases.

In addition, it is important to note that in Softgating, although the stray signals are mathematically removed, these signals are still physically existing at every stage of the measurement setup such as the remote mixer, DFC, amplifier and VNA. The high-power level of those signals can make them to fall in the non-linear regime of the devices.

Under these circumstances, Hardgating techniques appear to be more efficient and time saving. Hardgating have the advantage of real time filtering and the measurement is done at frequencies of interest.

### **1.6.6 Hard gating principle**

Hardgating systems based on pulsed measurement are often used in far-field antenna measurement, in compact range measurement and in RCS measurement to filter out the multipath signals and isolate the response of the antenna or of the target. The pulses transmission can be made using either a RF pulses generator or a CW gating system with fast RF switches that chop the CW into pulses. In our case, we decided to implement a chopped measurement system based on Hardgating technique. The advantage of using a Hardgating system based on RF fast switches rather than a pulses generator is to keep the same initial CW setup and use the pulsed measurement as an “add-on” options. In hard-gated measurements, an RF switch generates a short “window” in the time domain at the transmission side. A similar switch at the receiver side switches from passing to blocking states according to the travel time of the emitted pulse to receive the signal of interest and forward it to the receiver. Therefore, a versatile measurement system is maintained and it is possible to easily change the configuration from CW to chopped signals.

The cornerstone of the receiving system design in pulsed measurement is the spectrum spreading in the frequency domain. In fact, the Fourier transform of a CW signal is close to be a single frequency component in the frequency domain (theoretically it is a single frequency, in reality harmonic components are also existing). Most of the signal’s energy is contained within that spectra and can be entirely detected using a narrowband IF filter at the receiver (see sections 1.6.6.1 and 1.6.6.2).

In gated measurement, however, the transmitted signal is a periodic sequence of ON and OFF states. Each ON state is a short time transmission of the original CW signal. The Fourier transform of a gated signal is not a single frequency but it contains many spectra with an envelope of sinc form [61]. The Fourier coefficients of a pulsed signal can be calculated from  $F(\omega)$ :

$$F(\omega) = \frac{\tau}{T} \text{Sinc}\left(\frac{n\omega\tau}{2}\right) \quad (1.7)$$

Where  $\text{Sinc} = \frac{\text{Sin } x}{x}$ ,

$\tau = \text{pulse width}$ ,

$T = \text{pulse period}$ ,

$\omega = \text{angular frequency}$

$n = \text{integer}$

The total energy of the pulsed signal is the summation of all the spectra contained in the *Sinc* function. From equation 1.7 it can be seen that the width of a lobe in the frequency domain is inversely proportional to the pulse width  $\tau$ . Consequently, when the pulse width gets shorter the spectral energy spreads across a larger frequency band [62]. The spacing between two consecutive frequency components is inversely proportional to the pulse period  $T$  (Figure 1.48).

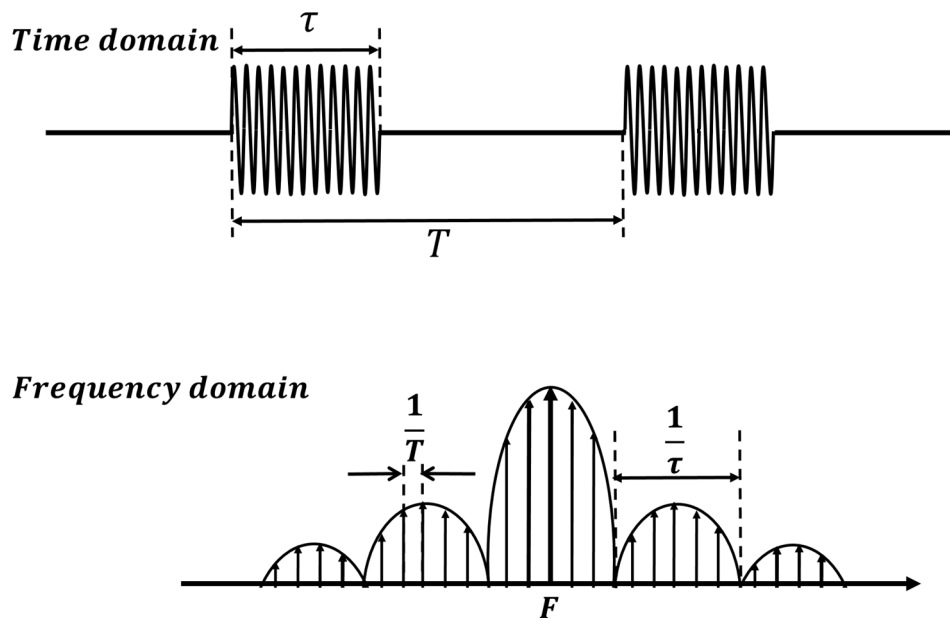


Figure 1.48 Characteristics of pulsed signals in time and frequency domains

The design of a Hardgating system depends mainly upon the pulse period, the pulse width and the IF filter bandwidth (IFBW) in the VNA. We can distinguish between two measurement modes dealing with pulsed signals: the narrowband mode and the wideband mode.

**1.6.6.1 Narrowband mode**

Also called averaged pulse measurements. In this mode, the receiver does not process the entire received frequency components, but rather only the central component. It is chosen when the pulse width is too short and consequently the frequency components are spread on so that their bandwidth is much larger than that of the IF filter of the receiver and it is impossible to select the whole signal's energy. In this mode, only the central spectra which represents the carrier RF frequency is selected by the IF receiver's filter and all the other frequency components are removed. From the time domain point of view, the receiver in the narrowband mode includes many pulses during a single sweep because the measurement time window, almost equal to  $\frac{1}{IFBW}$ , is much larger than  $T$  (Figure 1.49).

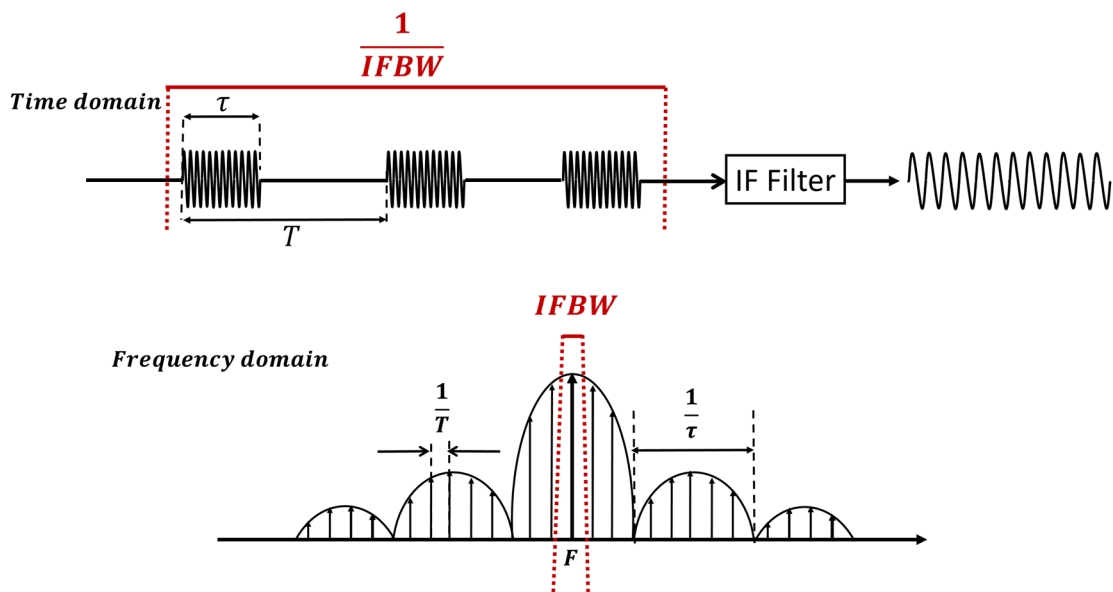


Figure 1.49 Narrowband mode in Hardgating measurement

The essential condition in narrowband mode Hardgating is to have the IFBW lower than twice the Pulse Repetition Frequency ( $IFBW < 2 \times PRF$ ), where  $PRF = \frac{1}{T}$ . This condition ensures that all the harmonics are filtered away.

**1.6.6.2 Wideband mode**

In wideband mode, also called synchronous acquisition mode [63], the receiver only measures the ON state or the pulse in the signal. It requires capturing the majority of the frequency components, so that the resulting filtered signal maintains its pulsed form. It is used when the majority of the pulsed spectrum is within the bandwidth of the receiver. The IF stage of the receiver utilizes a large bandwidth which is capable to select all the spectral components of the received pulse. In this mode, the receiver must be synchronized with the pulsed signal

so the measurement acquisition is only applied during the ON state of the signal. A pulse trigger of the same frequency as the pulses signal must be applied by the receiver.

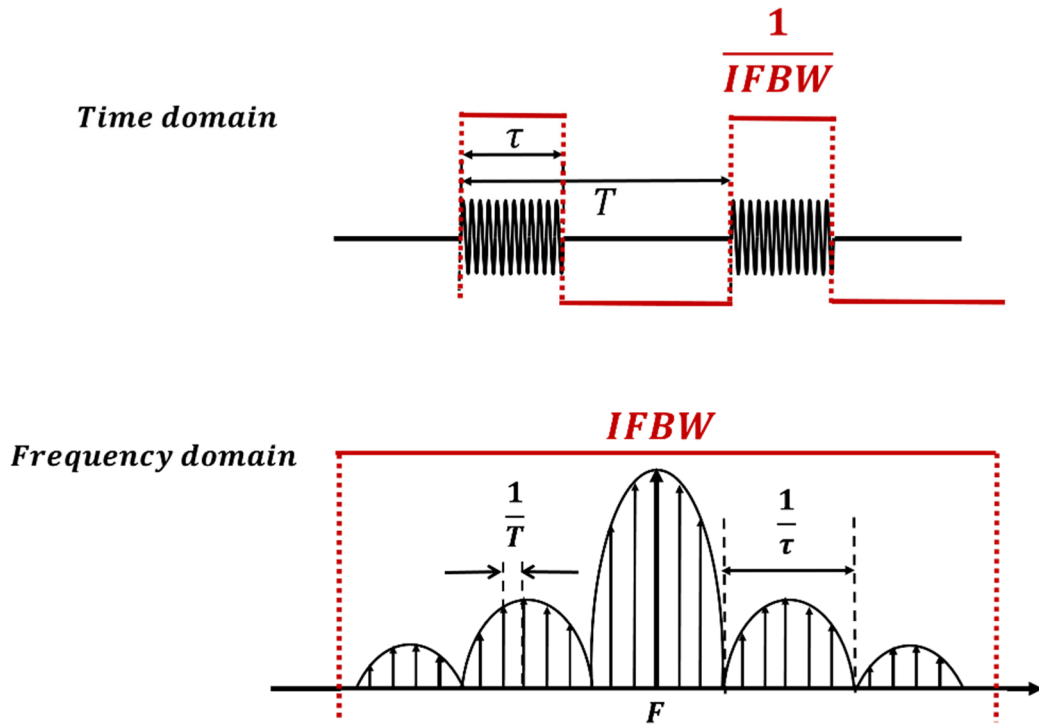


Figure 1.50 Wideband mode in Hardgating measurement

### 1.6.6.3 Advantages and disadvantages of narrowband and wideband modes

The main advantage in narrowband mode is that there are no conditions on the pulse width or in other words of the spectrum spread, because no matter how wide the spectrum is, only the center frequency is selected and the rest is filtered away. The other advantage is that no synchronization is needed between the pulsed signal and the receiver like the case of wideband mode. The disadvantage of narrowband detection is the loss in the dynamic range of the measured received signal due to the duty cycle. The corresponding degradation in the dynamic range (in other words the power loss) is expressed as  $20 \times \log_{10}(\frac{\tau}{T})$  in dB unit. This power loss increases as the pulse width decreases compared to the period. This loss could be compensated by using RF or IF power amplifications at the receiver side [61], [62], [64].

Wideband mode has better performance than narrowband mode since it does not suffer from duty cycle losses. It has also the advantages of providing a fast measurement speed because a single RF pulse is sufficient for the measurement to be made. However, the wide filter leads the receiver to acquire not only the fundamental frequency component but also the noise coming from high order harmonics of low amplitudes. Also, the measurable pulse width is limited by the available IFBW at the receiver in the wideband mode. As the pulse width gets

narrower, the spectral energy spreads out. As soon as the spread energy becomes wider than the available IFBW, the application of the narrowband mode becomes unfeasible. The minimum recommended pulse width in the literature is 200 ns [64]. Such large pulse widths can only exist in large chambers. Below this threshold, narrowband mode gives better results. Wideband mode is also very sensitive to the test/reference delays. The pulsed test signal and the trigger should be synchronized and presented to the receiver at the same moment. The paths lengths should be taken into consideration. Synchronization could be insured using specific devices (for example the pulse generator/synchronization device NSI-RF-5501 manufactured by *Nearfield Systems Inc* [64]).

### 1.6.7 Hardgating system in the CCRM setup

The main stray signals in the anechoic chamber of the CCRM have been identified through time domain analysis, and with respect to the geometrical configuration of the setup. The main ones are the leaking between the antennas and the reflections on the ground and on the metal supports.

The main parameters to be selected are the pulse width, the period and the delay between the transmission and the receiving gates. Ideally, the selected pulse width should be shorter than the delay between the target's response and the next arrival multipath signal to filter out this latter. At the same time, the receiving window shouldn't be switched off before the entire scattered energy has been received. The period should be selected to have an OFF state sufficiently large for all the multipath signals to be dissipated in the chamber before a new pulse is transmitted again. Since the traveling distances in the chamber are relatively small, the delays are short between target's response and the stray signals as it was shown in Figure 1.44 and Figure 1.45. According to the stray's identification in section 1.6.2 and section 1.6.3, we chose a pulse with of the pulse width of 8 ns (equivalent to 2.4 m) and a period of 50 ns (equivalent to 15 m). According to the small pulse width, a narrowband Hardgating mode is therefore used. The bandwidth of the IF filter in the VNA is set at 100 Hz, which is a narrow filter in order to avoid selecting the noise neighbor frequencies (Figure 1.51).

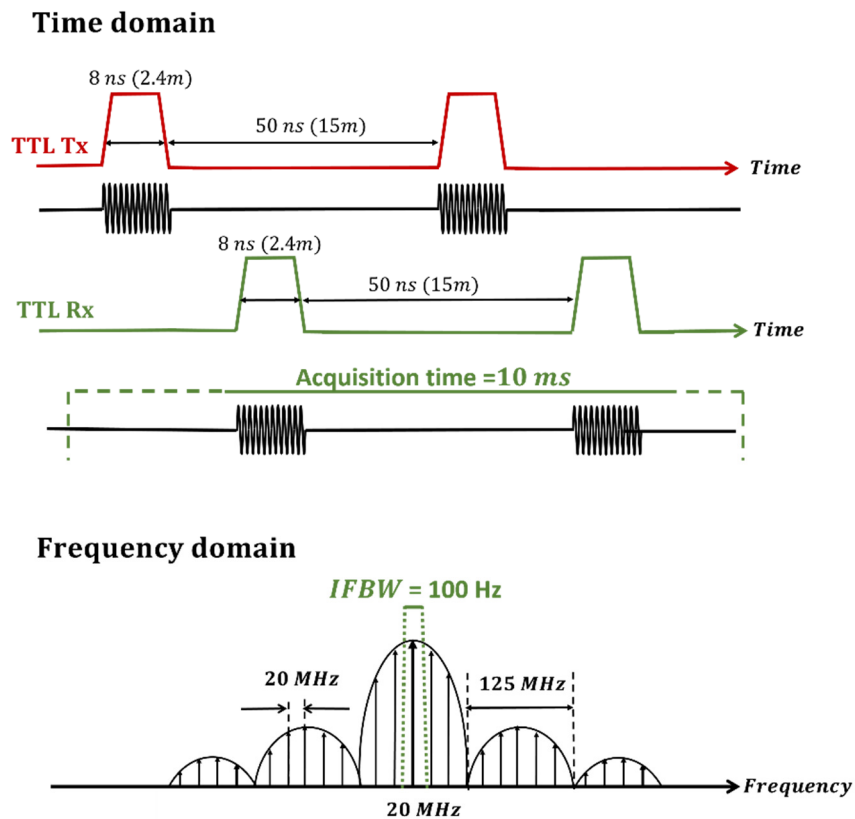


Figure 1.51 The parameters of the Hardgating system of the CCRM

The proposed Hardgating system utilizes a function generator (*Tektronix AFG3102C*) and two RF switches (*American Microwave Corporation SWCH1K-DC40-SK*) operating from DC to 40 GHz (Figure 1.52). The reference synthesizer generates a CW signal that propagates toward the transmitting antenna along a 11 meters cable. At the vicinity of the antenna the CW signal is fed to the input of the transmitting switch, this latter is fed with a TTL signal generated from the function generator. The TTL signal toggles between 0V to 4V to switch the transmitting switch ON and OFF respectively. The CW signal is therefore chopped into short pulses of 8 ns width which are emitted through the transmitting antenna. After a delay corresponding to the propagation time between the transmitter and the receiver, the receiving switch goes ON for 8 ns to capture the received pulse and forward it to the receiving mixer. The losses on the  $b_2$  signal are around 26 dB: 16 dB ( $20 \times \log_{10}(\frac{8}{50})$ ) due to the signal duty cycle and 10 dB insertion losses in the switches. These losses are compensated using an IF amplifier (*MITEQ AM-1663*) with 35 dB gain at the input of the VNA.

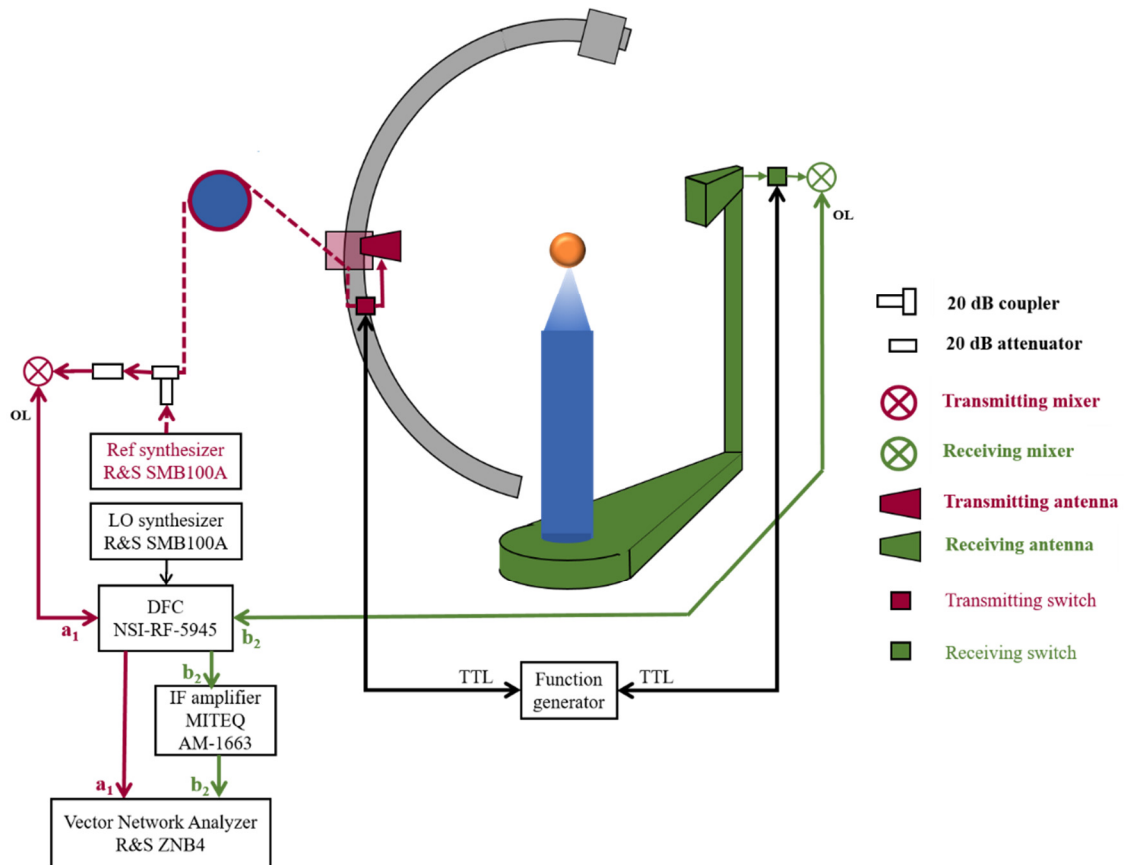


Figure 1.52 A schematic of the Hardgating setup of the CCRM used in bistatic configuration

on both measurement modes presented above, pulsing on the RF signal can be performed using SPST (Single-Pole, Single-Throw) switches. The time gate delay at the receiver should be equal to the travel time of the transmitted wave to the receiver's antenna. The pulse width is determined according to the traveling time of multipath signals. For example, if the line of sight (LOS) propagation time is 12 ns and that of the first unwanted return is 19 ns, then the pulse width of the receiver should not exceed 7 ns.

## 1.6.8 Some similar Hardgating systems

### 1.6.8.1 Stingray gated CW measurement system

It is a commercial Hardgating system developed to work with Agilent technologies Performance Network Analyzer (PNA). It is used in quasi-monostatic RCS measurements in the frequency band between 2 GHz and 18 GHz in large ranges [65], [66]. The RF signal is pulsed prior to the transmission by a pulse modulator and the timing setting is applied using a timing unit. The pulse width can be set from 1 ns to 10  $\mu$ s. The RF test and reference signals are down converted inside the pulse modulator unit and forwarded back to the PNA. Signal power amplification is processed in the pulse modulator after being receiving to increase the sensitivity.

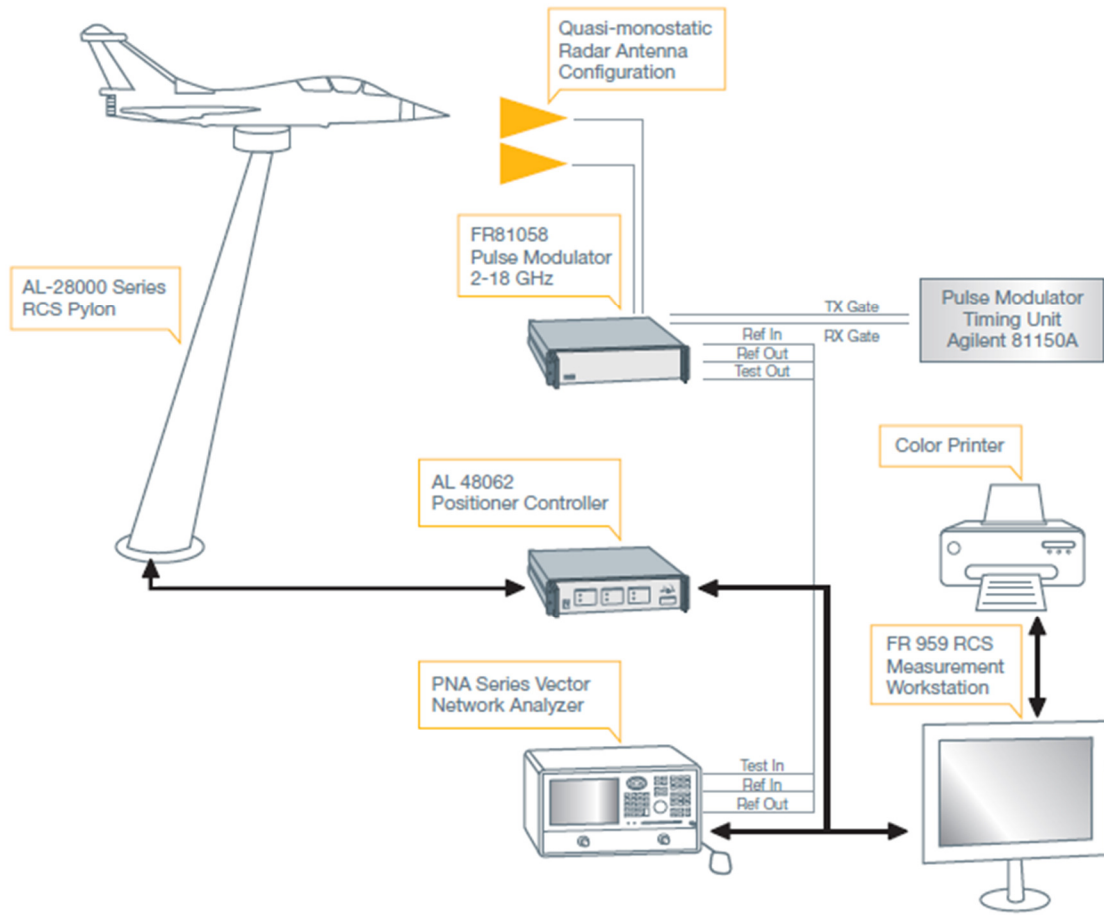


Figure 1.53 StingRay gated CW radar architecture [67]

### 1.6.8.2 The Hardgating system at the European Aeronautic Defense and Space Company

A Hardgating system was developed to suppress undesired signals at the measurement facility of the European Aeronautic Defense and Space Company (EADS) to be used for antenna pattern measurements and RCS measurement in anechoic chambers. The used Hardgating system is called HG2000 and it was developed by the EADS Astrium together with the laboratory for satellites communications at Munich University of applied sciences [68]. The HG2000 system is used for monostatic and bistatic RCS measurements in Compact Range (Figure 1.54) and the measurement setup utilizes remote mixers and an HP8530A vector network analyzer. As shown on the figure, the signal of interest (in green) is the last arrival with delay time and many undesired signals are existing. The pulse repetition time and the pulse width at the transmitter and the receiver are determined according to the corresponding delays and perceived angles of arrival in the chamber. The HG2000 system consists of a control unit directly interfaced to the data acquisition unit and a control computer [68].



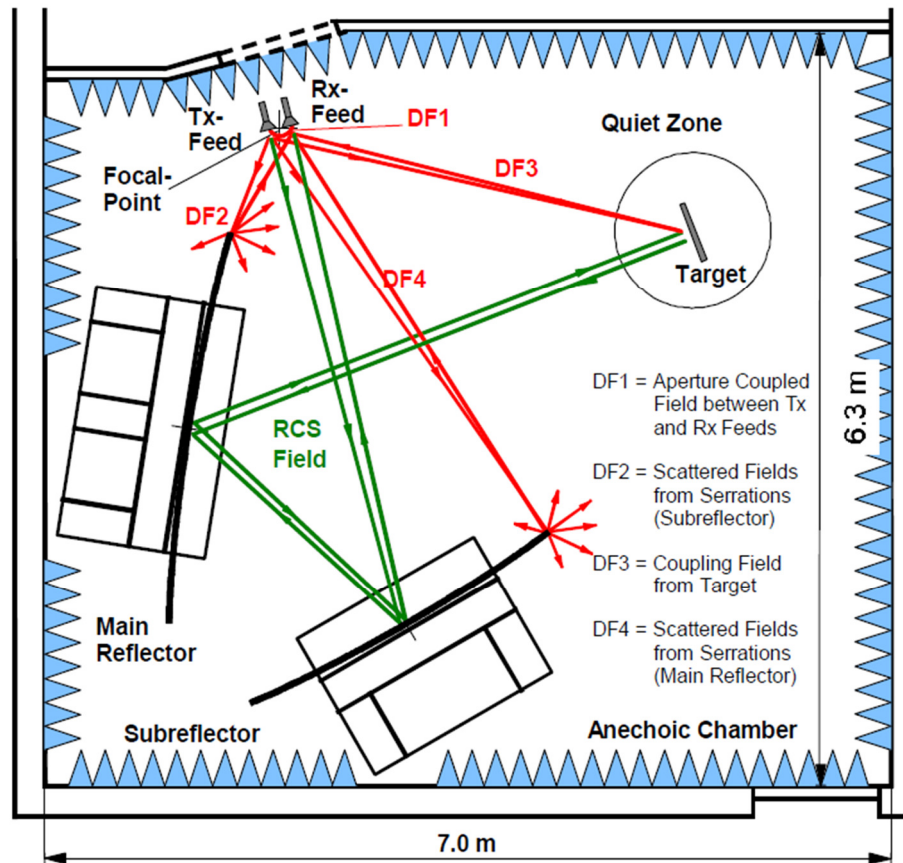


Figure 1.54 Compact Range measurements facility of EADS [69]

### 1.6.9 Performance validation of the Hardgating system

In order to assess the performance of the employed hard-gating setup, it was decided to perform bistatic hard-gated measurements on “well-known” targets and compare the results to soft-gated measurements on the same targets. Two targets were selected: a dielectric (Plexiglas) sphere with relative complex permittivity of  $2.6+0.01j$  for the frequency band between 2 GHz and 8 GHz, and a squat metal cylinder for the frequency band between 12 GHz and 18 GHz (Figure 1.55). Three reasons motivated the choice of these targets: their easy alignment due to their symmetry, the accurate knowledge of their electromagnetic properties and the reliable computation of their scattered fields.

The main difference between the hard-gated and soft-gated measurements of these targets is the number of frequencies. In soft-gated measurements, acquisitions at 450 frequencies were selected in the band of interest to make possible the time domain reconstruction of the signal. In the hard-gated measurements, only 7 frequencies with a step of 1 GHz were acquired between [2 GHz – 8 GHz] for the squat metal cylinder and between [12 GHz – 18 GHz] for the dielectric sphere. For the hard-gated measurements, the power losses related to the duty cycle of the windowed signal were overcome using an IF amplifier on the  $b_2$  signal.

The numerical computation are obtained with Mie theory for the dielectric sphere and with the commercial software CAPITOLE-EM from Nexio group [70].

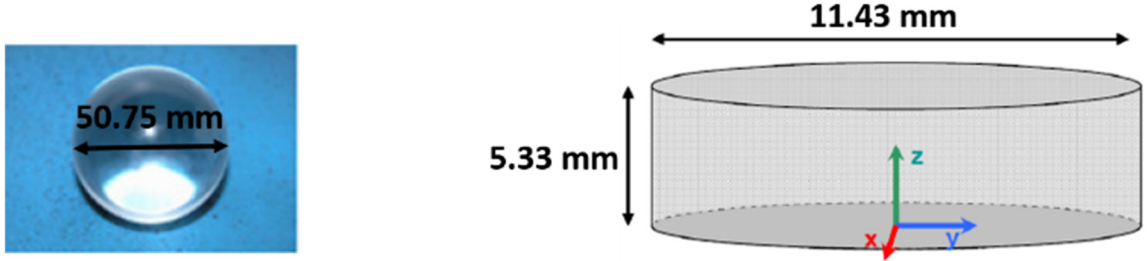


Figure 1.55 The Plexiglas sphere (left) and the squat metal cylinder (left)

Within this study it was very useful to apply different comparison criteria for a precise comparison. The choice of the criteria was inspired from a national inter-laboratory comparison of scattering measurements [71]. Several comparison criteria have been applied, some of them are classical one such as the correlation, the standard deviation and root mean square error. We focus on two different criteria: the Equivalent Scatterer (ES) and the Discrepancy Repartition function (DR). The Equivalent Scatterer (ES) is defined by the linear amplitude difference of the simulation and the measured scattered fields. The ES represents an equivalent parasitic backscatterer that perturbs the measurement.

$$ES_{dB} = 20 \times \log_{10} \left( \left| |E_{sca}^{meas}| - |E_{sca}^{sim}| \right| \right) \quad (1.8)$$

The  $ES_{dB}$  gives an estimation of the global signal to noise ratio. It should be interpreted with respect to the levels of the amplitude of the experimental fields. Therefore in its presentation hereafter we show the relative Equivalent Scatterer  $E_{dB}^{relative}$ :

$$ES_{dB}^{relative} = |ES_{dB} - E_{sca}^{meas}(dB)| \quad (1.9)$$

Where  $E_{sca}^{meas}(dB)$  is the amplitude in dB of the measured scattered field ( $E_{sca}^{meas}(dB) = 20 \times \log_{10}|E_{sca}^{meas}|$ ). When the value of  $ES_{dB}^{relative}$  is higher, that means the difference between the measurement and the noise is higher and the measurement is more accurate.

The DR provides the mean standard deviation of the differences around all the amplitude levels covered by the measured target:

$$\Delta = |E_{sca}^{meas}(dB) - E_{sca}^{sim}(dB)| \quad (1.10)$$

$$F_m(a < E_{sca}^{sim}(dB) < b) = mean(\Delta) \quad (1.11)$$

$$F_s(a < E_{sca}^{sim}(dB) < b) = std(\Delta) \quad (1.12)$$

The interval [a, b] must be large enough to acquire enough samples. It is equal to 0.25 dB in the presented examples.

Some measurement results for the squat metal cylinders are presented in Figure 1.56 at some frequencies with a comparison between simulation, non-gated, soft-gated and hard-gated measurements. The non-gated measurements are influenced by a noise that is more visible/evident at the low frequencies. The noise is removed with the two gating techniques.

In Figure 1.57 the  $ES_{dB}^{relative}$  criterion is applied to the three measurements in HH polarization and the three corresponding holograms are presented.

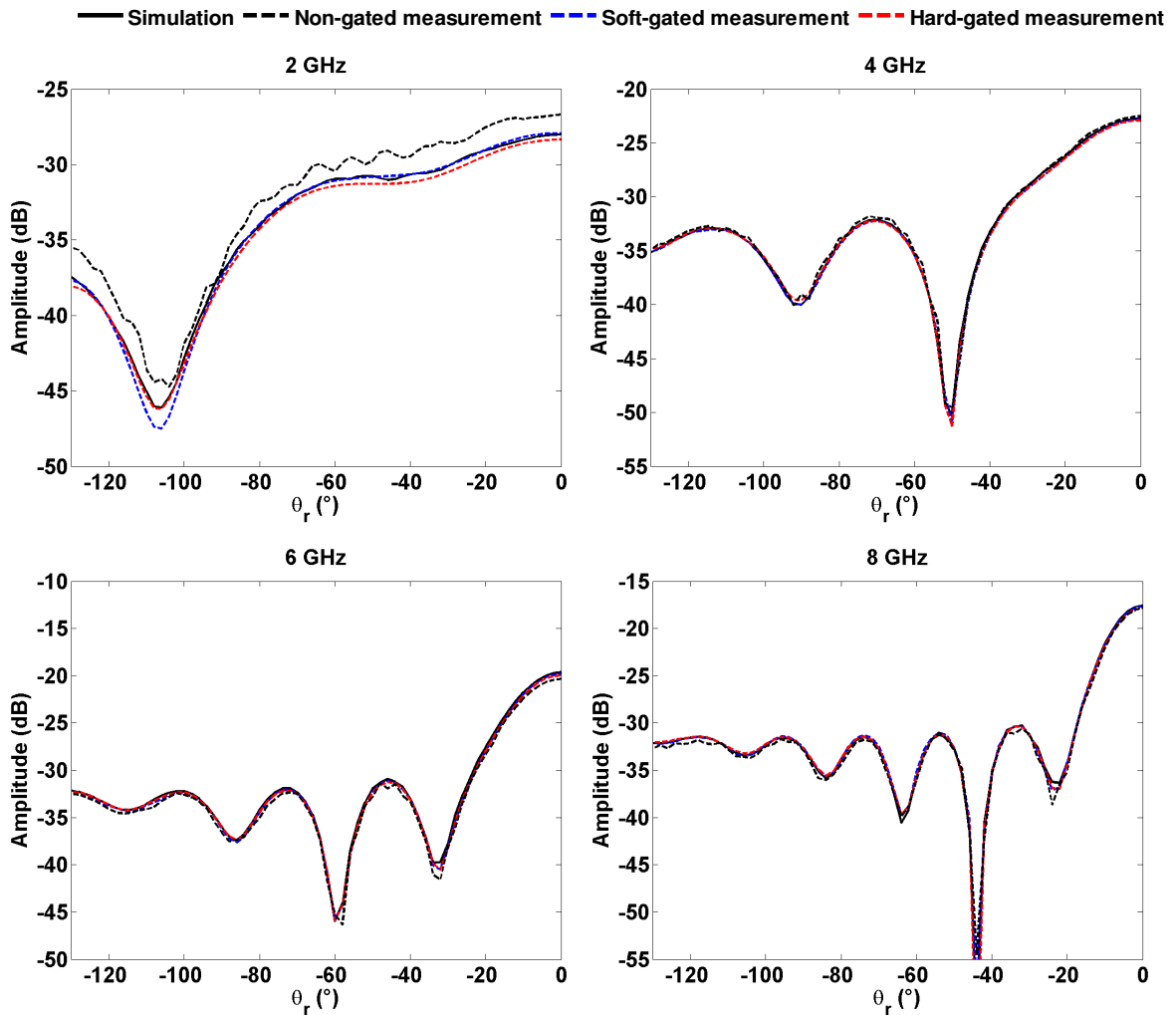


Figure 1.56 Amplitudes of fields scattered by the squat metal cylinder in HH polarization at 2 GHz, 4 GHz, 6 GHz and 8 GHz. Comparison between simulation, non-gated, soft-gated and hard-gated measurements

The non-gated measurement presents the lowest  $ES_{dB}^{relative}$  values among the three measurement cases. No significant difference is noticed with respect to the frequency except at 2 GHz where the measurement is very noisy with  $ES_{dB}^{relative}$  values around 0 dB. The  $ES_{dB}^{relative}$  values are considerably increased with the soft and hard gated measurements. Both gating techniques present comparable  $ES_{dB}^{relative}$  values in the backward directions ( $\theta_r < -50^\circ$ ) but in the forward direction ( $\theta_r > -50^\circ$ ) the soft-gated measurements slightly better.

The mean deviations of the DR criterion for the three measurements are plotted in Figure 1.58.

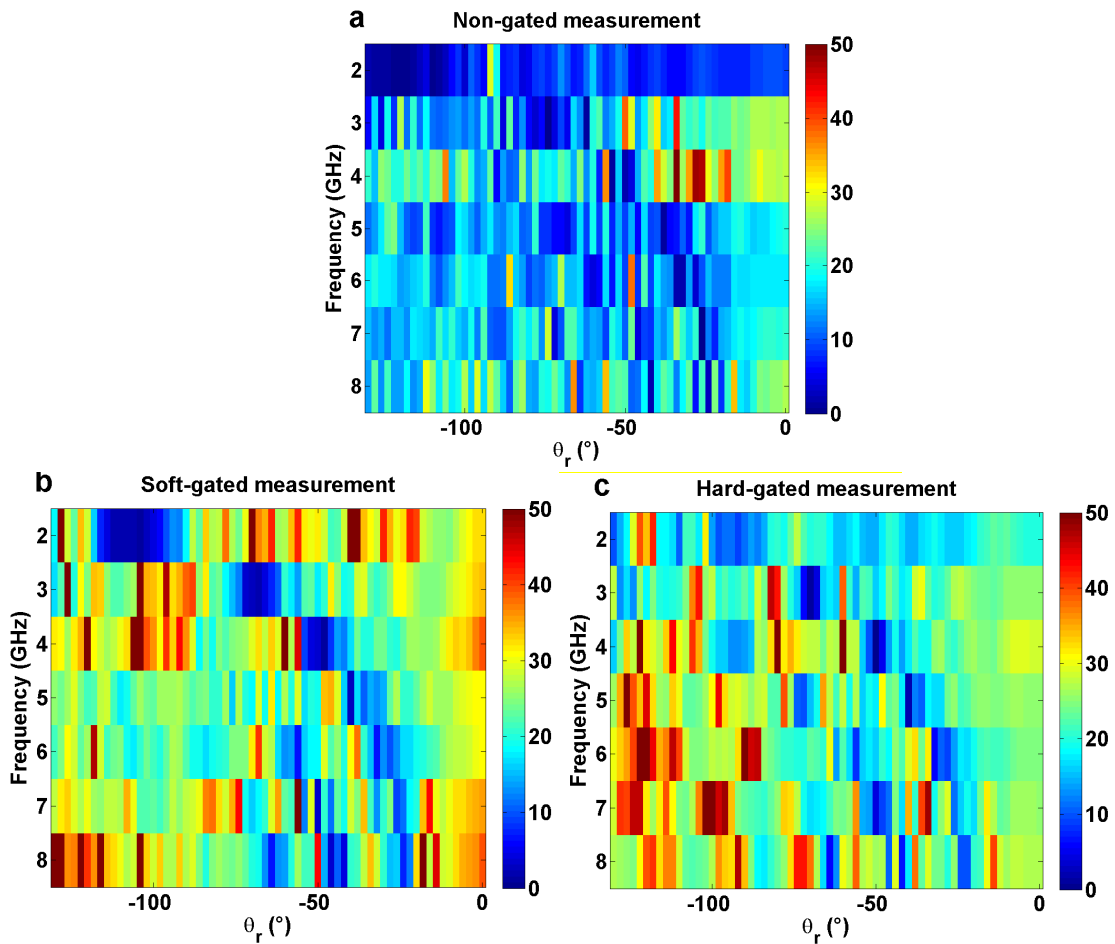


Figure 1.57 Holograms of the relative Equivalent Scatterer ( $ES_{dB}^{relative}$ ) as a function of the frequency and the receiving angle in HH polarization for the three measurement cases of the squat metal cylinder: (a) Non-gated measurement. (b) Soft-gated measurement. (c) Hard-gated measurement

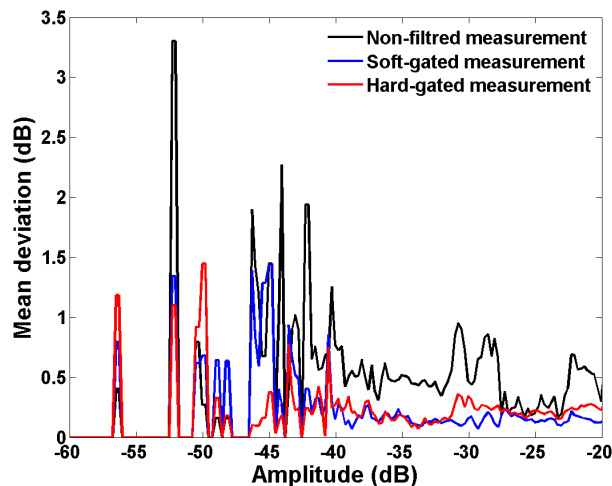


Figure 1.58 Mean deviation of the DR criterion for the measurements of the squat metal cylinder

This criterion is a statistic tool that provides direct information on the behavior of the measurement chain. The mean deviations of the two gated-measurements are lower than that of the non-gated measurement. The accuracy of the high amplitude levels ( $\theta_r$  close to  $0^\circ$ ) are

better in Softgating, that of intermediate amplitude levels ( $\theta_r$  around  $-50^\circ$ ) are better in Hardgating and that of the low amplitude levels ( $\theta_r$  close to  $-130^\circ$ ) is comparable in both Hardgating and Softgating. The results obtained with the squat metal cylinder showed that we are able to carry out good experiments with the proposed Hardgating system, and that this system has a good filtering capacity of the noise.

The same comparisons were applied on the measurement of the dielectric sphere. For this sphere, from the direct observation of the scattered fields (Figure 1.59) as well as from the observation of  $ES_{dB}^{relative}$  and DR comparison criteria in Figure 1.60 and Figure 1.61, it can be noticed that the Softgating and Hardgating didn't bring an enhancement on the measured field. The values of the comparison criteria for the three measurements are very similar. This is most probably related to the used Ku-band antennas which are more directive than the DRG horn antennas used for the squat metal cylinder and to the higher frequencies at which the anechoicity of the chamber is better.

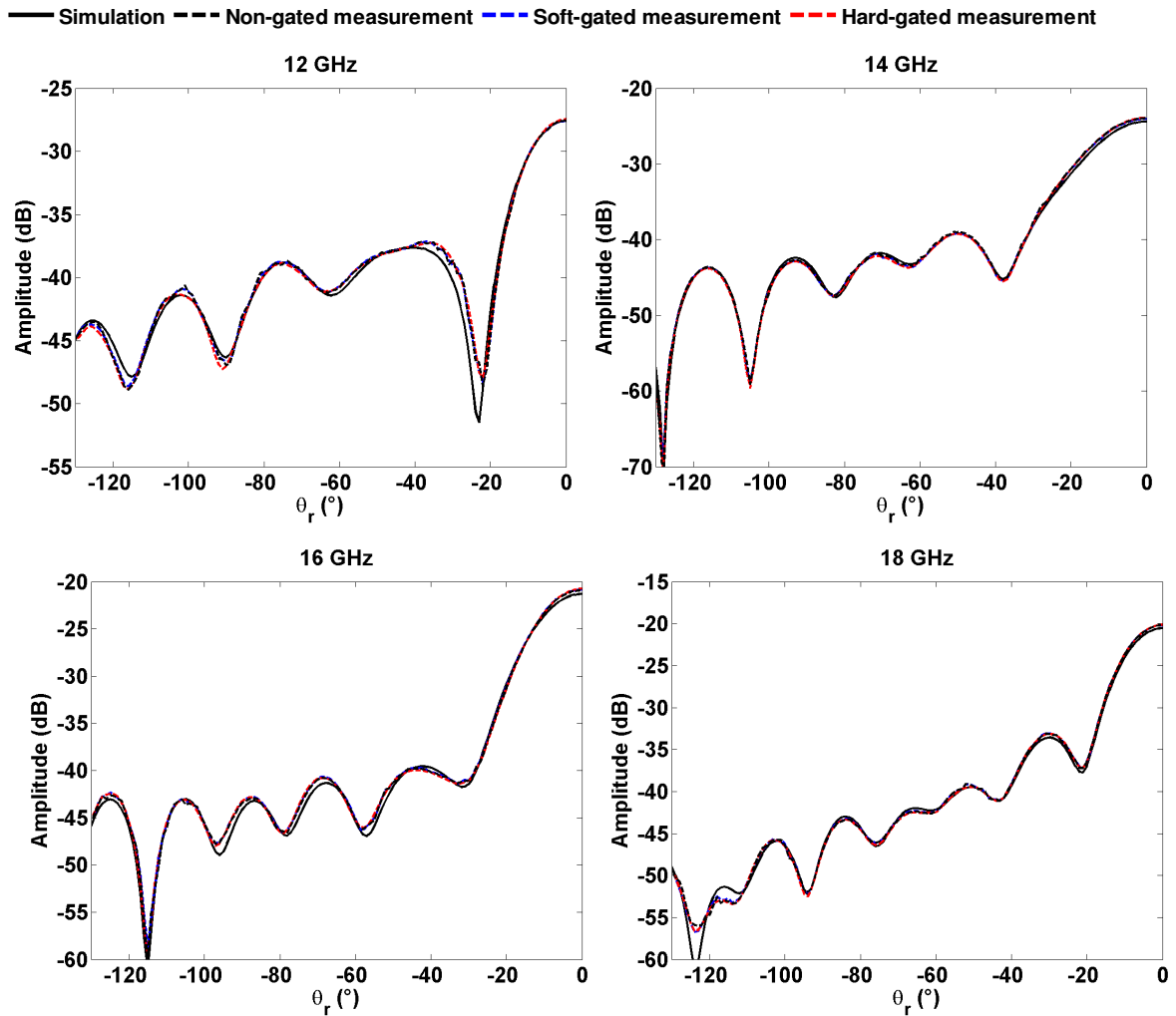


Figure 1.59 Amplitudes of fields scattered by the dielectric sphere in HH polarization at 12 GHz, 14 GHz, 16 GHz and 18 GHz. Comparison between simulation, non-filtered, soft-gated and hard-gated measurements

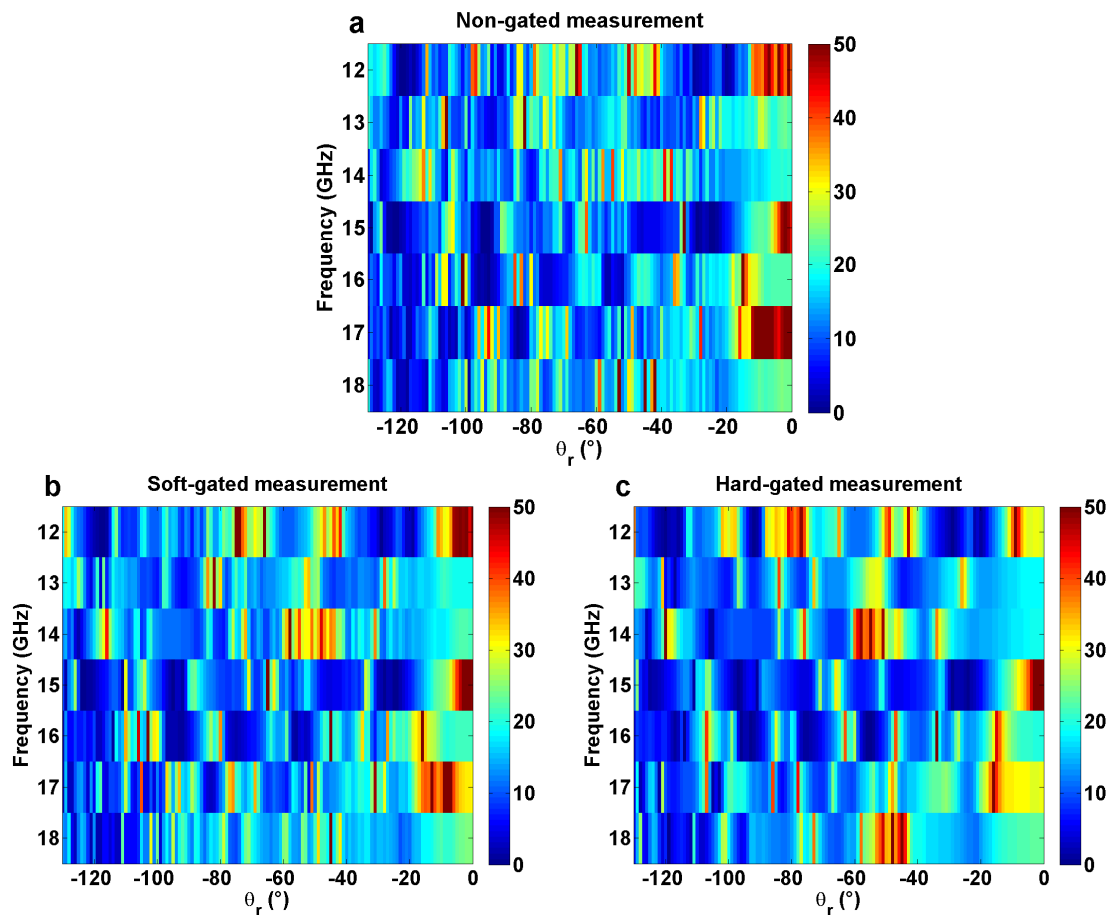


Figure 1.60 Holograms of the relative Equivalent Scatterer ( $ES_{dB}^{relative}$ ) as a function and the receiving angle for the three measurement cases of the dielectric sphere: (a) Non-gated measurement. (b) Soft-gated measurement. (c) Hard-gated measurement

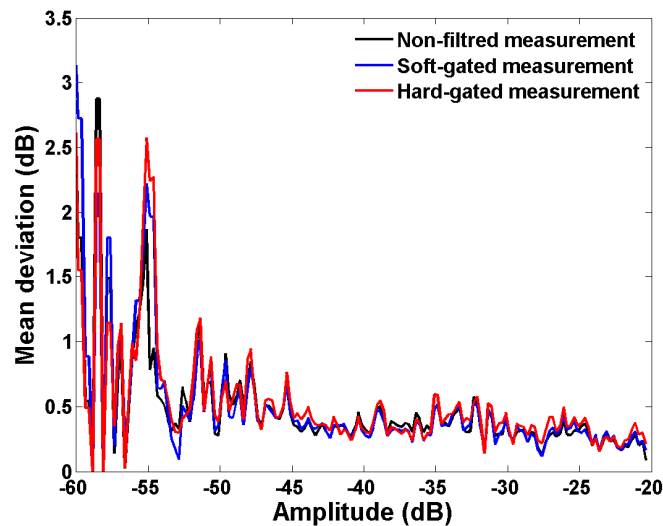


Figure 1.61 Mean deviation of the DR criterion for the measurements of the dielectric sphere

### 1.6.10 Conclusion

In this thesis, the problem of the stray signals that perturbs the measurement was addressed. In the past, Softgating based on FFT reconstruction and time windowing was used to

filter out stray signals. This technique suffered from very long measurement time due to the necessity to acquire large number of frequencies needed to reconstruct the signal in the time domain, despite that only few frequencies are needed in the studies. Especially in measurements for inverse problem purposes no filtering techniques were used and the application of Softgating was impossible (measurements in all the directions in a spherical configuration are needed which take already many days even at a single frequency). Moreover, soft gating can only be used with wideband antennas that allow a large frequency sampling.

Hardgating was raised as an alternative solution that makes real-time filtering and allows to simply carry out the measurement at the frequencies of interest which advantageously reduces the global measurement time. Such systems are common in large anechoic chambers for RCS measurements but the specificity of our case is the relatively small distances between the antennas and the TUT which implies short signals durations. An extensive study was made on the Hardgating categories from the literature and a new system based on two RF switches and a function generator was added to the setup of the CCRM. The system tested and showed good accuracy compared to the classical Softgating techniques. It is more efficient in quasi-monostatic configuration because the coupling between the antennas is high and it is easier to isolate the scattered signal due to its delay from the direct coupled one. In bistatic configuration it has good efficiency in the backward region but not in the forward scattering zone because the direct arrival from the antenna and the target's response are received almost at the same time, hence the difficulty to separate them. It is worthy to mention here that for the presented measurements of the squat metal cylinder and dielectric sphere in 1.6.9, the time to acquire one measured field (incident or total) with 450 frequencies in Softgating was around two hours, where that obtained in Hardgating with 7 frequencies was 20 minutes. However, the response of the TUT in time should be estimated before making the decision on the appropriate gating technique. Hardgating is not ideal with TUT with long duration response because some late arrival scattered energy may be filtered due to the short listening window at the receiving switch.

As a conclusion, the choice of Hardgating or Softgating is a question of tradeoff that takes into consideration the aforementioned advantages and disadvantages of each of them. Hardgating was used for the measurements of spheroidal analogs in section 3.1, of high permittivity spheres in section 3.2 and of trees analogs in chapter 4 where the TUT where only few frequencies where need. For the measurement of the spheres in chapter 2 and soot aggregates in section 3.2 the use of Softgating was more suitable because high frequency sampling was already needed.

## 1.7 RANDOM NOISE CHARACTERIZATION AND MEASUREMENT ACCURACY IMPROVEMENT

It is important to characterize the random error or the random noise affecting the measurements for two reasons:

1. To identify the associated uncertainties on each experimental scattered field.
2. To know the nature and the values of the real noise affecting the measurement. This information is crucial in the selection of the cost function used in the inversion reconstruction algorithms. In addition, the random noise level has impacts also on the quantitative result of the inversion algorithm. With the previous setup of the CCRM (see section 1.4), the random noise was characterized and it was assimilated to an Additive White Gaussian Noise (AWGN). Now with the current setup, it is fundamental to characterize the type of the associated noise.

The incident and total fields allowing to obtain the scattered field are affected by a random error. Therefore, the identification of the random error affecting the scattered field is deduced from the identification of the random noise affecting the incident and total fields.

### 1.7.1 Random error on the incident field

It has been concluded in [51] that the random error affecting the measurement at a given frequency and polarization and with a given antenna is dependent on the amplitude of the measured field. In a first step, I determine the distribution of the random error on the incident field in azimuthal circular configuration in VV polarization where the source is at a fixed position  $\theta_s = 90^\circ$ . At each receiving angle  $\theta_r$  and frequency  $f$ , I execute 500 times the measurement of the incident field in a repetitive process as shown in the example in Figure 1.62.

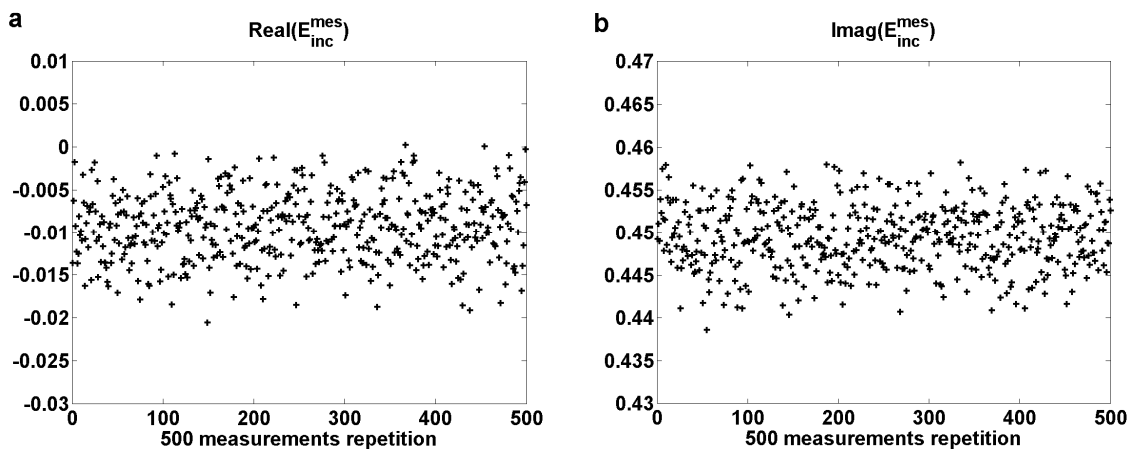


Figure 1.62 (a) Real part and (b) imaginary part of the 500 acquisitions of the incident field at 18 GHz for  $\theta_r = -120^\circ$  with the K-band horn antennas



Since we seek the noise distribution at all the amplitude levels, the measurement repetition is made at  $\theta_r$  between  $-130^\circ$  and  $0^\circ$  since at  $0^\circ$ , which is the forward incidence direction, the amplitude is the highest and at  $-130^\circ$  the amplitude is the lowest.

### 1.7.2 Standard deviation, random error and measurement uncertainties

Ideally, the  $N$  times repetition of the same measurement would yield the same measured values. In experiments, this is unrealistic because the measurement is subject to a random error. This random error is characterized through studying the amount of dispersion of the 500 measurements around a mean value. The dispersion is proportional to the amplitude of the incident field. The example in Figure 1.63 shows the amplitude in dB of the 500 acquisitions on the incident field at the receiving angles  $-120^\circ$  and  $0^\circ$ . At  $0^\circ$  the mean amplitude is higher than at  $-120^\circ$  and the dispersion is much lower.

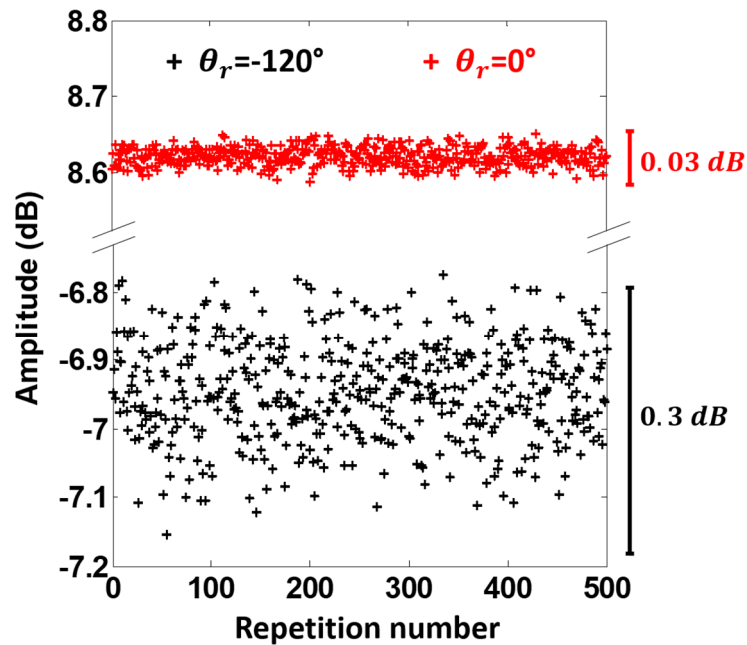


Figure 1.63 Amplitude in dB of the 500 acquisitions of the incident field at 18 GHz at the receiving angles  $-120^\circ$  and  $0^\circ$

From this repetition measurement over the total receiving angles, two important quantities are calculated: the standard deviation  $\sigma_{inc}$  of each 500 acquisitions, and the relative standard deviation of each 500 acquisitions, which is the standard deviation divided by the mean absolute value  $\sigma_{inc}/|E_{inc}|$ . The standard deviation determines the random noise and the relative standard deviation determines the measurement uncertainties. It has been explained in [51] that the random noise should be characterized individually on the real and imaginary parts, and the combination of both of them determines the random noise on the measured fields (total or incident).

From Figure 1.64, it is observed that the random noise on the real  $\sigma_{inc}^{Re}$  and imaginary  $\sigma_{inc}^{Im}$  parts on the incident field increase when the amplitude increases (Figure 1.64-a). However, the measurement uncertainties on the real ( $\sigma_{inc}^{Re}/|E_{inc}|$ ) and imaginary ( $\sigma_{inc}^{Im}/|E_{inc}|$ ) parts increase when the amplitude decreases because the signal is more sensitive to the noise when its amplitude level is low (Figure 1.64-b).

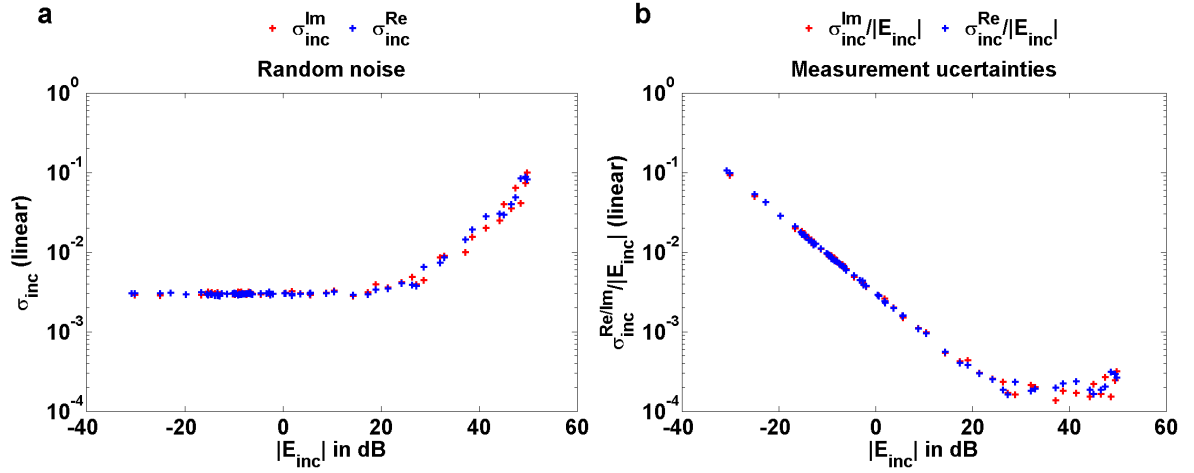


Figure 1.64 (a) Random noise (standard deviations) and (b) measurement uncertainties (relative standard deviation) on the real and imaginary parts of the incident field as a function of the amplitude of the incident field at 18 GHz with the K-band horn antennas

### 1.7.3 Random noise on the scattered field

The measured scattered field is affected by an Additive White Gaussian Noise (AWGN) denoted by  $e_{sca}^{random}$ . This random noise can be represented by a complex random variable whose real and imaginary parts have a standard normal distribution.

$$E_{sca}^{mes} = \overline{E_{sca}^{mes}} + e_{sca}^{random} \quad (1.13)$$

$$e_{sca}^{random} = N(0, \sigma_{sca}^{Re}) + jN(0, \sigma_{sca}^{Im}) \quad (1.14)$$

The random noise on the real and imaginary parts of the scattered field ( $\sigma_{sca}^{Re}, \sigma_{sca}^{Im}$ ) are obtained through the determination of the random noise affecting the corresponding incident ( $\sigma_{inc}^{Re}, \sigma_{inc}^{Im}$ ) and total ( $\sigma_{tot}^{Re}, \sigma_{tot}^{Im}$ ) fields:

$$\sigma_{sca}^{Re} = \sqrt{(\sigma_{inc}^{Re})^2 + (\sigma_{tot}^{Re})^2} \quad (1.15)$$

$$\sigma_{sca}^{Im} = \sqrt{(\sigma_{inc}^{Im})^2 + (\sigma_{tot}^{Im})^2} \quad (1.16)$$

This combination means that the hypothesis behind is that the noise on the incident and total fields are uncorrelated. As said previously, the random noise depends upon the amplitude of the measured signal but it also varies with the frequency and the used antennas. In Figure 1.65 we show the incident, total and scattered field by a 35 mm diameter metal sphere at 16 GHz

with the DRG antennas. As it was indicated in section 1.4.5, the radiation pattern of the DRG source antenna is not focused in the forward direction. Combined with the fact that the sphere is a low scatterer, the amplitudes of the corresponding incident and total fields on the figure have quite similar values at almost all the receiving angles.

The random noise affecting this measurement at 16 GHz and with the DRG antennas is presented in Figure 1.66. Using this random noise characterization, it is possible to associate a noise estimation to the incident and total field at each angular position depending on its amplitude, ranging between -50 dB and 0 dB.

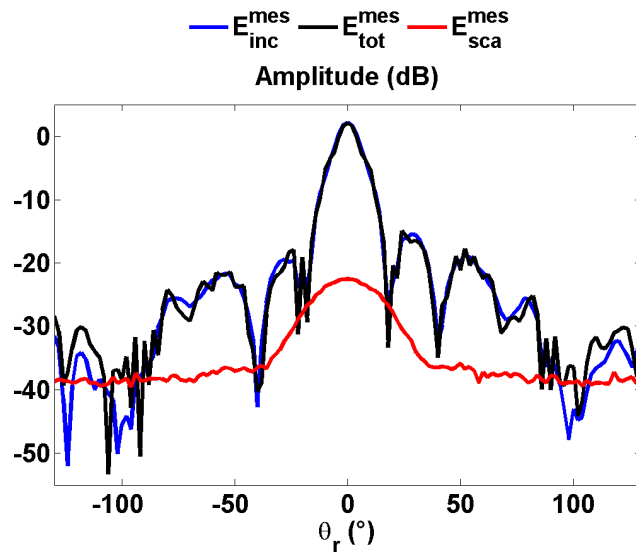


Figure 1.65 Total, incident and raw scattered field of a 35 mm metal sphere at 16 GHz with the DRG horn antennas

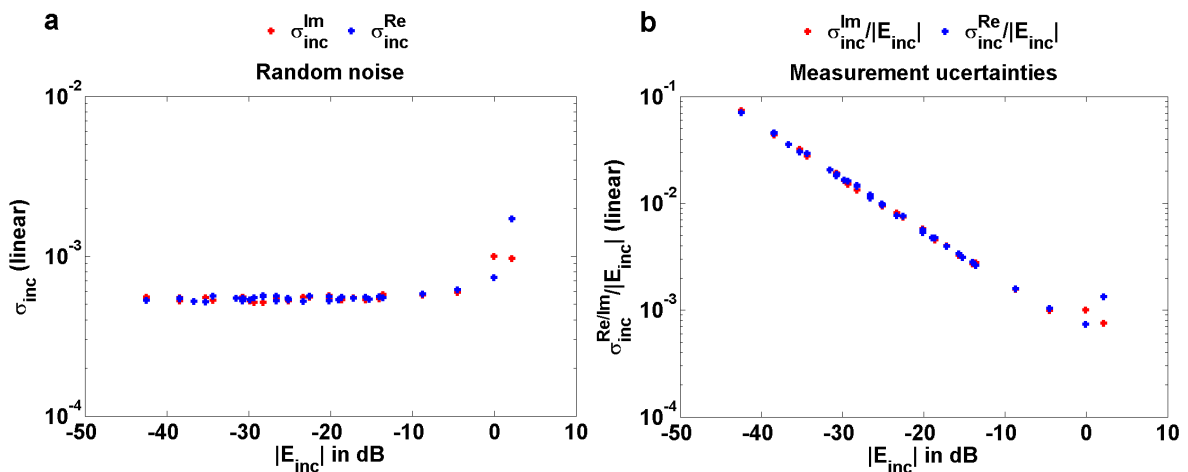


Figure 1.66 (a) Random noise (standard deviations) and (b) measurement uncertainties (relative standard deviation) on the real and imaginary part of the incident field as a function of the amplitude of the incident field at 16 GHz with the DRG horn antennas

Figure 1.67 represents the variations of the standard deviations ( $\sigma_{tot}^{Re}$ ,  $\sigma_{inc}^{Im}$ ,  $\sigma_{tot}^{Re}$ ,  $\sigma_{inc}^{Im}$ ,  $\sigma_{sca}^{Re}$ ,  $\sigma_{sca}^{Im}$ ) as a function on the receiving angle.

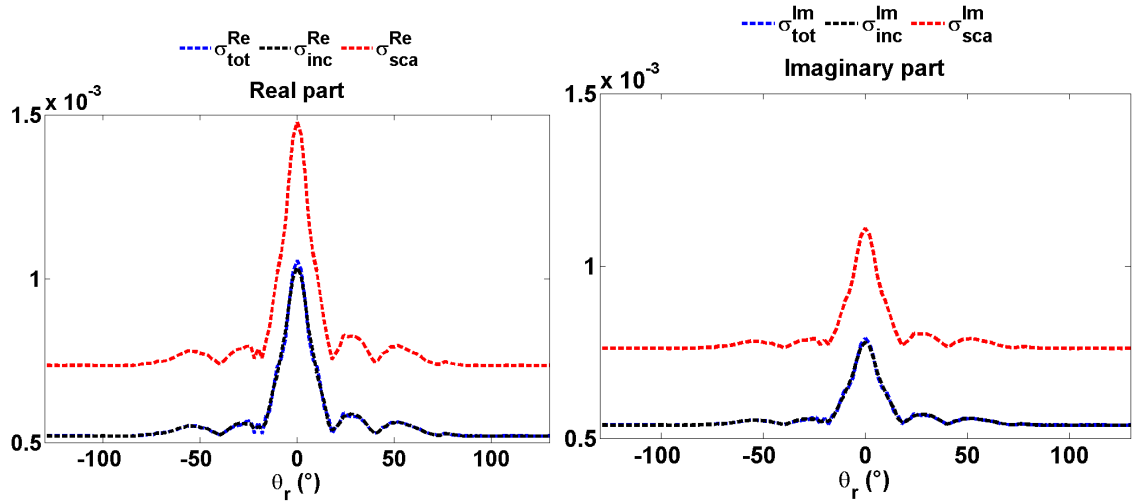


Figure 1.67 Variation of the standard deviation on the real and imaginary parts of the incident, total and scattered fields as a function of the receiving angles for the 35 mm diameter sphere at 16 GHz using the DRG horn antennas

The importance of this noise characterization study is that it allows to associate the error bars to each value of the measured scattered field in a way to quantify the uncertainties as the example shown in Figure 1.68. The uncertainties or error bars on the amplitude and phase are determined from the standard deviations variations on the scattered field (in red in Figure 1.67). At each frequency and at each angular position  $\theta_r$ , an array of 500 random numbers from the normal distribution is calculated (using the experimentally determined standard deviation). This distribution  $N$  has a mean value which is equal to zero and a standard deviation equal to the standard deviation of the real part (respectively imaginary part) of the scattered field. These distributions are next added to the complex value of the scattered field to determine the error margin  $e_{sca}$ :

$$e_{sca, f, \theta_r} = E_{sca, f, \theta_r}^{mes} + N(0, \sigma_{sca, f, \theta_r}^{Re}) + j \cdot N(0, \sigma_{sca, f, \theta_r}^{Im}) \quad (1.17)$$

The uncertainties bars on each value of the amplitude and the phase of the scattered fields are then determined by taking the extreme values of amplitude and phase of  $e_{sca}$  as shown in the equations from 1.18 to 1.21.

$$\min(e_{sca, f, \theta_r}^{Amplitude}) = \min|E_{sca, f, \theta_r}^{mes} + N(0, \sigma_{sca, f, \theta_r}^{Re}) + j \cdot N(0, \sigma_{sca, f, \theta_r}^{Im})| \quad (1.18)$$

$$\max(e_{sca, f, \theta_r}^{Amplitude}) = \max|E_{sca, f, \theta_r}^{mes} + N(0, \sigma_{sca, f, \theta_r}^{Re}) + j \cdot N(0, \sigma_{sca, f, \theta_r}^{Im})| \quad (1.19)$$

$$\min(e_{sca, f, \theta_r}^{Phase}) = \min(\text{phase}(E_{sca, f, \theta_r}^{mes} + N(0, \sigma_{sca, f, \theta_r}^{Re}) + j \cdot N(0, \sigma_{sca, f, \theta_r}^{Im}))) \quad (1.20)$$

$$\max(e_{sca, f, \theta_r}^{Phase}) = \max(\text{phase}(E_{sca, f, \theta_r}^{mes} + N(0, \sigma_{sca, f, \theta_r}^{Re}) + j \cdot N(0, \sigma_{sca, f, \theta_r}^{Im}))) \quad (1.21)$$

As it can be seen from the equations, the uncertainties on the amplitude and phase of the scattered field are overestimated by taking the maximum and minimum values of the distribution (Figure 1.68). The information on the uncertainties will be used as a criterion to test

the efficiency of the methods we propose in the next section on the settings optimization of the measurement setup. It will be also used in the permittivity determination method described in section 2.6.

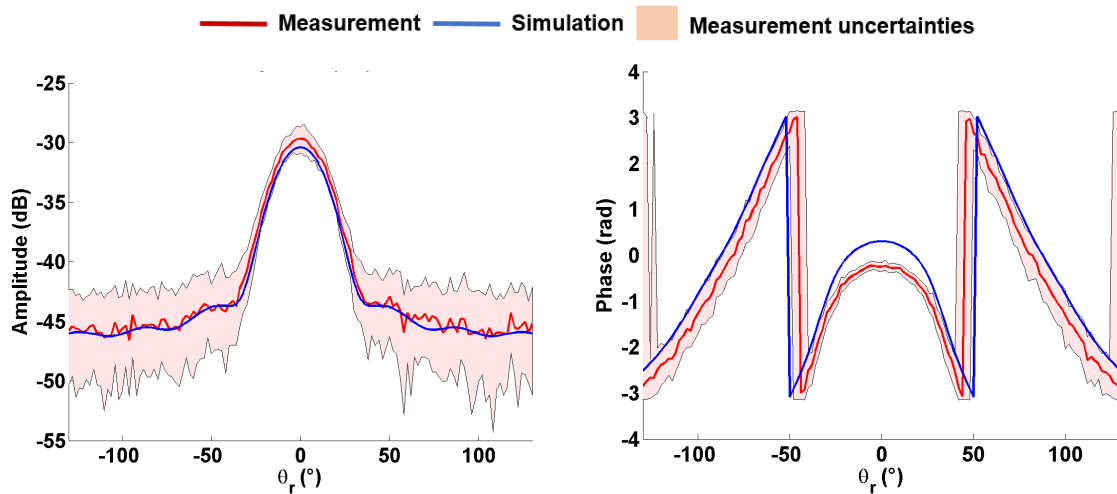


Figure 1.68 Amplitude and phase of the calibrated measured scattered field by a 35mm sphere at 16 GHz with the DRG horn antennas showing the associated uncertainties with comparison to simulation

#### 1.7.4 Challenges in improving the measurement accuracy

In the previous section I showed that the uncertainties on the experimental scattered field is directly depending on the amplitude of the total and incident fields. In the backward scattering region ( $\theta_r$  tending to  $-130^\circ$ ), the amplitude of the measured field is low and the uncertainties are high, which makes difficult obtaining good accuracy of the experimental scattered field. For instance in the example in Figure 1.68 we can easily identify the fluctuations appearing on the amplitude of the measured scattered field at the receiving angles beyond  $-50^\circ$  and  $50^\circ$ . We can imagine that with targets whose scattered fields have much lower amplitude (such as the presented in section 2.7, or the spheroids in section 3.1 with low real part of relative permittivity and with dimensions of the order of the wavelength), the amplitudes of the measured fields are much lower and they have higher uncertainties.

The straightforward solution one can think about in order to increase the measurement accuracy is to increase the amplitude level in the measurement setup, for instance by increasing the power source at the reference synthesizer or by using amplifiers. My work on the noise characterization revealed that such simple solution may not be the optimal ones due to two main challenges: the potential non-linearity at each device in the setup and the nature of the noise.

#### 1.7.4.1 *Non-linearity at the measurement devices*

Different devices are involved in the measurement setup: remote mixers, DFC, VNA, IF amplifier (see section 1.5.2). The amplitude of the signal at the input of each of them should be carefully adjusted to keep a linear behavior in the device. For instance, the 0.1 dB compression point is at -26 dBm for the remote mixers, at 10 dBm for the VNA and at -14.5 dBm for the IF amplifier. The signal amplitude at the input of each of them varies with respect to the chosen output power at the reference synthesizer, the gain of the antennas, and the attenuation in the RF cables. Therefore the choice of the source power cannot be fixed and should be adjusted according to the measurement configuration case by case, hence the importance of the configuration sheet I presented in 1.5.3. Moreover, the signal amplitude at the input of the devices, on the receiving side, depends upon the angular position of the receiver  $\theta_r$ . The highest signal amplitude is received at  $\theta_r = 0^\circ$  and the highest sensitivity to the nonlinearity is at this angle. When the receiver is in the backward region ( $\theta_r$  tending to  $1 \pm 130^\circ$ ) the signal amplitude at the devices is relatively far from the compression points of the devices but it becomes close to their noise levels.

As a result, a flexible setting of the power profile is required that takes into account all the aforementioned challenges.

#### 1.7.4.2 *Gaussian and non-Gaussian noise*

In the case of spherical measurement for inverse problem purposes, which represent an essential activity at the CCRM, the knowledge of the noise nature is crucial in inversion algorithms because it is involved in the choice of the appropriate cost function. With the previous measurement setup (section 1.4), the random noise affecting the measurement was referred to be additive, having a standard normal distribution and identic on the real and imaginary parts on the experimental scattered field [51].

Unfortunately, the noise characterization study with the current setup has shown that with measured amplitude level of the test signal  $b_2$  above -30 dBm, the random noise follows a non-Gaussian behavior. In order to test whether the noise has a Gaussian distribution or not, the statistics I used are relying on empirical quantiles diagrams [72]. This allows to plot the determined quantiles on each set of 500 acquisitions presented in section 1.7.1 and compare them to the quantiles of a well-known Gaussian theoretical distribution. Some examples of the 500 measurement acquisitions and their corresponding quantiles are presented in Figure 1.69 and Figure 1.70. It is clearly seen that in Figure 1.69 corresponding to  $\theta_r = -120^\circ$  the noise has a Gaussian distribution; the empirical quantiles coincide the diagonal.

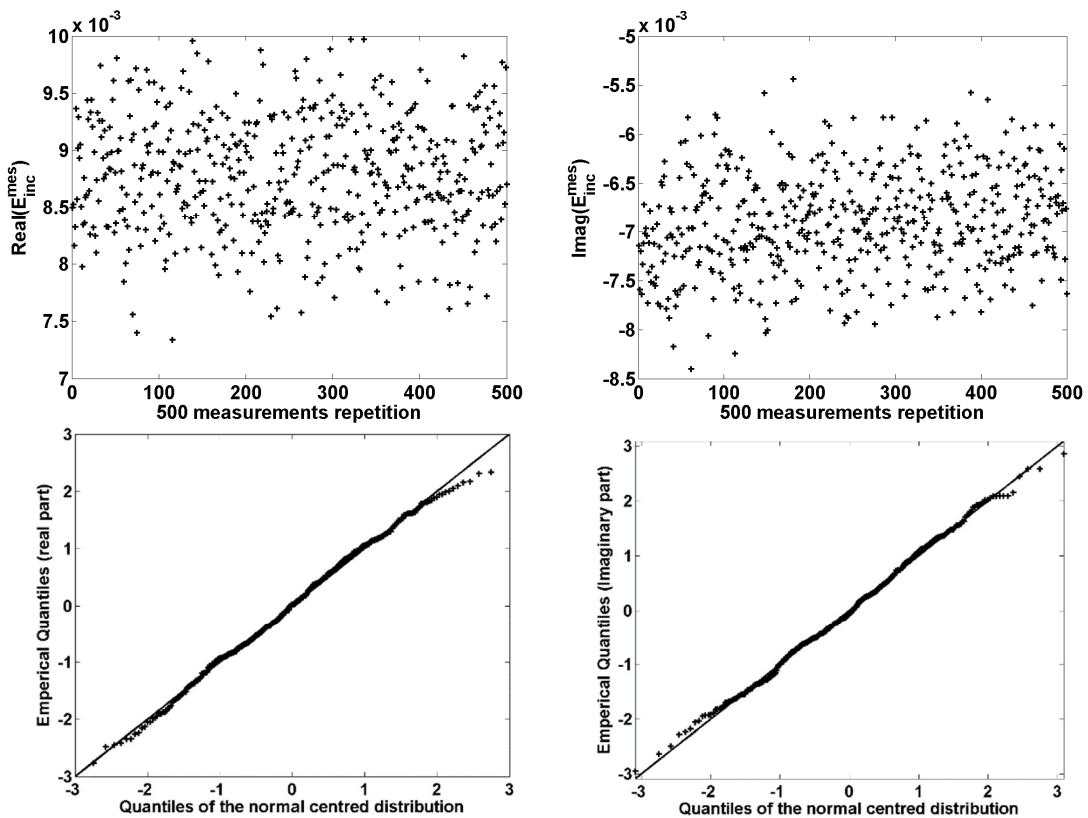


Figure 1.69 Real and imaginary parts on the 500 acquisitions and the corresponding quantiles diagrams at 16 GHz with the DRG horn antennas and at  $\theta_r = -120^\circ$  (Gaussian distribution)

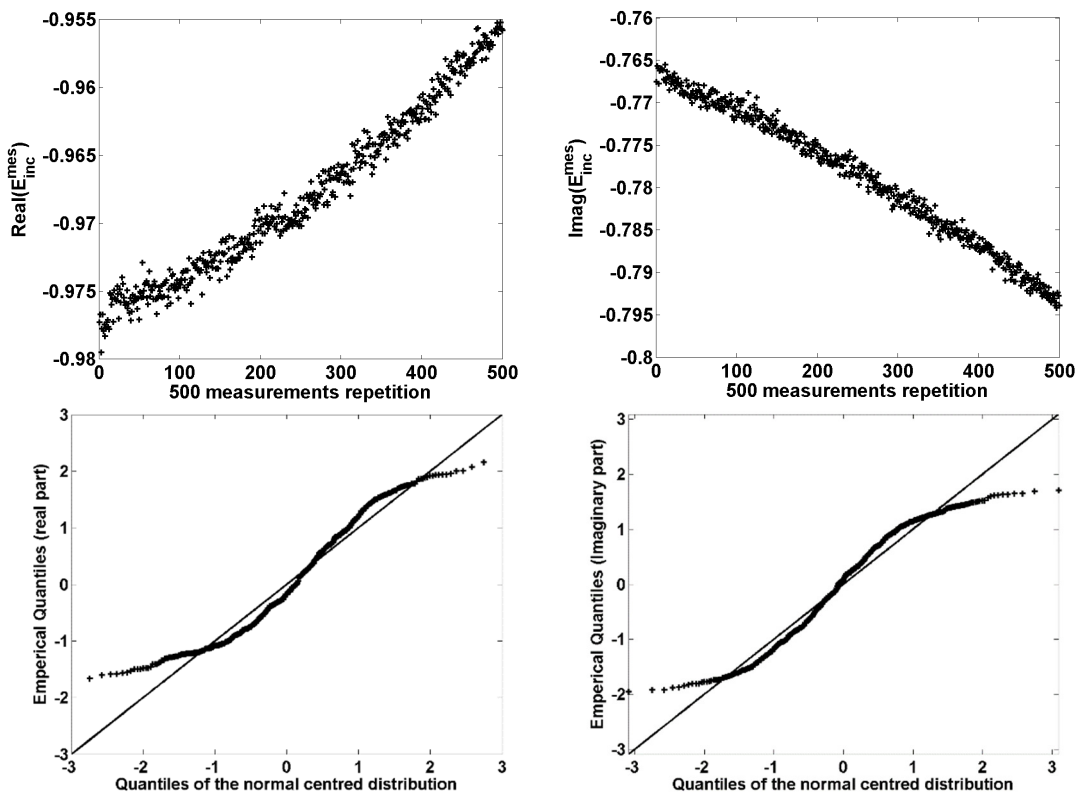


Figure 1.70 Real and imaginary parts on the 500 acquisitions and the corresponding quantiles diagrams at 16 GHz with the DRG horn antennas and at  $\theta_r = 0^\circ$  (Non-Gaussian distribution)

This is not the case in Figure 1.70 corresponding to  $\theta_r = 0^\circ$  because the level of  $b_2$  signal is relatively high (the empirical quantiles roughly deviate from the diagonal which represents the theoretical Gaussian distribution). As result, in order to keep using the same cost function in the inversion algorithm, the setting of the power profile must be chosen to respect a Gaussian noise.

Based on the challenges presented in the subsections 1.7.4.1 and 1.7.4.2, I have proposed an optimization of the setup configuration that improves the accuracy in the backscattering while avoiding the non-linearity behaviors in the devices and maintaining a Gaussian noise distribution. The novel proposed technique will be explained in the following section.

### 1.7.5 Optimization of the setup configuration

As the measured levels are mainly linked to the radiation pattern of the source antenna, our choice was to define three different power schemes to the measurement chain, which correspond directly to three angular regions (Figure 1.71). Basically, low magnitude levels are measured in the back scattering region (backward zone), medium levels in the intermediate angular region (intermediate zone), and high levels in the forward scattering region (forward zone). In each of these regions, we adapt the source power and the driven internal attenuators of the VNA to obtain the best accuracy of the measurements with the corresponding magnitude level range while maintaining a Gaussian noise distribution.

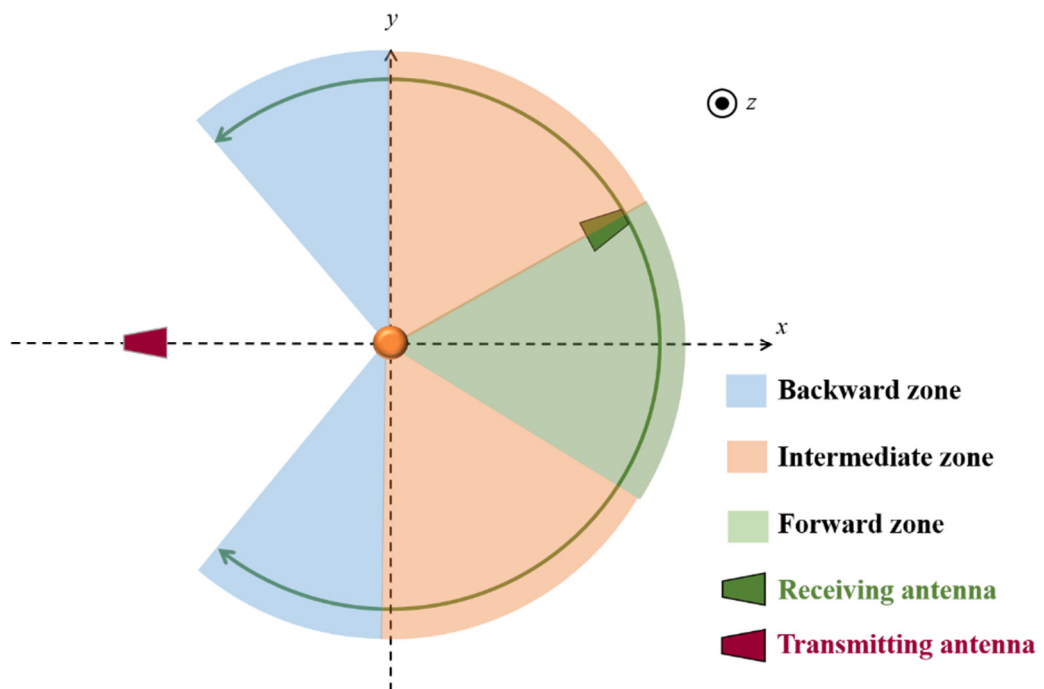


Figure 1.71 A schematic explaining the decomposition of the receiving excursion into three different zones, with different power profiles



The proposed optimization scheme consists of adapting separately the level of the source power of the reference synthesizer, and the internal attenuators on the  $b_2$  signal in the VNA in each of the three zones to make a tradeoff of the noise requirements between the backscattering and forward scattering regions through. A high power source will be used when the receiver is in the backward zone, and a low power source with potential attenuator on the  $b_2$  signal in the forward zone. An intermediate configuration will be applied in the intermediate zone.

With our *R&S* reference synthesizer and VNA, we can select a source power between 0 dBm and 15 dBm, and the internal attenuators we can select in the VNA are of 10, 20 and 30 dB. The optimal power profiles for the three zones with the DRG and K-band horn antennas are summarized in Table 1.2.

		Backward zone	Intermediate zone	Forward zone
DRG horn antennas	$\theta_r$	$\pm 130^\circ \rightarrow \pm 80^\circ$	$\pm 80^\circ \rightarrow \pm 60^\circ$	$\pm 60^\circ \rightarrow 0^\circ$
	Source power	15 dBm	10 dBm	0 dBm
	Attenuator on $b_2$	0 dB	0 dB	0 dB
K-band horn antennas	$\theta_r$	$\pm 130^\circ \rightarrow \pm 60^\circ$	$\pm 60^\circ \rightarrow \pm 35^\circ$	$\pm 35^\circ \rightarrow 0^\circ$
	Source power	10 dBm	0 dBm	0 dBm
	Attenuator on $b_2$	0 dB	20 dB	30 dB

Table 1.2 Power profiles of the three zones in optimized configuration for measurements with the DRG horn antennas and the K-band horn antennas

In Figure 1.72 I show an example of a measured field (total field corresponding to the 35 mm sphere at 16 GHz) with the optimized configuration using the three power profiles described in Table 1.2. I show the amplitude of the reference signal ( $a_1$ ), test signal ( $b_2$ ) and the  $b_2/a_1$  (the measured total field) as a function of the receiving angles. The same quantities are also presented in a non-optimized configuration. In the non-optimized configuration, the power profile is, over all the receiving angles, the same as the one of the “Forward zone”. It is well seen that in the optimized configuration, the  $b_2$  signal is measured in the backward zone with amplitude levels around -60 dBm, which is around 20 dBm higher than the case of the non-optimized configuration. The transitions between the zones at  $\pm 60^\circ$  and  $\pm 80^\circ$  can be noticed on the  $b_2$  and  $a_1$  signals but not on the  $b_2/a_1$  signal, since the differences are compensated. The measurement uncertainties in amplitude corresponding to the three zones are presented in Figure 1.73.

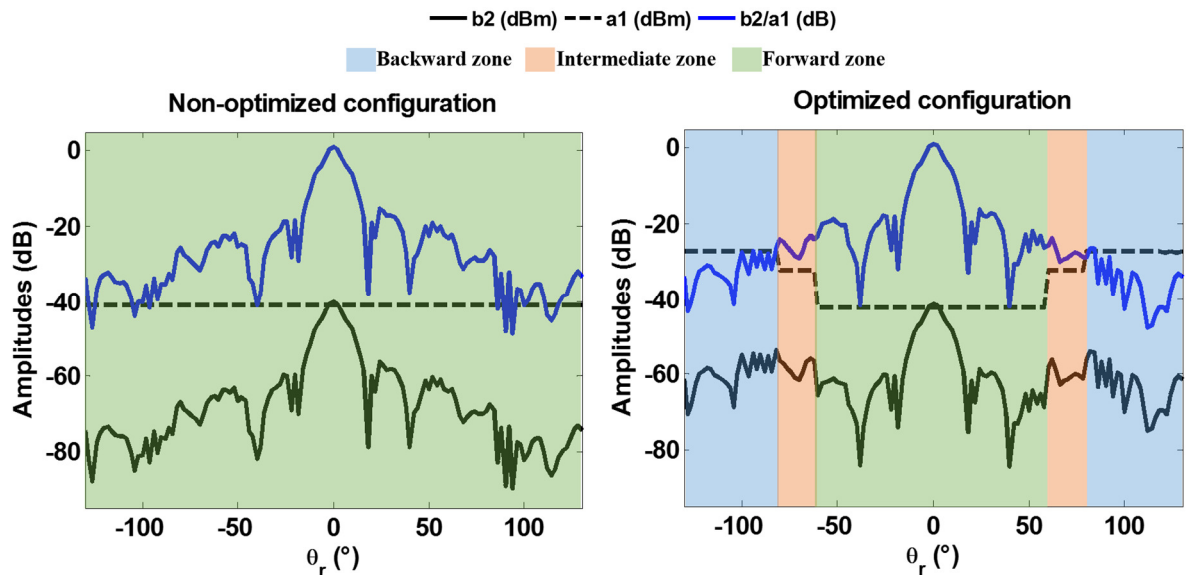


Figure 1.72 Amplitude levels of  $b_2$ ,  $a_1$  and  $b_2/a_1$  total signals in non-optimized and optimized (with zones decomposition) configurations in the case of the measurement of the 35 mm sphere with the DRG antennas at 16 GHz

Figure 1.73 presents the uncertainties on the amplitude measurement in the three zones. In the intermediate and backward zones, the uncertainties are unambiguously lower than those in the forward zone. This highest uncertainty is also the unique one in the non-optimized configuration. Consequently, and for the measured  $b_2/a_1$  signal in Figure 1.72-b in the backward zone with amplitude around -40 dB, the uncertainties were reduced from around 1 dB to around 0.1 dB. The measurement accuracy was increased in the backward region. This can also clearly be seen on the comparison of two measurements on the 35 mm sphere, one performed in a non-optimized configuration and the other with an optimized configuration (Figure 1.74). The different fluctuations appearing at the receiving angles beyond  $\pm 50^\circ$  were completely enhanced.

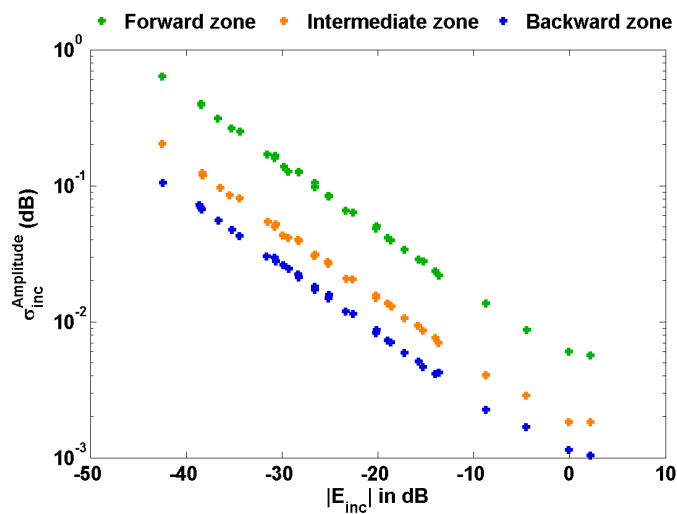


Figure 1.73 Amplitude measurement uncertainties in (dB) corresponding to the three power profiles at 16 GHz with the DRG horn antennas (obtained from repetitive measurements in each configuration)

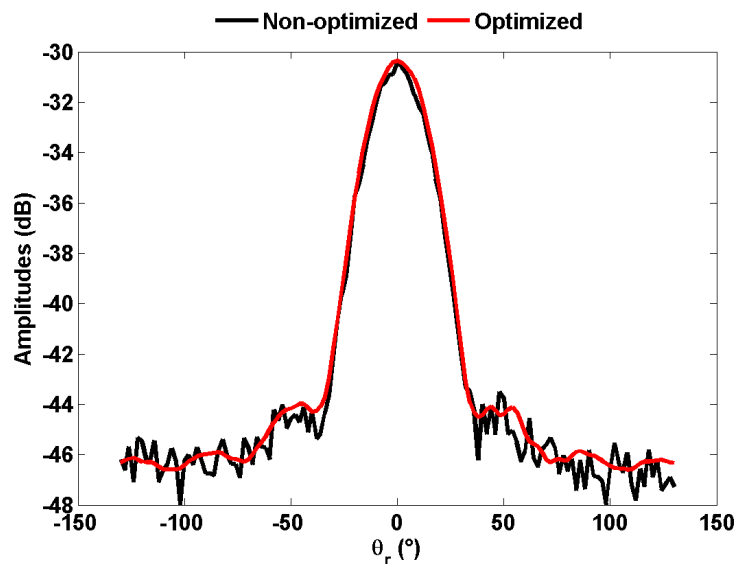


Figure 1.74 Comparison between the amplitudes of the calibrated fields scattered by the 35 mm metal sphere at 16 GHz in non-optimized and optimized configuration

### 1.7.6 Measurement of very low scattering objects in optimized configuration

The straightforward application of the optimized configuration is the measurement of low scattering objects whose investigation was almost impossible in the past due to domination of the experimental noise on their measurements. By low scattering objects we mean objects with low amplitudes of the scattered field that can be down to -90 dB as it is the case with the spheres of low real part of permittivities presented in section 2.7 or the objects of small dimensions compared to the wavelength such as the soot aggregate analog presented in section 3.2. The measurement of the fields scattered by those targets has become only possible using an optimized configuration with the current setup. In order to show the advantage of the optimization on the measurements I take as example some of the most delicate measurements that have been made during this thesis, which are the measurements on 35 mm diameter spheres with a real part of complex relative permittivity ranging between 1.4 down to 1.02. These spheres were fabricated and measured in the context of the control of the relative permittivity of materials, and is further discussed in chapter 2. The amplitude and phase of the fields scattered by the sphere with lowest relative permittivity ( $\epsilon = 1.02 + 0j$ ) are presented in Figure 1.75 and Figure 1.76 in both optimized and non-optimized configurations.

For this sphere, the total and incident fields are almost identical, and the extraction of the scattered field from their subtraction is of high vulnerability to noise. Moreover, the permittivity of this sphere is comparable to that of the expanded polystyrene mast and the transparency of this latter is no longer valid. The coupling in this case between the mast and the

sphere presents a new noise source. The optimized configuration has allowed for this low scattering sphere to obtain relatively acceptable accuracy which was not possible in the past.

### **1.7.7 Conclusion**

In this section, I presented the noise characterization method and the determination of the uncertainties on the measurement of the scattered field. A novel accuracy enhancement technique was proposed which consists on zones decompositions with different power profiles. This technique has allowed to reduce the measurement noise especially in the backward directions in bistatic azimuthal configuration. The use of this optimization was crucial in the measurement of low scattering targets. After that, this technique was used for the measurements of spheres with low real part of relative permittivity in sections 2.8 and the soot aggregates with small dimensions compared to the wavelength in section 3.2.

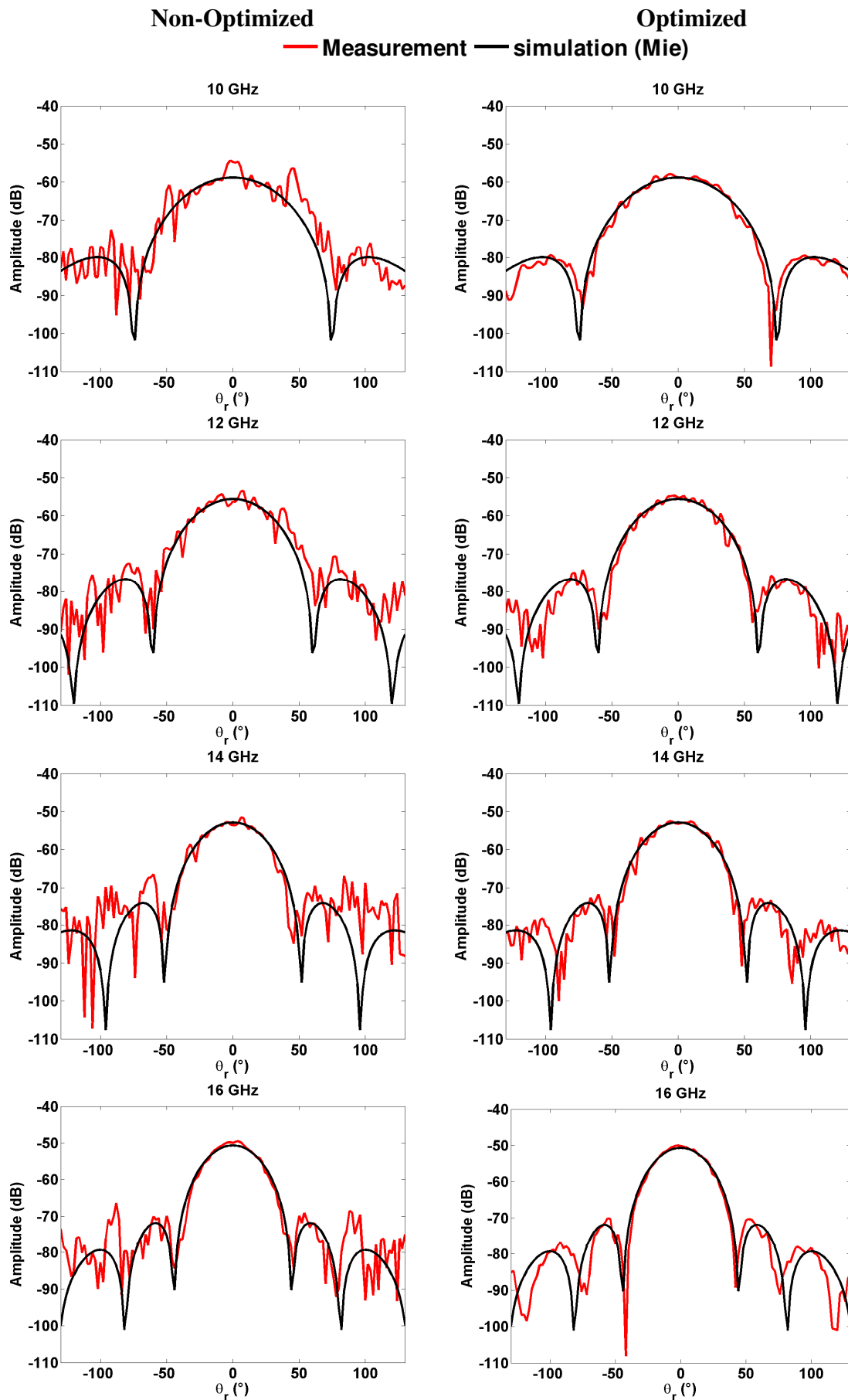


Figure 1.75 Amplitude of experimental scattered field by a 35 mm sphere with real part of relative permittivity of 1.02 in (left) non-optimized configuration and (right) optimized configuration

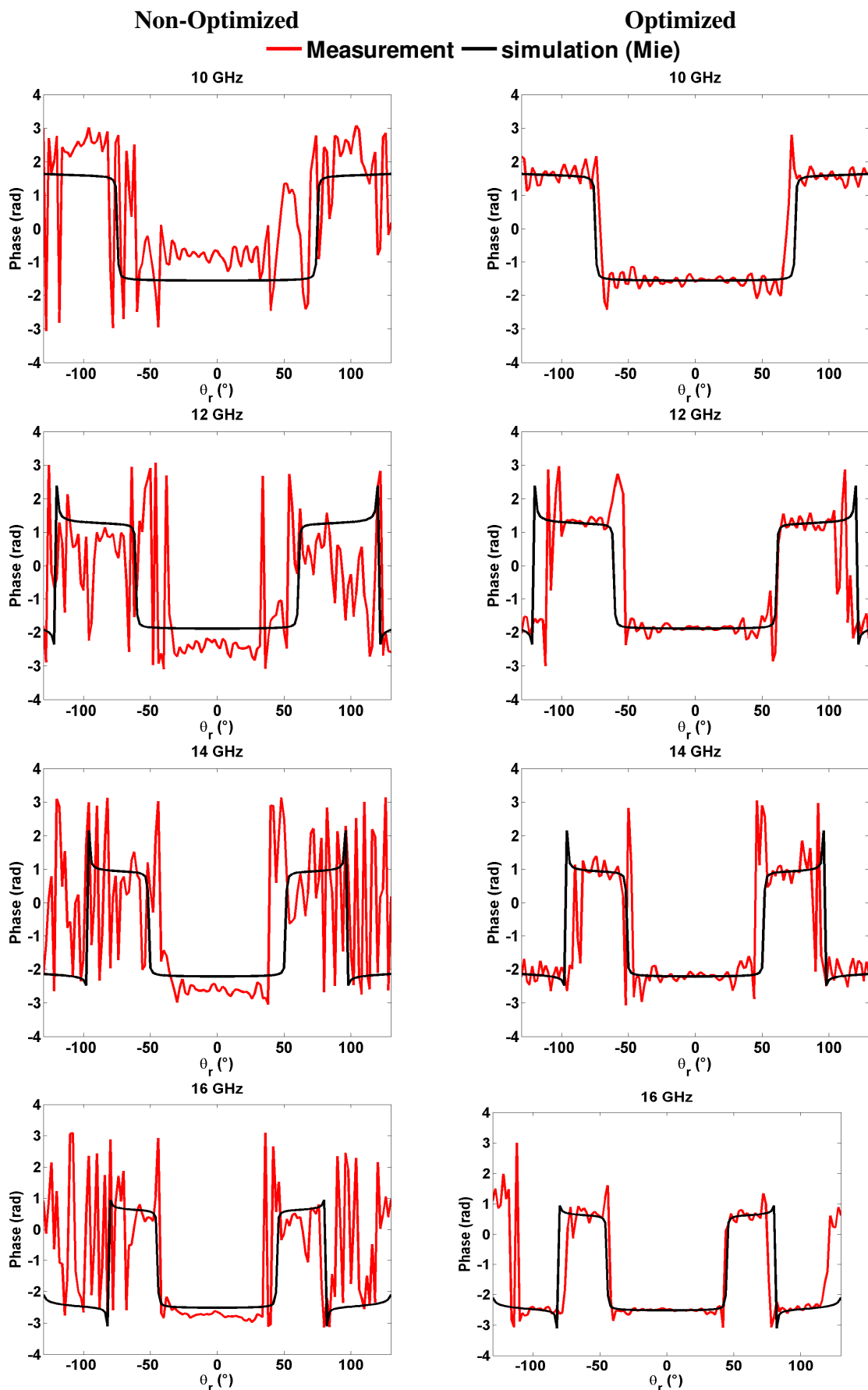


Figure 1.76 Phase of experimental scattered field by a 35 mm sphere with real part of relative permittivity of 1.02 in (left) non-optimized configuration and (right) optimized configuration

## 1.8 CONCLUSION

This thesis addresses widening the applicability of the microwave analog experiments as promising solution to investigate electromagnetic scattering by particles and large targets as a reference to assess the limits of approximate models. One of its objectives is to enhance the measurement accuracy of the experimental setup of the CCRM and to make possible the investigation of analogs that were difficult to measure in the past. Since the measurement chain was renewed before this thesis it was fundamental to characterize and optimize its performance.

In this chapter, the new measurement setup was presented and a new quasi-monostatic configuration that did not exist in the past was developed. The configuration was tested with a quasi-monostatic angle of  $12^\circ$  and will be detailed in chapter 4. The transmitting and receiving remote mixers were placed at the vicinity of this latter to avoid the propagation of the RF signals in moving long distances cables and avoid power losses and phases shift in the cables.

The problem of the stray signals that perturbs the measurement was addressed and a Hardgating system utilizing two RF switches and a function generator was installed and tested with comparison to Soft-gated measurements. The system showed good efficiency especially in quasi-monostatic configuration. The straightforward benefit of this system is the measurement time saving since it became unnecessary to acquire a high number of frequency, which is fundamental in classical Softgating techniques. In the example presented in section 1.6.9 a 85% time saving was achieved with comparison to Softgating. The employment of this system will be very helpful in measurements for inverse problem purposes where measurements durations are very long and Softgating is impossible.

The random noise characterization and the determination of the uncertainties on the measured of the scattered field were also presented in this chapter. A novel accuracy enhancement technique was proposed which consists on zones decompositions with different power profiles. This technique has allowed to reduce the measurement noise especially in the backward directions in bistatic azimuthal configuration. The use of this optimization was crucial in the measurement of low scattering targets. This technique was used for the measurements of low scattering analogs such as the spheres and spheroids with low real part of relative permittivity and the soot aggregates with small dimensions compared to the wavelength.

## 2 ADDITIVE MANUFACTURING OF ANALOGS WITH CONTROLLED PERMITTIVITY

---

### 2.1 INTRODUCTION

The fabrication of analogs mimicking the same geometric and electromagnetic properties of the initial objects of interest is unambiguously the fundamental requirement in microwave analog experiments. Widening the domains of applicability of the microwave analogy requires widening the manufacturing capabilities. Until the beginning of this thesis, the studied analogs were obtained using classical machining techniques which consist of taking a bloc of commercial bulk material with relative permittivity as close as possible to the desired one and shaping it into the form of the desired analog. Some preliminary works have also been made with additive manufacturing techniques but the control of the permittivity was still an open question [10]. However, the technique of subtracting from raw material has many limitations:

1. Machining of analogs with complex shapes is in most of the time quite complicated and time consuming. For instance, the soot aggregate analog consisting of a aggregation of spheres presented in section 1.4.10.1 was only obtainable using a 3D micro milling machine adapted to manipulate spheres of 5 mm diameter, then the spheres were stuck together with glue.
2. The control of the complex relative permittivity of analogs is very challenging because most of the commercial materials that could be machined are polymers with real part of relative permittivity between 2 and 3 and almost null imaginary part. Obtaining analogs with real part of relative permittivities below 2 can be achieved using some low-density foams as it will be explained in section 3.1.2, but their low density makes them too frail to be machined correctly and their homogeneity cannot be guaranteed. Moreover, it is difficult to find commercial materials with non-null imaginary part of relative permittivity, which is the case for the soot aggregates.
3. It is also difficult to machine heterogeneous objects whose different parts have different relative permittivity values.

In this context, additive manufacturing technologies appear as a promising way to obtain analogs with complex geometries to be created without need for expensive tooling and in



a very reasonable time. In addition, additive manufacturing technologies are also being extensively used to control the relative permittivity of objects, either through manufacturing some composite materials or through creating specific geometrical structures that allow to modify the global electromagnetic properties of the objects such as 3D objects with graded refractive index [73].

From the point of view of analogs of interest, we distinguish between three categories in term of relative permittivity: analogs with real part of relative permittivity below 2 such as analogs of photosynthetic microorganisms (see section 3.1) [74], analogs with high permittivity such as silicon particles analogs and trees analogs (see section 3.2 and chapter 4) [11], [75], analogs with non-null relative permittivity imaginary part such as soot aggregate particles (see section 3.2) [76]. Moreover, the analogs of interest can be simple shaped (spheres, spheroids), complex shaped (aggregate of spheres) and can be homogeneous and heterogeneous.

In order to take profit of the additive manufacturing technologies in the control of our analogs, we have established a collaboration with the “Centre de Transfert et de Technologie du Mans” (CTTM). Throughout this collaboration we have been able to design, manufacture and characterize objects with controlled electromagnetic properties. The main novelty that resulted from this collaboration is a proposed technique that allow to obtain “on-demand” homogeneous and heterogeneous objects with low real part of relative permittivity (between 1 and 3). To the best of my knowledge, this is the first time this range of permittivity is addressed in the microwaves.

In the rest of this chapter I will present my work on the control of the electromagnetic properties through additive manufacturing and permittivity determination method as well as the obtained results.

## **2.2 ADDITIVE MANUFACTURING IN STEREOLITHOGRAPHY**

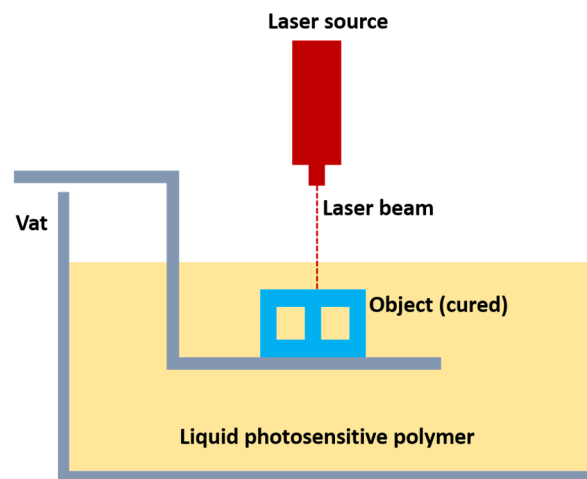
Additive manufacturing, also called 3D printing, is defined as the set of technologies allowing to form objects by building up matter through layer by layer deposition, unlike the matter removal procedure used in the traditional machining techniques. The Computer-Aided Design (CAD) softwares together with the automated machines, afford the manufacturing of objects of inaccessible shapes and material properties with classical technics. For an object to be fabricated, it goes through two steps of the manufacturing chain: the model design and the physical manufacturing. The first step consists of creating a 3D model of the object to be printed using a CAD software package. The CAD file is often next converted to an STL file

(Standard Tessellation Language) which is a tessellated representation of the model, readable by a 3D printer. The second step is the transfer of the STL file to the machine which is controlled by a computer and rebuilds the object in a layered model. The machine then builds up the object through deposition of the material in layers.

Although all the additive manufacturing technologies use the principle of layers deposition of matter, there are differences between them in term of the type of the used material, of the way the machine deposits the material and of the fabrication resolution. The American Society of testing and Materials (ASTM) has classified in 2010 the additive manufacturing technologies into 7 categories [77]:

1. Stereolithography or vat polymerization
2. Material jetting
3. Binder jetting (powder and binder)
4. Material extrusion (Fused Deposition Modeling)
5. Powder Bed Fusion (Selective Laser Sintering)
6. Sheet lamination
7. Direct Energy Deposition

The stereolithography is one of the most common categories for the high resolution it provides (Figure 2.1).



*Figure 2.1 Principle of the stereolithography process utilizing a vat of liquid photopolymer resin*

It lies on curing a photosensitive liquid polymer by exposition to ultraviolet light (UV). The liquid is placed in vat and the 3D printer uses digital light processing technology to emit a light providing the required energy to induce the chemical reaction between the liquid molecules and bind them to form a highly cross-linked polymer [78]. The process of draining and

exposure to UV light is repeated until the object is complete, with the vat completely drained and leaving the solid 3D object. At the end, a post-processing step is required to remove the residual resin parts from the solid state printed structure. The advantage of the stereolithography over the other techniques are the high level of accuracy and the good finishing and the relative quick process.

### 2.3 RELATIVE COMPLEX PERMITTIVITY OF MATERIALS

Based on the Maxwell equations, the interaction between a material and an electromagnetic wave is characterized by three constitutive parameters: the complex permittivity  $\varepsilon$ , the complex permeability  $\mu$  and the conductivity  $\sigma$ . The permittivity  $\varepsilon$  can be defined as:

$$\varepsilon = \varepsilon_0 \varepsilon_r$$

Where  $\varepsilon_0 = \frac{1}{\mu_0 c^2} \approx 8.85 \times 10^{-12} F/m$  is the permittivity of the vacuum and  $\varepsilon_r$  is the relative permittivity of the material that describes the ease by which that material may be polarized. The relative complex permittivity can be decomposed in real and imaginary parts:

$$\varepsilon_r = \varepsilon' + j\varepsilon''$$

For an isotropic material, the term  $\varepsilon'$  is the dielectric constant and the term  $\varepsilon''$  is the electric loss factor.

Along this thesis I only use the complex relative permittivity to define the electric properties of materials.

### 2.4 MICROWAVE APPLICATIONS USING ADDITIVE MANUFACTURING

Many research laboratories are nowadays implementing the additive manufacturing technologies in the fields of communication and imaging, ranging from lightweight electronic devices for aerospace applications to antennas and RF components to wireless communication. In these fields, most of the interests are oriented toward dielectric materials. Nevertheless, some other research activities employ also the additive manufacturing of metal to control the targets properties in RCS measurements [79] but also for waveguides manufacturing.

At the initiation of our work on the control of the electromagnetic properties of materials through additives manufacturing techniques, and before we established our collaboration with the CTTM, the literature guided us toward several research institutes that share with us the same interest. Primary exchanges have been made with the institute Xlim in France and the University of Texas El Paso (UTEP) in attempts for collaborations establishments. These

institutes use the additive manufacturing and the material development in the RF devices innovation. Exchanges also recently started with the laboratory Lab-STICC at the Université de Bretagne Occidentale (UBO) on the fabrication of absorbing materials [80].

In this section, I give some examples from the literature about their activities in applying additive manufacturing to obtain desired electromagnetic properties in addition to some of the activities of the Department of Materials at University of Oxford.

#### 2.4.1 Ceramic additive manufacturing at Xlim Institute (France)

The Xlim laboratory in France has developed a 3D stereolithography technique for the fabrication of ceramic microwave components. As the design and the fabrication of advanced RF components such as antennas, filters and others, requires the satisfaction of the electrical and dimensional constraints, the additive manufacturing shows up as the best candidate. On the one hand, it allows the optimization of the size and the shape of the component. On the other hand, ceramics represent a good candidate for such applications thanks to their high  $\epsilon'$  and the low loss tangent.

The use of ceramic particles in stereolithography represents a real challenge. Basically, the liquid resin needs to be very fluid in order to insure a proper flat surface and avoid deformations. However, with ceramic particles the resin becomes too viscous which is inappropriate for the manufacturing process. At the same time, the percentage of ceramic must be higher than 50% in volume in order to maintain satisfying mechanical and electrical properties. The proposed technique at Xlim consists of using a highly selective photosensitive resin with a high volume percentage of ceramic (around 65%) to have a thick and viscous suspension rather than a fluid mixture. The 3D printer was technically modified and adapted to deal with viscous suspensions but still using an ultraviolet laser. The ceramic paste is placed in a special container and a piston delivers a layer of a thickness of  $1 \mu$ , then a profile blade spreads uniformly the paste layer which is next photo-polymerized by the laser [81]. This process has been developed by the Sciences des Procédés Céramiques et de Traitement de Surface center (SPCTS) and the Centre de Transfert de Technologies Céramiques (CTTC) [81] and it is summarized in Figure 2.2.

This fabrication technique has been used for a wide variety of applications from complex 3D periodic structures to advanced millimeter wave antennas and bandpass filters. Among the commonly used ceramics in this technique we cite the Zirconia ( $\epsilon' = 31.2, \tan\delta = 1.8 \times 10^{-3}$  at 30 GHz), the Alumina ( $\epsilon' = 9.0, \tan\delta = 5 \times 10^{-5}$  at 10 GHz)

and the high performance  $\text{Ba}_3\text{ZnTa}_2\text{O}_9$  (BZT) ceramics ( $\epsilon' = 30.2$  and  $\tan\delta = 1.9 \times 10^{-4}$  at 33 GHz). Some examples of the realized components is presented in Figure 2.3.

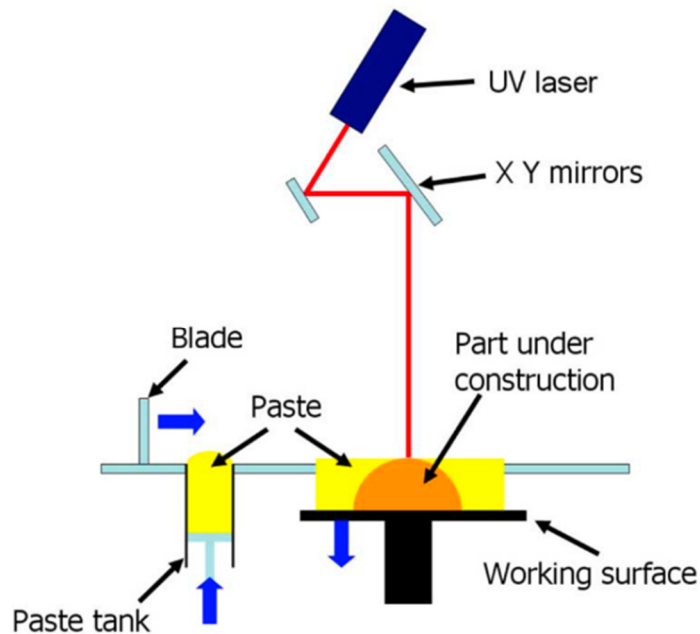


Figure 2.2 Ceramic stereolithography setup used at Xlim [82]

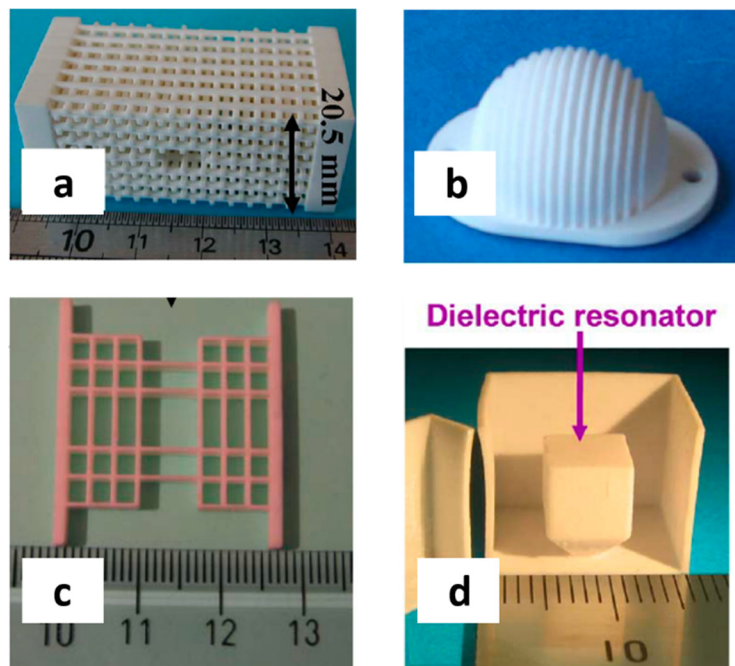


Figure 2.3 RF microwave components fabricated at Xlim using the developed ceramic stereolithography technique. (a) Large bandpass monolithic waveguide operating at 26 GHz located in a woodpile made out of Zirconia [83]. (b) 60 GHz integrated lens antenna of 3 cm width made out of Alumina [82]. Zirconia plate used as input/output access to a narrow Ka bandpass filter operating at 33 GHz [84]. (d) Alumina resonant structure working at 12.57 GHz dedicated to RF filtering applications composed of a main structure containing the dielectric resonator and a surrounding cavity [85]

### 2.4.2 Additive manufacturing in University of Texas at El Paso (United States)

The W.M. Keck center for 3D innovation at the University of Texas at El Paso is a multidisciplinary research facility focused on the use and development of additive manufacturing technologies. The institute offers a broad selection of additive manufacturing technologies and materials including, in addition to the stereolithography, the material extrusion, the laser sintering in addition to metal based additive manufacturing. The used 3D printers are many and they are of different brands. The fabrication of components for microwaves and telecommunication applications is an active application field at the institute for academic research and industrial project. Therefore, the electromagnetic characteristics of the fabricated materials are measured in different methods. In the X-band, typically, the materials are characterized in waveguide using the Nicholson-Ross-Weir method [86]. The most used base materials are plastics of  $\epsilon'$  between 2 and 30 and a loss tangent near to zero. In [87] a metamaterial structure was fabricated using fused deposition modeling with an homogeneous material, a polycarbonate acrylonitrile butadiene styrene (ABS) blend, of  $\epsilon'$  of 2.45 at 15 GHz. The structure is a photonic crystal that flowed an unguided incident electromagnetic field around a  $90^\circ$  without diffracting and scattering by spatially varying the unit cells through the lattice (Figure 2.4-a). Also in [88] an artificially anisotropic metamaterials is reported which was manufactured in fused deposition modeling using polycarbonate material (PC) of  $\epsilon'$  of 2.57 (Figure 2.4-b).

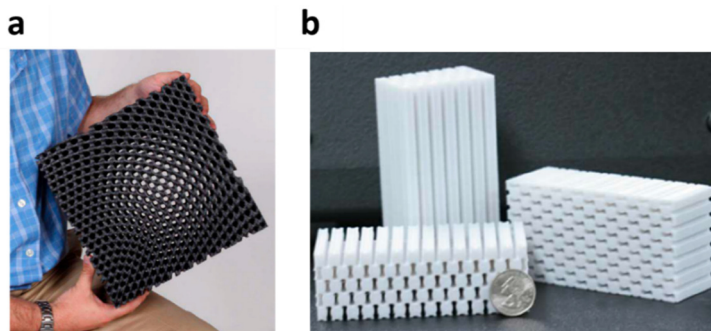


Figure 2.4 (a) Spatially variant self-collimating lattice [87]. (b) Anisotropic metamaterials [88]

In [89] the authors present the production of a new nanocomposite material. The material consists of a photocurable epoxy matrix mixed with carbon nanotubes. The fabrication was made in stereolithography and complex shapes objects were investigated. The impact of different percentages of multi-walled carbon nanotubes on the mechanical properties of the material was studied (Figure 2.5). Although the electromagnetic characteristics were not questioned in that work but we cite it since it has some similarities with works we have done during this thesis to control the electric losses in the objects.



Figure 2.5 Chess rook fabricated in stereolithography from epoxy/carbon nanotubes mixture [89]

### 2.4.3 Ceramics/polymers manufacturing at the University of Oxford

The extensive use of high real permittivity materials in technology sectors related to electronics and communication has emerged the development of ceramic/polymers composite materials. Such composites combine the high real part of permittivity of ceramics together with the mechanical properties of polymers. The Department of Materials at the University of Oxford has established studies on the microwave dielectric properties of Barium titanate ABS/BaTiO<sub>3</sub> composites in Fused Deposition Modeling 3D printing. The work in [90] explicitly provide the detailed relative permittivity measurements of ABS/BaTiO<sub>3</sub> composites with many different weight (wt) percent of BaTiO<sub>3</sub>.

BaTiO<sub>3</sub> microparticles were dispersed in ABS to form filaments with loadings of 0 to 70 wt% of BaTiO<sub>3</sub> with increment of 10 wt%. The permittivity measurement on solid disc-shaped samples of all the filaments in a Split-Post Dielectric Resonator (SPDR) at 15 GHz showed a considerable increase of  $\epsilon'$  as the fraction of BaTiO<sub>3</sub> in the composite increases. Figure 2.6 shows measured value of  $\epsilon'$  at each loading fraction of BaTiO<sub>3</sub>. Some examples of printed objects are shown in Figure 2.7 that show the compatibility of the composite filament with the manufacturing of complex-shaped objects.

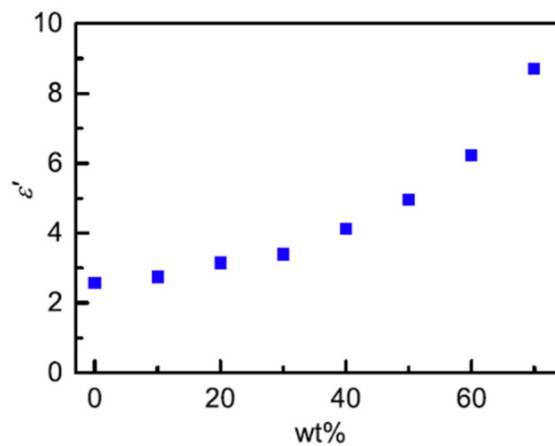


Figure 2.6 The Real part of the relative permittivity of 3D parts for various loading fractions of BaTiO<sub>3</sub> between 0 wt% and 70 wt% at 15 GHz [90]

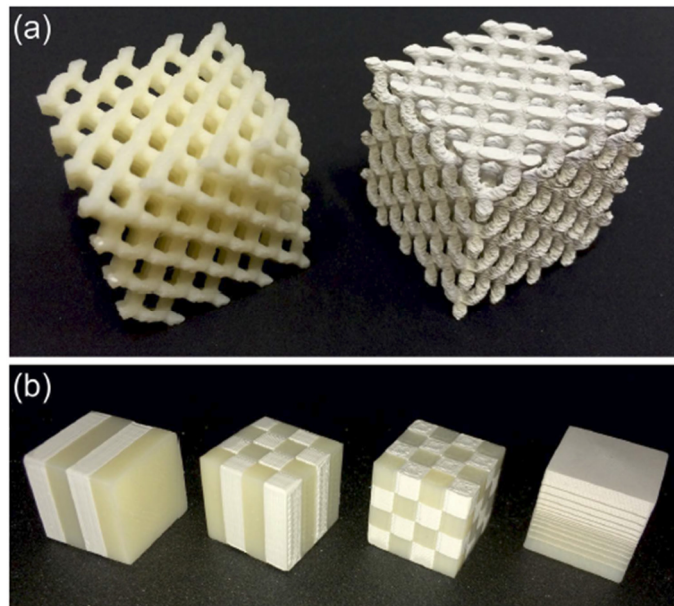


Figure 2.7 3D-printed polymer composite parts. (a) Rod-connected diamond photonic crystal structures printed in ABS polymer (left,  $\epsilon' = 2.57$ ) and 50 wt% BaTiO<sub>3</sub>/ABS polymer composite (right,  $\epsilon' = 4.95$ ). (b) 1D, 2D, and 3D periodic structures and a 1D graded structure printed using a combination of ABS polymer and 50 wt% BaTiO<sub>3</sub> in ABS polymer composite [90]

## 2.5 ANALOGS FABRICATION IN STEREOLITHOGRAPHY : COLLABORATION WITH THE CENTRE DE TRANSFERT ET DE TECHNOLOGIE DU MANS

In the aim to widen the controllability of the analogs electromagnetic properties with a good control of their geometries through implication of the additive manufacturing technologies, we have established a collaboration with the CTTM. The CTTM is a transfer center specialized, among other sectors, in the research and development in materials innovation and manufacturing processes. Within this collaboration my role is to propose the structures such as the way to create porous structures to obtain low  $\epsilon'$  analogs (see 2.7) or the additives to be included that may answer our needs for high  $\epsilon'$  analogs (see sections 2.8 and 2.9) and collaborators at the CTTM work on the material mixture for fabrication process using their 3D eprinter.

### 2.5.1 The used stereolithography 3D printer

The CTTM uses a stereolithography 3D printer from the Ember society. The basic photosensitive resin is the acrylate of black or white color. We determined the relative permittivity of the bulk material from the far-field scattering measurement on a sphere of 35 mm and it is  $\epsilon_r = 2.9 + 0.08j$ . The permittivity estimation method is detailed in section 2.6. The volumetric mass density of the bulk material is 1200 Kg/m<sup>3</sup>. The thickness of every photopolymerized layer is 25  $\mu\text{m}$ . We should mention here that the dimensions of the printer's vat



are  $64 \times 40 \times 134$  mm. Therefore, the maximum printable object's size cannot exceed these limits. Larger objects are manufactured partially and reassembled later. Notice that all the tests on the permittivity control were applied to spheres which allows us to estimate their permittivity from comparison to Mie theory and all sphere have a diameter of 35 mm. This diameter was chosen according to the geometrical limits of the printer.

## 2.6 PERMITTIVITY ESTIMATION FROM FAR FIELD SCATTERING MEASUREMENT

In the microwave domain numerous methods have been proposed to derive permittivity measurements such as methods based on resonators or cavities, transmission line using coaxial cells, and rectangular waveguides. During this thesis I used the far field scattering measurement on spheres to determine the relative permittivity of materials based on the method explained in [91]. A sphere of a given diameter is manufactured from the homogeneous material whose permittivity determination is required and the microwave scattering by that sphere is measured in the anechoic chamber. In this method, we assume isotropic and non-magnetic materials. The field scattered by the sphere depends upon five parameters: its diameter, position of its center, real and imaginary part of relative permittivity and the frequency. As the diameter, the center position and frequency are well known, it is possible to determine the permittivity of the sphere through an inverse problem process. The analytical scattered field by the sphere is calculated with Mie series [92], avoiding supplementary model errors. All the scattering measurements on the spheres for permittivity estimation were made in the bistatic azimuthal circular configuration of the setup at  $\varphi_s = 90^\circ$  and for  $\theta_r$  from  $-130^\circ$  to  $130^\circ$ . Due to the symmetry of the sphere, any plane containing the sphere center can be selected. The VV polarization case was selected for all the measurements (but it could also be made in HH polarization). The relative permittivity of the material was determined through comparison of the measured scattered field by the sphere to the analytical computation obtained with Mie theory. The procedure is detailed in the following subsections.

### 2.6.1 Comparison criterion $F$ based on Root Mean Square Error calculation

The complex permittivity of the sphere is determined through comparison between the measurement and the simulation of the scattered field at every working frequency. The analytical computation of the scattered field is made for a range of combination of real and imaginary parts of permittivity. This range is first selected to be large enough around the material permittivity value that one can find in the literature. For instance, for polymer materials I chose the first permittivity guess range between 1 and 5 for  $\varepsilon'$  (with a step of 1) and between

0 and 1 for  $\varepsilon''$  (with a step of 0.5). This range is later reduced as well as the sampling step through an iterative process. At each complex permittivity value a comparison criterion  $F$  is computed between the simulation and the measurement which is the Root Mean square Error (RMSE). The complex permittivity that yield the lowest value of  $F$  is considered the correct value:

$$F_f = \sum_{\theta_r=-130^\circ}^{+130^\circ} |Re(E_{sca,\theta_r}^{mes} - E_{sca,\theta_r}^{Mie})|^2 + \sum_{\theta_r=-130^\circ}^{+130^\circ} |Im(E_{sca,\theta_r}^{mes} - E_{sca,\theta_r}^{Mie})|^2 \quad (2.1)$$

Where  $E_{sca}^{mes}$  is the measured scattered field,  $E_{sca}^{Mie}$  is the simulation (with Mie) scattered field and  $f$  is the frequency. However, each measurement point is compulsorily disturbed by some measurement errors and it is important to take this error into account. As the drift errors and the stray signals are considered eliminated from the measurement, and considering a good alignment of the sphere, the measurement error are considered as pure random noise. The characterization of the random noise is discussed in section 1.7. It has been considered to be an additive complex random variable whose real and imaginary parts are normally distributed [93]. The criterion  $F$  with consideration of the noise becomes:

$$F_f^{noise} = \sum_{\theta_r=-130^\circ}^{+130^\circ} \frac{|Re(E_{sca,\theta_r}^{mes} - E_{sca,\theta_r}^{Mie})|^2}{\sigma_{sca}^{Re}} + \sum_{\theta_r=-130^\circ}^{+130^\circ} \frac{|Im(E_{sca,\theta_r}^{mes} - E_{sca,\theta_r}^{Mie})|^2}{\sigma_{sca}^{Im}} \quad (2.2)$$

Where  $\sigma_{sca}^{Re}$  and  $\sigma_{sca}^{Im}$  are respectively the associated standard deviations on the real part and imaginary parts of the scattered field. The standard deviations depend on the amplitude and on the frequency of the scattered field.

With such spheres, the highest amplitude value of a scattered field is in the forward direction. When the random noise is not taken into account in the cost function calculation, the measurement points corresponding to the forward scattering direction are too predominant in the value of the criterion  $F$  and the contributions of the other angles are weak. However, when the noise is taken into account, each measurement point is weighted with respect to its uncertainty.

## 2.6.2 Uncertainties on the permittivity value

As an example on the permittivity estimation, we present the case of a 35 mm diameter sphere of pure acrylate material, manufactured in additive manufacturing at the CTTM. The associated criterion  $F_{min}^{noise}$  at 18 GHz is shown in Figure 2.8 as a function of the real and imaginary parts of permittivity. As it can be seen on the figure, over the chosen permittivity range, a single minimum is reached by  $F_{min}^{noise}$  at the correct values of  $\varepsilon'$  and  $\varepsilon''$  with a RMSE around -50 dB.

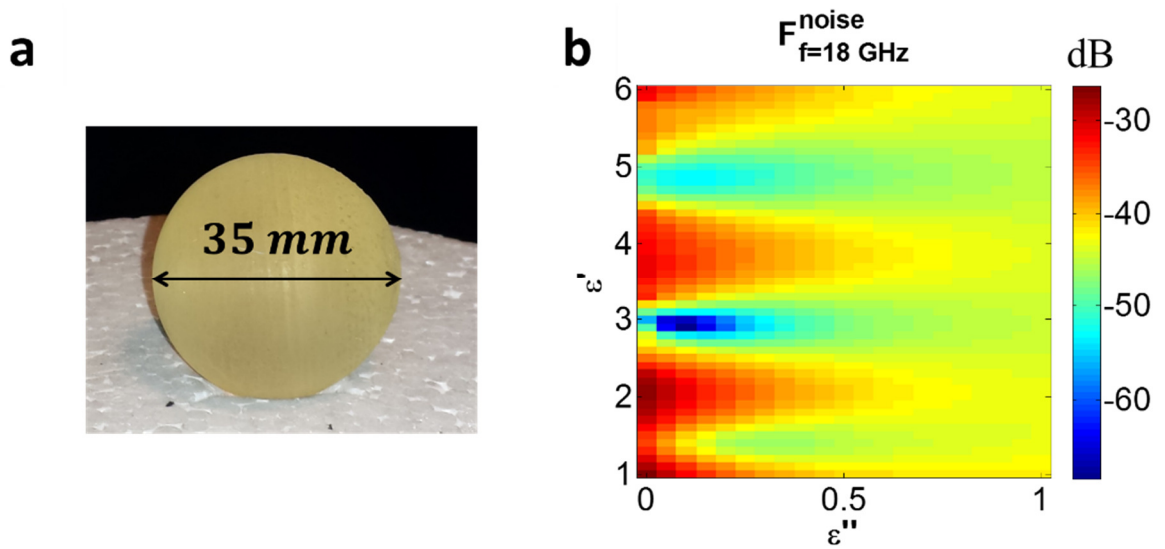


Figure 2.8 (a) The acrylic sphere. (b) Map in dB of the criterion  $F_{min}^{noise}$  for  $\epsilon' \in [1, 6]$  and  $\epsilon'' \in [0, 1]$  at 18 GHz

The determined relative permittivity value is  $2.9+0.08j$ . Next, each permittivity value is associated with its uncertainty defined as the variation of the real and imaginary part of permittivity which lead to a variation of 3 dB on the criterion  $F^{noise}$  around the minimal value  $F_{min}^{noise}$ . The uncertainty on the determined permittivity is therefore defined as the range of variation within eight permittivity values around the determined value as explained in Figure 2.9. The estimated complex permittivity of the acrylic sphere is presented in Figure 2.10 as a function on the frequency.

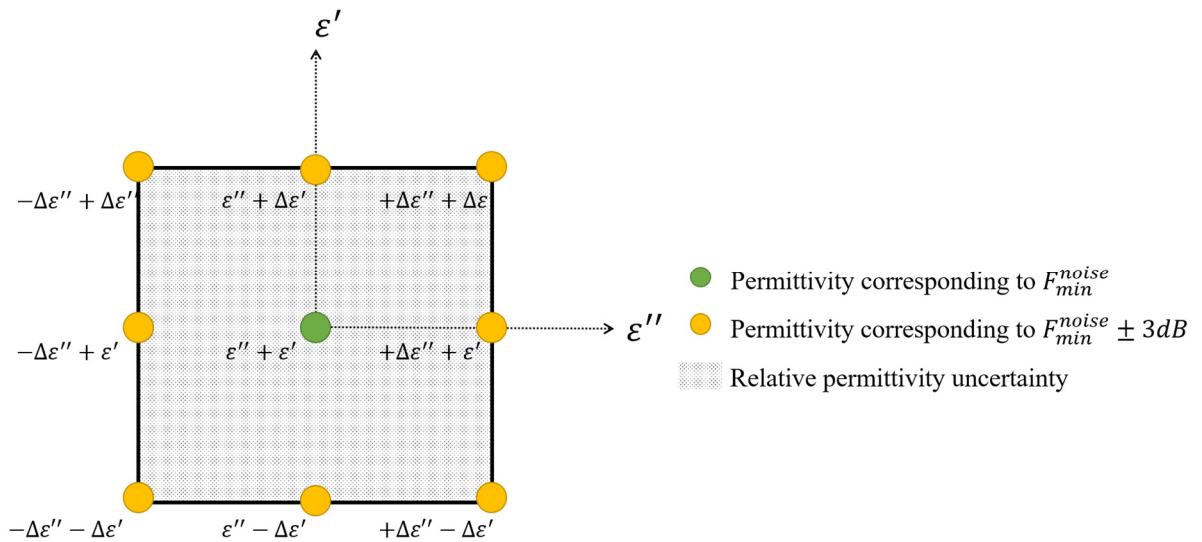


Figure 2.9 Definition of the uncertainty on the determined relative permittivity from the variation of the criterion  $F^{noise}$  of 3dB around  $F_{min}^{noise}$

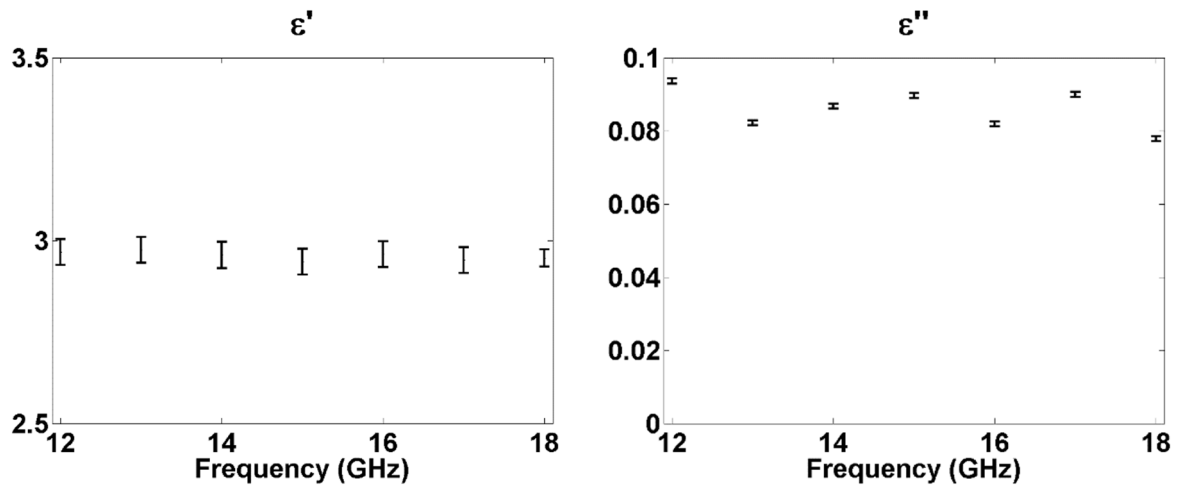


Figure 2.10 Estimated real and imaginary parts of permittivity and the associated uncertainty of a 35mm diameter sphere of acrylate material fabricated in additive manufacturing with respect to the frequency

## 2.7 FABRICATION OF POROUS OBJECTS WITH LOW PERMITTIVITY ( $1 < \epsilon' < 3$ )

The fabrication of low permittivity objects ( $\epsilon'$  tending to 1) in additive manufacturing isn't an easy task (studies on low permittivity objects have been first made during this thesis through machined objects, see section 3.1). Most of the commercial 3D printers use plastics as base materials that usually have  $\epsilon'$  between 2 and 3 and that of our machine is around 3 ( $\epsilon' = 2.9$ ). To reach lower  $\epsilon'$  values, new fabrication strategies should be adapted. To reach this goal, we have proposed a novel technique to create a controlled porosity inside an analog through the control of the air-to-material ratio.

Our idea was to create the porosity through the creation of a meshed structure having the geometry of the desired object. Our technique is explained in Figure 2.11. First the geometry of the analog, here the sphere, is designed then it is meshed into tetrahedrons using the free meshing software "Gmsh" [13] (Figure 2.11-a). The mesh yields the positions of the nodes and the edges connecting them. Second, the generated file in ".msh" format is sent to our collaborators at the CTTM who generate cylinders from the edges by giving then a certain diameter. This work is made using the commercial software CATIA [14](Figure 2.11-b). After the cylinders are created, the CAD file is generated and used by the 3D printer (Figure 2.11-c) to generate the layers. Finally, the object is fabricated through layer by layer manufacturing (Figure 2.11-d). The advantage of this technique is that it allows to create randomly distributed porosities inside the object to have this latter equal to an homogeneous equivalent medium.

The mesh size and the cylinders diameter are the two parameters that govern the filling of the global volume of the sphere with the resin and allow thus to adjust the permittivity on

demand. For instance, a permittivity of 1.4 can be obtained with an association of mesh size of 1.6 mm and cylinders diameter of 0.35mm, but also can be obtained with a mesh size of 6.6 mm with cylinders diameter of 1.1 mm.

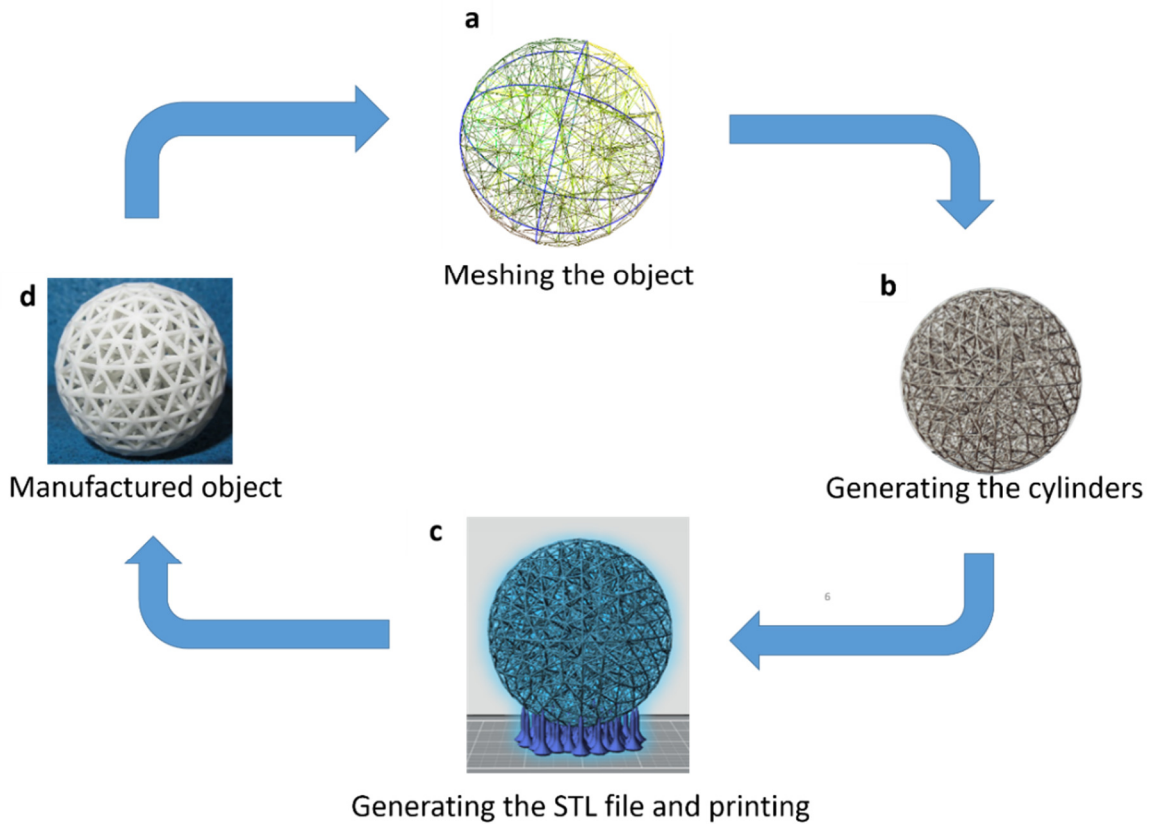


Figure 2.11 Porosity control using meshed geometry

The keystone in this method is to homogenize the bulk material (acrylate) and the air together in order obtain, according to the working wavelength, a homogeneous and isotropic material. This homogenization is dependent on the two aforementioned parameters: mesh size and cylinder diameter.

### 2.7.1 Parameters selection for on-demand permittivity

As said previously, the bulk material has a  $\epsilon'$  equal 2.9 and an almost null imaginary part. In order to develop a procedure that allow us to roughly evaluate the required cylinder diameter and/or mesh size that answer our requirements in permittivity, we can estimate the volumetric mass density and consider firstly a linear relation between this one and  $\epsilon'$ . Therefore, the required density for a desired permittivity of the air-acrylate mixture is obtained according to Maxwell Garnett theory [94]. Indeed, this is a simple and basic method to predict the permittivity from the quantity of matter to the quantity of air ratio that has limited validation. Yet, in the frame of this work it satisfies our need in term of simplicity and it shows a

quite good accuracy for the permittivities between 1 and 3. The prediction of the required density leads back to the determination of the mass of the meshed sphere for the desired permittivity. As a result, the required cylinder diameter, for a given mesh size, is simply estimated from the required sphere mass. The procedure is explained in Figure 2.12.

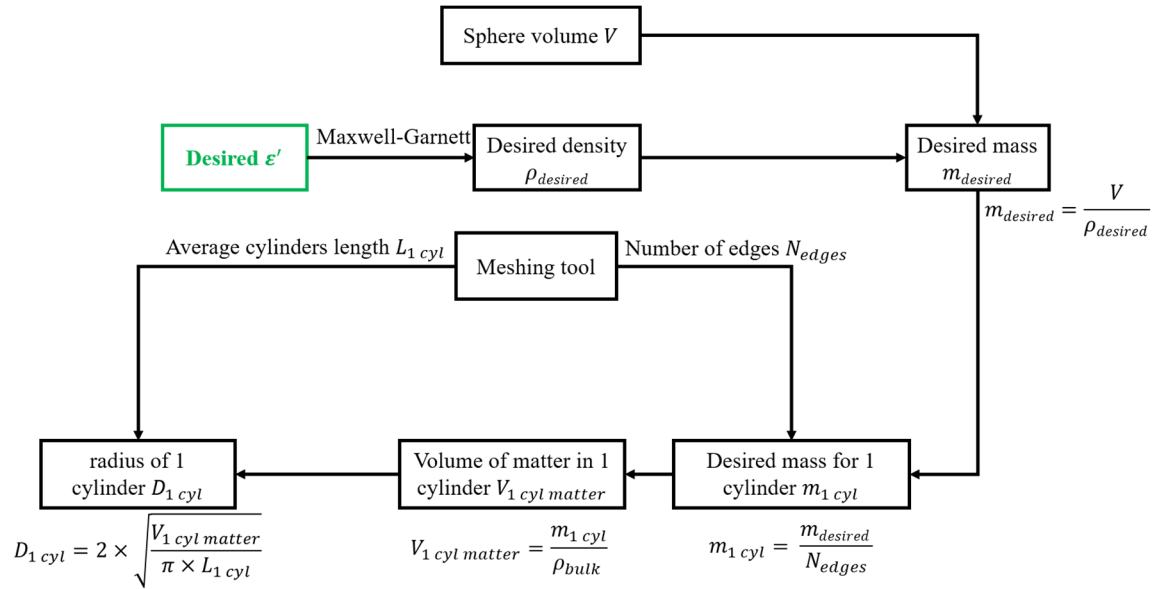


Figure 2.12 Procedure of the meshing parameters prediction for a chosen permittivity estimation Spheres samples and permittivity determination

In the rest of this section, the spheres will be named by the material they are made out of, with the cylinders diameter in the exponent and the mesh size in the index. For instance, *Acrylate*<sub>4.7</sub><sup>0.56</sup> means the sphere with the bulk material acrylate, mesh size of 4.7 mm and cylinders diameter of 0.56 mm (Figure 2.13).

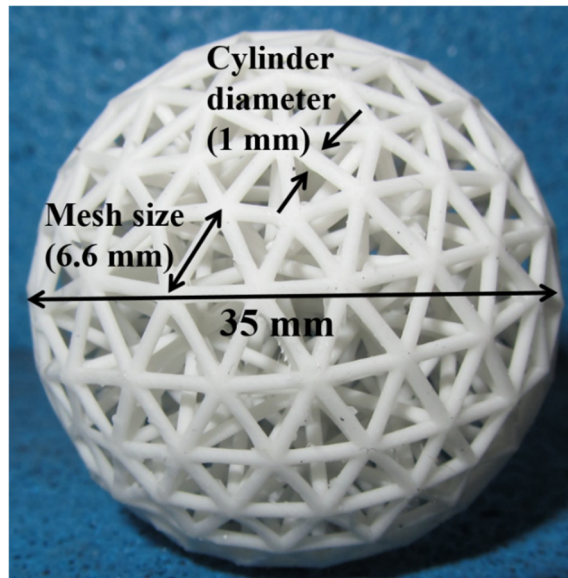


Figure 2.13 Photography of the meshed sphere  $Acrylate_{6.6}^1$  showing the sphere diameter (35 mm), the mesh size (6.6 mm) and the cylinders diameter (1 mm)

### 2.7.2 Measurement of low permittivity spheres in optimized configuration

The permittivity of the spheres is determined from bistatic scattering measurement according to the method described in section 2.6. The scattering measurements are made in an optimized configuration using the power decomposition schemes into three different profiles (see section 1.71.7.5). For each sphere, the scattering measurement is made in four orientations at  $\theta_o = -90^\circ, 0^\circ, 90^\circ, 180^\circ$ . This allows to assess the reproducibility of the measurement and the isotropy of the sphere. Ideally for a sphere the scattered field must be the same whichever is the orientation. We have fabricated different spheres of dielectric constants between 1 and 3 with different meshing schemes and cylinders diameters. The cornerstone in this technique is the choice of the mesh size. The mesh size should be small enough compared to the wavelength in order to insure a good homogenization and to be in the conditions of an equivalent homogeneous medium. We made our measurements in the frequency band from 2 GHz to 18 GHz and the smallest wavelength  $\lambda_0$  is equal to 16.7 mm in the free space. In a homogeneous material, the wavelength is equal to  $\frac{\lambda_0}{\sqrt{\epsilon'}}$ . Therefore, the first sphere we made had a desired  $\epsilon'$  around 1.4, mesh size of 1.4 mm ( $=\frac{\lambda_0}{10 \times \sqrt{1.4}}$  where  $\lambda_0 = 16.7$  mm) and cylinders diameter of 0.35 mm ( $Acrylate_{1.4}^{0.35}$ ). In Figure 2.14 we show the determined values of  $\epsilon'$  from the far field scattering at the four orientations. The permittivity values are reproducible with respect to the orientations and almost constant with respect to the frequency. Amplitude and phase of the measured scattered field are shown according to the uncertainties determination method described in section 1.7.3.

For the simulated scattered fields, the uncertainties on the permittivity determination are also shown and are determined according to the method in 2.6.2. The simulations are obtained with Mie theory and they correspond to a homogeneous sphere of 35 mm diameter and with the relative permittivity values in Figure 2.14, frequency per frequency. It is noticeable from the comparisons in amplitude and phase that the simulation and the measurement have the same behavior and all the simulated fields are within the uncertainty of the measurement. These results show success in obtaining low permittivity values that match the predicted values, but also a success in the measurement of their low scattered fields thanks to the power zones decomposition technique (amplitudes of the scattered fields down to -60 dB, equivalent to  $-44 \text{ dBm}^2$  in RCS).

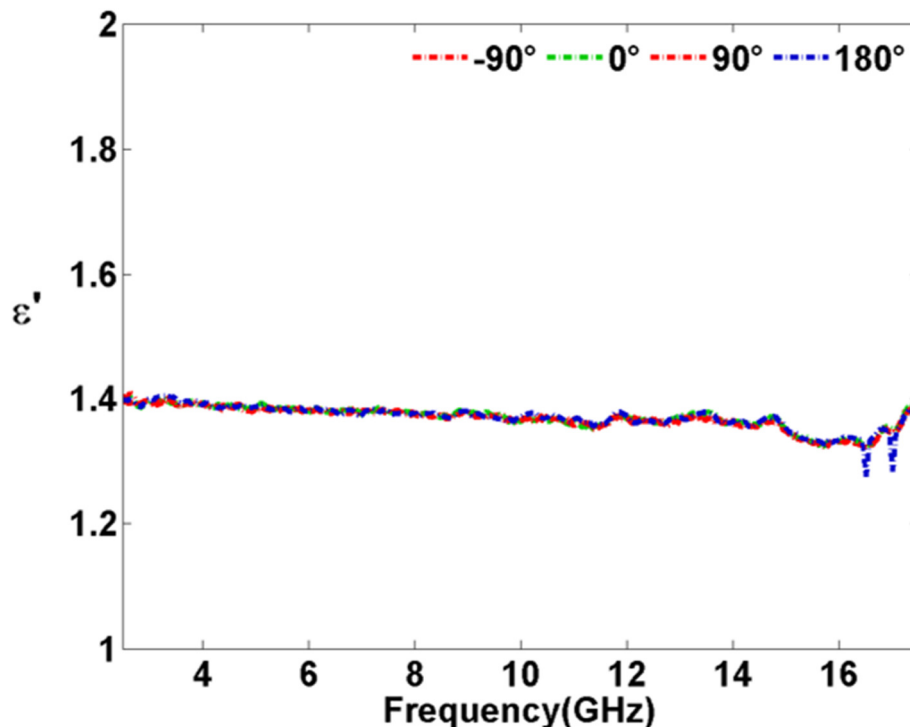


Figure 2.14 Real part of the relative permittivity of the sphere  $Acrylate_{1.4}^{0.35}$  determined at the four orientations ( $\theta_o = -90^\circ, 0^\circ, 90^\circ$  and  $180^\circ$ ) as a function of the frequency

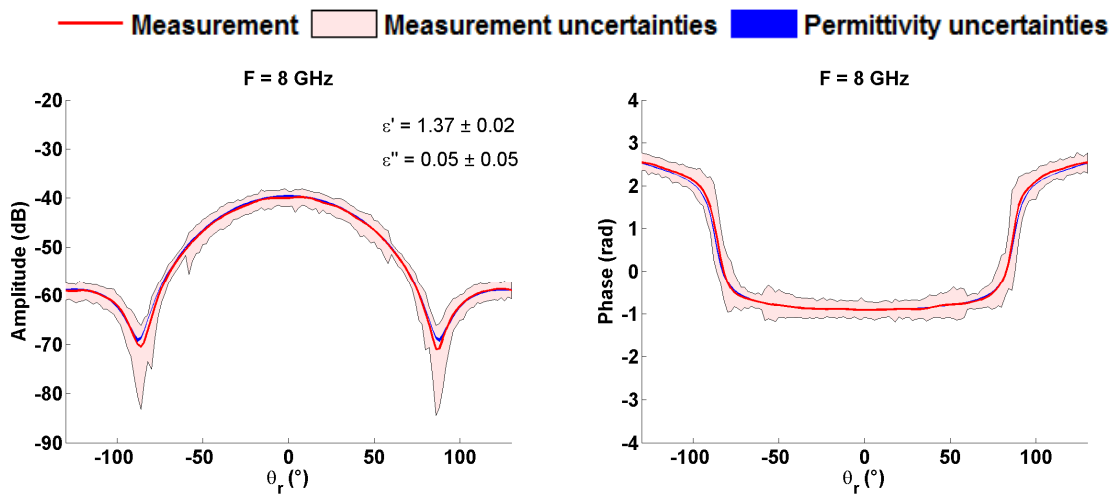
A comparison between the measured scattered fields and the simulated scattered fields for the sphere  $Acrylate_{1.4}^{0.35}$  is shown in Figure 2.15. On the figures, the uncertainties on the measurement are shown. Very good agreement between simulation and measurement can be observed in amplitude and phase, even at the angular regions where the amplitude is quite low (-60 dB and below), thanks to the optimized state of the measurement setup.



The test executed on the sphere  $Acrylate_{1.4}^{0.35}$  gave promising results about the control of  $\epsilon'$ . The measured values of  $\epsilon'$  are in a good agreement with the predicted ones. Moreover, the determined permittivity values are reproducible with respect to the orientations.

However, the encountered difficulty while working on the design of this sphere is the long processing time to generate the cylinders for a high number of edges (the number of edges are proportional to the number of meshes, and both increase when the mesh size decreases). The sphere  $Acrylate_{1.4}^{0.35}$  contains 40167 edges. The post-processing time to generate cylinders with diameter 0.35 mm from those edges is very long (more than 24 hours). If one needs to fabricate analogs with large volumes, the number of edges will increase and the cylinders generation time will be cumbersome.

Therefore, we decided to create spheres with larger mesh sizes and consequently with lower number of edges than the  $Acrylate_{1.4}^{0.35}$  sphere to identify the limits of the proposed permittivity control method. We have designed and fabricated different meshed spheres with diameter 35 mm and with mesh sizes of 4.7 mm and 6.6 mm which has led to 804 and 1870 cylinders per sphere respectively (respectively 50 times and 20 times less than those of  $Acrylate_{1.4}^{0.35}$ ). Their desired  $\epsilon'$  are ranging from 1.02 to 2.3. The photography of those spheres and their properties are summarized in Figure 2.16.



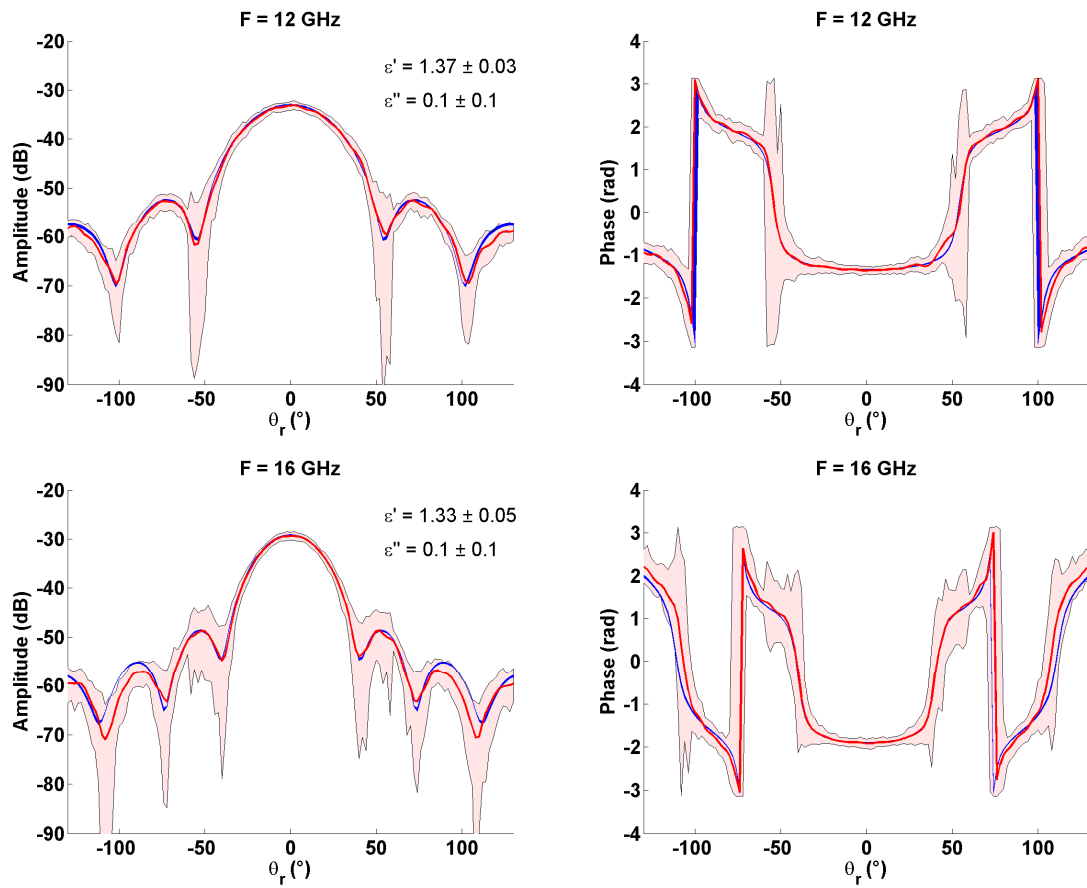


Figure 2.15 Amplitude and phase of the measured scattered fields by the meshed 35 mm diameter sphere  $\text{Acrylate}_{1.4}^{0.35}$  with comparison to the Mie simulation of equivalent homogeneous sphere. The relative permittivity value corresponding to each frequency is shown on the amplitude figures


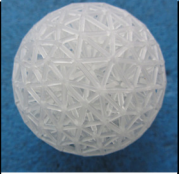

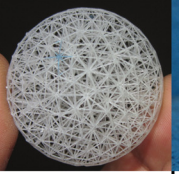

Name	$Acrylate_{6.6}^{2.5}$	$Acrylate_{6.6}^1$	$Acrylate_{4.7}^{0.56}$	$Acrylate_{4.7}^{0.2}$	$Acrylate_{1.4}^{0.35}$
					
Mesh size (mm)	6.6	6.6	4.7	4.7	1.4
Mesh size ( $\lambda_{max}$ )	$\frac{\lambda_{max}}{15}$	$\frac{\lambda_{max}}{20}$	$\frac{\lambda_{max}}{30}$	$\frac{\lambda_{max}}{31}$	$\frac{\lambda_{max}}{90}$
Mesh size ( $\lambda_{min}$ )	$\frac{\lambda_{min}}{1.6}$	$\frac{\lambda_{min}}{2.2}$	$\frac{\lambda_{min}}{3.3}$	$\frac{\lambda_{min}}{3.5}$	$\frac{\lambda_{min}}{10}$
Number of cylinders	804	804	1870	1870	40167
Cylinders diameter (mm)	2.5	1	0.56	0.2	0.35
Density (Kg/m <sup>3</sup> )	913	207	123	55	295
Air volume percentage	3 %	83 %	90 %	98 %	73 %
Measured $\epsilon'$	2.3	1.25	1.15	1.02	1.4
estimated $\epsilon'$ (Maxwell-Garnett)	2.8	1.21	1.13	1.02	1.35

Figure 2.16 Photos and properties of the manufactured dielectric meshed spheres.  $\lambda_{min}$  corresponds to the highest frequency 18 GHz and  $\lambda_{max}$  corresponds to the lowest frequency 2 GHz. The values of the measured  $\epsilon'$  are obtained from an average over all the frequencies

The  $\epsilon'$  of the spheres  $Acrylate_{6.6}^{2.5}$ ,  $Acrylate_{6.6}^1$ ,  $Acrylate_{4.7}^{0.56}$  and  $Acrylate_{4.7}^{0.2}$  were determined from far field scattering measurements at 4 orientations, the same as the  $Acrylate_{1.4}^{0.35}$  sphere. The results of  $\epsilon'$  as a function of the frequency are presented in Figure 2.17. First, one can notice from the figure that  $Acrylate_{6.6}^{2.5}$  undergoes high variations of  $\epsilon'$  with respect to the frequencies from 2.2 to 2.5 with many oscillations. We can also distinguish discrepancies with respect to the orientations which indicate that the interaction of the sphere with the incident wave isn't reproducible with respect to the orientation. My explanation for this behavior is most probably an inhomogeneity in the sphere mixture between acrylate and air. The cylinders diameter for this sphere is quite large (2.5 mm) and the sphere is even not perfectly circular. This hypothesis is further consolidated by the comparison in amplitude and phase of the experimental scattered fields of this sphere with the simulated ones obtained with Mie theory presented in Figure 2.18. Unlike the case of  $Acrylate_{1.4}^{0.35}$ , the simulated fields of  $Acrylate_{6.6}^{2.5}$  are not within the uncertainties of the measurements. At the 3 presented frequencies, the forward amplitude lobe from experiments has higher level than that from simulation where the secondary lobes have lower levels. In addition, the minima do not occur at the same receiving angles. These discrepancies amplitude and phase are the most visible at 16 GHz.

This emphasizes the hypothesis of inhomogeneity whose detection is easier at shorter wavelengths compared to the sphere's size.

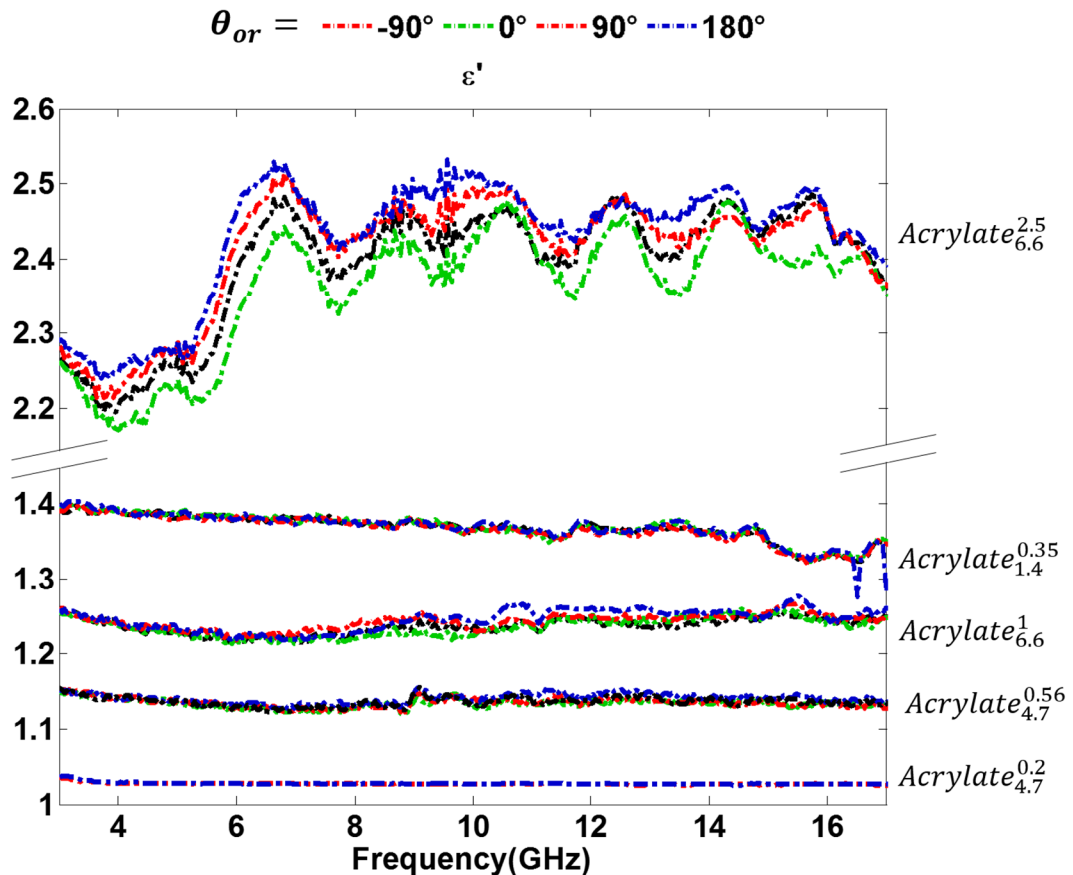


Figure 2.17 Real part of relative permittivity for the 5 meshed spheres presented in (Figure 2.16) as a function of the frequency. For each sphere, 4 permittivity determinations are made, corresponding to the 4 orientations of the sphere. The names of each sphere are written at the right hand side of the figure

For  $Acrylate_{6.6}^1$ , the determined values of  $\epsilon'$  are almost constant over the frequencies and the differences with respect to the orientations are negligible (I should mention here that the only difference between  $Acrylate_{6.6}^{2.5}$  and  $Acrylate_{6.6}^1$  is the cylinder's diameter which is reduced from 2.5 mm to 1 mm). The differences between experimental and simulated scattered fields for this sphere in Figure 2.19 are smaller than the case on  $Acrylate_{6.6}^{2.5}$ . They present good agreement in the forward scattering direction.

Yet, some differences can still be especially distinguished on the phase of the scattered field over the receiving angles beyond  $50^\circ$  and  $-50^\circ$  at 12 GHz and 16 GHz (Figure 2.19). As a result, the mesh size of 6.6 seems to not be ideal to obtain an equivalent homogeneous sphere. Moreover, cylinder diameters greater than 1 mm should be avoided.

The results obtained with the two previously presented spheres have encouraged us to explore new spheres with smaller mesh size as well as with smaller cylinder diameters. We have therefore manufactured the two spheres  $Acrylate_{4.7}^{0.56}$  and  $Acrylate_{4.7}^{0.2}$  whose properties

are shown in Figure 2.16. Two main challenges follow the manufacturing and the characterization of these spheres.

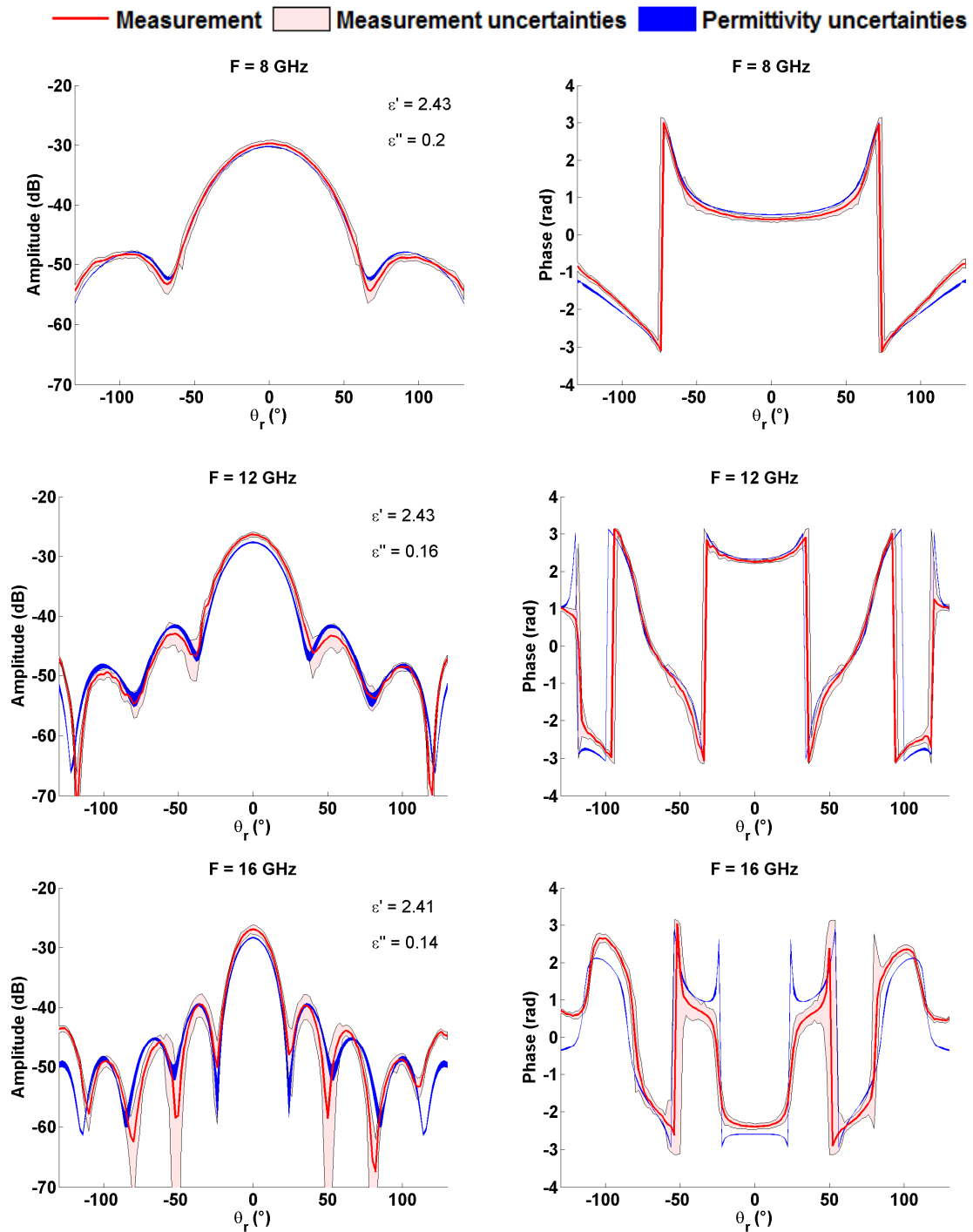


Figure 2.18 Amplitude and phase of the measured scattered fields by the meshed 35 mm diameter sphere Acrylate<sub>6.6</sub><sup>2.5</sup> with comparison to the Mie simulation of equivalent homogeneous sphere. The relative permittivity value corresponding to each frequency is shown. The presented measured fields result from an average over the 4 orientations

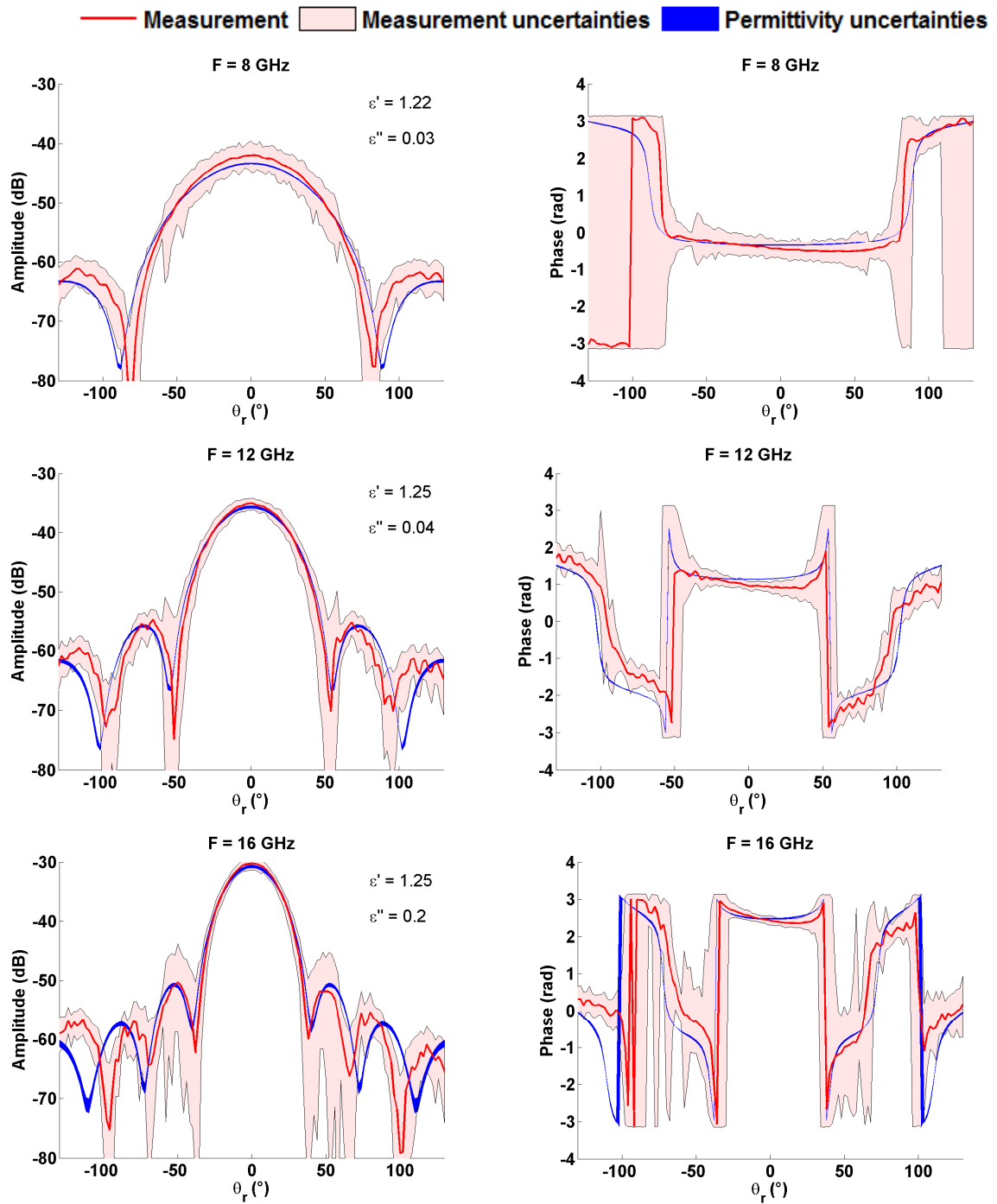


Figure 2.19 Amplitude and phase of the measured scattered fields by the meshed 35 mm diameter sphere Acrylate<sub>6,6</sub><sup>1</sup> with comparison to the Mie simulation of equivalent homogeneous sphere. The relative permittivity value corresponding to each frequency is shown. The presented measured fields result from an average over the 4 orientations

First, their cylinders diameters are quite small (0.56 mm and 0.2 mm respectively) which require high resolution of the 3D printer to avoid shrinking in the sphere. Second, they are mostly containing air (90% and 98% respectively) which correspond to predict real part of relative permittivities of 1.1 and 1.02 respectively. The measurement of such very low

scattering targets is extremely sensitive to the noise and experimental errors and the measurement uncertainties are high. Without the zones decompositions optimized configuration of the measurement setup (described in 1.7.5) it would have been impossible to measure their scattered fields. The measured  $\varepsilon'$  of these two spheres as a function of the working frequencies are shown in Figure 2.17. They present almost a constant value with respect to the frequency which is expected for such high porous materials and they have no differences with respect to the spheres orientations. The comparison between experimental and simulated scattered fields are shown in Figure 2.20 and Figure 2.21 for *Acrylate*<sub>4.7</sub><sup>0.56</sup> and *Acrylate*<sub>4.7</sub><sup>0.2</sup> respectively.

For *Acrylate*<sub>4.7</sub><sup>0.56</sup> and despite the noise affecting the experimental scattered fields, a good agreement is achieved at the three selected frequencies. The amplitude lobes from experiments and simulations have the same levels and the minima occur at the same angular positions. Moreover, the phases from experiments meet well the simulations even in the backscattering region over receiving angles back to  $-130^\circ$  and  $130^\circ$ . For *Acrylate*<sub>4.7</sub><sup>0.2</sup> the experimental scattered field are much noisier and the uncertainties are very high. The amplitude of the scattered field reaches very low values down to  $-100$  dB as shown on the simulation plots. From an experimental point of view, it is difficult to measure fields with amplitude below  $-80$  dB especially with the DRG wideband horn antennas, used in the measurement on these spheres, which are not highly directives (see section 1.4.5). Still, at amplitude above  $80$  dB the experimental scattered fields follow the same angular variation in amplitude and phase as the simulated ones.

As a result, the spheres with mesh size of  $4.7$  mm and with rather small cylinders diameter are equivalent to homogeneous spheres over the working frequencies. This meshing scheme represents the minimal limit in mesh size. However, the investigation of other spheres with the same mesh size but greater cylinders diameter (typically  $1$  mm) still worth verification to verify the impact of increasing the cylinders diameter on the homogenization of the sphere.

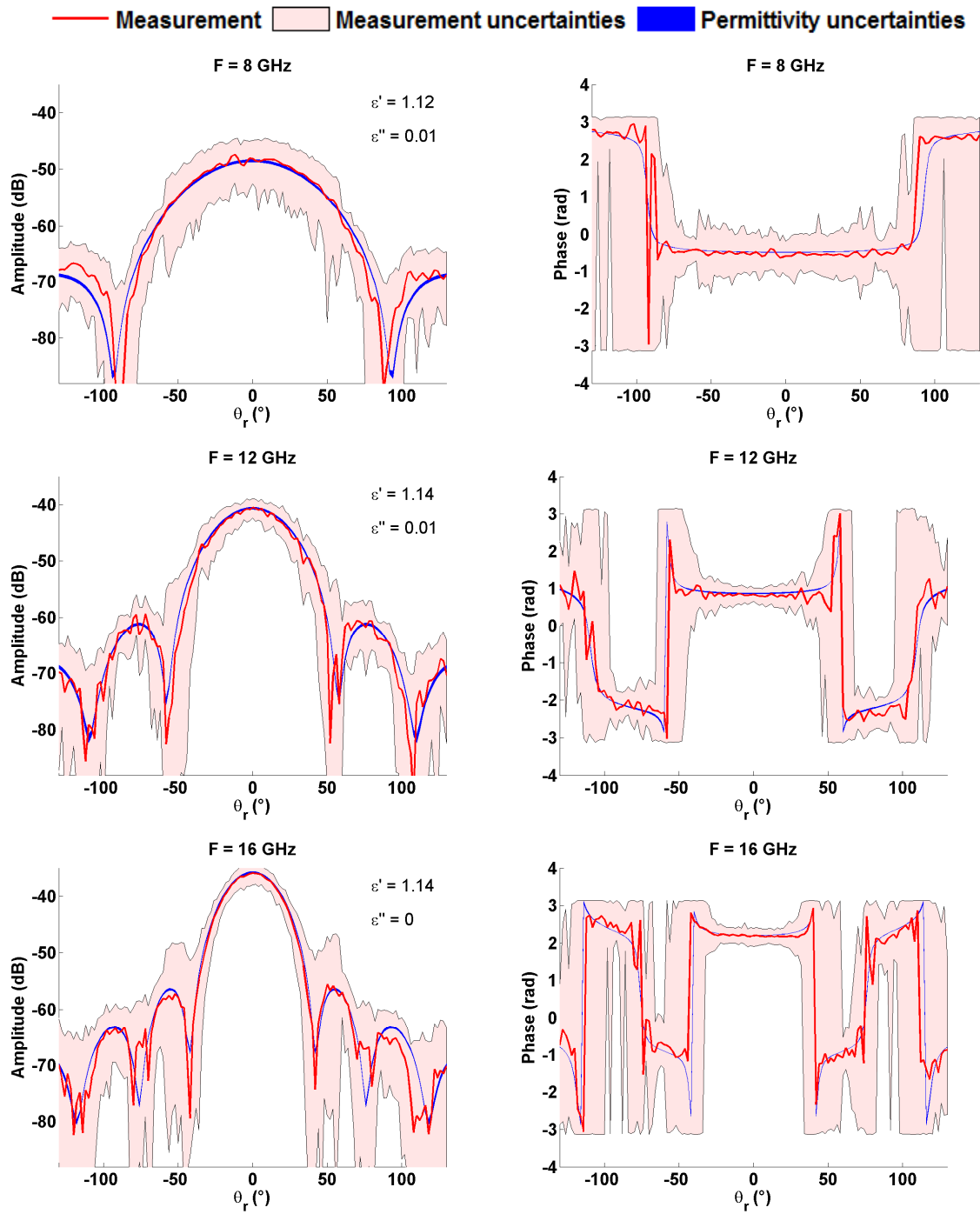


Figure 2.20 Amplitude and phase of the measured scattered fields by the meshed 35 mm diameter sphere Acrylate<sub>4.7</sub><sup>0.56</sup> with comparison to the Mie simulation of equivalent homogeneous sphere. The relative permittivity value corresponding to each frequency is shown. The presented measured fields result from an average over the 4 orientations



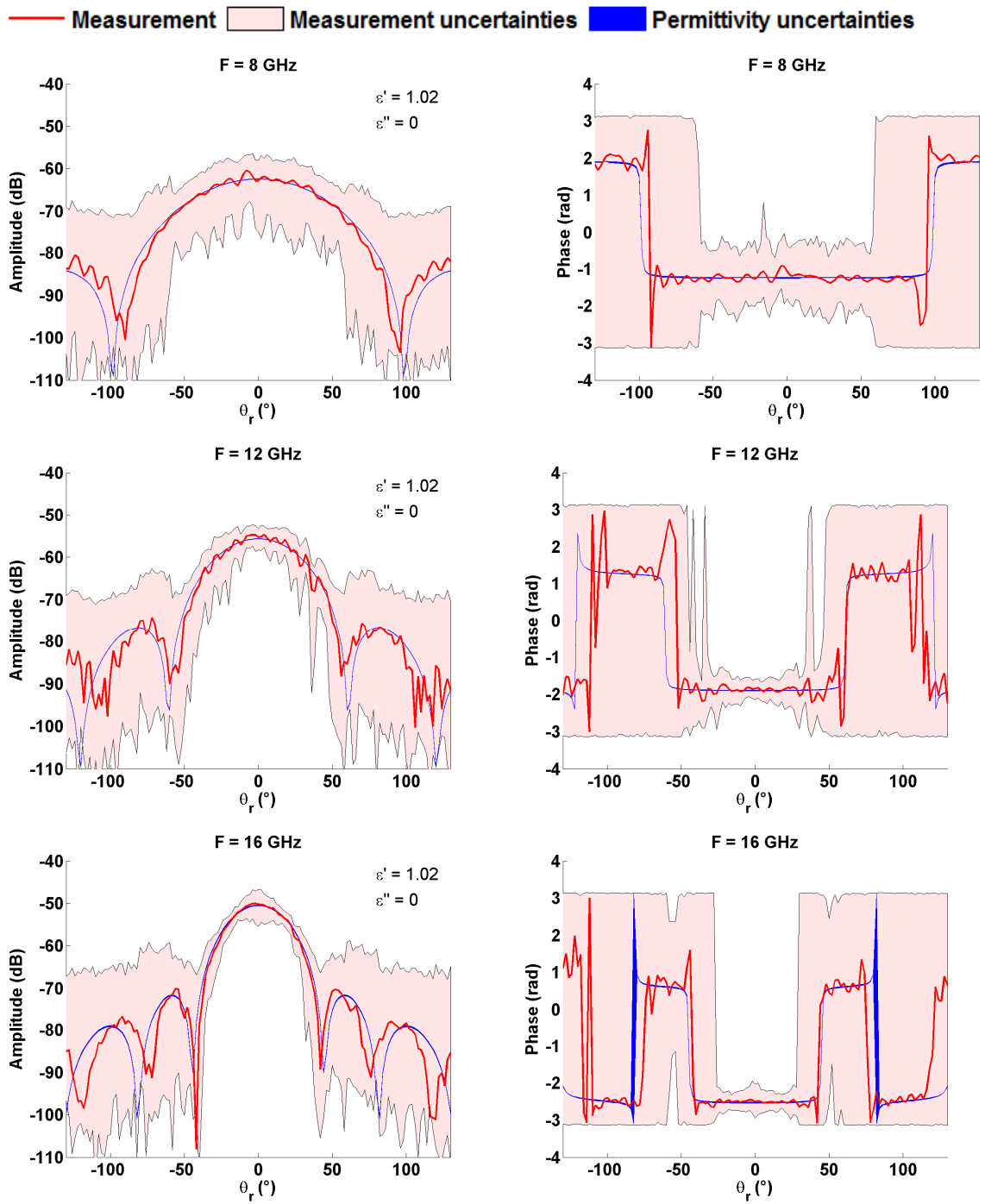


Figure 2.21 Amplitude and phase of the measured scattered fields by the meshed 35 mm diameter sphere Acrylate<sub>4.7</sub><sup>0.2</sup> with comparison to the Mie simulation of equivalent homogeneous sphere. The relative permittivity value corresponding to each frequency is shown. The presented measured fields result from an average over the 4 orientations

## 2.8 FABRICATION OF OBJECTS WITH HIGH PERMITTIVITY ( $\epsilon' > 3$ )

In this section, I focus on our fabrication and test of objects with high  $\epsilon'$ . I define a “high” value of  $\epsilon'$  the one that is greater than the conventional polymers, which are between 2 and 3. The bulk acrylate material used by the 3D printer of the CTTM has  $\epsilon'$  of 2.9 and

almost a null  $\epsilon''$ . The methodology we propose to fabricate lossless high  $\epsilon'$  analogs consists on developing composite mixtures through adding high  $\epsilon'$  particles to the acrylate resin. The control of  $\epsilon'$  of the final object in this case can be adjusted by selecting the type of additive and its percentage in the mixture. The typical additive candidates are the ceramics because they present higher  $\epsilon'$  than that of polymers and they have very low  $\epsilon''$ . Among the commonly used ceramics in additive manufacturing for hyperfrequency applications zirconia  $ZrO_2$  ( $\epsilon' = 31.2$  at 30 GHz) [83], alumina  $Al_2O_3$  ( $\epsilon' = 9.0$  at 10 GHz) [82] and barium titanate  $BaTiO_3$  ( $\epsilon' > 100$  at 10 GHz) [95].

It should be stressed that in most of the previously cited examples on the use of ceramics particles in the additive manufacturing of microwave components, the 3D printer parameters have been modified and adapted to the manufacturing of resins with high viscosity in stereolithography technology or specific filaments have been fabricated in material jetting technology. However, in our case the adaptation of the 3D printer for high  $\epsilon'$  objects (acrylate resin filled with high  $\epsilon'$  particles) is still under study and the tests will continue to enhance the process.

### 2.8.1 Use of alumina ceramic

The first ceramic candidate we chose is the alumina. Although it does not have very high  $\epsilon'$  (it is around 9 in the microwaves), but it is a lightweight material so that we can expect adding high percentages of it without being heavy for the printer's holding head.

#### 2.8.1.1 Meshed acrylate/alumina spheres

The early primary test on the manufacturing of acrylate + alumina mixture have been applied to a meshed sphere with 35 mm diameter, 6.6 mm mesh size and 1 mm cylinders diameter. Indeed, there is no interest to work on porous spheres when seeking high permittivity objects because the porosity will decrease the global  $\epsilon'$  of the object. Nevertheless, two reasons motivated us to apply the tests with additives on meshed spheres: first, to identify the maximum fractional volume of alumina we can add to an acrylate resin while avoiding heavy weight of the sphere. Second, to maintain a fast fabrication time with the 3D printer.

We began the testing process with a small percentage of alumina with 0.5 % of the global weight of the sphere. As long as the sphere is entirely manufactured, the alumina percentage is incremented in the resin and a new sphere is tested. Overall, we have manufactured meshed spheres with 0.5%, 1%, 5%, 10%, 20% and 50% of alumina. Some samples of the acrylate/alumina meshed spheres are presented in Figure 2.22.

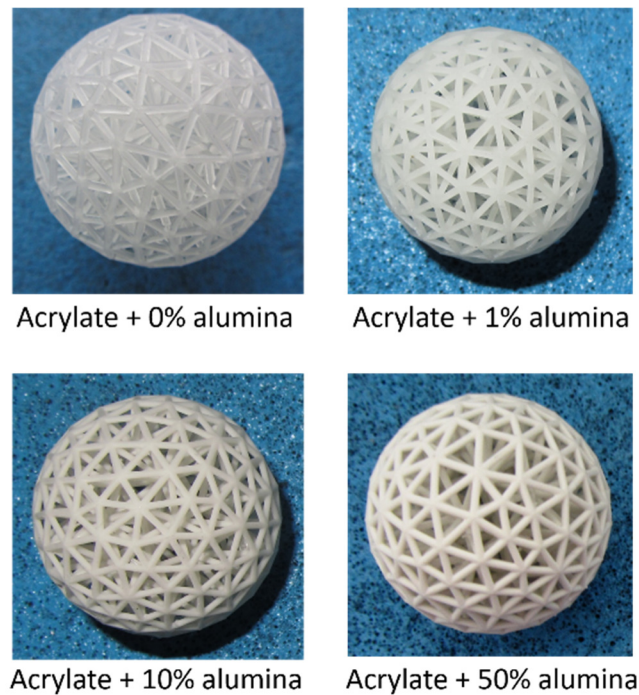


Figure 2.22 Some of the acrylate/alumina 35 mm diameter meshed spheres

The maximum percentage of alumina we were able to add is 50%. The fabrication process failed with higher percentages because the presence of alumina particles blocked the photopolymerization of the acrylate resin. The alumina particles have weak influence on  $\epsilon'$ . No variation on  $\epsilon'$  was noticed on the spheres with alumina between 0.5% and 10%. Compared to the sphere with 0% alumina with an average  $\epsilon'$  of 1.25, the one with 50% alumina has a  $\epsilon'$  of 1.3.

### 2.8.1.2 Full acrylate/alumina spheres

After the tests performed on the meshed spheres, the fabrication of full acrylate/alumina was attempted. Two full acrylate/alumina spheres were manufactured with a percentage of alumina of 10% and 20%. The maximum achievable percentage of alumina in the full spheres was 20%. The fabrication of spheres with higher percentage of alumina failed because the presence of alumina particles blocked the complete photopolymerization of the liquid resin and only few layers were successfully manufactured.

The determined relative permittivities of the two spheres are presented in Figure 2.23. Compared to  $\epsilon'$  of the pure acrylate sphere equal to 2.9, the alumina additives slightly increased  $\epsilon'$  in the sphere with 10% alumina to an average of 3.3 ( $\epsilon'$  decreases linearly with respect to the frequency from 3.4 at 3 GHz to 3.2 at 17 GHz). The behavior is quite similar with respect to the four orientations, although they present a difference around 0.1 (Figure 2.23-a). The sphere with 20% alumina presented  $\epsilon'$  of the same order of that of the sphere

with 10% alumina over the working frequency. However, the values of  $\epsilon'$  have periodic variations over the frequencies (Figure 2.23-b).

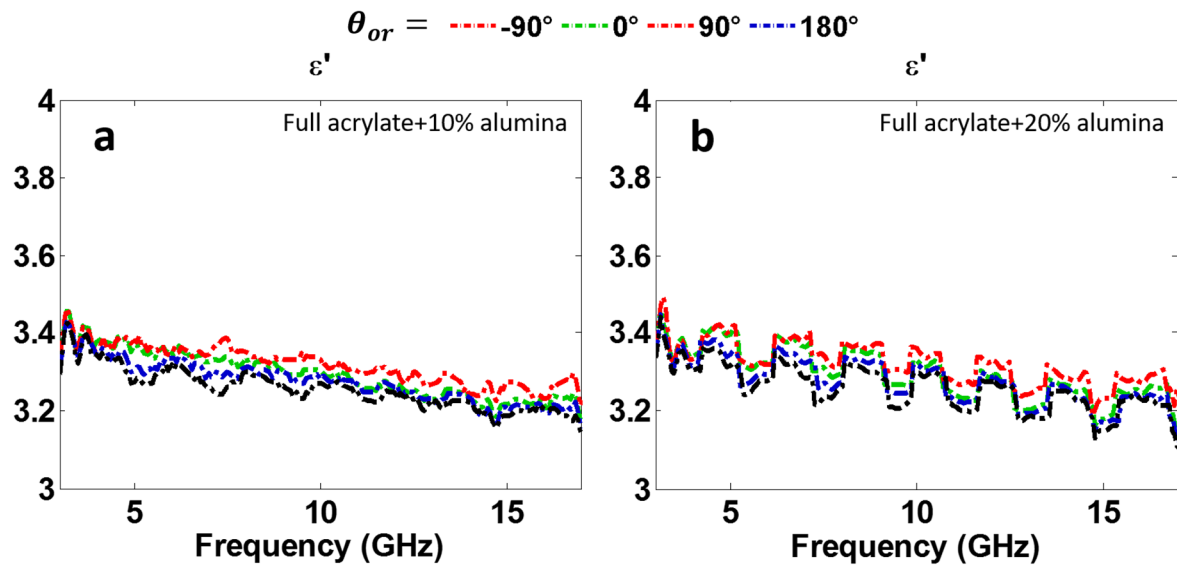


Figure 2.23 Real part of relative permittivity  $\epsilon'$  of the 2 full acrylate/alumina spheres a function of the frequency. For each sphere, 4 permittivity determination are made, corresponding to the 4 orientations of the sphere. (a) Acrylate+10% alumina. (b) Acrylate+20% alumina

It was difficult to understand the origin of this behavior since the acrylate+20% alumina sphere has some defects. After the manufacturing, the sphere showed many circular cracks in its body. The cause of those cracks may be the high weight of the (Figure 2.24). Those cracks made the sphere imperfectly spherical.

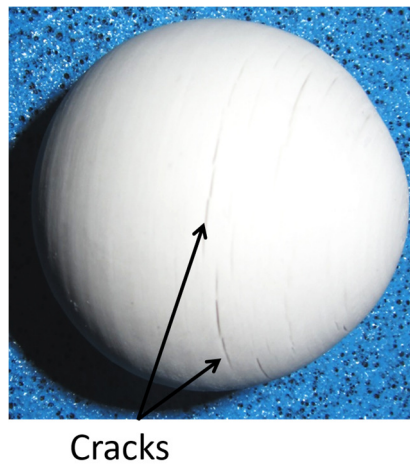


Figure 2.24 The 35 mm diameter acrylate/20% alumina. The cracks on the body of the sphere are indicated by the arrows

### 2.8.2 Use of barium titanate ceramic

The second ceramic we chose to obtain high  $\epsilon'$  is the barium titanate ( $\text{BaTiO}_3$ ). The literature indicates  $\epsilon'$  above 100 in the microwaves for this ceramic [95]. Unfortunately, our attempt to manufacture full acrylate +  $\text{BaTiO}_3$  particles failed because those particles are

heavy. Only the manufacturing of meshed acrylate spheres with 0.5%, 1% and 5% succeeded. However, their permittivity measurement showed no influence of the BaTiO<sub>3</sub> particles on the global  $\epsilon'$  of the spheres. The results are summarized in Tableau 2.1.

BaTiO <sub>3</sub> percentage	0 %	0.5%	1%	5%
$\epsilon'$	$1.25 \pm 0.01$	$1.25 \pm 0.01$	$1.27 \pm 0.01$	$1.22 \pm 0.01$

Tableau 2.1 Measured values of  $\epsilon'$  for the meshed spheres with BaTiO<sub>3</sub> particles at 16 GHz

## 2.9 FABRICATION OF LOSSY OBJECTS ( $\epsilon'' \neq 0$ )

Most of the work on the permittivity control for microwave applications focus on dielectric lossless composites (the control of the permittivity mainly addresses  $\epsilon'$  and consider a null  $\epsilon''$ ) or lossy materials to applications such as absorbers in the high hyperfrequencies [80]. However, when it comes to the microwave analogy, some particles of interest have a non-null imaginary part of permittivity. The straightforward example is the soot aggregate particles that are carbonaceous structures with non-negligible  $\epsilon''$  and the manufacturing of soot aggregates analogs require the work on lossy composites.

Our idea was to introduce conducting particles into the acrylate resin to increase  $\epsilon''$  of the final mixture. The use of meshed structures here is helpful because it will be possible to adjust  $\epsilon''$  through adding a convenient quantity of conducting particles but also to adjust  $\epsilon'$  through increasing or decreasing the porosity in the structure.

Two types of additives with high conductivity were selected: carbon micro-particles (C) and zinc oxide liquid (B-K3-5-ZnO<sub>10</sub>). Several resins have been prepared with different percentage of additives to realize spheres with the same geometrical parameters of *Acrylate*<sub>6,6</sub><sup>1</sup>.

Unfortunately, the manufacturing of composites with only 0.5% of additives succeeded. The manufacturing of composites with higher percent of carbon micro-particles either on meshed or full spheres failed during the material deposit because the illuminating laser couldn't reach all the acrylate liquid due to the presence of the black carbon particles (Figure 2.27). For the zinc oxide, this additive has been solidified as soon as it is introduced in the acrylate resin. Photos and properties of those spheres are presented in Figure 2.25. Their measured permittivities values are presented in Figure 2.26 and compared to those of the same sphere without additives.

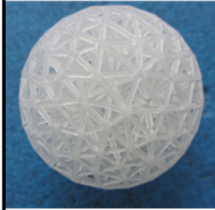
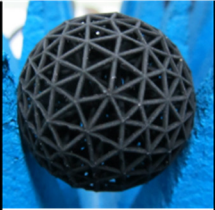

	Acrylate + 0 wt% additive	Acrylate + 0.5 wt% Carbone	Acrylate + 0.5 wt% Zinc oxide
			
Mesh size (mm)	6.6	6.6	6.6
Number of cylinders	804	804	804
Cylinders diameter (mm)	1	1	1
Density (Kg/m <sup>3</sup> )	204	224	157
Air volume percentage	83 %	83 %	83 %

Figure 2.25 Photos and properties of the manufactured meshed spheres with carbon and zinc oxide

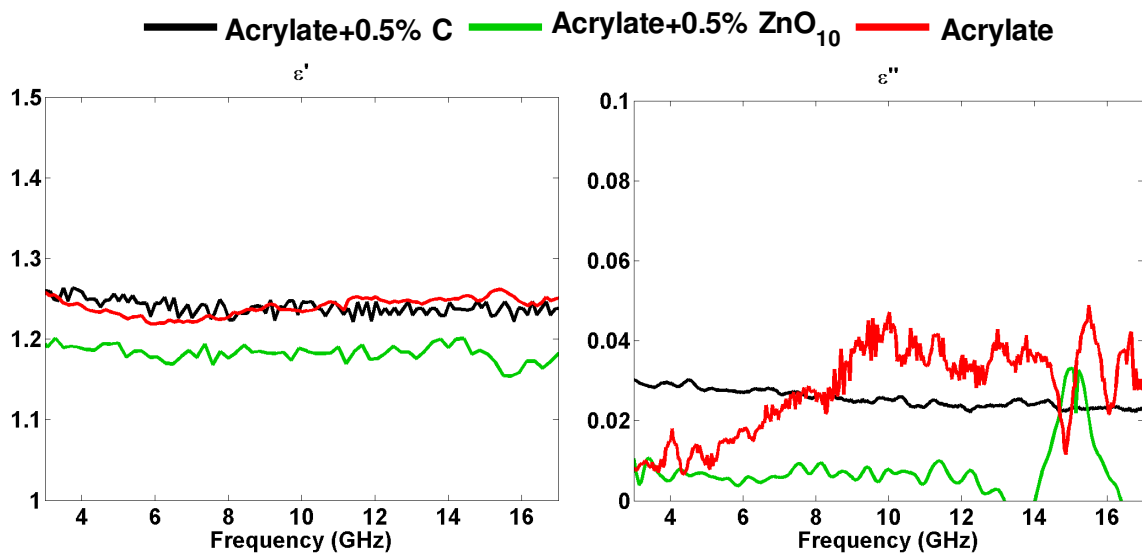


Figure 2.26 Relative permittivities of the spheres acrylate+0.5 % carbon, acrylate+0.5 % ZnO10 and Acrylate as a function of the frequency. The represented values for each sphere is an average of the permittivity over the 4 orientations. (a) Real part. (b) Imaginary part

The values of  $\epsilon'$  and  $\epsilon''$  clearly show that the 0.5% from the two additives has no influence on the electromagnetic properties of the spheres.  $\epsilon''$  remained almost null and  $\epsilon'$  is almost unchangeable for the sphere acrylate + 0.5% C.  $\epsilon'$  of the sphere acrylate + 0.5% ZnO<sub>10</sub> is slightly smaller (around 1.2) because the material density if the sphere is lower (see Figure 2.25).



*Figure 2.27 A failed attempt to manufacture a full acrylate with carbon spheres. Only a quart of the sphere was manufactured*

## 2.10 CONCLUSION

In this chapter, I presented our contribution to control the electromagnetic properties of analogs in stereolithography in the frame of our collaboration with the CTTM. Within this collaboration my role was to propose the way to create porous structures to obtain low  $\epsilon'$  analogs, such as the meshed structures, and to find from the literature the additives that might be included to obtain high  $\epsilon'$  analogs and lossy analogs. The role of collaborators at the CTTM is to prepare the mixtures and develop the manufacturing processes. Three categories were investigated in term of relative permittivity: objects with low permittivity ( $\epsilon' < 3$ ), objects with high permittivity ( $\epsilon' > 3$ ) and objects with non-null imaginary part of permittivity ( $\epsilon'' \neq 0$ ) where 3 is  $\epsilon'$  of the bulk acrylate material used by the 3D printer. The tests were realized on spherical samples for simplicity purposes and their complex permittivities were determined from far-field scattering measurements but objects with non-spherical and complex shapes can also be obtained.

For the low permittivity objects, the objectives were successfully achieved. We are now able to obtain targets with on demand low  $\epsilon'$  between 1 and 3, the principle consists on manufacturing objects with random porosity through creating meshed structures. The value of  $\epsilon'$  is decreased through decreasing the material density in the objects, and this latter is adjusted through selecting the convenient length and diameter of the meshes edges. Therefore, the meshed porous object is equivalent to a homogeneous medium. The realized tests reveal that there are limits in the choice of the edges diameters and lengths beyond which the structure is not homogenized. The smaller the mesh size, the more homogenized the object. At the same time, the objects with high number of meshes required long processing time to generate cylinders from the meshes edges. A trade off should be made between these two conditions

especially with large volume objects as it will be explained in section 3.3. Overall, the experiments on the manufactured spheres showed satisfactory results and low  $\epsilon'$  spheres down to 1.02 were obtained.

Furthermore, this technique was used to manufacture spheroidal analogs mimicking microorganisms with  $\epsilon'$  tending to 1.1 which were difficult to obtain using the classical machining techniques. The great novelty that brought such a technique is that we became able to obtain low permittivity spheroids with number of heterogeneities, where the difference in  $\epsilon'$  between the parts constituting the heterogeneous is slight, no more than 0.2. Such unobtainable before this thesis. These analogs were fabricated and their scattering was measured but still need to be compared with simulations (at that time).

For high  $\epsilon'$  objects, we proposed to add alumina and barium titanate ceramics to the acrylate resin. Unfortunately, the highest achieved value of  $\epsilon'$  was 3.3 with 20% of alumina. The fabrication of spheres with higher percentages of additives failed for different reasons:

1. The opacification of the resin after adding the additives, which requires longer irradiation time.
2. The viscosity of the resin which increases when the percentage of additives increases.
3. The fall of the additive particles of the resin to the ground of the vat. This falling is faster when the additives are heavier. At the early minutes of the fabrication, the vat becomes rich with particles and pull the sphere from its support.
4. The high weight of the sphere, that can make the sphere fabrication to fail, or can also create deformation of cracks in its shape.

Some propositions to overcome these difficulties are being investigated such as reducing the sizes of the particles, or using other anti-deposition particles. Moreover, as seen in the bibliography, other technologies of 3D printing such as FDM can may be tested.

For the lossy objects with non-null  $\epsilon''$ , tests with carbon and zinc oxide were realized on meshed spheres. Only low percentage of 0.5% of both of them allowed to manufacture complete spheres, which was negligible to increase  $\epsilon''$ . Works are actually in progress on copper conducting particles and the adaptation of the stereolithography process for higher permittivities will probably also help to increase the possible percentage. As said previously, there are also hopes to control the imaginary part in Material Extrusion technology. However, since that will need to fabricate the specific filaments for each material composite, it would be more interesting to succeed with stereolithography.



### 3 MICROWAVE ANALOG EXPERIMENTS IN BISTATIC CONFIGURATION

---

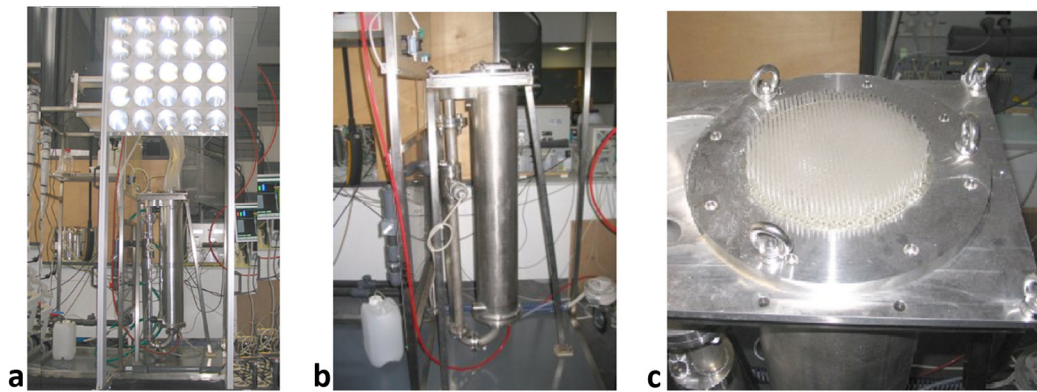
In this chapter, I present the performed bistatic scattering experiments throughout this PhD. Experiments are made to investigate scattering by microalgae analogs, silicon spheres analogs and soot particles analogs. This chapter is divided into three sections. For the summarized description of the motivations behind each of the three studies and the summaries on the results, the reader is referred to the individual introductions and conclusions of the sections.

#### 3.1 SPHEROIDAL LOW SCATTERING MICROALGAE ANALOGS

##### 3.1.1 Introduction

In this section, I discuss the implementation of microwave analog experiments on low scattering targets of very low permittivity. The motivation behind this research originated from the development of experimental devices dealing with visible light, called photobioreactors. This topic is a collaborative work with the research group *SIGMA* at Institut Pascal in Clermont-Ferrand in France whose main activity is the development of this technology. My contribution in this work was to use the microwave analogy to provide experiments on microalgae spheroidal analogs with  $\epsilon'$  tending to 1. The aim of the study is to investigate the lowest scattering targets that can be accurately measured with the setup of the CCRM, as a first step to use the microwave analogy in the future as a reference to validate approximate calculations. Experiments on analogs with  $\epsilon'$  below 2 has never been made before this thesis. My role was to propose the fabrication method of the analogs and to carry out the experiments. The rest of this introduction explains well the motivation behind this work.

The photobioreactors are technological devices within which it is possible to study the photosynthesis reactions on cultivated photosynthetic micro-organisms (Figure 3.1). The development of photosynthetic engineering is helpful in numerous research areas: biofuel production for green chemistry, mitigation of CO<sub>2</sub> emission in global warming studies, decontamination of wastewater and many others. This technology allows to optimize the photosynthesis mechanism through continuous tracking of the consumed amount of light energy. Therefore, the cornerstone in this field is the study of the radiative transfer in the aquatic microorganism suspensions [96]. This interest toward the determination of radiative properties of photosynthetic micro-organisms is not restricted to photobioreactors engineer but great interests exist also in oceanography.



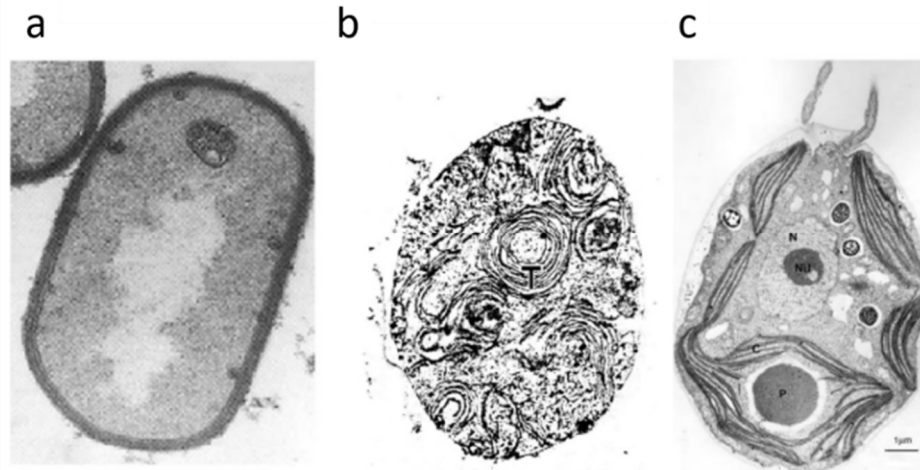
*Figure 3.1 A photo of the photobioreactor "DiCoFluV" developed at Institut Pascal in France. The incident solar radiations are captured and concentrated using Fresnel lenses shown on the upper side of (a). They are then driven to a reactor (b) using a huge number of fiber optics (c) [96]*

It has been proved that it is possible to derive the radiative transfer equations from Maxwell's equations under a certain number of assumptions [97]–[99], such as far-field scattering conditions, huge number of particles in the domain and some others conditions [100]. In photobioreactors and in oceans these conditions are standing and the problem can therefore be simplified to the resolution of an electromagnetic scattering [20], [27], [101], [102]. The photosynthetic microorganisms in aquatic medium are consisting up to 80% of water. Therefore, their electromagnetic contrasts are very close to that of their surrounding medium, hence their name “optically soft particles”. Their equivalent in free-space refers to a low  $\epsilon'$  material.

However, investigating electromagnetic scattering by optically soft particles represents a major challenge. On the one hand, many of them have dimensions much greater than the wavelength, which might lead to numerical difficulties with some complex shaped or strongly elongated scatterers with locally small radius of curvature [26], [103], [104]. On the other hand, they have low relative permittivities with weak electromagnetic signatures, which makes difficult their measurement in the optical domain due to the uncertainties and the high sensitivity to noise [6], [27].

However, micro-organisms have types of heterogeneities, sizes and shapes, for which the application of the usual numerical methods to solve the Maxwell equations can be impracticable in many cases. They can be very large compared to the wavelength with size-parameters ranging from  $1.5\lambda$  to  $30\lambda$  and they can be up to 50 times longer than wide. They also may have complex shapes and heterogeneities with sharp internal refractive index variations [20] as shown in Figure 3.2. Therefore, the use of electromagnetic approximations becomes necessary for studying many cultivated micro-organisms.

In this context, accurate microwave experiments on micro-organism analogs are a promising way to investigate the accuracy of the approximations, especially when no reference solution is available. Microwave analog experiments can particularly help in the two following cases:



*Figure 3.2 Diversity of photosynthetic microorganisms with different complexity in term of shape and refractive index. (a) A photosynthetic bacteria having three different refractive indices over the central part, the coat and the nucleus. (b) A cyanobacteria containing many cellular features with shape heterogeneity. (c) A microalgae with two nucleus and many other cellular features [20]*

### **1. Validation of the anomalous diffraction approximation**

Our collaborators of Institut Pascal utilize the anomalous diffraction approximation to solve the electromagnetic scattering problem of photosynthetic micro-organisms. However, no reference solutions are existing in order to evaluate the error made using this method. It is so far being compared to results obtained with Lorenz-Mie method on spheres but this validation doesn't take into account the shape of the object.

### **2. Validation of shape idealization**

Although the anomalous diffraction approximation allows to explore objects of ordinary shapes, it is much more practical to idealize the initial shape to a representative shape. For instance, it is easier to approximate the model of a spirulina to a straight cylinder, but this assumption needs also to be validated.

#### **3.1.2 Fabrication of spheroidal microalgae analogs**

The microwave analog experiments are good candidates to validate such an approximate model. However, the free-space microwave analogs of those micro-organisms have very low permittivity values, down to 1.1 in their real part. Such objects are considered very low scattering targets, the measurement of their scattered signal is very sensitive to all kind of

experimental errors. It is also non-trivial to manufacture precise analogs of complex shapes with low  $\varepsilon'$  values. Therefore, the aim of this study is first to assess the ability of the experimental setup of the CCRM to provide accurate measurements on targets with low  $\varepsilon'$ , with simple shapes and homogeneous structure, for which the numerical solutions are obtainable with Maxwell equations. When the efficiency of the experimental setup is validated, our goal is to only refer to it in the future for the assessment of the anomalous approximations for objects with complex shapes, large sizes in term of the wavelengths and even heterogeneous structures.

We decided to focus in this study on spheroidal scatterers. First, the spheroid corresponds already to the shape of a great number of microalgae species in photobioreactors engineering. Second, it is possible to obtain the computation of the scattered field for spheroids with the numerical methods we use: FEM and T-Matrix.

The typical microalgae have size-parameters  $x$  ranging between 5 and 200. Their aspect ratio  $R$  can be as low as 0.02. The size-parameter  $x$  is defined as  $\frac{2\pi r_{eq}}{\lambda_e}$  where  $r_{eq}$  is the radius of the equivalent sphere in volume and  $\lambda_e$  is the incident wavelength. The aspect ratio  $R$  is the ratio between the horizontal axis and the axis of revolution of the spheroid. It is inversely proportional to the spheroid's elongation. We have chosen two types of spheroids: the first one has a quasi-spherical shape, where the other is more elongated. Their characteristics and names are summarized in Table 3.1. The size-parameters and the elongation have been chosen to allow a reasonable computation time with FEM and T-Matrix.

Shape	Name	Size-parameter $x$	Aspect ratio $R$	Wavelength	Frequency
Quasi-spherical	Hardy	14	0.8	16.7 mm	18 GHz
Elongated	Laurel	5.4	0.2	16.7 mm	18 GHz

Table 3.1 Characteristics of the chosen analogs

The microalgae are suspended in water that constitutes up to 80 % of their compositions. They have low contrasts compared to their embedding medium. They have, with respect to their medium, relative permittivities of real part between 1.04 and 1.21 and a very low imaginary part ( $\varepsilon'' < 10^{-4}$ ). Materials with such electromagnetic properties are mainly containing air in the microwaves and they are difficult to be accurately manufactured in desired shapes. Therefore, we decided to choose a non-absorbing material ( $\varepsilon'' = 0$ ) with the lowest obtainable real part of permittivity. The chosen bulk material for machining the spheroidal analogs is rigid polyurethane foam that is commercially available in different bulk densities. Three different densities were selected: 200 Kg/m<sup>3</sup>, 300 Kg/m<sup>3</sup> and 400 Kg/m<sup>3</sup>. From each of

them, one Laurel and one Hardy of identical shapes were machined. In addition, one sphere was machined from each of the three foams in order to determine its relative permittivity using the method detailed in section 2.6. The relative permittivities of the six spheroids are summarized in Table 3.2 and their photos are shown in Figure 3.3.

Name of the spheroid		Bulk density	Relative permittivity $\epsilon$
Laurel <sub>1.45</sub>	Hardy <sub>1.45</sub>	400 Kg/m <sup>3</sup>	1.45 + 0j
Laurel <sub>1.39</sub>	Hardy <sub>1.39</sub>	300 Kg/m <sup>3</sup>	1.39 + 0j
Laurel <sub>1.29</sub>	Hardy <sub>1.29</sub>	200 Kg/m <sup>3</sup>	1.29 + 0j

Table 3.2 Names, material density and permittivity of the spheroidal analogs

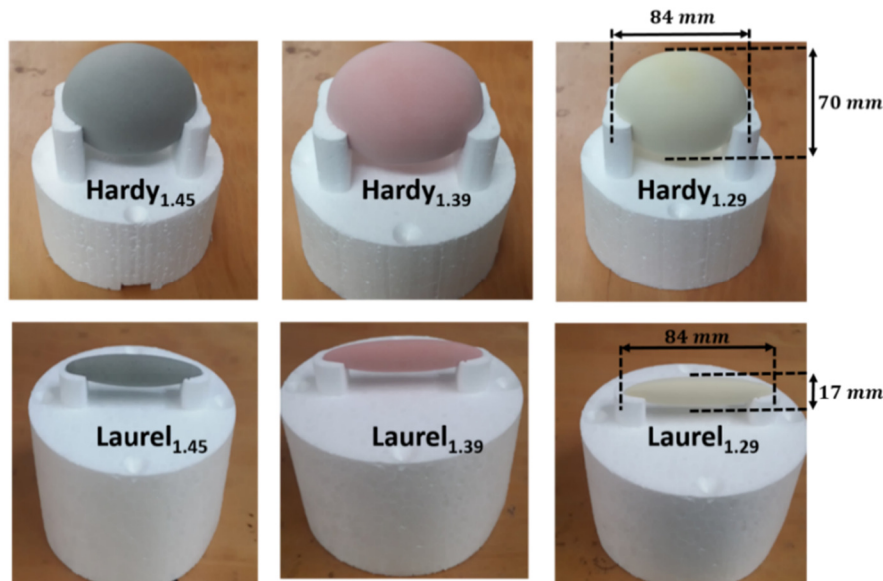


Figure 3.3 Photography of the machined spheroidal analogs

### 3.1.3 Measurement protocol

The measurements were made at 18 GHz, which is the highest reachable frequency with the experimental setup, with the K-band horn antennas in VV and HH polarizations. They are made in Hardgating mode. The choice of this frequency together with the choice of the spheroids dimensions were selected to have the desired size-parameters. Two holders made of expanded polystyrene of permittivity around 1.03 [105] were especially fabricated for the positioning of the spheroids to insure an accurate alignment. The measurements were carried out in the azimuthal plane with a fixed position of the source at  $\theta_s=90^\circ$  and with receiving angles  $\theta_r$  between  $-130^\circ$  and  $+130^\circ$  (Figure 3.4). Since the spheroids are axisymmetric, three orientations of the spheroids are selected using the central rotating mast:  $\theta_{or} = 0^\circ$ ,  $45^\circ$  and  $180^\circ$  (Figure 3.5). The used configuration of the measurement setup for the measurement of the microalgae analogs is summarized in Figure 3.6.

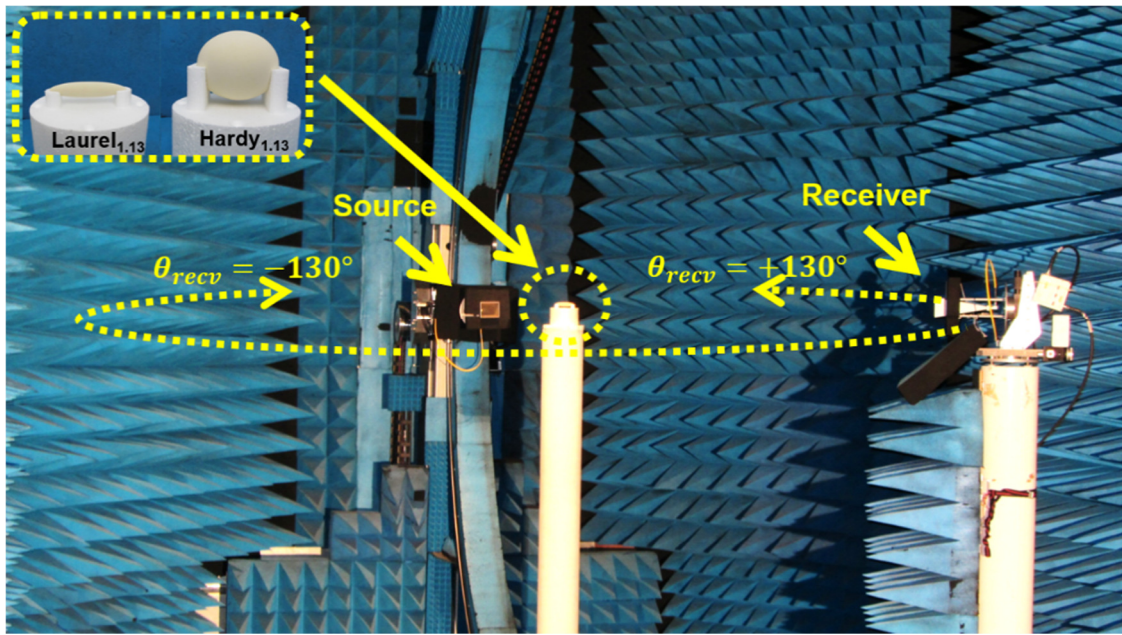


Figure 3.4 Measurement of the spheroidal analogs in azimuthal bistatic configuration

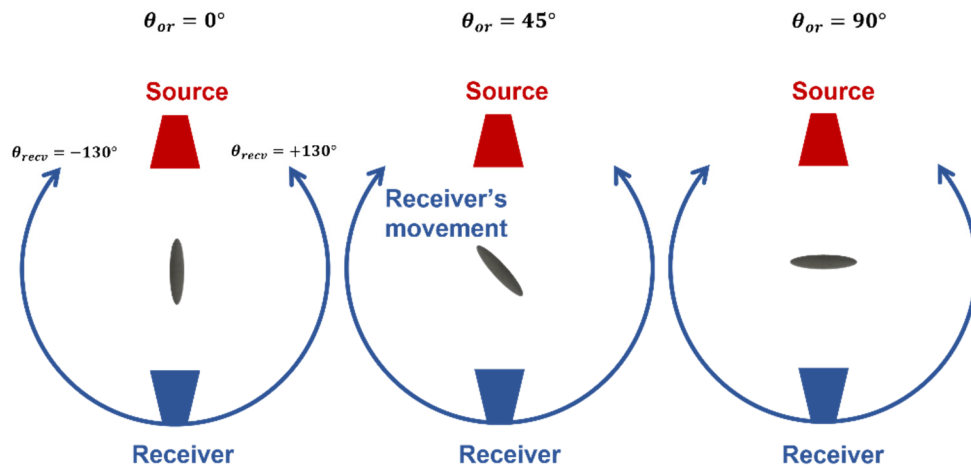


Figure 3.5 Schematics of the scattering configurations seen from the top showing the three studied orientations on the spheroids

### 3.1.4 Numerical simulations

Two calculation methods have been used to validate the measurements: T-Matrix and Finite Element Method (FEM). T-Matrix is a numerical method based on functional decomposition. It has been used in this work with a freely available code [15]. The input parameters to this code are the wavelength, the refractive-index, the aspect ratio, the radius of the equivalent sphere in volume and the incidence angle and the receiving angles. The FEM has been applied using a “homemade” code which is not limited to regular and small domains, but it is applicable to complex shapes.





This software is applied to the weak form of the Helmholtz equation based on a scattered field formulation of the problem [35]. The electric field is expanded onto linear edge basis functions related to the edges of tetrahedrons generated by a free unstructured mesh generator. The whole domain is discretized with a characteristic length equal to  $\lambda/15$  yielding a linear system with more or less 900,000 unknowns with the selected targets. The obtained linear system is solved with a direct solver or with a domain decomposition technique.

### 3.1.5 Scattering over the full angular range

Figure 3.7 shows the amplitudes and the phases of the fields scattered by Hardy<sub>1.29</sub> and Laurel<sub>1.29</sub> in VV polarization at  $\theta_{or} = 45^\circ$  (see the middle schematic of Figure 3.5). These two spheroids have the lowest permittivity among the studied ones, therefore they are the least scattered ones and they have the highest sensitivity to experimental errors (and they may have potential interactions with the polystyrene holders). Furthermore, their orientation at  $45^\circ$  leads to low amplitudes over the angular range between  $50^\circ$  and  $130^\circ$ . As it can be seen on the figure, the experiments are in a good agreement in amplitude and phase with the two simulations obtained with FEM and T-Matrix over the full angular range. From Figure 3.7-a and Figure 3.7-b all the lobes of the experimental scattered field are identified and the measurement is precise even at low amplitude levels, down to -80 dB. The amplitudes of the fields scattered by Hardy<sub>1.29</sub> present higher levels than those of the fields scattered by Laurel<sub>1.29</sub>. In the forward scattering direction at  $\theta_{or} = 0^\circ$ , the amplitude of the field scattered by Hardy<sub>1.29</sub> is around 20 dB higher than that of the field scattered by Laurel<sub>1.29</sub>, because Hardy has a larger volume (the size-parameter of Hardy is 14, which is 2.6 times that of Laurel). The amplitude of the field scattered by Hardy<sub>1.13</sub> has a dynamic range around 50 dB, where that of Laurel<sub>1.13</sub> is around 60 dB. This is related to the low aspect ratio of Laurel<sub>1.13</sub> which leads to a scattered signal of relatively low amplitude in the backward directions.

It is worthy to shed light on the spikes appearing on the phase plots of the experimental and simulated fields from Laurel<sub>1.29</sub> in Figure 3.7-c. These spikes occur on the receiving angles at which the amplitude of the scattered field in Figure 3.7-a reaches a minimum. This behavior is a mathematical artifact that makes the phase easily undergo rotations between  $-\pi$  and  $\pi$  when the amplitude is very low, hence it is absent on the phases from Hardy<sub>1.29</sub> in Figure 3.7-d. As a matter of fact, the particular geometric and electromagnetic properties have made the measurements of the fields scattered by Laurel<sub>1.29</sub> more challenging than those scattered by Hardy<sub>1.29</sub>, especially in the backward region. The quasi-constant phase of the field scattered by Laurel<sub>1.29</sub> (around 1 radian) over the receiving angles between  $-25^\circ$  and  $-100^\circ$  in Figure



3.7-c is related to the spheroid's orientation since at these receiving angles the receiver is facing the largest surface of the target. This is also the reason behind the wide lobe on the amplitude in Figure 3.7-a.

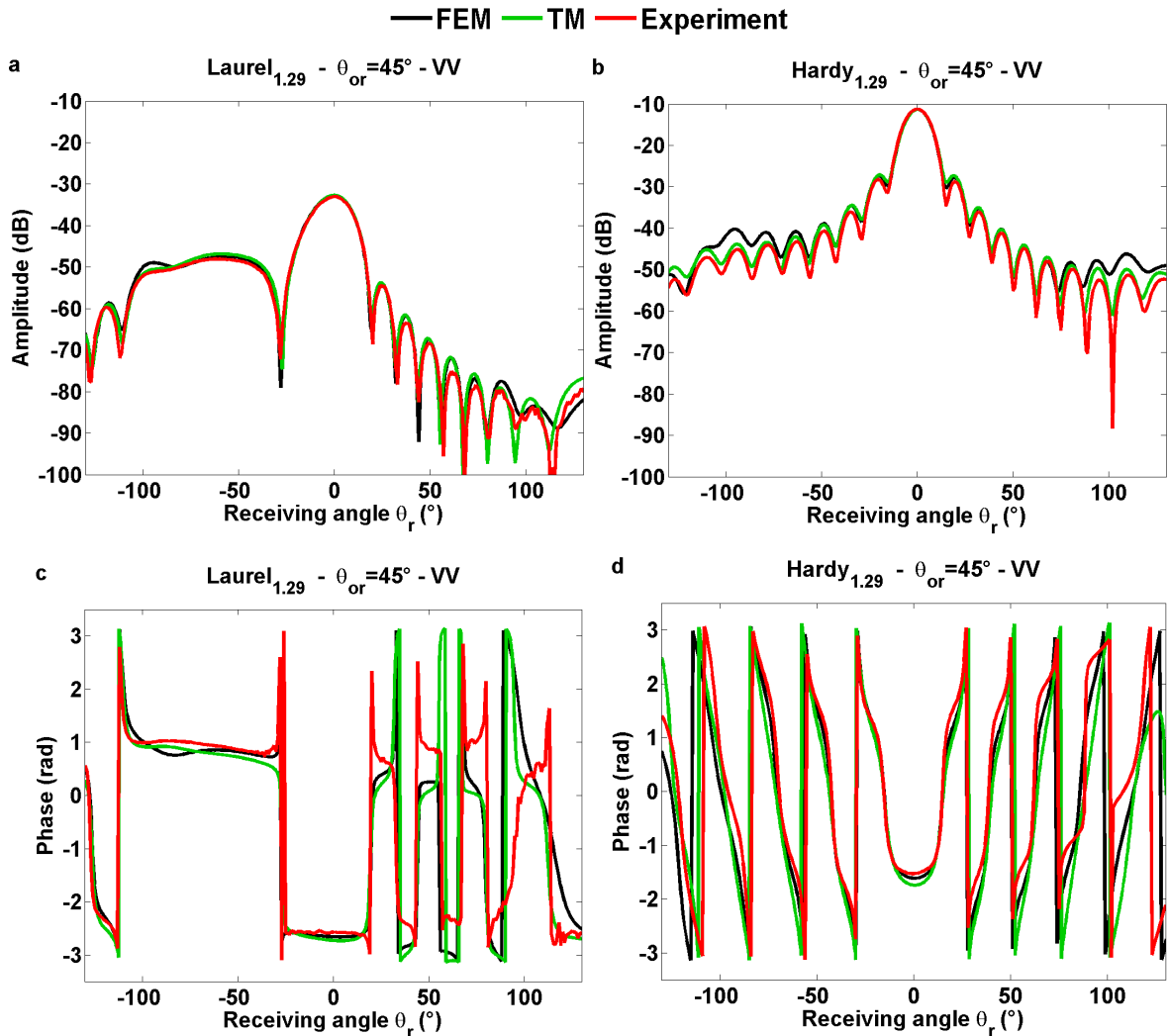


Figure 3.7 Experimental and simulated scattered fields from Laurel<sub>1.29</sub> and Hardy<sub>1.29</sub> as a function of the receiving angles at  $\theta_{or} = 45^\circ$  in VV polarization. (a) Amplitude of the field scattered by Laurel<sub>1.29</sub> in dB. (b) Phase of the field scattered by Laurel<sub>1.29</sub> in radian. (c) Amplitude of the field scattered by Hardy<sub>1.29</sub> in dB. (d) Phase of the field scattered by Hardy<sub>1.29</sub> in radian

When comparing the scattered fields with respect to the orientation, we can clearly notice the influence of the spheroid's shape. The width of the forward lobe is inversely proportional to the length of the target's face illuminated by the incident wave. For instance in the case of Laurel<sub>1.29</sub> at  $\theta_{or} = 90^\circ$  (Figure 3.8-b), the wave incident from the source is facing the spheroid on its long surface, in this case Laurel strongly scatters the energy in the forward direction, hence the narrow main lobe (around  $30^\circ$ ). For  $\theta_{or} = 0^\circ$ , however, the incident signal illuminates the spheroid "on the nose" and the forward lobe broadens to around the double ( $60^\circ$ ). For Hardy<sub>1.29</sub>, and since it has a quasi-spherical shape, the spatial distribution of the

scattered energy is quite similar between  $\theta_{or} = 0^\circ$  and  $\theta_{or} = 90^\circ$  (Figure 3.8-c and Figure 3.8d).

The distinguished asymmetry on the amplitude and phase obtained with Laurel are due to its elongated shape (low aspect ratio). However, on Hardy the asymmetry is negligible because it is quasi-spherical.

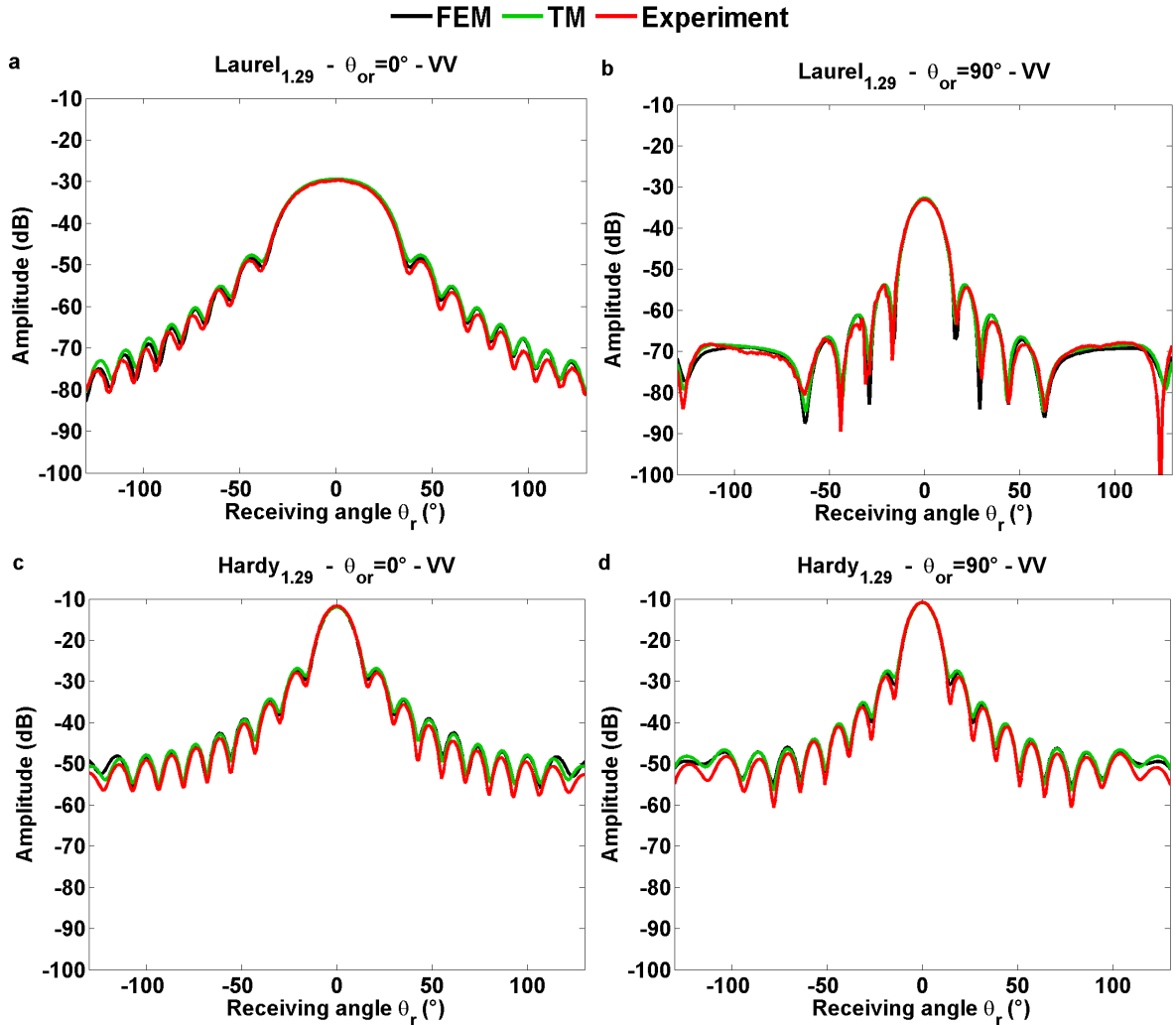


Figure 3.8 Experimental and simulated scattered fields from  $Laurel_{1.29}$  and  $Hardy_{1.29}$  as a function of the receiving angles at  $\theta_{or} = 0^\circ$  and  $\theta_{or} = 90^\circ$  in VV polarization. (a), (c) Amplitude of the fields scattered by  $Laurel_{1.29}$  in dB at  $\theta_{or} = 0^\circ$  and  $\theta_{or} = 90^\circ$  respectively. (b), (d) Phase of the fields scattered by  $Laurel_{1.29}$  in radian at  $\theta_{or} = 0^\circ$  and  $\theta_{or} = 90^\circ$  respectively

### 3.1.6 Measurement uncertainties related to the random noise

The uncertainties on the experimental scattered field are determined from the uncertainties on the total and incident fields. It has been discussed in section 1.7 that the measurement accuracy is mainly dependent on the amplitude level of the measured signal. This amplitude is dependent upon settings of the measurement setup (source power, amplification, attenuation, etc.) and the gain and the directivity of the antennas on the working frequency.

Obviously, when the antennas are facing each other (forward scattering region) the amplitude of the received signal is high and the error is low. For the total field, in addition to the same aforementioned criteria, the additional parameter to the measurement uncertainties is the capacity of the target to scatter the electromagnetic radiation. The higher scattering the target is, the lowest the uncertainties are.

Two parameters can govern the accuracy of the experimental scattered field: the absolute amplitude of each of the incident and total field and the difference between these two fields. For instance, in Figure 3.9 the total and incident fields have quite comparable values in the forward direction (receiving angle between  $-50^\circ$  and  $50^\circ$ ). The total field has a type of oscillation around the incident field. Within this angular range, the amplitude of the total field is greater than  $-50$  dB and for such amplitude values the best measurement accuracy is achieved (see Figure 3.11).

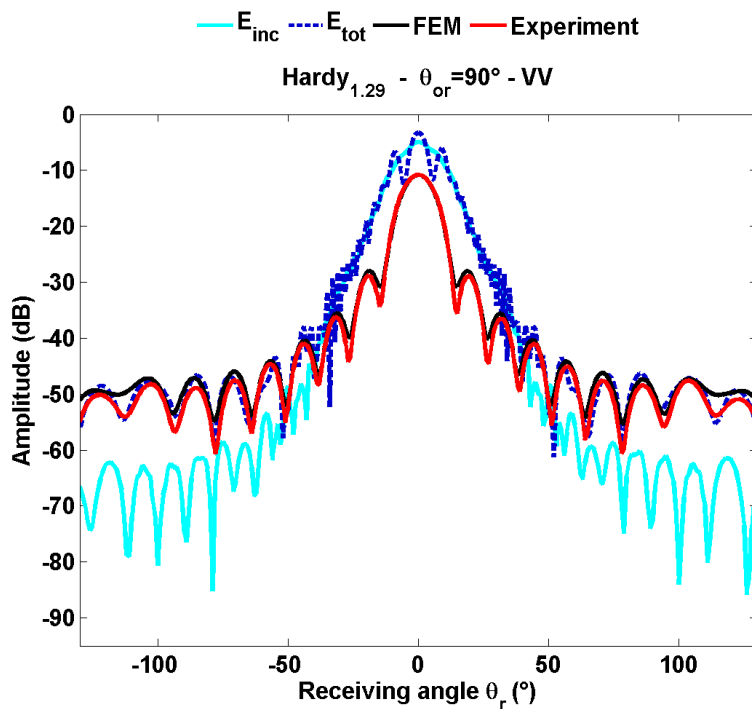


Figure 3.9 Experimental scattered fields from  $Hardy_{1.29}$  in VV polarization at  $\theta_{or} = 90^\circ$  with respect to the amplitudes of the incident and total field

In the near backward region, for  $\theta_r$  beyond  $\pm 50^\circ$ , the total field becomes lower but also begin to have an important deviation from the incident field (a difference between 10 dB and 20 dB). This non-trivial difference between the total and incident field makes enough precise the extraction of the information from the total field. It is noticeable that, typically for the receiving angles around  $-100^\circ$ , the scattered field is almost nothing but the total field itself. The amplitude of the total field of  $Hardy_{1.29}$  varies overall between  $-55$  dB and  $-5$  dB which

allows to achieve according to the uncertainties scheme in Figure 3.11 an error around  $10^{-3}$  dB. As a result, an accurate and non-noisy measurement is obtained with this spheroid, although it presents some discrepancies compared to the FEM simulation but these discrepancies are mostly referred to permittivity uncertainties.

In the case of Laurel, since it has smaller size-parameter than that of Hardy, it has weaker scattering and the uncertainties on its measurement are higher. In order to emphasize the influence of the two aforementioned parameters governing the accuracy of the experiment we compare in Figure 3.10 the scattering by Laurel<sub>1.29</sub> in VV and HH polarizations.

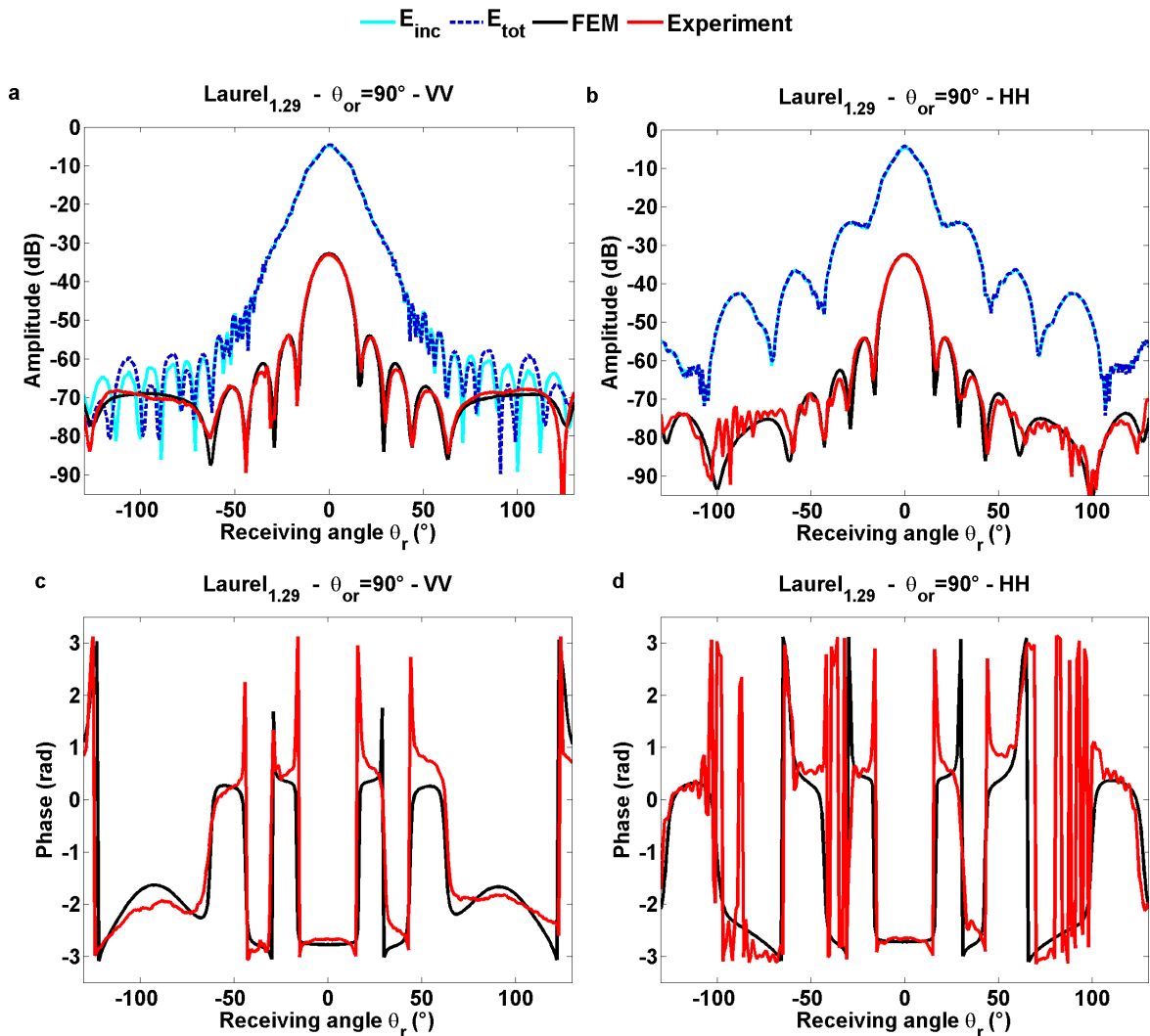


Figure 3.10 Comparison between experimental scattered fields from Laurel<sub>1.29</sub> in VV and HH polarizations at  $\theta_{or} = 90^\circ$  with respect to the amplitudes of the incident and total field. (a) Amplitudes of the incident, total and scattered fields in VV. (b) Amplitudes of the incident, total and scattered fields in HH. (c) Phase of the scattered field in VV. (d) Phase of the scattered field in HH. The incident and total field are compensated by the same calibration coefficient applied on the scattered field

In the forward scattering region for both polarization cases the behavior is almost the same as for Hardy<sub>1.29</sub> the total and incident fields have quite comparable levels higher than -

50 dB and good accuracy is achieved. In the backscattering region, we can distinguish an accuracy difference between the measurement in VV (Figure 3.10-a and c) and that in HH (Figure 3.10-b and d).

Typically, in the angular range from  $\pm 100^\circ$  and  $\pm 60^\circ$  the HH experiments are noisier in amplitude and phase than those in VV. Over that angular range on the experiments in VV polarization incident field has low amplitude between -80 dB and -60 dB. The total field has an amplitude of the same order because the scattered field is low (around -70 dB). The total field is associated with a rough increase on the uncertainties (green color on Figure 3.11). However, it is still possible to identify the spheroid's scattering contribution to the total field where this latter fluctuates around the incident field and as a result it was possible to obtain a precise measurement of the scattered field in amplitude and phase. In HH polarization, the antennas are less directive and the incident field amplitude is around 20 dB higher than that of the VV polarization over the same backscattering region between  $\pm 100^\circ$  and  $\pm 60^\circ$ .

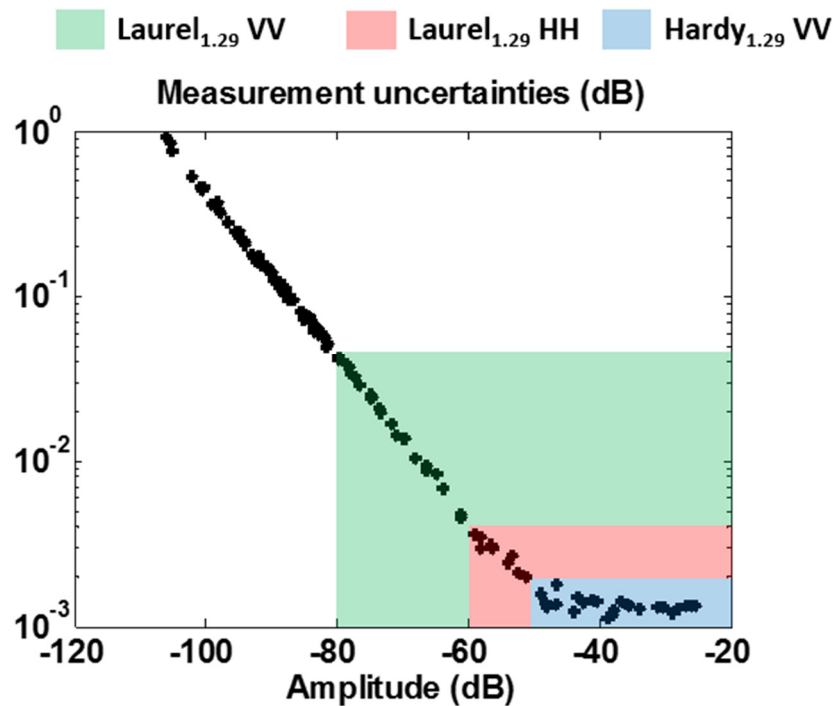


Figure 3.11 Uncertainties on the measurement of the electric field (incident and total) for *Laurel*<sub>1.29</sub> and *Hardy*<sub>1.29</sub> in VV and HH polarizations as a function of the amplitude

Although in this case the measurement uncertainties are lower than the case of VV as shows the red square on Figure 3.11, the experimental scattered field is quite erroneous in amplitude and phase and the noise is appearing in the form of fast oscillations. This difficulty

in extracting the scattered field is due to the high similitude between the total and incident fields.

### 3.1.7 Conclusion

In this part microwave analogy was used to investigate the electromagnetic scattering with spheroidal homogeneous objects of low permittivity. Two spheroids with different aspect ratios, one elongated and one quasi-spherical, were studied and each of them in three different copies corresponding to different values of  $\varepsilon'$ . Here I focused on the results obtained with the spheroids with the lowest permittivity  $\varepsilon' = 1.29$ . The spheroids were manufactured from low densities rigid polyurethane foams. The experimental results were confronted to numerical simulations obtained with two different computational methods: FEM and T-Matrix. Measured and simulated scattered fields were compared in intensity and phase. As expected, the accuracy of the scattered field determination is related to the measured signals levels which are dependent on the object's size-parameter and permittivity. As the targets are soft, the measurements were quite sensitive to noise and to measurement errors. The study shows that the incident and total fields are quite comparable, hence the high vulnerability in extracting the scattered field from their subtraction. However, the use of the Hardgating system, the use of high gain antennas and the choice of an optimal configuration for the measurement setup, have all allowed to obtain a good agreement between the experiment and the two numerical simulations. The obtained results from this work were the core of the scientific publication in [74].

Meanwhile, the challenge in the perspectives of this work is to fabricate low permittivity analogs with complex shapes and/or with heterogeneities. Such a problem is difficult to solve with the classical machining methods. In the light of this challenge, we take benefit from the work on the shape and permittivity control in additive manufacturing within the collaboration with the CTTM to widen the selection of photosynthetic micro-organisms for microwave analog experiments.

Recently, we have manufactured the same Hardy and Laurel but in a mesh structure according to the method in 2.7 with estimated values of  $\varepsilon'$  down to 1.15, which was impossible to obtain from foams machining. Moreover, in order to investigate heterogeneous analogs, three different copies of Hardy were also manufactured with a difference in  $\varepsilon'$  between the outer part and the inner part of the spheroid. These spheroids are a promising application of the work on the permittivity control with the CTTM. Their experimental exploration is in progress and it will be the core of a scientific publication.

## 3.2 HIGH REFRACTIVE INDEX DIMER

### 3.2.1 Introduction

This section addresses the implementation of microwave analog experiments on High Refractive Index HRI spheres with diameter smaller than the wavelength. This topic is a collaborative work with researchers from the group of optics in the department of applied physics at the University of Cantabria in Spain, who have developed the theoretical part of the work. My contribution is to experimentally proof that with a dimer of two high  $\epsilon'$  sub-wavelength particles, it is possible to obtain a perfect switching effect (ON and OFF output states) through controlling the polarization of the incident signal, as a consequence of the mutual electric and magnetic interactions of the particles. The work shows that small dielectric HRI spheres can be proposed as new multifunctional elements for building optical devices and opens an extra way to control the directionality of the scattered light. The experiments were validated by numerical simulations provided by the partners at the University of Cantabria and the issued results from this collaborative work were published in the Nature Communications journal [75].

### 3.2.2 Motivation and background

Scattering by particles smaller than the wavelength of the incident radiation in optics is one of the most active research branches in electromagnetic interaction with matter. It has undergone vigorous investigations leading to applications in areas related to health, material analysis, communications, and others [106]. For metal particles and despite their strong response like gold and silver in infrared and visible spectral ranges, their inherent ohmic losses make them less attractive for some particular applications, among which those concerning optical communications [107]. High-refractive-index (HRI) dielectric particles with low absorption have been proposed as an interesting alternative to overcome the losses with metal particles. Some of their most important advantages are related to the fact that light can travel through them without being absorbed and their compatibility with well-known technologies as they can be made with either classical pure semi-conductors like silicon [108]–[110] and germanium or semiconductor compounds. Moreover, they can be designed to control the direction of the scattered radiation. In a previous work [12], microwave analog experiments were made to reveal specific conditions in electromagnetic scattering by a single HRI sphere, known as Kerker conditions [111], under which scattered radiation can be concentrated either in the back or forward scattering regions through varying the wavelength on the incident beam (Figure 3.12).

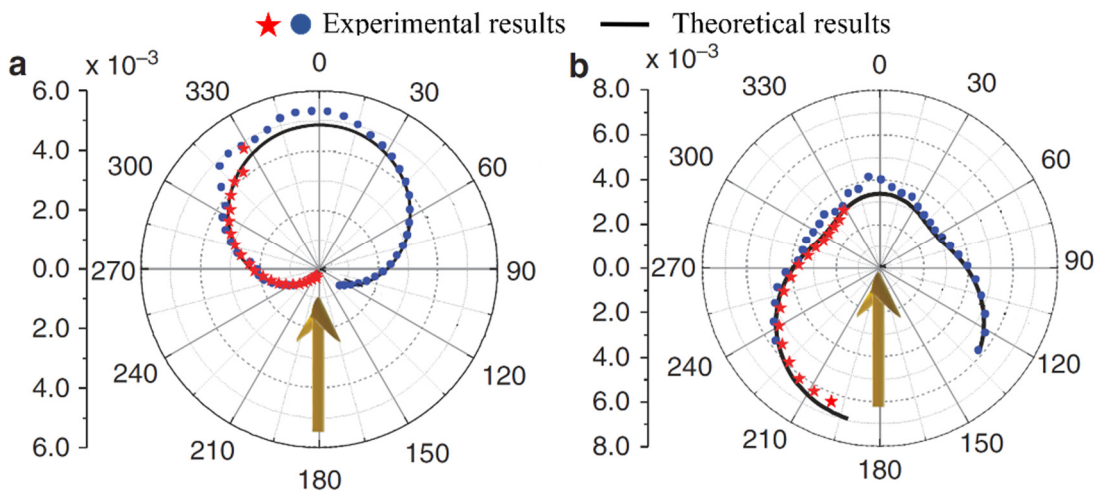


Figure 3.12 Intensity of the Far-field scattering pattern under Kerker conditions of a 9 mm sphere with  $\epsilon = 16.5 + 0j$ . The illumination direction is indicated by the yellow arrow. (a) zero-backward condition ( $\lambda = 84$  mm). (b) minimum-forward condition ( $\lambda = 69$  mm)[12]

These effects, which in the literature are called magnetodielectric, are a consequence of the coherent effects between the excited electric and magnetic dipolar modes. In general, whispering gallery modes are responsible for resonances involved in these phenomena, which can be either electric or magnetic, even though the particle is non-magnetic at all [112]. Their coherent contribution produces interference effects leading to peculiar directionality phenomena which can result in various applications for optical communication purposes. This can be achieved by taking advantage of the coherent effects not only between dipolar contributions but also between these and modes of higher order.

By pursuing this idea, here we introduce the possibility of using a HRI dimer as an elementary unit for building in-plane binary switching devices. In the forward direction, the scattered (wanted) signal is mixed with the incident beam which usually has a much higher intensity. In that case, it is necessary to add an extra element (light shielding plate) to avoid direct radiation which can mask the real forward scattered radiation and this has been recently proposed in [113]. In the backward direction, the scattered field is not easy to isolate without using some sort of beam-splitter with the corresponding complication in designing the scattering arrangement and as it can be shown, it is not possible to get perfect switching even if the two spheres do interact. Therefore, back and forward directions need additional elements which complicate the optical configuration for building operational optical circuits. Thus, other directions, different from back and forward, seem more appealing for practical in-plane optical circuits design. In this work, we show that the scattered intensity at  $90^\circ$  from the incident direction can be null or maximum by playing with the polarization of a single frequency excitation and with a dimer whose components are close enough to interact in a controlled



way. This interesting behavior converts the dimer element in a two-output (beam splitter) switching unit whose binary state depends only on the polarization of the exciting radiation.

### 3.2.3 Dimer configuration and measurement protocol

The electromagnetic interaction between two homogeneous identical HRI spheres (particles analogs) has been investigated. The radius  $R_1 = R_2 = R$  of the spheres are equal to 9 mm and their permittivity is  $\epsilon_r = 15.7 + 0.2j$ . This permittivity was determined from far field scattering measurements as explained in section 2.6. The spheres are smaller than the wavelength  $\lambda$  of the illuminating radiation and we define the size-parameter  $q$  as  $2\pi R/\lambda$ . The dimer is oriented along the  $y$  axis and is illuminated by a linearly polarized plane wave propagating along the  $z$  axis. The polarization of the incident wave is either parallel to the dimer connecting axis (longitudinal configuration) or perpendicular (transverse configuration) as it is shown in Figure 3.13.

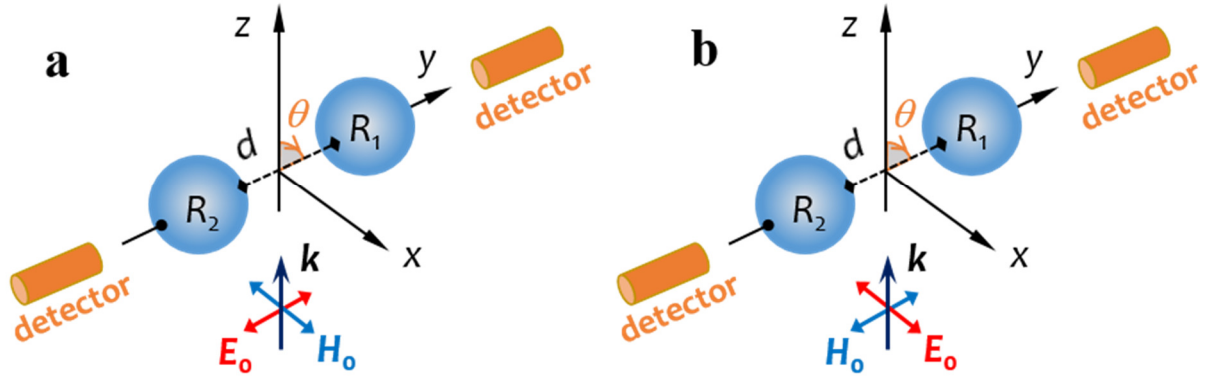


Figure 3.13 Scattering configuration: a homogeneous sphere dimer with the same radius is illuminated by a monochromatic plane wave propagating along the  $z$  axis and linearly polarized either parallel to the dimer connecting axis. (a) Longitudinal configuration (P). (b) Transverse configuration (S).  $\theta$  is the scattering angle

The gap separation distance between the two spheres is denoted by the dimensionless relative parameter  $d_0 = \frac{d}{R}$  where  $d$  is the separation distance between the two external boundaries of the spheres, is either 3 mm or 18 mm and  $R$  is 9 mm. Therefore, the two considered distances are  $d_0 = 1/3$  (small gap  $\rightarrow$  strong interaction) and  $d_0 = 2$  (large gap  $\rightarrow$  weak interaction).

The scattering experiments have been performed in the frequency range from 3 GHz to 9 GHz, corresponding to  $\lambda$  from 100 mm to 33 mm. Each of the two gaps cases ( $d_0 = 1/3$  and  $d_0 = 2$ ) was measured in both polarizations HH and VV in azimuthal circular configuration and with the DRG horn antennas. Special expanded polystyrene holders were fabricated to align the spheres and control the gap between them. Since the spheres are smaller than the wavelength and the DRG horn antennas are not very directive, the corresponding total and incident field are quite comparable and their subtraction is sensitive to the experimental noise.

To overcome the noise influence, the measurements were performed using the Hardgating system then the drift correction and angular lowpass filter post-processing were applied to the experimental scattered fields. Figure 3.14 shows the measurement procedure, the dimer and the control of the gap using the specific holder. The used configuration of the measurement setup for the measurement is summarized in Figure 3.15.

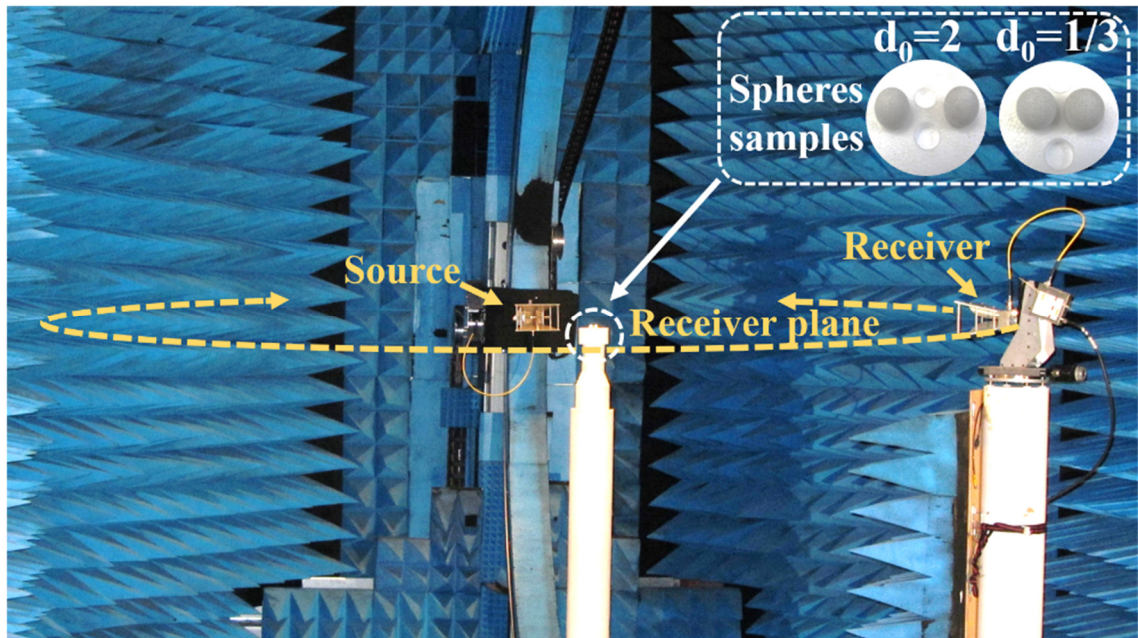


Figure 3.14 The measurement procedure of the field scattered by the dimer in azimuthal bistatic configuration. In this configuration, the HRI spheres are placed in their specific polystyrene holder, one next to the other as shown in the inset

The corresponding numerical simulations have been developed by our collaborators at the University of Cantabria by means of a FEM implementation using the commercial software COMSOL Multiphysics [114]. With the software, the differential form of Maxwell's equations in the frequency domain are solved together with the boundary conditions.

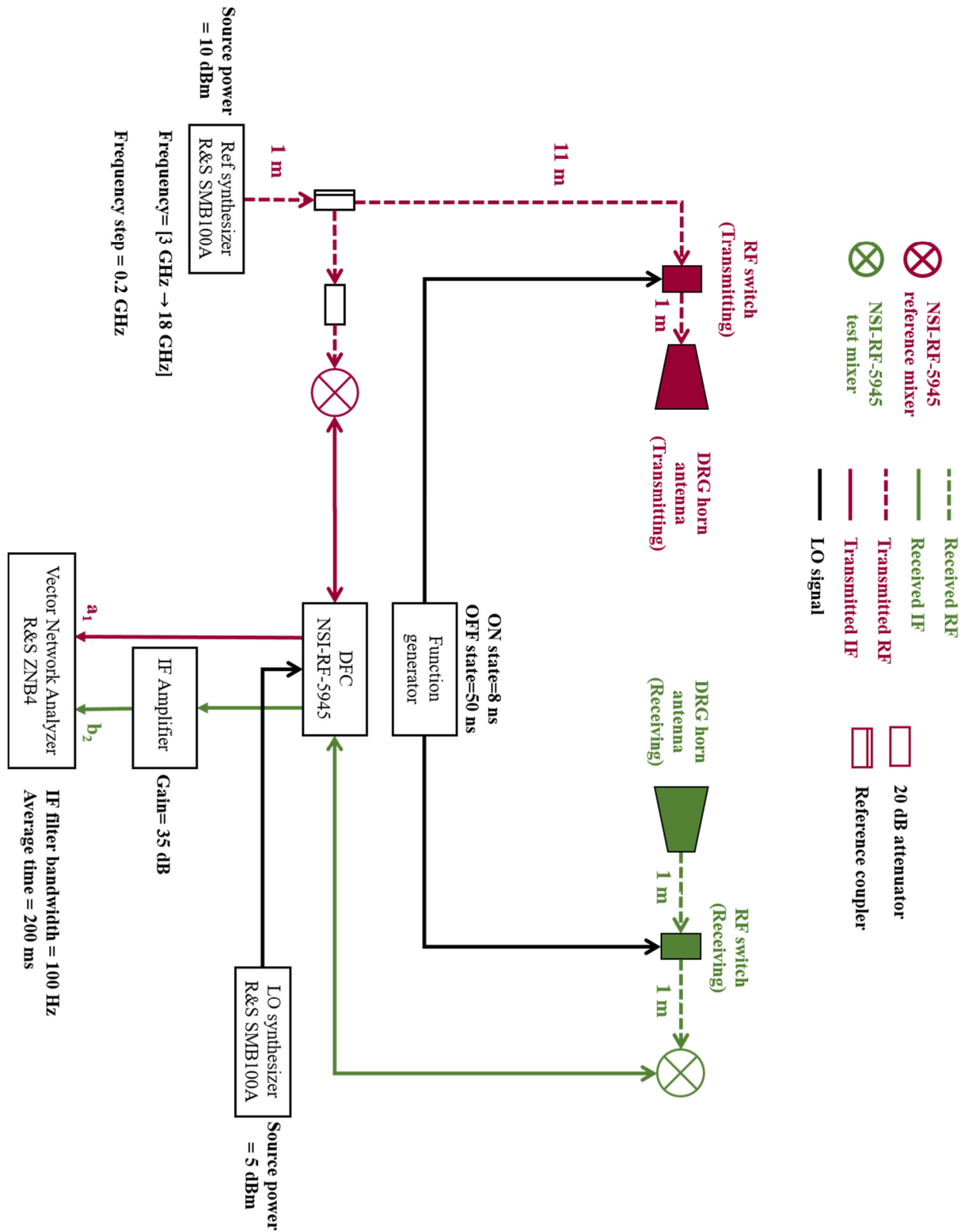


Figure 3.15 Schematic showing the settings of the measurement setup for the measurement of the dimer analog. Measurements are made in Hardgating mode with the DRG horn antennas

### 3.2.4 Dipolar resonance

The basics of amplitude scattering matrix has already been extensively described in the literature [92]. The amplitude of the field scattered by an arbitrary particle is a linear function of the amplitude of the incident field. The relation between incident and scattered fields is conveniently written in matrix form:

$$\begin{pmatrix} E_{\parallel sca} \\ E_{\perp sca} \end{pmatrix} = \frac{e^{ik(r-z)}}{-ikr} \begin{pmatrix} S_2 & S_3 \\ S_4 & S_1 \end{pmatrix} \begin{pmatrix} E_{\parallel inc} \\ E_{\perp inc} \end{pmatrix} \quad (3.1)$$

$E_{\parallel sca}$  ( $E_{\perp sca}$ ) is the component of the scattered field that is parallel (perpendicular) to the scattering plane.  $E_{\parallel inc}$  and  $E_{\perp inc}$  are respectively the parallel and perpendicular components of the incident field.  $k = 2\pi N_2/\lambda_0$  is the wave number in the medium,  $N_2$  is the refractive index of the object ( $N_2 = \sqrt{\epsilon}$ ), and  $\lambda_0$  is the wavelength of the incident field in free space,  $e^{ik(r-z)}$  is the incident plane wave and  $\frac{e^{ik(r-z)}}{-ikr}$  is the outgoing scattered wave. The matrix  $\begin{pmatrix} S_2 & S_3 \\ S_4 & S_1 \end{pmatrix}$  is the amplitude scattering matrix (unitless).

When the object is a sphere,  $S_3 = S_4 = 0$ . Therefore, the relation between incident and scattered field is:

$$\begin{pmatrix} E_{\parallel sca} \\ E_{\perp sca} \end{pmatrix} = \frac{e^{ik(r-z)}}{-ikr} \begin{pmatrix} S_2 & 0 \\ 0 & S_1 \end{pmatrix} \begin{pmatrix} E_{\parallel inc} \\ E_{\perp inc} \end{pmatrix} \quad (3.2)$$

Where

$$S_1 = \sum_n \frac{2n+1}{n(n+1)} (a_n \pi_n + b_n \tau_n) \quad (3.3)$$

$$S_2 = \sum_n \frac{2n+1}{n(n+1)} (a_n \pi_n - b_n \tau_n) \quad (3.4)$$

The complex Mie coefficients  $a_n$  and  $b_n$  are obtained from matching the boundary conditions at the surface of the sphere and they are expressed in terms of spherical Bessel functions.  $\pi_n$  and  $\tau_n$  are the Mie angular functions. The order of the coefficients  $a_n$  and  $b_n$  is proportional to the size-parameter of the sphere [92].

For a single sphere with the concerned radius (9 mm) and permittivity ( $\epsilon_r=15.7+0.2j$ ), the scattering coefficient  $Q_{sca}$  and its corresponding partial multipolar contributions are obtained with Mie theory and are presented in Figure 3.16 as a function of the size-parameter  $q$ .  $Q_{sca}$  shows the contribution of the partial magnetic dipole MD ( $q$  around 0.7), electric dipole ED ( $q$  around 1), magnetic quadrupole MQ ( $q$  around 1.1) and electric quadrupole EQ ( $q$  around 1.4). It is clear that, for  $q < 1$ , dipolar modes exist.

The electric and magnetic scattered fields created by a single sphere can be expressed according to the Green methodology as

$$E_{sca}(r) = \frac{k^2}{\varepsilon_0 \varepsilon_h} G_E(r - r_0) \cdot p_0 + iZk^2 G_M(r - r_0) \cdot m_0 \quad (3.5)$$

$$H_{sca}(r) = -i \frac{1}{Z} \frac{k^2}{\varepsilon_0 \varepsilon_h} G_M(r - r_0) \cdot p_0 + k^2 G_E(r - r_0) \cdot m_0 \quad (3.6)$$

$G_E$  and  $G_M$  being the free-space electric and magnetic dyadic Green's function respectively.

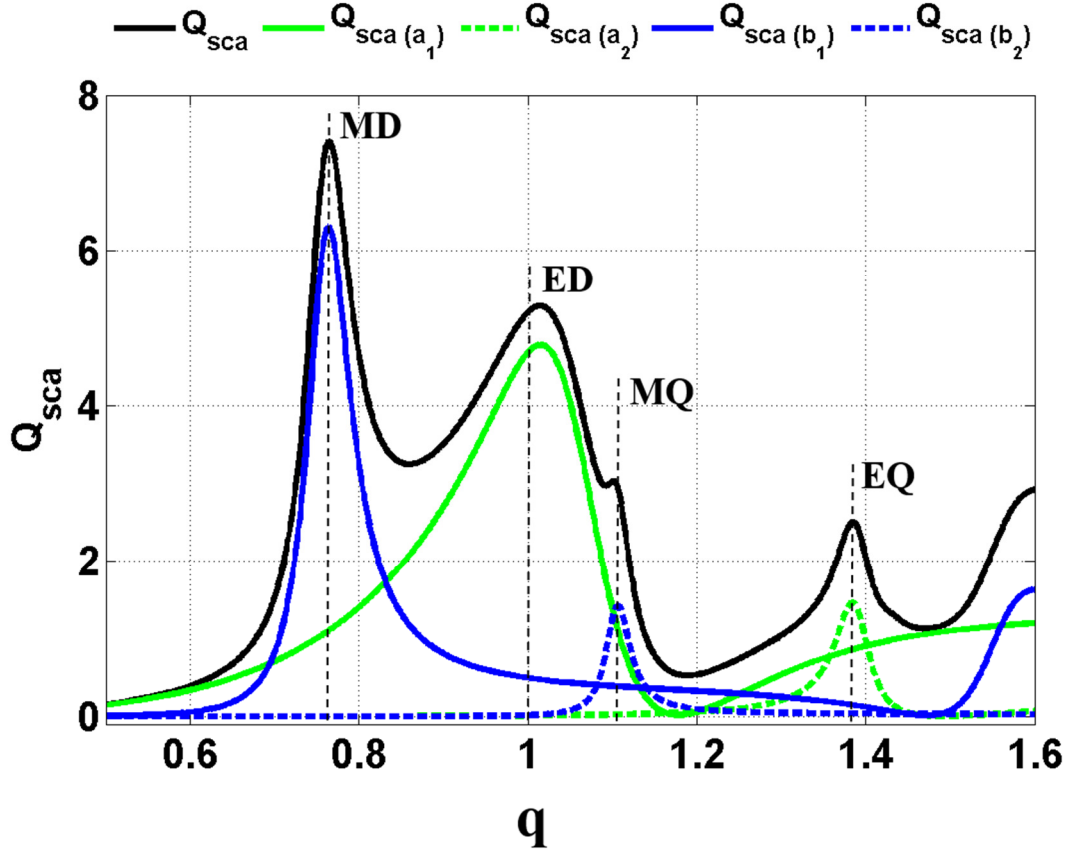


Figure 3.16 Scattering coefficient  $Q_{sca}$  and its first four multipolar contributions for a sphere with  $\varepsilon = 15.7 + 0.2j$  and radius 9 mm. The partial electric and magnetic dipolar and quadrupolar contributions are indicated by the vertical dashed lines

In the case of the dimer, each one of the two spheres is modeled by two orthogonal dipoles, one electric  $\mathbf{p}$  and one magnetic  $\mathbf{m}$ , which are both perpendicular to the propagation direction. This configuration is depicted in Figure 3.17. The electric and magnetic scattered fields created by both particles of the dimer can be expressed attending to the Green methodology as

$$E_{sca}(r) = \sum_{j=1,2} \left\{ \frac{k^2}{\varepsilon_0 \varepsilon_h} G_E(r - r_j) \cdot p_j + iZk^2 G_M(r - r_j) \cdot m_j \right\} \quad (3.7)$$

$$H_{sca}(r) = \sum_{j=1,2} \left\{ -i \frac{1}{Z} \frac{k^2}{\varepsilon_0 \varepsilon_h} G_M(r - r_j) \cdot p_j + k^2 G_E(r - r_j) \cdot m_j \right\} \quad (3.8)$$

The detailed analytical study describing the contribution of both of the spheres to the scattered intensity and the underlying physics behind it can be found in the publication issued from this work in [75].

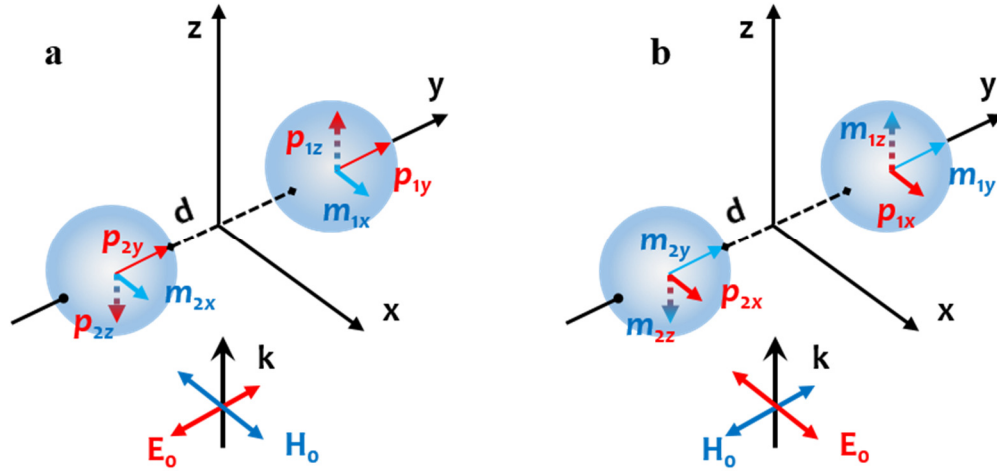


Figure 3.17 Orientation of the induced dipoles in (a) longitudinal configuration and (b) transverse configuration. The red vectors represent the electric quantities, while the blue vectors represent the magnetic ones.  $E_0$  corresponds to the polarization of the electrical incident field and  $H_0$  corresponds to the polarization of the magnetic incident field. Both correspond to a plane wave with incidence direction  $k$ . They generate an electric dipole  $p$  and a magnetic dipole  $m$  in each sphere. The interaction between the two spheres (each of radius  $R$ ) generates a non-null Z-component for the electric dipole or for the magnetic dipole. This depends on both the orientation of the dimers and the polarization of the impinging wave.  $d$  corresponds to the gap distance between the two spheres

### 3.2.5 Linear polarization degree

The linear polarization degree,  $P_L(\theta)$ , is determined through the scattered intensities at a scattering angle  $\theta$ , when the exciting signal is linearly polarized, oriented perpendicular and parallel to the scattering plane [92], as :

$$P_L(\theta_r) = \frac{I_s(\theta_r) - I_p(\theta_r)}{I_s(\theta_r) + I_p(\theta_r)} \quad (3.9)$$

$I_s(\theta_r)$  and  $I_p(\theta_r)$  are the intensities of the scattered fields at the scattering angle  $\theta_r$  when the incident radiation is linearly polarized respectively in perpendicular and parallel to the scattering plane (plane ZY in Figure 3.13).  $I_s$  corresponds to the transverse configuration and  $I_p$  corresponds to the longitudinal configuration. This polarimetric parameter  $P_L$  is an efficient alternative to determine the extinction efficiency in electromagnetic experiments for particles sensing and it can provide information about the electric or magnetic nature of resonances [12]. In Figure 3.18, we plot the spectral behavior of  $I_s$ ,  $I_p$  and  $P_L$  at  $\theta_r = 90^\circ$  (right angle scattering), for the small and large gap cases in the dipolar spectral region where only the

electric and magnetic dipolar contributions exist. It is possible to distinguish the dipolar electric (ED) and magnetic (MD) resonances, labeled in Figure 3.18 as ED and MD respectively. When comparing small and large gap cases, one of the most remarkable differences is the values of  $P_L(90^\circ)$  around  $q = 0.8$ . For the small-gap case,  $P_L(90^\circ)$  reaches -1, while for the large one it clearly deviates from this value. According to equation (3.9), it is clear that  $P_L(90^\circ) = -1$  corresponds to a null value of  $I_s(\theta_r)$ . It has been shown in [115] that negative values of  $P_L(90^\circ)$  correspond to magnetic resonances. Around  $q = 0.8$ , as the distance between the spheres decreases, the intensity  $I_p$  increases while  $I_s$  decreases. In particular,  $I_s$  reaches null values for  $d_0 = 1/3$ , at  $q = 0.773$  while  $I_p$  reaches simultaneously its highest value. The reason behind this behavior is first the coupling between the two particles that generates a supplementary induced magnetic dipole orientated along the propagation direction, when the transverse configuration is considered. Second, even if the induced electric and magnetic dipoles are less than  $\lambda/2$  apart, they both generate electric fields which destructively interfere at  $q = 0.773$  for  $90^\circ$  scattering angle. Indeed, at that frequency, the interference of the electric field created by the electric and magnetic dipoles in both particles is destructive as their phase difference is  $\pi$ . Furthermore, the amplitude of the electric field created by the electric and magnetic induced dipoles in the first particle is the same as that created by the induced dipoles in the second particle. Thus, at that particular frequency, the dimer as a whole works as a pure magnetic unit ( $P_L(90^\circ) = -1$ ).

The fact that, at the same spectral position, denoted in the following as the switching frequency,  $I_p$  and  $I_s$  take so different values has important consequences for switching purposes. When both components of the dimer are close enough to interact, the ensemble behaves as a polarization switching element. This switching behavior is observed for different scattering angles. However, we operate at  $90^\circ$  for two main reasons. First, the maximum difference between the parallel and perpendicular to the scattering plane intensities is obtained for the right-angle scattering configuration, which means that a clear difference between two states of the switching device can be easily detected. Second, detecting at  $90^\circ$  is a good way to avoid any parasitic effect due to the incident radiation (considering a reasonably focused incident beam) making this dimer geometry and the incoming wave probably the best configuration for this switch to be of great practicality. Another remarkable feature is that we can obtain information about the charge distributions in the particles, observing the existence of a pure magnetic dipole at the switching frequency through the polarimetric parameter  $P_L(90^\circ)$ . In general, we have an additional feature due to the symmetry of the electromagnetic problem: two identical outputs can be handled at the same time with the same scattering unit and for



one incidence. This feature is similar to that of a beam splitter. Although this switching effect can be also observed for an isolated sphere, the dimer presents two main advantages. First, the difference between the high and low (or ‘ON’ and ‘OFF’) states is higher than with a single sphere. Second, the low state is zero (without noise), which makes it easier to detect and the high state reaches higher values than for an isolated sphere.

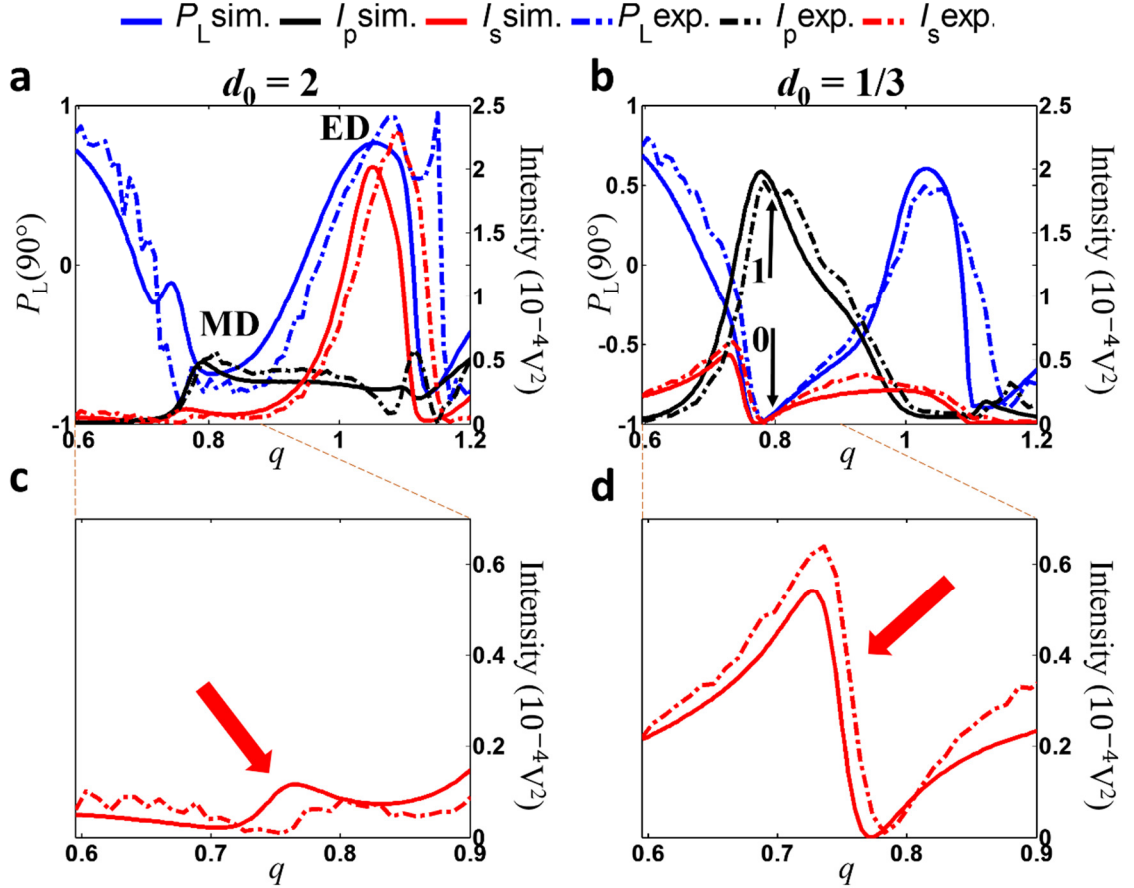


Figure 3.18 Linear polarization degree  $P_L$  and scattered intensities from experiments and simulations at  $90^\circ$  for the sphere dimer as a function of the size-parameter  $q$  with (a)  $d_0=2$  and (b)  $d_0=1/3$ . The exciting field is linearly polarized and the electric field is either perpendicular ( $I_s$ ) or parallel ( $I_p$ ) to the scattering plane (see Figure 3.13). (MD=Magnetic dipole resonance, ED=Electric dipole resonance). The low (OFF)/high (ON) states are indicated with 0/1 and black arrows. (c) and (d) are zoomed details for  $I_s$  of plots (a) and (b) respectively

In Figure 3.19 the scattering diagrams for both polarizations and for the two gaps are shown in the scattering plane ZY in the spectral range of the switching frequency. With the small gap, a large difference is observed between the scattered intensity values at  $90^\circ$  when comparing the two considered polarizations. However, for the large gap, the scattered intensities in the two polarization cases are both very small, which means that this switching effect is not observable at this wavelength when the particles do not interact.



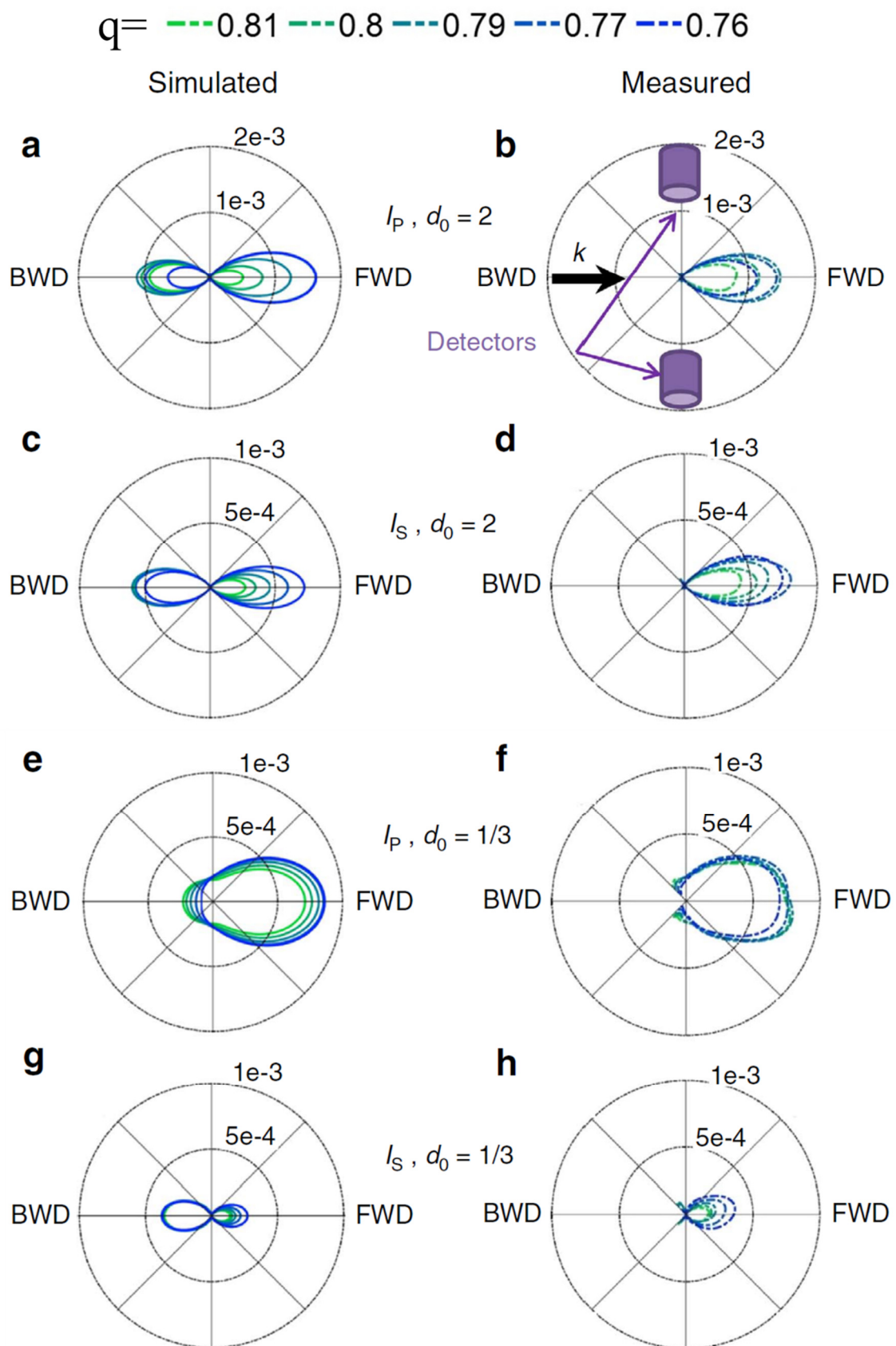


Figure 3.19 Polar plots showing the angular variations of the intensities  $I_s$  and  $I_p$  of the scattered fields around the switching frequency for  $q$  between 0.76 and 0.81 in large gap ( $d_0=1/3$ ) and ( $d_0=2$ ) cases

In practical conditions, a switch must be built in order to be performing even within the most challenging conditions. With this in mind, the experiments shown in Figure 3.20 have been made with a rather focused incoming wave (as a laser beam can be), in order to fully assess the potential of dimers as optical switches. Those experiments are presented here without any kind of processing and are definitely raw measurements, as they would be with an actual device. Figure 3.20-c and d are showing the intensity acquired directly from the  $b_2$  signal at the receiver when measured with or without the dimer (the signal is not even referenced to the signal  $a_1$  delivered to the source antenna, and no frequency variation is compensated). Only plots in Figure 3.20-b are obtained from the  $(b_2/a_1)$  signal. Notice that the small differences between the measured fields in the three experiments with the P polarization observed in Figure 3.20-d are mainly due to the antenna's imperfection, which are visible in Figure 3.20-c. Figure 3.20-d definitely provides a scientific evidence that a simple measurement of the intensity seen at  $\pm 90^\circ$  when changing the polarization of the incoming wave can undeniably be used as the 'ON' and 'OFF' states of a switching device.

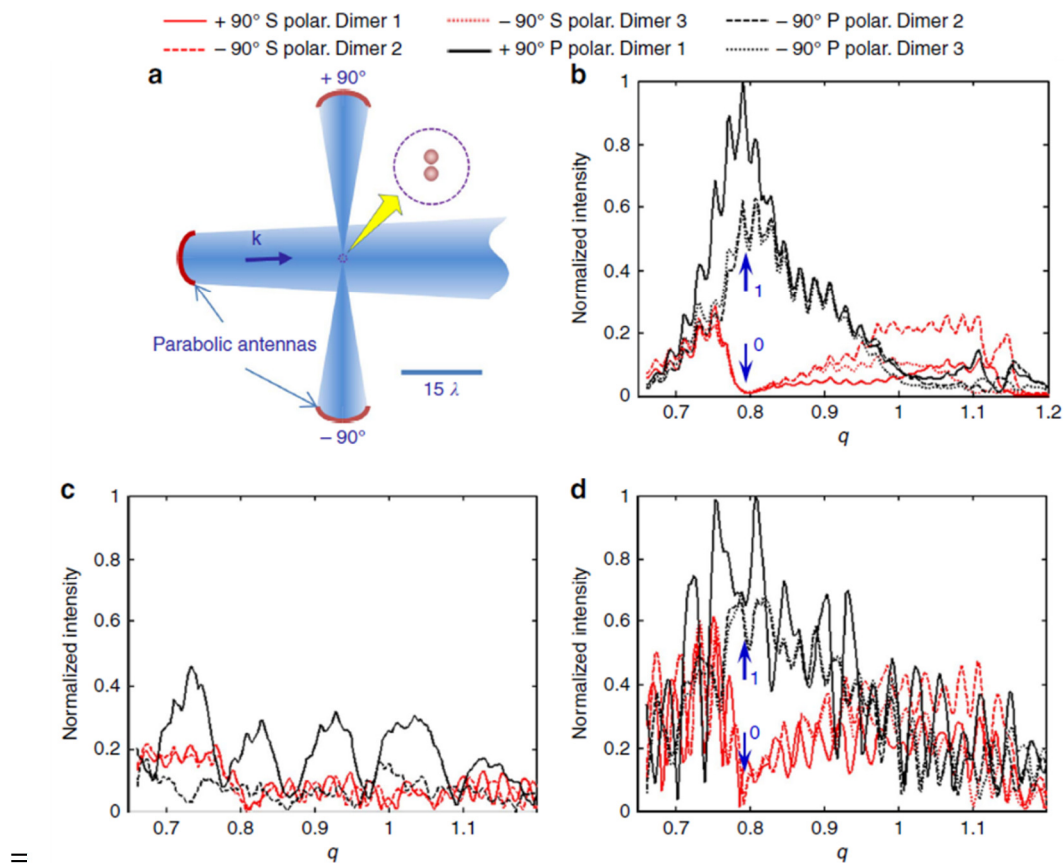


Figure 3.20 (a) Experimental setup with directive C-band parabolic antennas. (b) Raw measured scattered fields for  $\theta_r = \pm 90^\circ$ . (c) Raw measured incident fields. (d) Raw measured total fields. These measurements have been made 3 times for three different dimers selected from a set of four identical spheres (all of them have diameter of 18 mm and  $\epsilon_r = 15.7 + 0.2j$ )

### 3.2.6 Conclusion

Within the work presented in this section we introduced microwave analog experiments to validate a theoretical principle of using homogenous dimer of HRI dielectric spheres as a perfect binary polarization controlled switching device in the optical region. This has been done by acquiring the scattered intensities at a right-angle scattering configuration. It has also been shown that this arrangement leads to the highest offset between the two polarization switching states and the binary state depends only on the polarization of the exciting radiation. An OFF state corresponds to null intensity is obtained in HH polarization and an ON state corresponds to high intensity is obtained in VV polarization. The origin of the switching effect is (i) the presence of a supplementary magnetic dipole generated by the coupling effect between the two spheres and (ii) the interference between the electric and magnetic dipoles induced by the incident beam in both particles of the dimer.

A good agreement was reported between numerical calculations and experimental measurements. This work was published in the Nature Communications journal [75].

### 3.3 SOOT AGGREGATES

#### 3.3.1 Introduction

The electromagnetic interaction with soot is of interest to many researchers working on environmental aerosol and combustion diagnostics [116]. The determination of their radiative properties is crucial to understand their presence in the radiative heat transfer. In a combustion medium, soot aggregates are spread out in the gaseous mixture. It is therefore a problem of interaction between an electromagnetic wave and a group of aggregates and the scattering coefficients have to be determined for an ensemble of aggregates. Theoretically, one can differentiate between dependent and independent scattering regimes as function of size-parameters and volume fraction, i.e., the volume of the particles in the overall medium volume. In the case of soot aggregates, the latter at microscopic level have a size-parameter around  $10^{-1}$  and a particle volume fraction of  $10^{-4}$ , hence the distance between an aggregate and its neighbors is very large compared to the wavelength and the regime is independent. Therefore, the interaction with a cloud of particles can be obtained from the summation of interaction with all the individual particles. Researches in light and heat transfer addressing the case of soot aggregates are usually interested in the determination of the Extinction, Absorption and Scattering cross sections, denoted by  $C_{ext}$ ,  $C_{abs}$ , and  $C_{sca}$  respectively. The Extinction Cross Section is nothing but the summation of the absorption and the scattering. The definitions of these three quantities are discussed in the subsection 3.3.2.

This section addresses the implementation of microwave analog experiments on analogs of soot aggregates particles and shows the determination of the Extinction Cross section from the measured scattered field. Two microwave analogy studies are explored whose objectives are explained hereunder in the framework of two research collaborations. Within these two collaborations my contribution consisted first on fabricating the soot analogs with the help of the CTTM and to carry out scattering measurement in a bistatic azimuthal configuration. Next, the interesting quantity  $C_{ext}$  is determined from experiments using the optical theorem from the measured complex value of the scattered field only in the forward direction ( $\theta_r = 0^\circ$ ).

1. The first collaboration is in the framework of a collaboration with the Laboratoire Energétique Moléculaire et Macroscopique, Combustion (EM2C) at Centrale-Supélec in France. Our collaborators at EM2C have applied a Scanning Electron Microscopy (SEM) tomography on a soot aggregate sampled directly from the combustion of a propane-air flame [117]. This tomographic reconstruction is much richer in terms of

information than the classical 2D analysis technique that has been used in the past for complex morphology description (

2. Figure 3.21). The reconstructed 3D geometry of soot is discretized and then submitted to a DDA code to evaluate the soot radiative properties. The DDA method consists of discretizing the object into cubic elements where each cube is a dipole. In each dipole  $j$  there is a dipole moment ( $P_j$ ), that is dependent on the incident field, on the incident fields at a dipole  $j$  from its neighbor dipoles and on its polarizability. The polarizability means the capacity of a material to be polarized. The conditions to apply this method is to have a small volume element (cube) compared to the incident wavelength but also to have a negligible phase change of the incident field inside the volume element. In other words, the element size should be chosen in a way to have all the points inside it being in the same electromagnetic conditions. Therefore, the aim of using the microwave analogy on this soot analog is to test if we are able to experimentally determine an accurate measurement of the Extinction cross Section and to test limits of the discretization in the DDA method on the calculated  $C_{ext}$  and on the complex values of the scattered fields through comparisons between experiments and calculations.

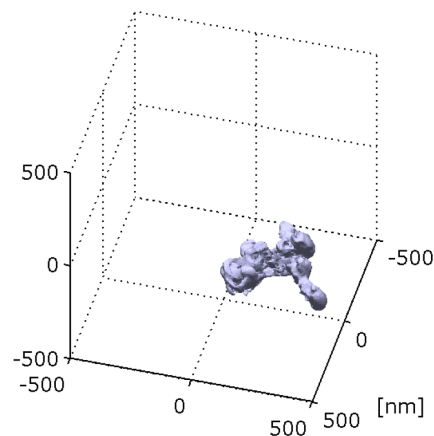


Figure 3.21 Tomography of the soot particle collected from a propane-air flame [117]

3. The second collaboration is with the laboratory Complexe de Recherche Interprofessionnel en Aérothermochimie (CORIA) in France. In the frame of this study, the researchers with whom we collaborate at CORIA have addressed in some of their researches the impact of the morphology of the soot on their scattering properties and specifically the effects of necking and overlapping between the primary particles [76]. The overlapping represents and penetration between the primary particles (Figure 3.22-a) and the necking is the smooth transition in the contact area between the primary particles (Figure 3.22-b). The microwave analog experiments here are focusing

only on the necking effects. The necking can be seen as a sign of aging of the particle as a function of time. A young soot particle has almost no necking effect but, throughout the time, the necking appears as a coat that increases the volume of the particle. The aim of the scattering experiments here it is to test whether it is possible or not to track the necking presence through the measurement of the Extinction Cross Section  $C_{ext}$ .

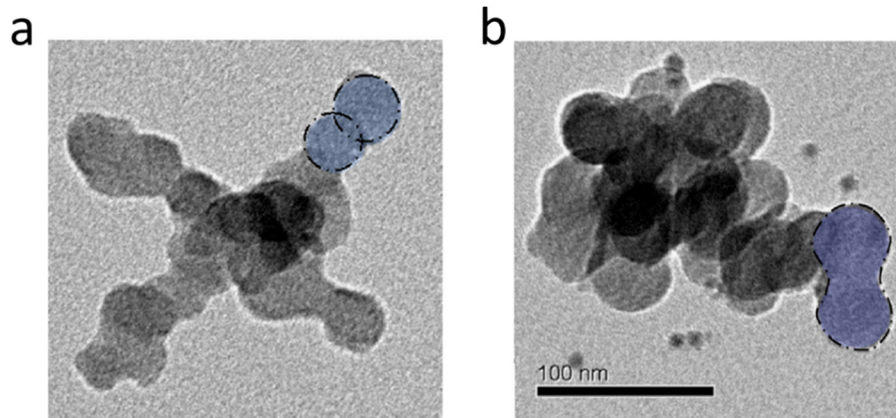


Figure 3.22 TEM images of combustion generated soot aggregates showing the effects of (a) necking and (b) overlapping [76]

### 3.3.2 Extinction and Optical theorem

Considering an incident electromagnetic wave and a receiver placed in the forward direction of the incidence radiation and satisfying the far-field conditions. The rate at which the electromagnetic energy is received by the detector with the absence of an object is denoted by  $U_0$ . The situation is depicted in Figure 3.23-a. Now if we consider an object O placed in the beam of the incident wave, the incident wave is no longer captured by the receiver due to interactions with the object and is replaced with the total wave. The received power by the receiver is denoted by  $U$ , where  $U < U_0$ . The situation is depicted in Figure 3.23-b. We say that the presence on the particle has resulted in extinction of the incident wave, which is the reduction of the power received by the receiver when an object is present. The difference  $(U - U_0)$  in the energy flow is accounted by absorption in the object and scattering by it [92], [118]. The extinction depends on the electromagnetic properties of the object, its shape, orientation, polarization state, and size compared to the wavelength. Extinction has received extensive consideration in the literature because of its importance as a fundamental aspect of electromagnetic scattering theory.

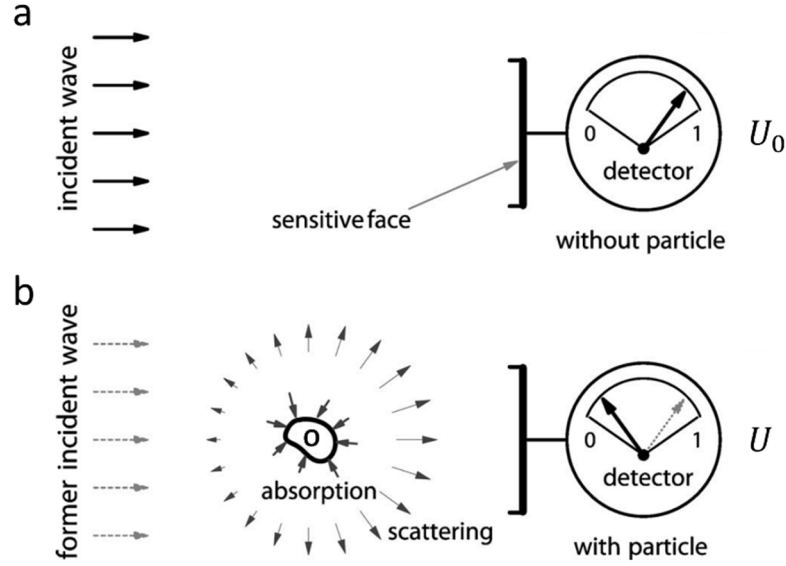


Figure 3.23 effect of extinction explained with an incident electromagnetic illumination and a receiver. (a) with absence on particle. (b) with the presence of a particle [118]

If the system is defined by the volume space in which the object is placed, the extinction power  $W_{ext}$  is equal to the net power lost by the system due to the scattered  $W_{sca}$  and absorbed  $W_{abs}$  power by the object:

$$W_{ext} = W_{sca} + W_{abs} \quad (3.10)$$

The scattering, absorption and extinction cross sections  $C_{sca}$ ,  $C_{abs}$ ,  $C_{ext}$  are defined from the Powers in equation 3.10, by normalizing the latter by the energy flux of the incident wave  $I^{inc} = \frac{(\epsilon_0/\mu_0)^{1/2}|E_0^{inc}|^2}{2}$ , where  $E_0^{inc}$  is a constant vector describing the amplitude and polarization of the wave,  $\epsilon_0$  is the complex permittivity and  $\mu_0$  is the complex permeability of the medium (vacuum here) [118].

$$C_{ext} = \frac{W_{ext}}{I^{inc}} \quad (3.11)$$

$$C_{ext} = C_{sca} + C_{abs} \quad (3.12)$$

In measurement it is difficult, even impossible, to measure the  $C^{ext}$  through the individual measurement of  $C_{sca}$  and  $C_{abs}$  over the complete sphere surround the object. A more straightforward method is to use the optical theorem in [119]. It states that the Extinction Cross Section can be determined from the imaginary part of the scattered field in the forward direction ( $\theta_r = 0^\circ$ ):

$$C_{ext} = \frac{4\pi r}{k} \text{Im}(e^{-jkr} \times E_{sca, \theta_r=0^\circ}) \quad (3.13)$$

Which is equivalent to:

$$C_{ext} = \frac{4\pi}{k^2} \text{Re}(\overline{jkre^{+jkr}} \times E_{sca, \theta_r=0^\circ}) \quad (3.14)$$

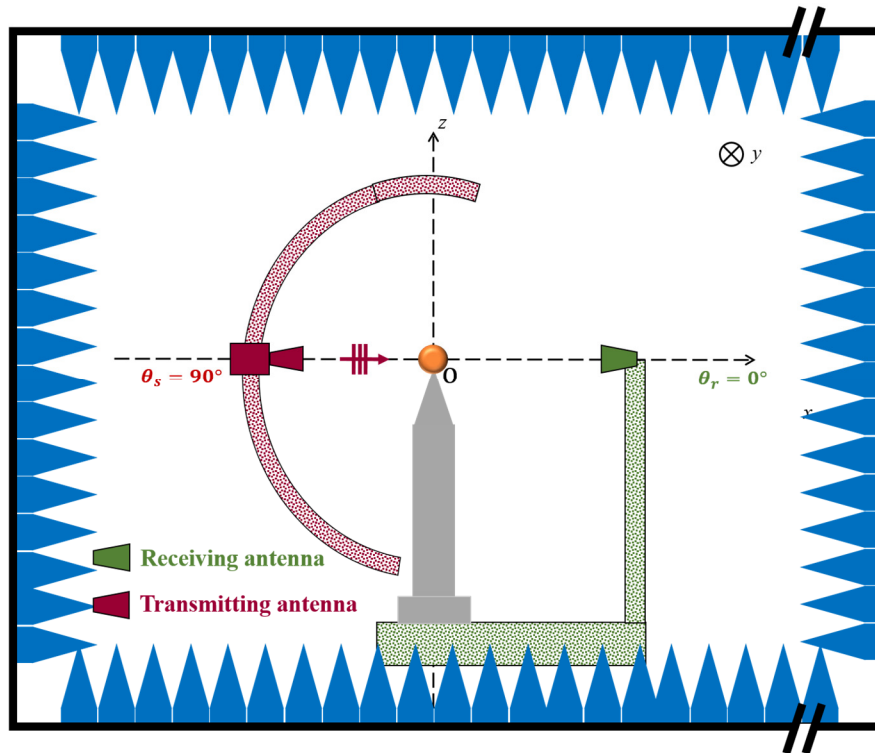


Figure 3.24 The corresponding configuration to the measurement of the Extinction Cross Section

### 3.3.3 Analogs fabrication

The STL files of the initial soot particles were provided by our collaborators at EM2C and CORIA. For the soot aggregate with realistic morphology, denoted  $AG_{SEM}$ , its largest dimension is 500 nm and the wavelengths of interest in the optical domain are between  $0.25 \mu\text{m}$  and  $2.25 \mu\text{m}$ . Both the dimensions and the wavelengths were scaled to the microwave domain with a scale factor  $k = 66666$  (Figure 3.25).

For the soot particles with kinds of overlapping and necking, our starting point was the aggregates investigated in [76], and shown in Figure 3.26, where  $Cov$  represents the overlapping degree between the primary particles ( $Cov = 0$  corresponds to no overlapping) and  $\alpha$  represents the necking degree between them ( $\alpha = 0$  corresponds to no necking). We decided to focus on the necking effect and we choose for the microwave analog experiments the aggregates in the middle row of Figure 3.26 with the same overlapping degree ( $Cov = 0.2$ ) and three different necking degrees ( $\alpha = 0.005, 0.5, 1$ ). These three aggregates are denoted by  $AG_{0.005}$ ,  $AG_{0.5}$  and  $AG_1$  respectively. Their sizes, together with the corresponding working wavelengths in the optical domain between  $0.1 \mu\text{m}$  and  $1 \mu\text{m}$ , were scaled to the microwaves



with a scale factor  $k = 154450$ . Therefore, for all the soot analogs the measurements are carried out in the frequency range between 2 GHz and 18 GHz.

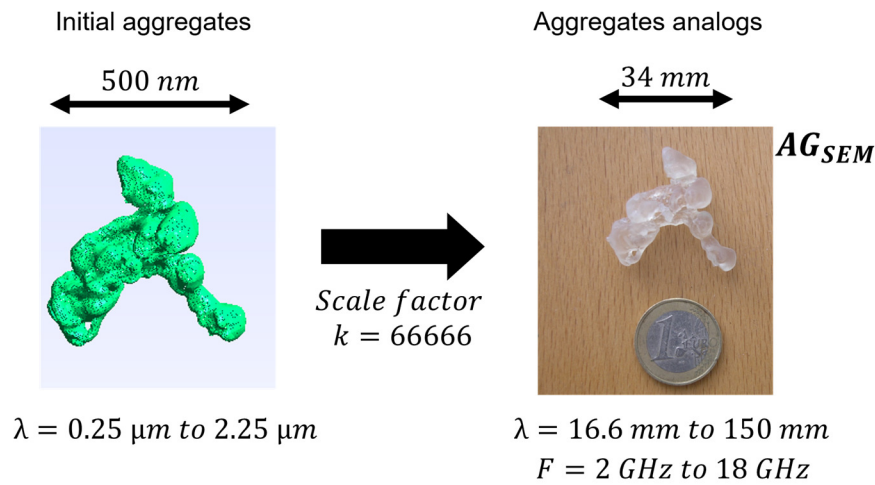


Figure 3.25 The initial soot aggregate particle from propane-air flame and its corresponding analog  $AG_{SEM}$  manufactured in stereolithography at the CTM. The particle dimensions and the working wavelengths are multiplied by 66666

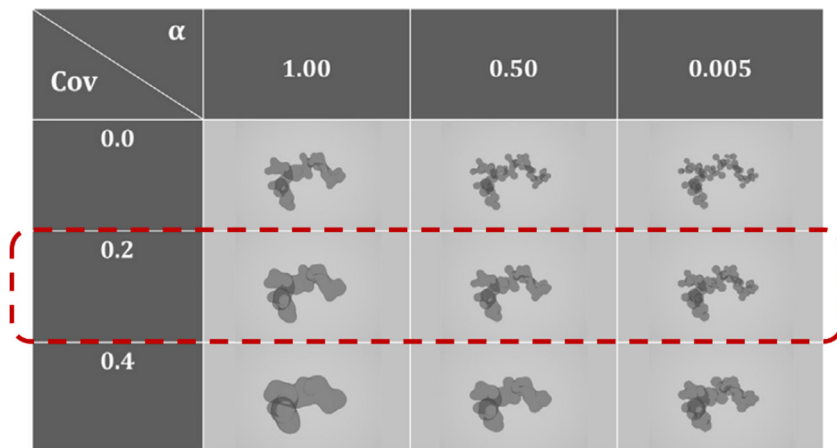


Figure 3.26 Illustration of a set of 9 virtual aggregates with different degrees of necking and overlapping. The three aggregates we chose for microwave analog experiments are indicated by the red dashed rectangle

Ideally, the fabricated analogs should have similar permittivity to the initial soot particle. The permittivity of the soot particles at the initial optical range has a non-null imaginary part. For instance in [76] the permittivity of the considered particles over the optical range has  $\epsilon'$  between 2 and 3 and  $\epsilon''$  between 0.6 and 0.8. However, at the moment of working on these soot analogs we had no solution yet to control the imaginary part of permittivity of materials. Therefore, the analogs were manufactured from the bulk acrylate material of the 3D printer of the CCTM, with  $\epsilon_r = 2.9 + 0.08j$ .

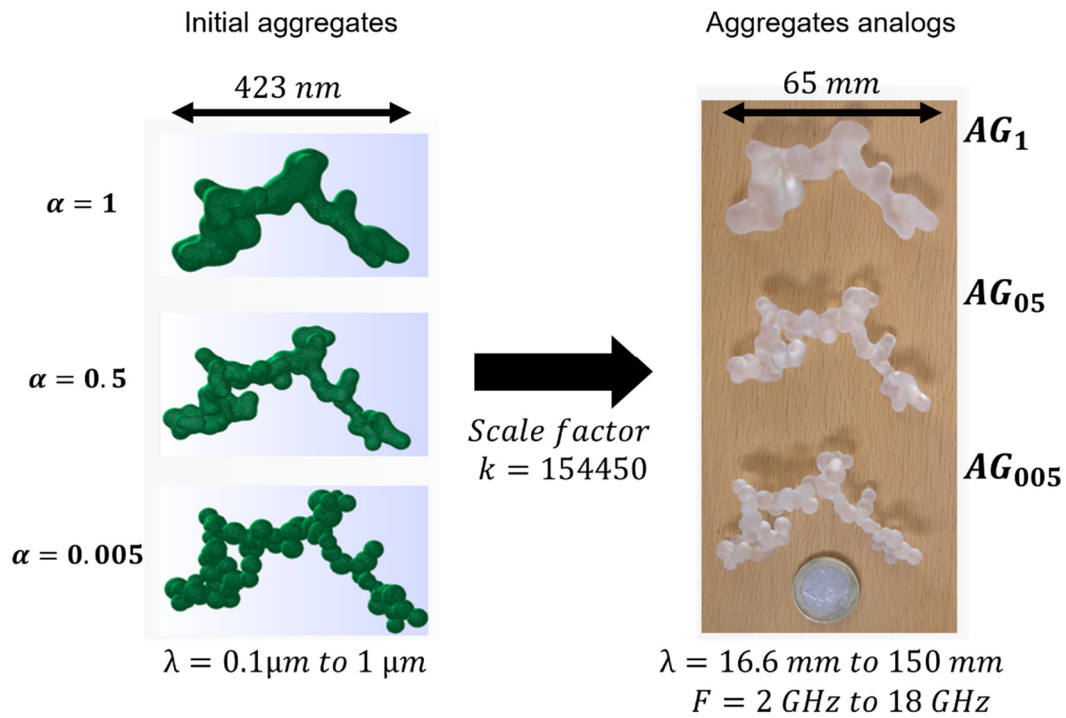


Figure 3.27 The initial numerically generated soot aggregate particles with three degrees of necking ( $\alpha = 0.005, 0.5$  and  $1$ ) and their corresponding analogs ( $AG_{005}, AG_{05}$  and  $AG_1$ ) manufactured in stereolithography at the CTTM. The particles dimensions and the working wavelengths are multiplied by 154450

### 3.3.4 Numerical simulations

For the realistic aggregate  $AG_{SEM}$  with realistic morphology, two numerical methods have been used: DDA and MOM, both of them are based on a volume integral formulation and use a cubic decomposition of the 3D aggregate model. The DDA simulations were obtained with a code made by Franck Enguehard from EM2C and the MOM simulations were obtained with a code made by Christelle Eyraud at Institut Fresnel. Since for this aggregate we aim to analyze the impact of the discretization degree with comparison to experiments, the 3D model of aggregate obtained from tomography reconstruction, was discretized in three different discretizations. The difference between them is the size of cubes constituting the discretized model. They are named “discretization 50”, “discretization 25” and “discretization 13” where 50, 25 and 13 represent the longest dimension of the aggregate in term of number of cubes (Figure 3.28). The cube side size as a function of the wavelength  $\lambda$  in the material is equal to  $(\frac{\lambda}{229} \rightarrow \frac{\lambda}{14})$  for the discretization 50,  $(\frac{\lambda}{73} \rightarrow \frac{\lambda}{7})$  for the discretization 25 and  $(\frac{\lambda}{36} \rightarrow \frac{\lambda}{3})$  for the discretization 13, where  $\lambda = \frac{\lambda_0}{\sqrt{\epsilon'}}$  and  $\lambda_0$  is the wavelength in the free space.  $\lambda_0$  is between  $\frac{c_0}{2 \text{ GHz}}$  and  $\frac{c_0}{18 \text{ GHz}}$  and  $c_0$  is the light velocity in free space.

Indeed, the sizes greater than  $\frac{\lambda}{10}$  may be insufficient but the goal of these discretizations is to verify the minimum required cube size. Next, the field scattered by each of the three objects was calculated with DDA and MOM methods and the  $C_{ext}$  was calculated.

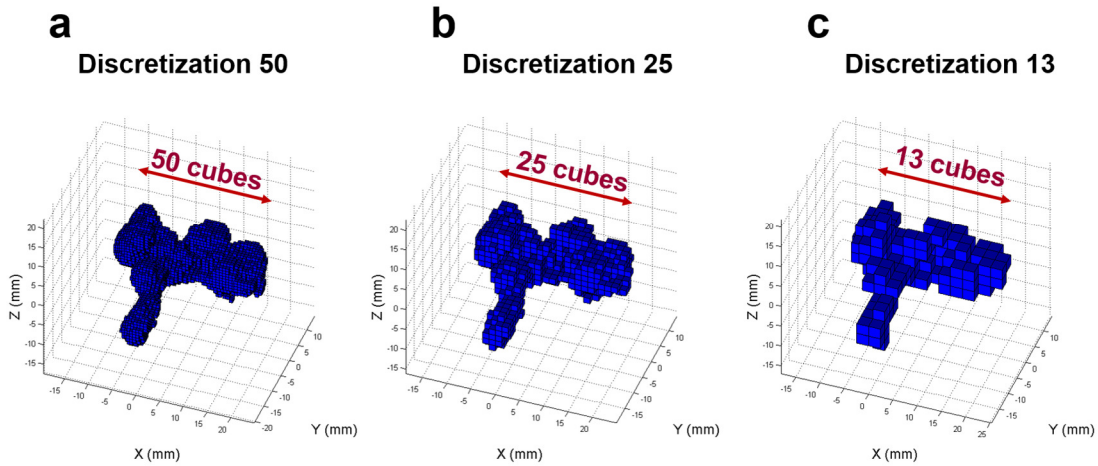


Figure 3.28 The three different discretization of the aggregate  $AG_{SEM}$  of realistic morphology

For the necking aggregates  $AG_{005}$ ,  $AG_{05}$  and  $AG_1$  the numerical simulations were obtained with the same aforementioned MOM code. The discretization of the three models was enough fine to obtain accurate solutions.

### 3.3.5 Measurement protocol

The measurements were made between 2 GHz and 18 GHz, using the DRG horn antennas in VV polarization in azimuthal circular configuration. The frequency step is 0.05 GHz, and it is chosen sufficiently small to have a precise determination of the variation of the Extinction Cross Section as a function of the frequency. Since the frequency band of interest is already large enough, and the frequency step is small, the Softgating mode was selected here. The alignment of the aggregate analogs in the measurement setup was achieved using specific holders made of expanded polystyrene (of permittivity around 1.03) following the alignment method in 1.4.7. For each target, four orientations were investigated at  $\theta_o = -90^\circ, 0^\circ, 90^\circ$  and  $180^\circ$  (Figure 3.30).

The scattering measurement on the aggregates analogs is an application in which it was crucial to use an optimized configuration with zones decomposition because they are low scattering targets. The first measurements on these aggregates were made before the improvement of the measurement accuracy. The experimental scattered fields were very noisy. After the configuration optimization utilizing the zones decomposition was proposed (see 1.7.5),

the measurements were repeated and better accuracy was achieved using the power decomposition schemes into three different profiles (summarized in Figure 3.31). The used configuration of the measurement setup for the measurement is summarized in Figure 3.32. A comparison between experiments, DDA 50 simulation and MOM 50 simulation in amplitude is presented in Figure 3.33, in non-optimized and optimized configurations which confirms the interest of the optimization.



Figure 3.29 The alignment procedure showing the aggregate  $AG_{005}$  on the expanded polystyrene holder with the dielectric alignment spheres

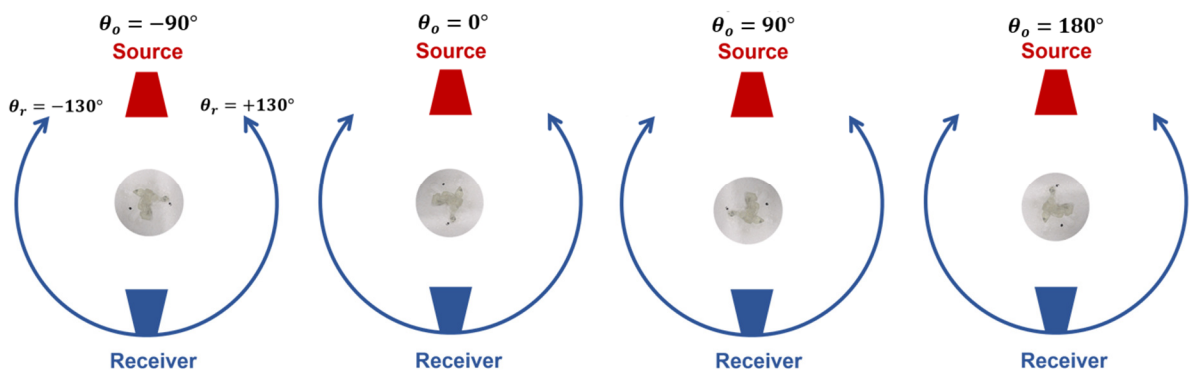


Figure 3.30 Schematics of the scattering configurations seen from the top showing the four studied orientations on the aggregates analogs

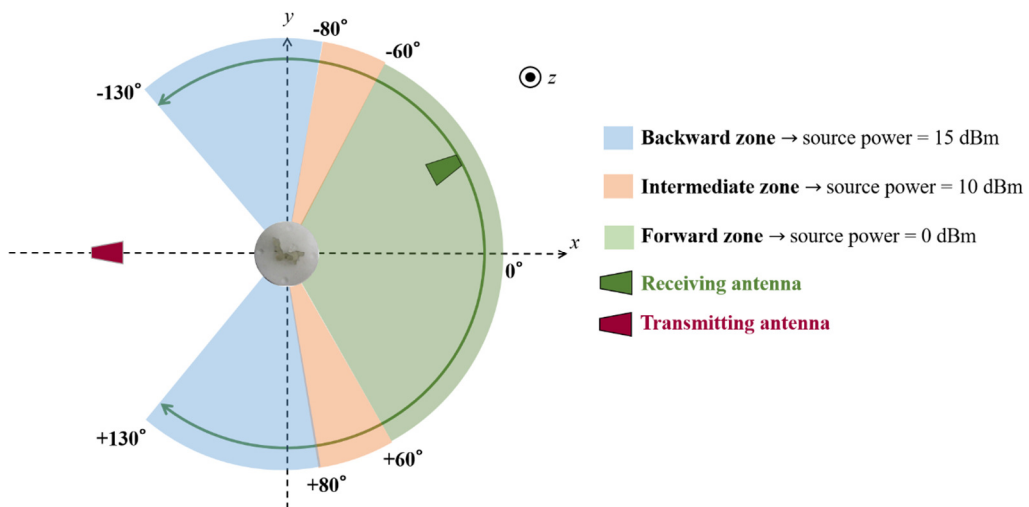


Figure 3.31 A schematic explaining the used optimized configuration based on decomposition of the receiving excursion into three different zones, and the selected power profiles in each zone

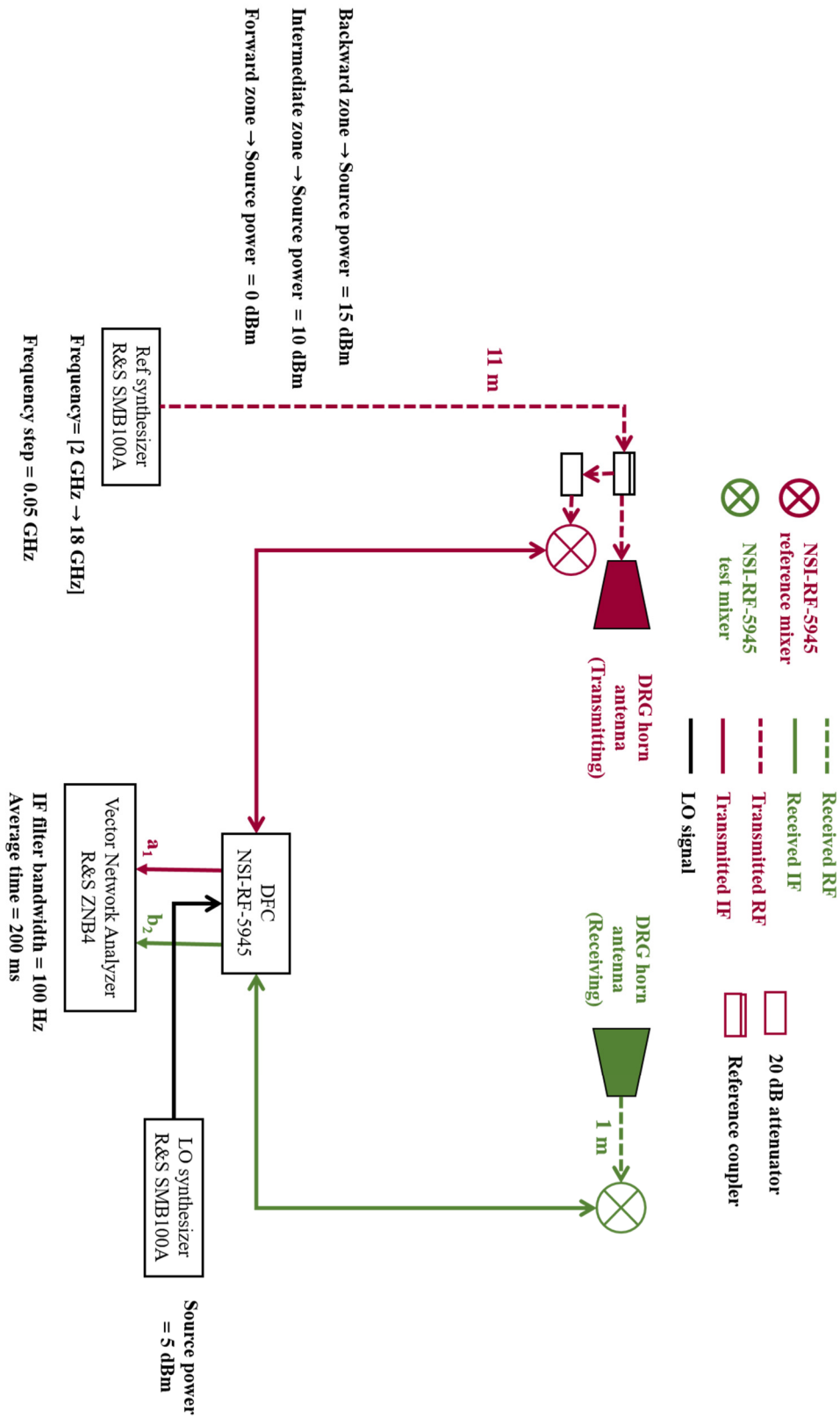


Figure 3.32 Schematic showing the settings of the measurement setup for the measurement of the soot analogs. Measurements are made in Softgating mode with the DRG horn antennas

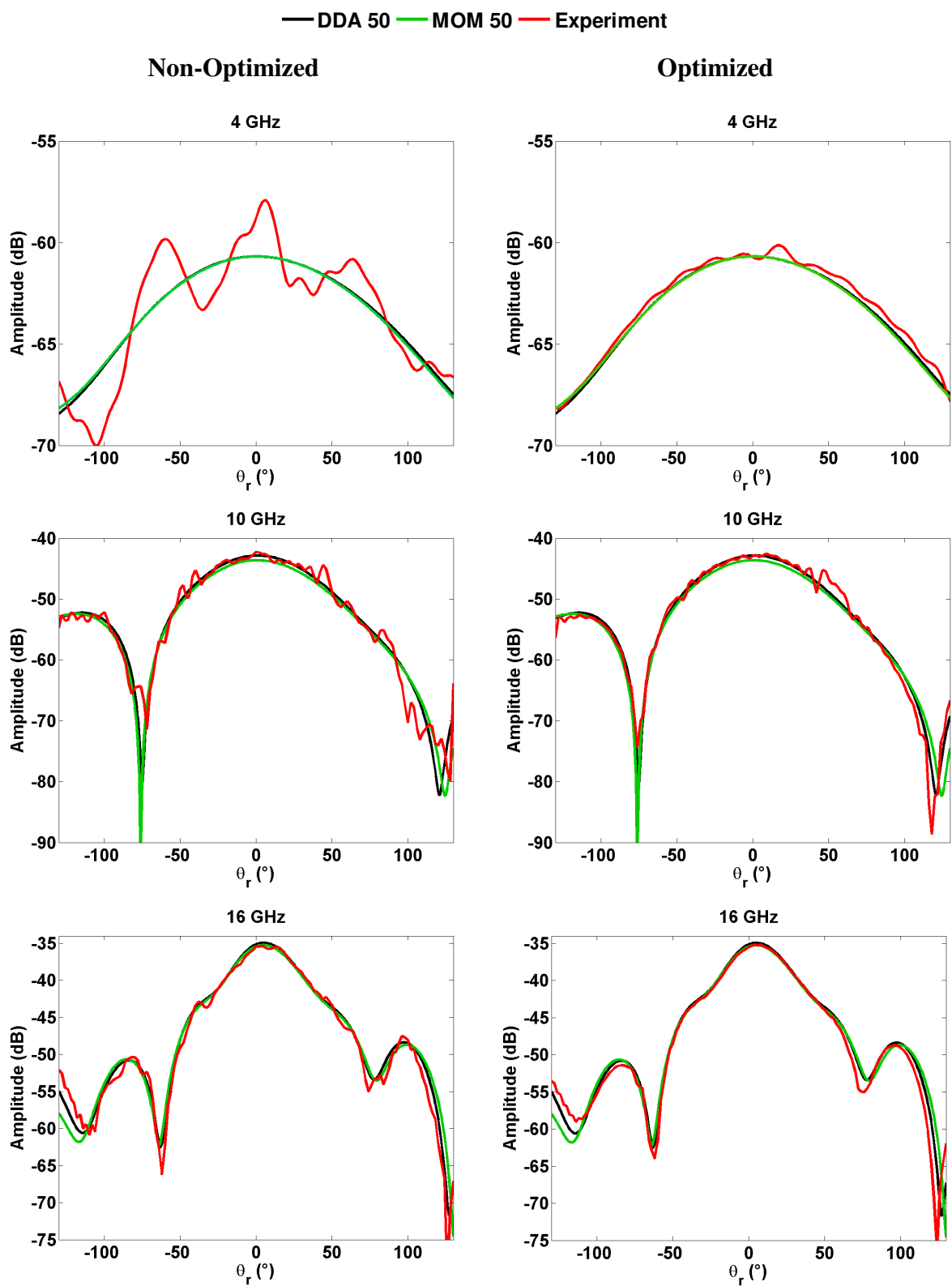


Figure 3.33 Amplitudes of scattered fields from experiments, DDA 50 and MOM 50 by the aggregate of realistic morphology in (left) non-optimized configuration and (right) optimized configuration at 4 GHz, 10 GHz and 16 GHz

### 3.3.6 Extinction Cross Section Measurement

We focus the discussion here on the measurements made with the three analogs  $AG_{005}$ ,  $AG_1$  and  $AG_{SEM}$ . The measurements were performed in the frequency range between 2 GHz and 18 GHz. However, the analogs do not have the same size and this should be taken into account when analyzing the results. The  $C_{ext}$  is presented as a function of the size-parameter  $x = \frac{2\pi R}{\lambda}$ , where  $R$  is the radius of the equivalent sphere in volume of the aggregate, to highlight the impact of the analog's volume on the results. The size-parameters range of each of the three aggregates are presented in Table 3.3.

	$AG_{SEM}$	$AG_{005}$	$AG_1$
Frequency	2 GHz $\rightarrow$ 18 GHz	2 GHz $\rightarrow$ 18 GHz	2 GHz $\rightarrow$ 18 GHz
$R(mm)$	8.1	10.6	13.36
$x = \frac{2\pi R}{\lambda}$	0.25 $\rightarrow$ 3	0.3 $\rightarrow$ 4	0.4 $\rightarrow$ 5

Table 3.3 Summary of the size-parameters with respect to the frequency of the aggregates analogs  $AG_{SEM}$ ,  $AG_{005}$  and  $AG_1$

The experimental  $C_{ext}$  was determined for each of them from the single measurement of the scattered field in the forward direction at  $\theta_r = 0^\circ$  as explained in equation 3.13 according to the optical theorem. We remind here that the determination of  $C_{ext}$  utilizes the imaginary part of the scattered field, thus it can be only obtained with setups supporting vector measurement (amplitude and phase measurement). This measurement is very challenging: For each frequency, it relies uniquely on the measurement of the complex value of the scattered field in the forward direction which is the most difficult to extract. The incidence and total field have very similar values and their complex subtraction is sensitive to the random noise, as it can be seen in Figure 3.34. Moreover, the forward direction is where the amplitudes of the measured fields are the highest. Therefore, any power excess at this angle will create a non-linearity in the receiving devices and perturbs the measurement.

Although only one angular position is utilized by the optical theorem, the measurements have been made over the total angular excursion between  $\theta_r = -130^\circ$  and  $\theta_r = 130^\circ$  to allow the application of the drift correction and angular low pass filter post-processing.

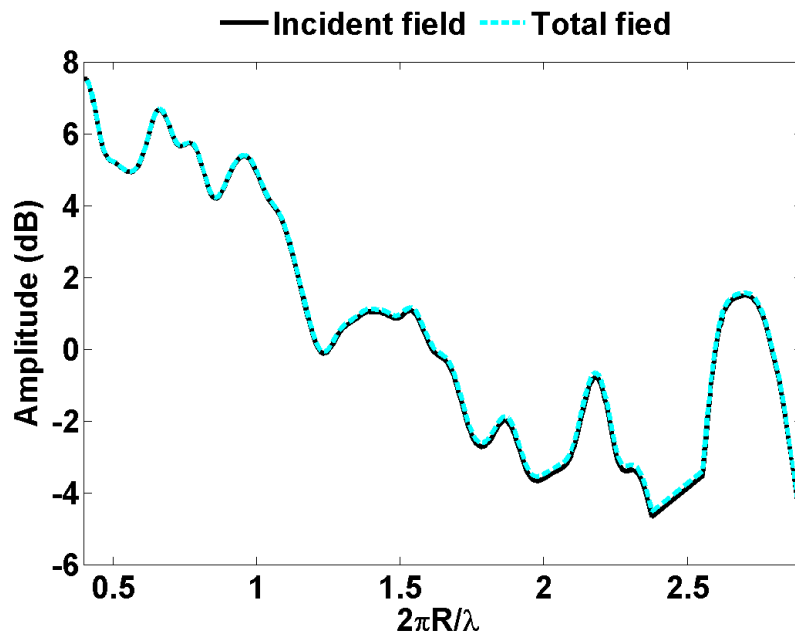


Figure 3.34 Amplitude in dB of the incident and total fields corresponding to the measurement of  $AG_{SEM}$  as a function of the size-parameter

For the realistic aggregate  $AG_{SEM}$ , the experimental  $C_{ext}$  is presented in Figure 3.35 and compared to DDA (a, b) and MOM (c, d) simulations corresponding to the three discretization. The  $C_{ext}$  are presented in  $m^2$  (a, c) and  $dBm^2$  (b, d). The Extinction Cross Section varies between  $-100 dBm^2$  and  $-60 dBm^2$  for  $x$  between 0.5 and 3 (b, d). The measured  $C_{ext}$  is very similar to DDA 50 simulation in (a). The noise on the measurement is very high for  $x$  below 1 where  $C_{ext}$  quite low values, below 80 has  $dBm^2$  and the discrepancies with simulation are high. In this region the signal to noise ratio is low and the experimental determination is difficult. When  $x$  increases, and specifically above 1, the noise is reduced and the measured  $C_{ext}$  is in a good agreement with the simulated one.

From Figure 3.35-a, where the experimental  $C_{ext}$  is compared to the DDA simulation, the  $C_{ext}$  plots from DDA 50, DDA 25 and DDA 13 are very comparable when the  $x$  is below 1.6. In this range of  $x$  it is not necessary to have a highly discretized model. When the size-parameter increases the discrepancies between the three simulations increase and it is therefore necessary to rely on the simulation correspondent to the highest discretization (DDA 50) for accurate results.



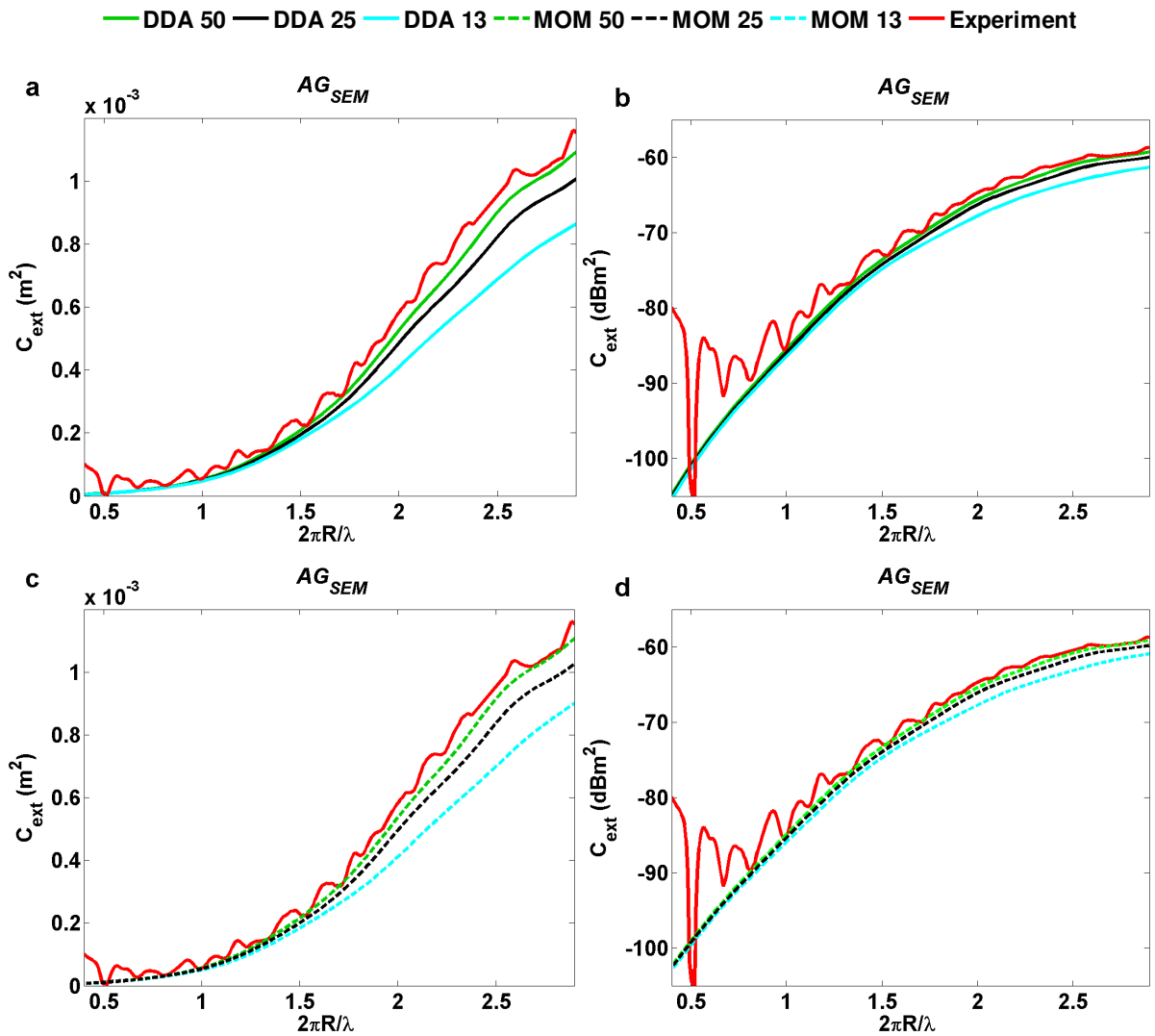


Figure 3.35  $C_{ext}$  from experiment, three DDA simulations and three MOM simulations for the aggregate  $AG_{SEM}$  as a function of the size-parameter. (a) Experiment and DDA simulations in  $m^2$ . (b) Experiment and DDA simulations in  $dBm^2$ . (c) Experiment and MOM simulations in  $m^2$ . (d) Experiment and MOM simulations in  $dBm^2$

From Figure 3.35-a and Figure 3.35-b (respectively Figure 3.35-c and Figure 3.35-d) where the experimental  $C_{ext}$  is compared to the DDA (respectively MOM) simulation, the  $C_{ext}$  plots from DDA 50, DDA 25 and DDA 13 (respectively from MOM 50, MOM 25 and MOM 13) are very comparable for  $x$  is below 1.6. In this range of  $x$  it is not necessary to have a highly discretized model. When  $x$  increases, the discrepancies between the three simulations increase. There are two reasons for this behavior at high values of  $x$ . First, when the cube's size is large (typically for DDA 13 and MOM 13), the object "seen" by the incident wave is different from the real target that is seen by the illumination in the experiment. Second, the considered approximation that the field inside each cubic cell is uniform become false as  $x$  increases.

Overall, the measurement of  $C_{ext}$  is validated by the fact that the two simulation methods give very close values. It is necessary to rely on the simulations made with the DDA 50 and MOM 50 for accurate results.

The Extinction Cross Sections of  $AG_{005}$  and  $AG_1$  from experiment and simulation are shown in Figure 3.37 at the two orientations  $\theta_o = 0^\circ$  and  $\theta_o = 90^\circ$  (Figure 3.36).

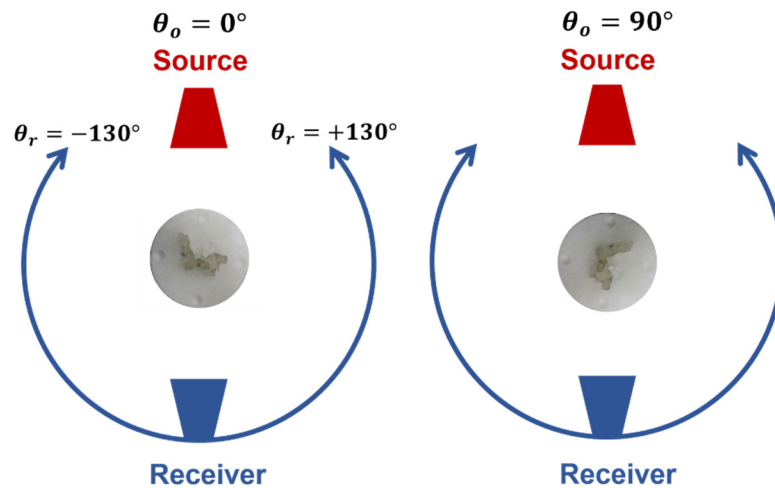


Figure 3.36 Schematic showing the orientation of the aggregates  $AG_{005}$  and  $AG_1$  at  $\theta_o = 0^\circ$  and  $\theta_o = 90^\circ$

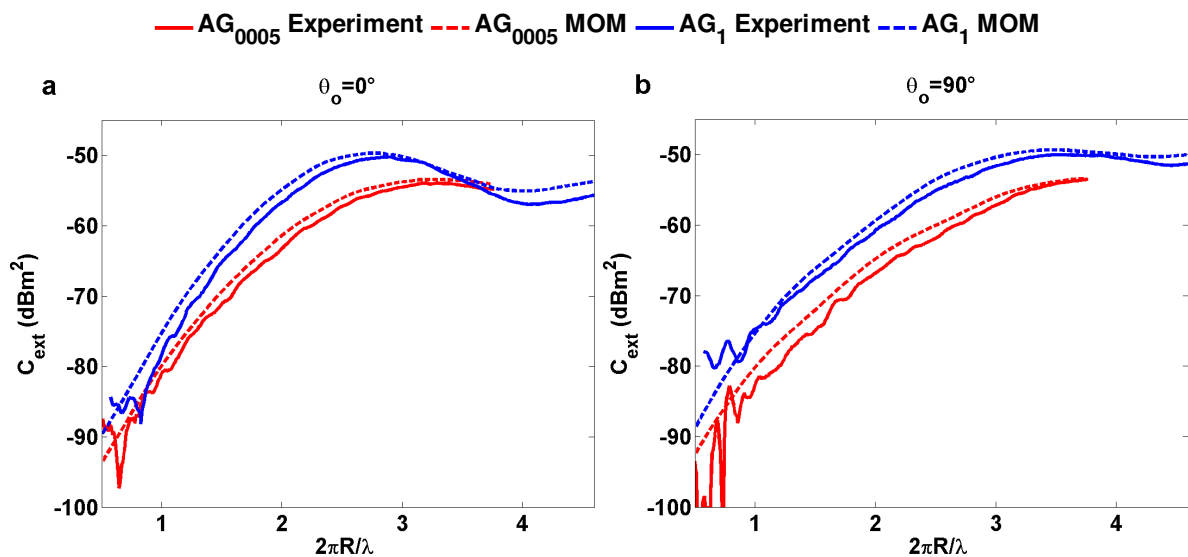


Figure 3.37  $C_{ext}$  from experiment and MOM simulation in  $\text{dBm}^2$  for the two aggregates  $AG_{005}$  and  $AG_1$  as a function of the size-parameter in two orientations (a)  $\theta_o = 0^\circ$  and (b)  $\theta_o = 90^\circ$

$AG_{005}$  and  $AG_1$  have larger volumes than  $AG_{SEM}$ , thus their size-parameter is larger as seen on the figure. The values of their  $C_{ext}$  reach higher values than those of  $AG_{SEM}$ , up to  $-50 \text{ dBm}^2$ . The experimental results are in a quite good agreement with the simulated ones for the two aggregates at the two orientations except for  $x$  below 1 where the values of  $C_{ext}$  are quite low ( $-80 \text{ dBm}^2$  and below) and the noise fluctuations appear.

### 3.3.7 Conclusion

In this section, we addressed the measurement of the Extinction Cross Section of soot aggregates analogs thanks to the optical theorem. First, the soot aggregates were scaled from the optical domain to microwaves and the soot aggregate of complex shape were manufactured in stereolithography at the CTTM. The investigated analogs have different volumes, which advantageously allow to evaluate the accuracy of the measured  $C_{ext}$  with respect to the analog size.

The  $C_{ext}$  was measured according to the optical theorem. Thus, the specificity of this measurement is that it uses only the measured scattered field in the forward scattering direction, which is the most sensitive to the experimental noise.

The comparison between measurement and simulation showed that accurate measurement of the Extinction Cross Section is obtained for values above  $-80 \text{ dBm}^2$ . Below this value, the measurement is quite noisy and we can consider that the accuracy of the measurement setup reaches its limit.

Moreover, it was possible to refer to the experimental  $C_{ext}$  to evaluate the impact of the discretization of the aggregate 3D model in the DDA and MOM on the calculation accuracy.

## 4 MICROWAVE ANALOG EXPERIMENTS IN QUASI-MONOSTATIC CONFIGURATION

---

### 4.1 INTRODUCTION

This chapter addresses microwave analogs experiments in quasi-monostatic configuration within a research collaboration with the Laboratoire d'Electronique et Electromagnetisme (L2E) at the Université Pierre et Marie Curie in France. Our collaborators at L2E work on the numerical development of a model for the electromagnetic scattering from large scenes composed by metal targets and dielectric targets. The aim of the numerical model is to evaluate the more suitable radar configuration for targets detection in forest environment [120]. Within this collaboration, my role was to prepare the measurement setup of the CCRM for quasi-monostatic experiments and to carry out controlled measurements on a scaled model of dielectric and metal objects.

### 4.2 MEASUREMENT PROCEDURE

The measurements are made using the quasi-monostatic configuration discussed in 1.5.4. Radar scattering models for a metal target existing in a forest environment are usually designed to operate in the VHF band between 320 MHz and 480 MHz. The microwave analog situation is reduced with a scaling factor of 1/25 and the experiments are made in the frequency band from 8 GHz to 12 GHz. The ground is represented by a flat metal plate with 1 m diameter, considered infinite.

The metal plate is glued on top of an expanded polystyrene support, which is placed on the top of the central mast. The metal plate is present during the measurement of the total and incident fields. The targets to be measured are therefore aligned at the center of the metal plate. The measurement configuration was explained in section 1.5.4. The measurements are made using the X-band horn antennas and the quasi-monostatic angle between them is  $12^\circ$ . The distance between the antennas and the origin O at the center of the metal plate is 1.648 m, which is around 41 m at the initial scale. The displacement of the wagon carrying the antennas on the vertical arch is denoted by the angle  $\varphi_s$ . The measurements are made in the two co-polarization cases  $\theta\theta$  and  $\varphi\varphi$  defined in 1.4.3. The measurement configuration is summarized in Figure 4.1 and Figure 4.2. The measurements are made using the Hardgating system with a frequency step of 0.5 GHz between 8 GHz and 12 GHz.

The commonly used radars for the detection of metal targets in forests require elevation angles between  $20^\circ$  and  $70^\circ$ . We therefore focus the analysis of the results at  $\theta_s$  between  $20^\circ$  and  $70^\circ$ . The settings of the setup are summarized in Figure 4.3.

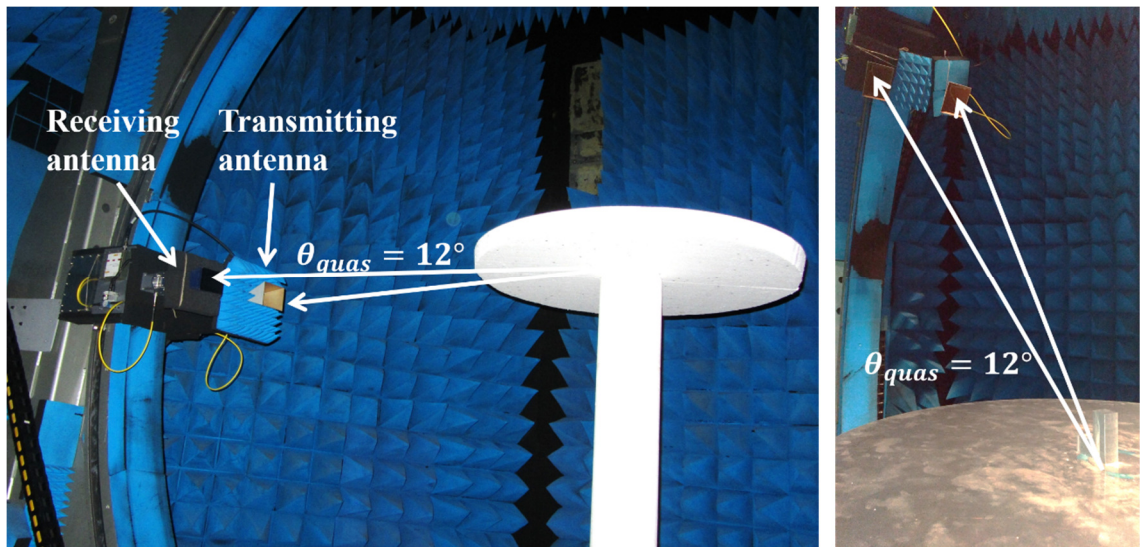


Figure 4.1 Photography of the quasi-monostatic measurement showing the transmitting and receiving antennas on the wagon, the metal plate and the quasi-monostatic angle

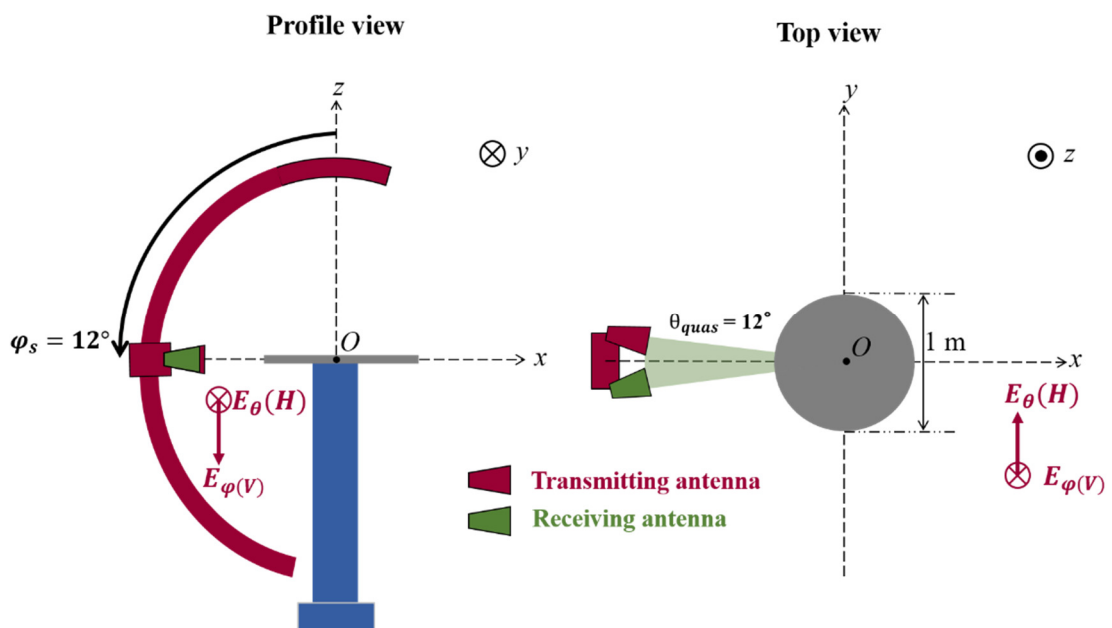


Figure 4.2 Schematic explaining the quasi-monostatic measurement and the polarizations definition

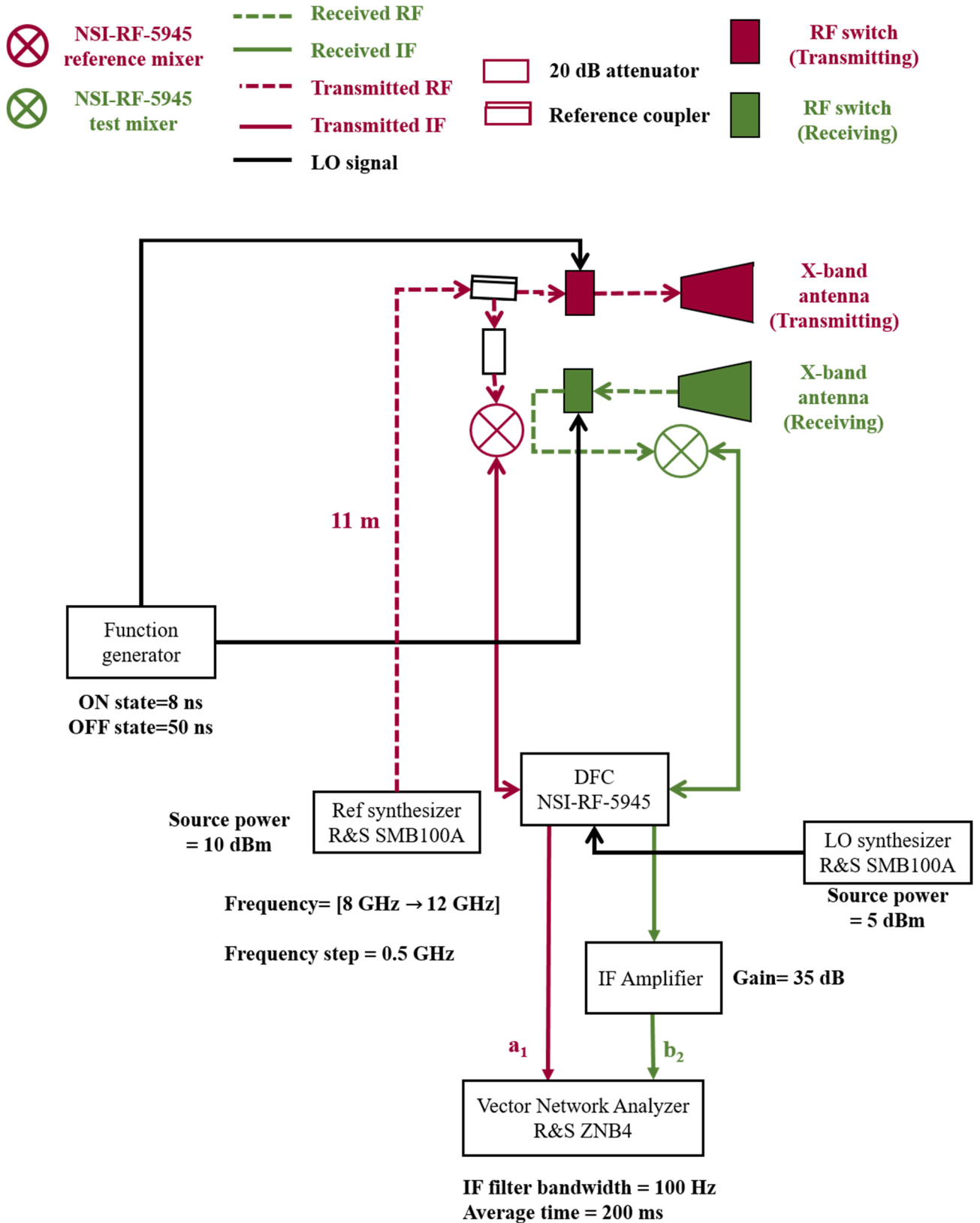


Figure 4.3 Schematic showing the settings of the setup for the quasi-monostatic measurement of the forest scaled model. Measurements are made in Hardgating mode with the X-band antennas

### 4.3 REFERENCE TARGET: SQUAT METAL CYLINDER

A metal squat cylinder was chosen as a reference target to calibrate the measured scattered field. The cylinder has a diameter of 95 mm and a height of 44.45 mm. During the measurement, the center of the cylinder is aligned at the center of the metal plate on one of its two parallel faces. It was chosen for two reasons: first, it has relatively high electromagnetic signature which can overcome the experimental noise. Second, it is asymmetric in the measurement configuration so that its scattered field is variable with respect to the monostatic angle  $\phi_s$ . Examples of the fields scattered by this cylinder are presented in Figure 4.4 in  $\theta\theta$  and  $\phi\phi$  polarizations at 9 GHz and 11 GHz. They are compared to simulations obtained with the developed numerical software. Quite good measurement accuracy was obtained for this target.

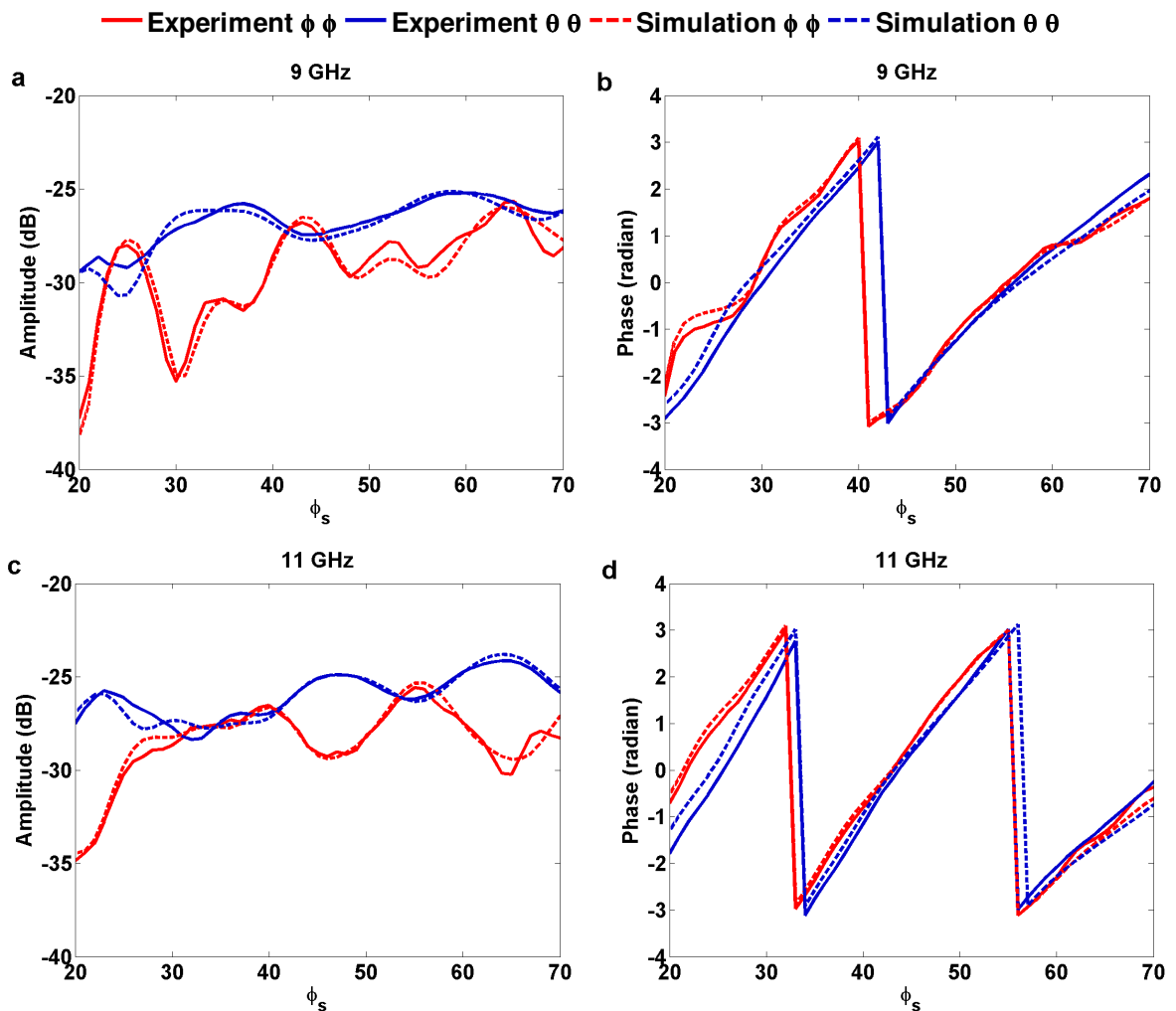


Figure 4.4 Comparison between experimental and simulated fields scattered by the squat metal cylinder. (a) Amplitudes at 9 GHz. (b) Phases at 9 GHz. (c) Amplitudes at 11 GHz. (d) Phases at 11 GHz

#### 4.4 SINGLE METAL AND DIELECTRIC TARGETS

We started with simplified configurations where a simple target is placed on the metal plate. One dielectric and one metal targets were chosen. The dielectric target is a Plexiglas cylinder of square section ( $160\text{ mm} \times 9\text{ mm} \times 9\text{ mm}$ ) with  $\epsilon = 2.6 + 0.02j$  (Figure 4.5-a). The PEC metal target has the shape of L with dimensions ( $28\text{ mm} \times 76\text{ mm} \times 68\text{ mm}$ ) (Figure 4.5-b). The measurement configuration is shown in Figure 4.6.

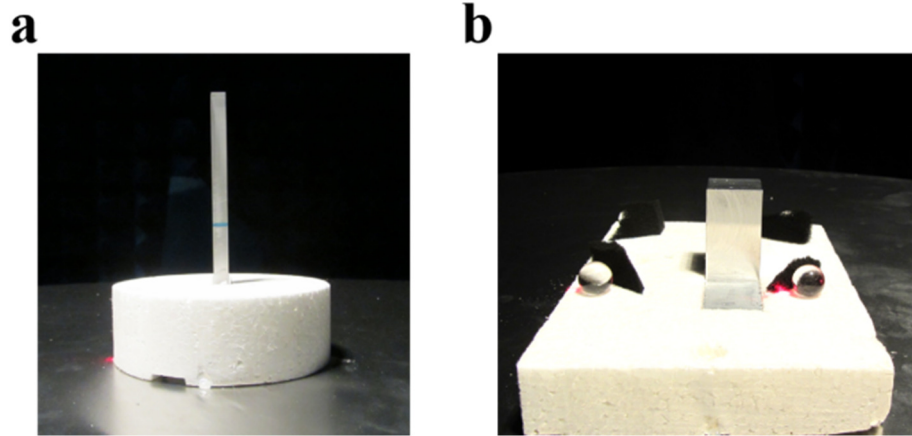


Figure 4.5 (a) The Plexiglas cylinder. (b) The metal cylinder

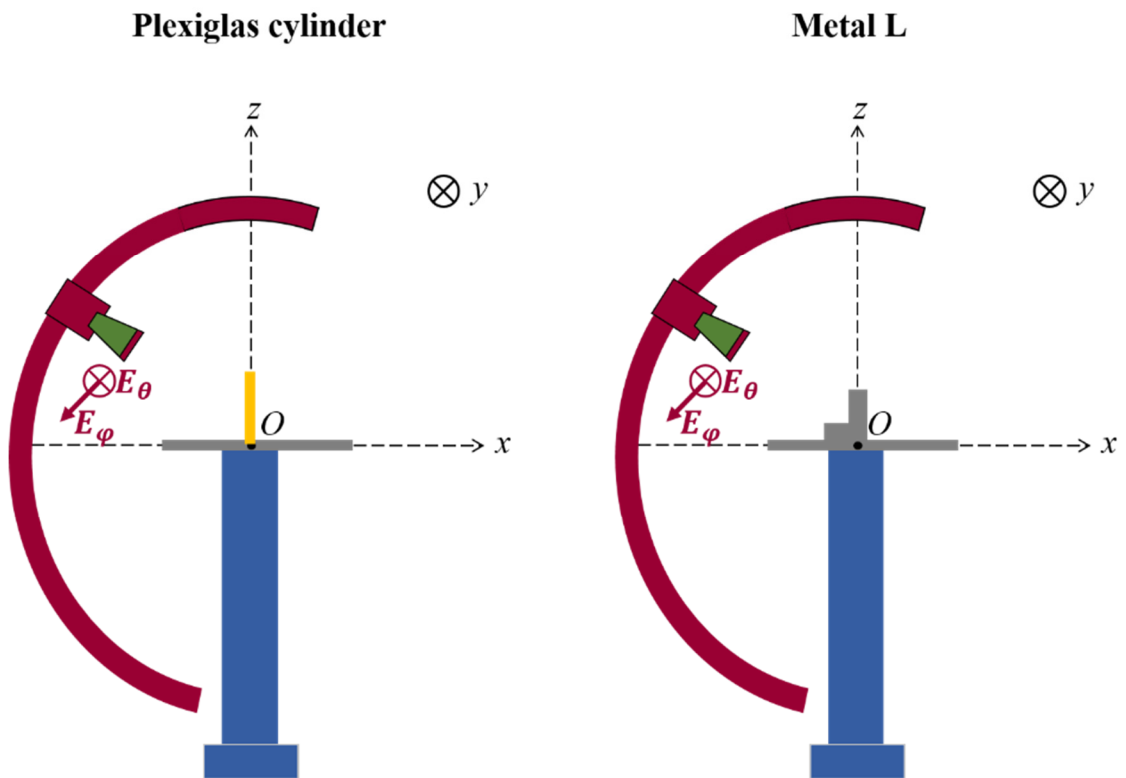


Figure 4.6 Schematic showing the placement of the Plexiglas cylinder and the metal L during the measurement



The experimental fields scattered by the Plexiglas cylinder and metal L are compared to simulations at 9 GHz and 11 GHz in  $\theta\theta$  and  $\varphi\varphi$  polarizations in Figure 4.7 and Figure 4.8. The fields are very comparable in amplitude and phase and a good agreement is obtained.

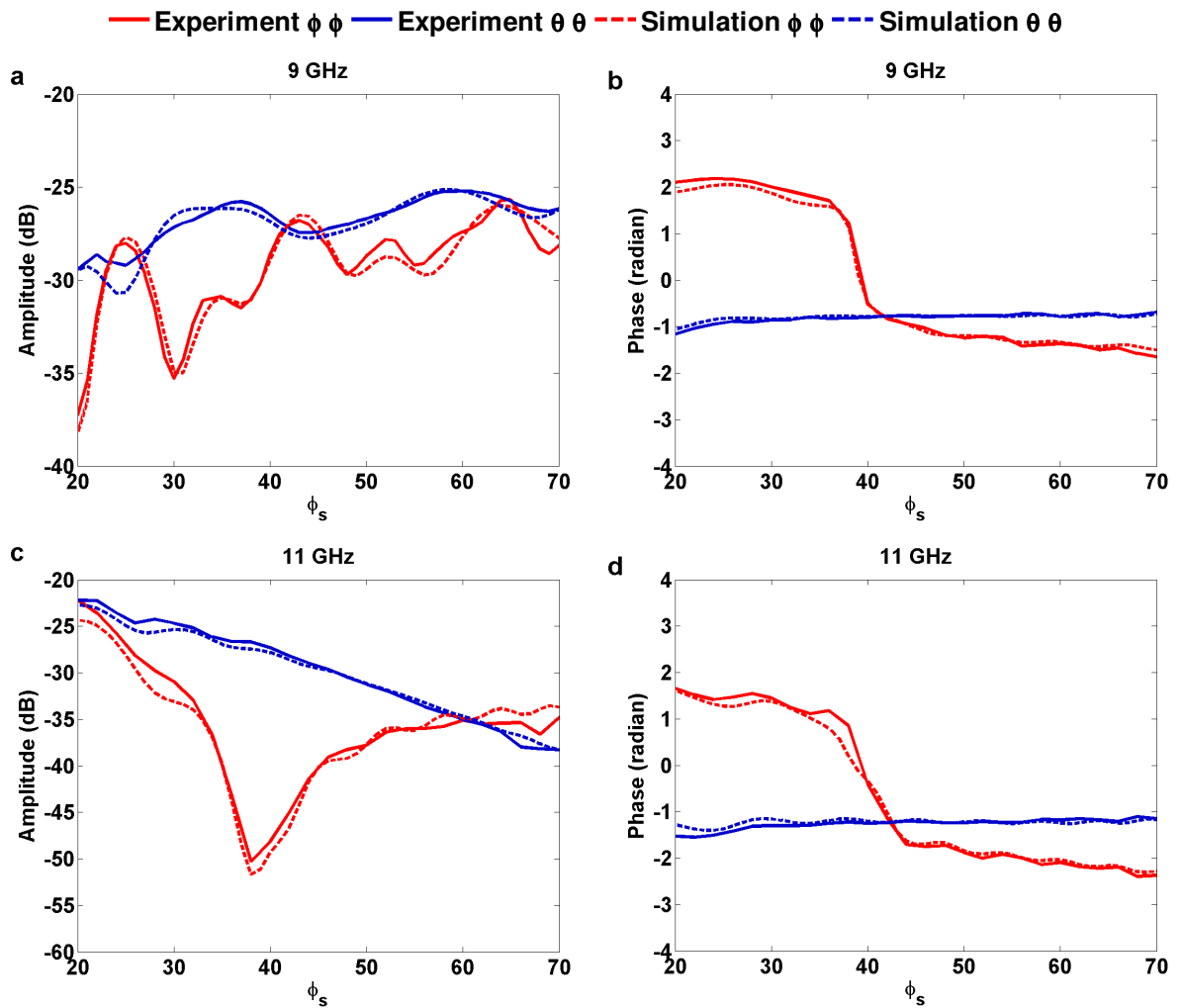


Figure 4.7 Comparison between experimental and simulated fields scattered by dielectric Plexiglas square cylinder in both  $\varphi\varphi$  and  $\theta\theta$  polarizations. (a) Amplitudes at 9 GHz. (b) Phases at 9 GHz. (c) Amplitudes at 11 GHz. (d) Phases at 11 GHz

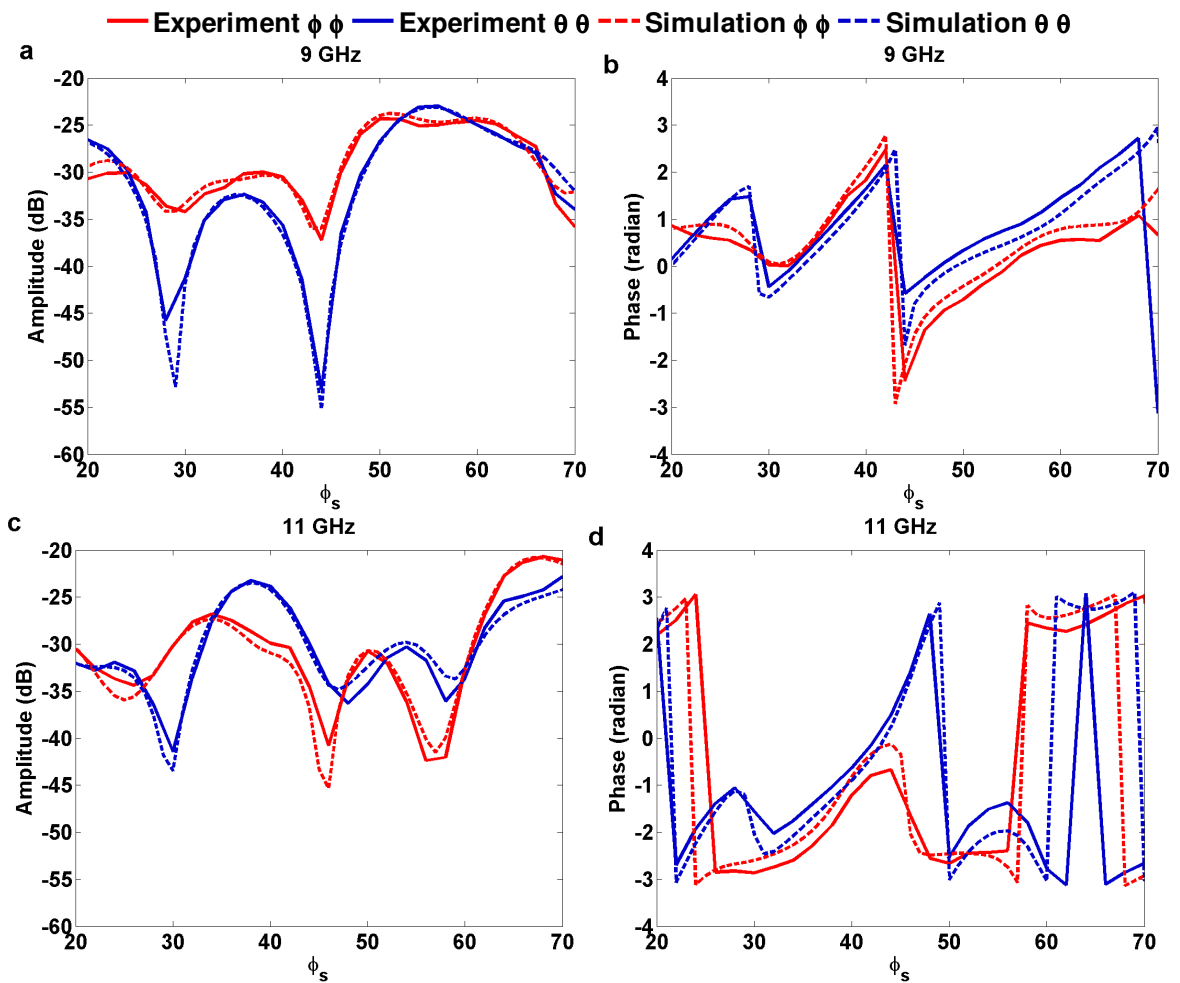


Figure 4.8 Comparison between experimental and simulated fields scattered by metal L in both  $\phi\phi$  and  $\theta\theta$  polarizations. (a) Amplitudes at 9 GHz. (b) Phases at 9 GHz. (c) Amplitudes at 11 GHz. (d) Phases at 11 GHz.

## 4.5 METALLIC AND DIELECTRIC TARGETS

After validating the accuracy of the measurement on a single target, the next step was to measure a combination of a metal target together with a dielectric target. The metal target is the same L object previously presented. The Plexiglas cylinder is not the ideal candidate to present the dielectric target since it has low permittivity and its signature will be masked by that of the metal L. In order to have a cylinder with high permittivity, close to that of trees, we processed as following: first, an empty cylinder with dimensions ( $160\text{ mm} \times 9\text{ mm} \times 9\text{ mm}$ ) was fabricated in 3D printing. The width of the walls of this cylinder is 1 mm. Second, a high permittivity liquid was prepared to be filled in the empty cylinder. This liquid was prepared by our partner Olivier Meyer at the laboratory GeePS at Centrale-Supelec who has also measured its complex permittivity. The real and imaginary parts of its permittivity are presented in Figure 4.9 as a function of the frequency. As seen on the figure, the permittivity has important variations with respect to the frequency.

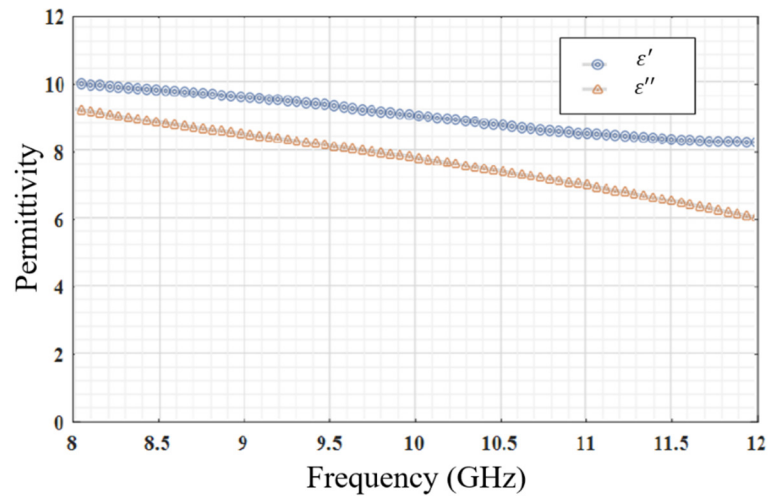


Figure 4.9 Variation of the real and imaginary parts of permittivity of the prepared liquid as a function of the frequency

Three positions of the dielectric cylinder around the metal L were studied to test the influence of the position of dielectric target of the global scattered field. We have considered the cases where the dielectric is ahead, behind and beside the metal L. The exact positions are shown on the schematic in Figure 4.10 and pictures of targets are shown in Figure 4.11.

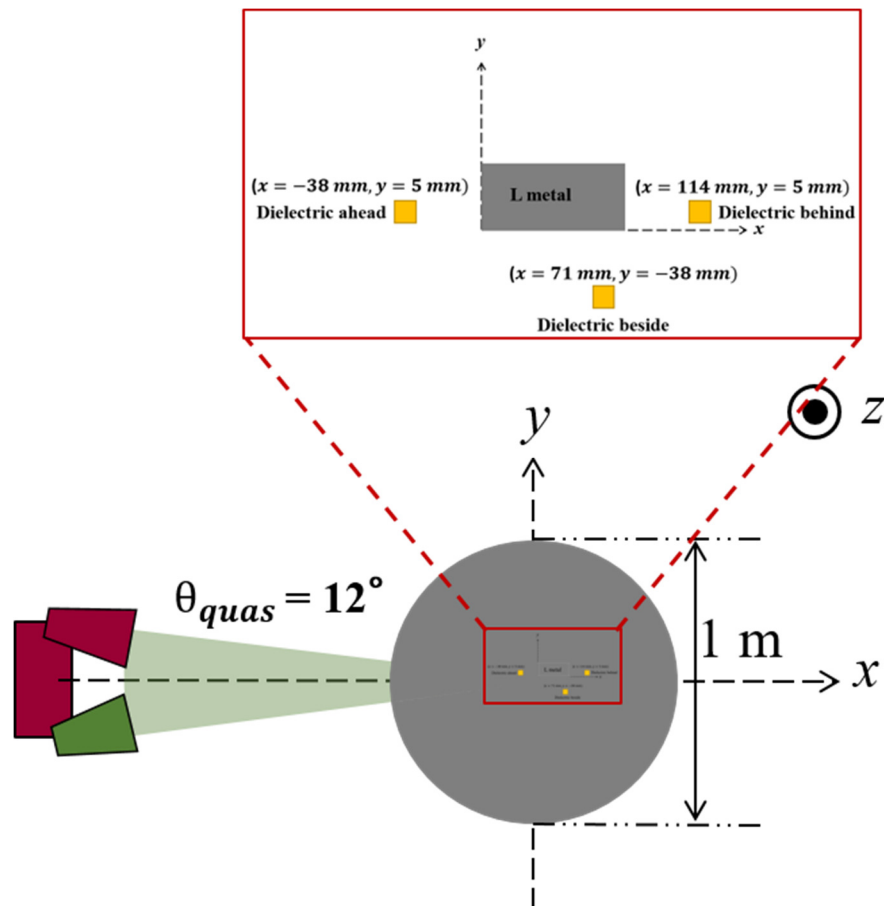
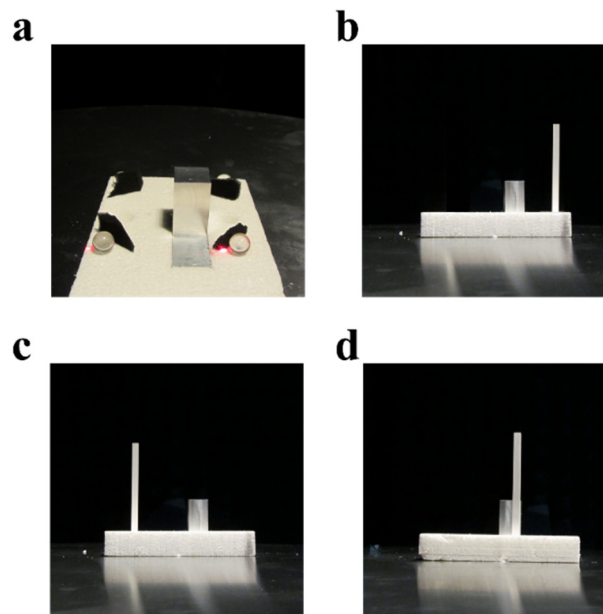


Figure 4.10 Schematic showing the positions of the dielectric cylinders and the metal L in the three studied cases



*Figure 4.11* Photography of the combinations of the dielectric cylinder and metal L placed in their polystyrene holder. (a) L alone. (b) L + dielectric behind. (c) L + dielectric ahead. (d) L + dielectric beside

The measurements were made separately in the three situations, for the dielectric ahead, behind and beside the metal L, and indeed, with the L alone that was presented in the previous section. The experimental results are compared to the simulations in amplitude and phases in the three situations of positions at three different frequencies in Figure 4.12, Figure 4.13, and Figure 4.14. From the comparisons, it can be noticed that the experiments and simulations have the same behavior, and more in phases than in amplitudes. However, the discrepancies are non-trivial, and they are much higher than for the metal L and Plexiglas dielectric presented in the previous section. Those discrepancies are most probably related to inaccurate values of the permittivity in the simulation codes, because there were high uncertainties on the measured values of permittivity. In addition, the cylinder containing the high permittivity liquid was not modeled in the simulation algorithm but only the liquid was modeled, which can also introduce differences. In the holograms in Figure 4.15 we compare the amplitudes of the measured scattered fields as a function of the frequency and the monostatic angle between the metal L alone and the three configurations of L + dielectric cylinder. From those comparisons it can be noticed that the scattered fields in the case of the dielectric cylinder ahead and beside the metal L are different from the case of the L alone which means the dielectric has important contribution in the scattered field (Figure 4.15-a, c and d). However, the results are very similar between the L (Figure 4.15-a) and L + dielectric behind (Figure 4.15-b) which indicates that in the latter case the scattered field is issued mainly from the L. In fact, the presence of the L has masked the effect of the dielectric.

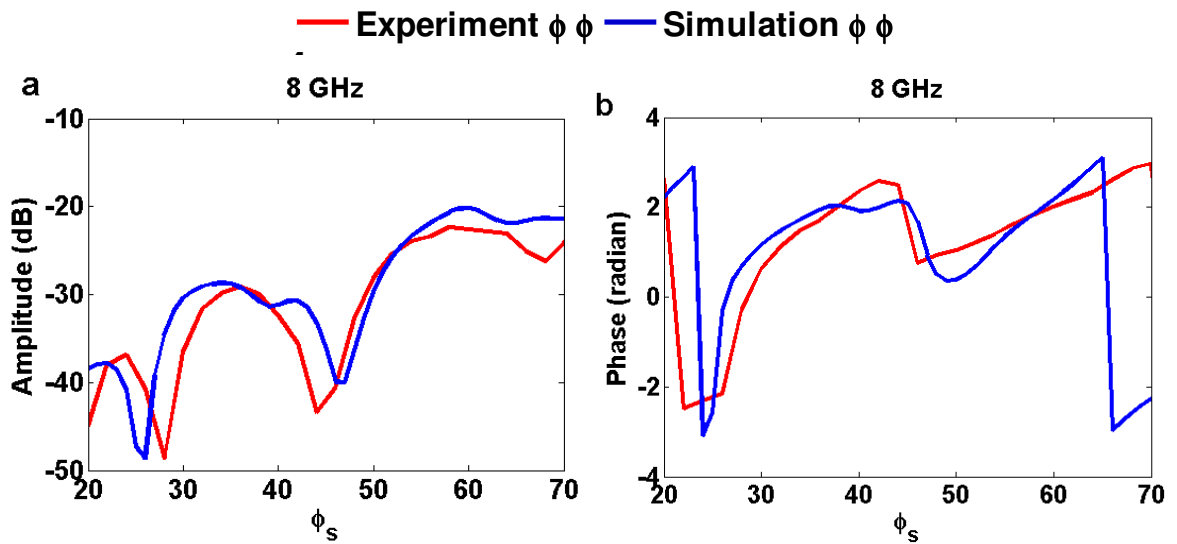


Figure 4.12 Variation of the scattered field in amplitude and phase from experiments and DEMOS simulation at 8 GHz in  $\phi\phi$  polarization for the case of dielectric is behind the metal L

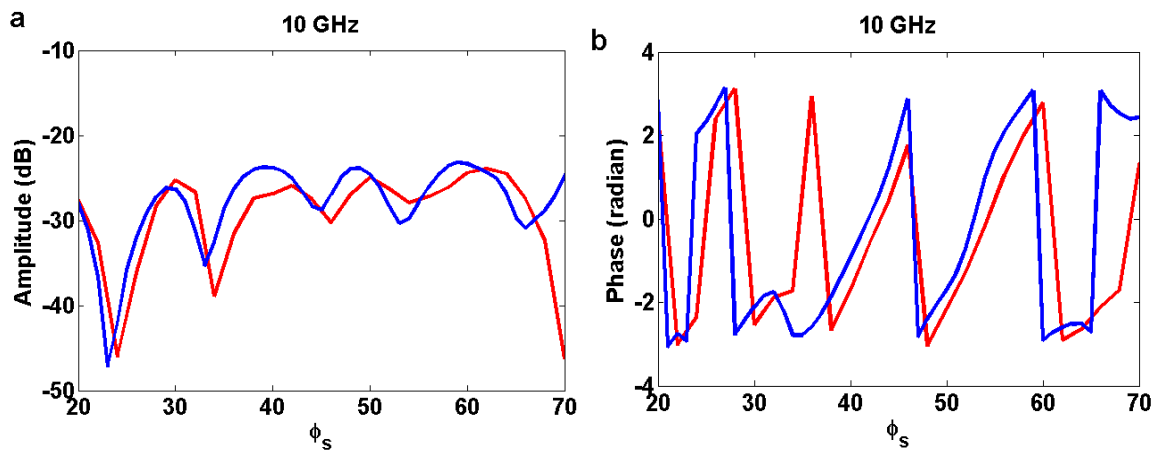


Figure 4.13 Variation of the scattered field in amplitude and phase from experiment and simulation at 11 GHz in  $\phi\phi$  polarization for the case of dielectric is ahead the metal L

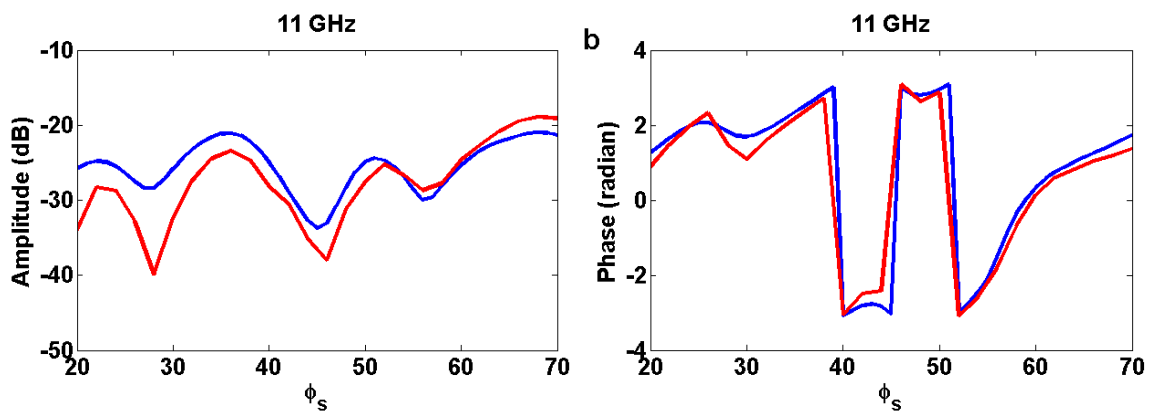


Figure 4.14 Variation of the scattered field in amplitude and phase from experiments and DEMOS simulation at 11 GHz in  $\phi\phi$  polarization for the case of dielectric is beside the metal L

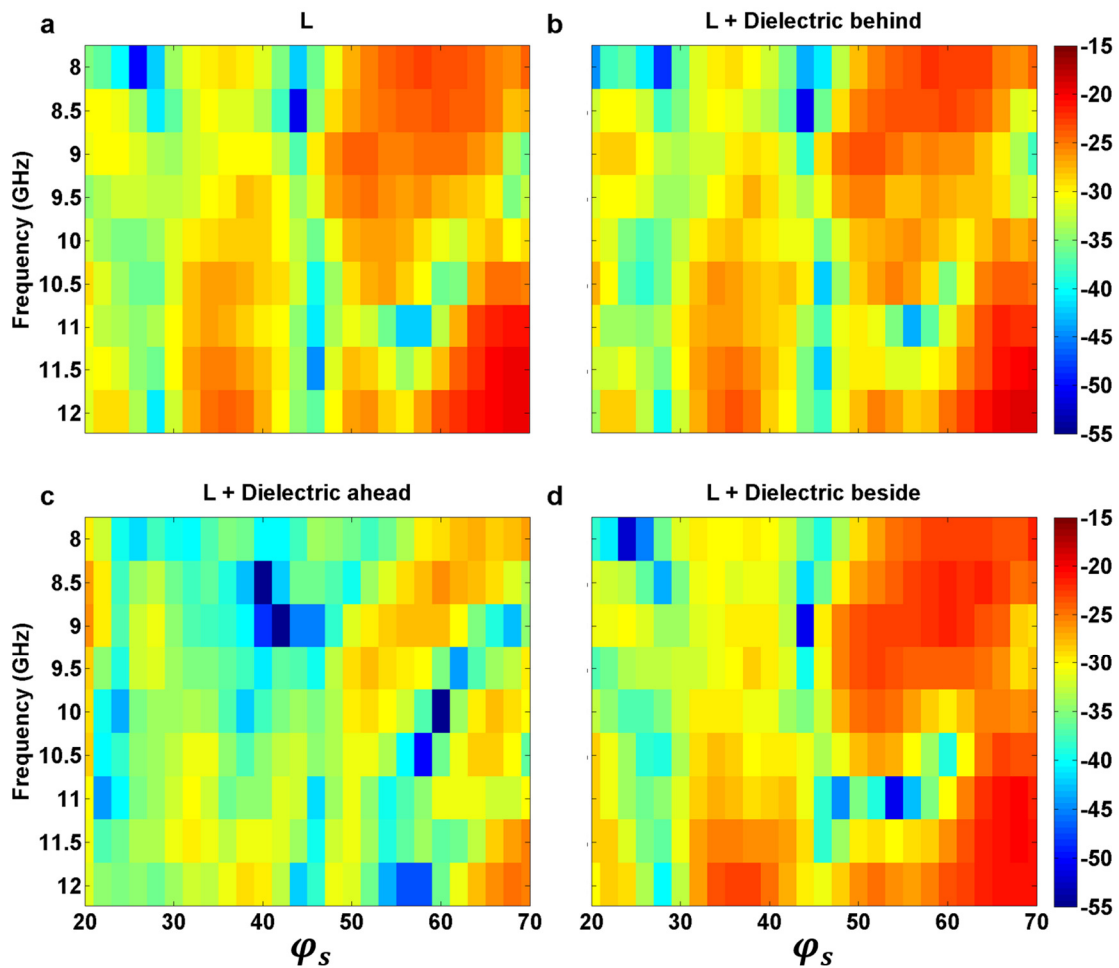


Figure 4.15 Holograms of the amplitudes of the experimental scattered fields obtained with (a) metal L. (b) metal L+ dielectric behind. (c) L + dielectric ahead. (d) L + dielectric beside

#### 4.6 FOREST SCALED MODEL: TREES ANALOGS WITH METAL TANK

In this last section, we propose to study the scattering by a complex scene containing trees analogs and a complex shaped metal object. The aim to use such configuration is to study the effect of the trees to hide the signature of the metal target. In order to mimic the forest model, five trees analogs were fabricated in additive manufacturing. The inner volume of the trees is empty and it was filled with the same high permittivity liquid which was used with the cylinder in 4.6. The trees are exactly the same, each of them has a height of 20 cm and it has 6 branches. The metal target was chosen to be a scaled model of a real tank, with the same scaling factor of 1/25 used along this study. The tank is 10.40 cm height, 12.80 cm width and 6 cm depth. The tank analog was first manufactured with plastic in additive manufacturing. Next, in order to make it PEC, it was totally covered with aluminum tape with thickness of 1 mm. The trees and tank analogs are shown in Figure 4.16.

A specific polystyrene holder was fabricated to align the trees and the tank in the measurement setup on top of the circular metal plate. Each of the three cases of the tank alone, trees alone and trees + tank was measured separately, and each of them in the four orientations shown in Figure 4.17.

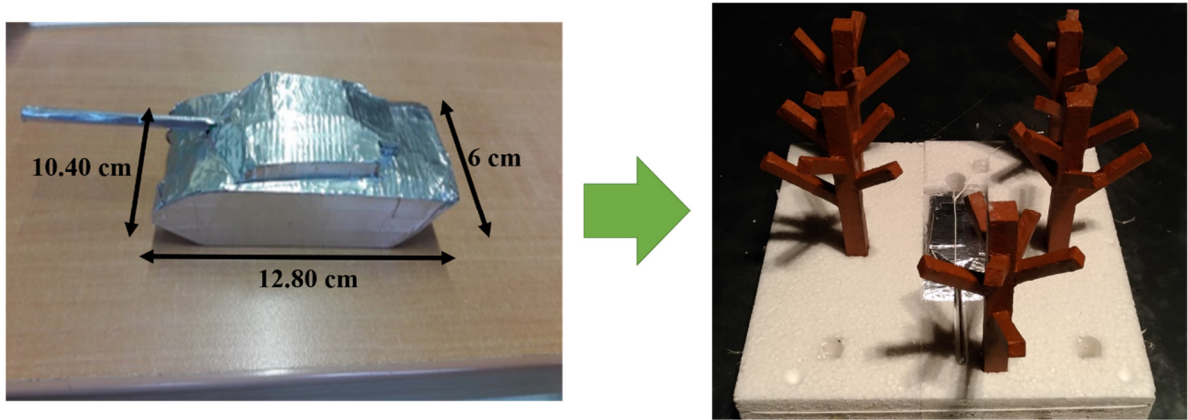


Figure 4.16 Pictures of the trees and tank analogs. (a) Tank analog alone. (b) The complete scene composed by the five trees analogs and the tank at the middle, all of the place at the center of the specific polystyrene holder

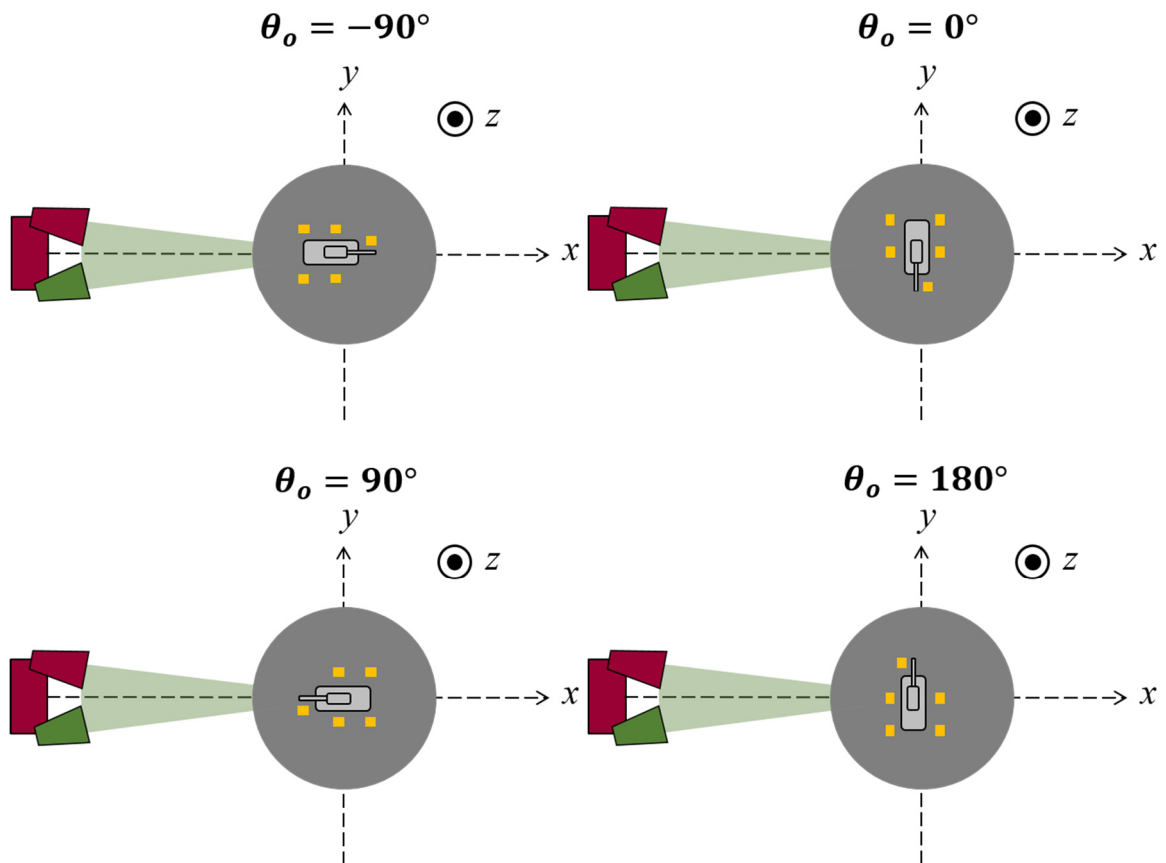


Figure 4.17 The four investigated orientations of the scene composed of the five trees analogs and the tank analog

We mention here that this complex scene was not studied in simulation and we only present the corresponding experimental results. The Figure 4.18 shows a comparison in amplitude and phase of the experimental results in the studied scenarios: tank, trees and tank + trees. The results correspond to the case of  $\theta_o = 90^\circ$ . It can be noticed from the figures that the fields scattered by the trees and the fields scattered by the trees+ tank are very comparable in amplitude and phase and both of them have important differences with the fields scattered by the tank alone. It can be noticed from this behavior that the electromagnetic signature of the tank is hidden by the presence of the trees.

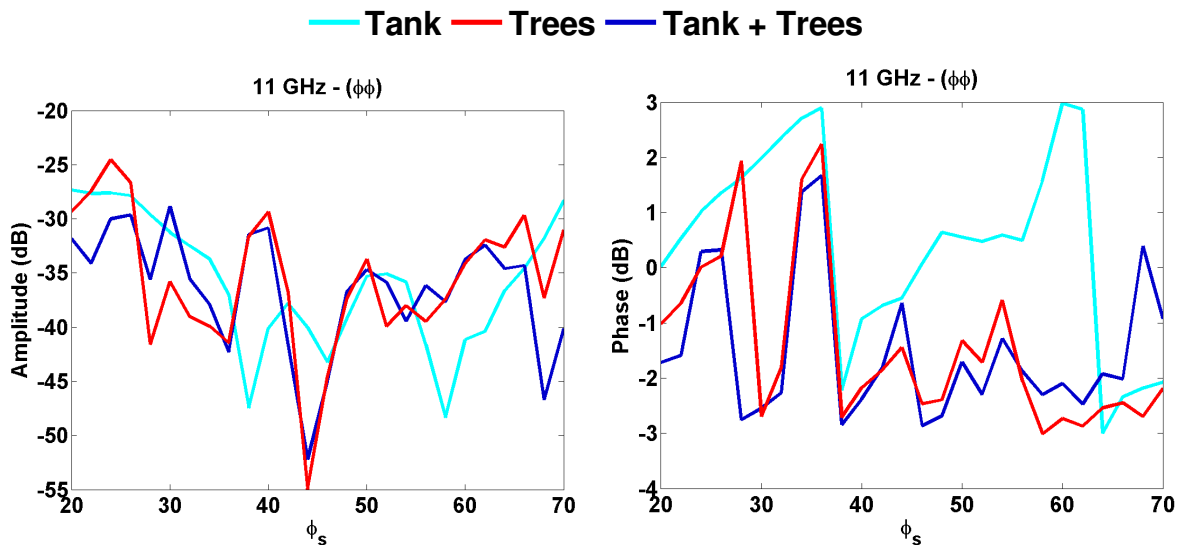


Figure 4.18 Experimental scattered fields by the tank, trees and tank + trees at 11 GHz in  $\varphi\varphi$  polarization in amplitude and phase

The Figure 4.19 shows the amplitudes holograms of the scattering corresponding to the three studies cases in both  $\varphi\varphi$  and  $\theta\theta$  polarizations as a function of all the frequencies and the receiving angles. When comparing the three holograms in  $\varphi\varphi$  ( $\theta\theta$ ) polarization to each other in the figures a, c, and e (b, d and f), one can notice that the field scattered by the tank has comparable amplitude values for almost all the receiving angles and frequencies (above -25 dB) and that they are different from those of the trees and trees + tank. In these two latter cases, the scattered fields are quite comparable and most of the amplitudes are below -25 dB. This comparison shows that the presence of the trees, and specifically at  $\theta_s$  above  $45^\circ$ , masks at least partially the field scattered by the tank.



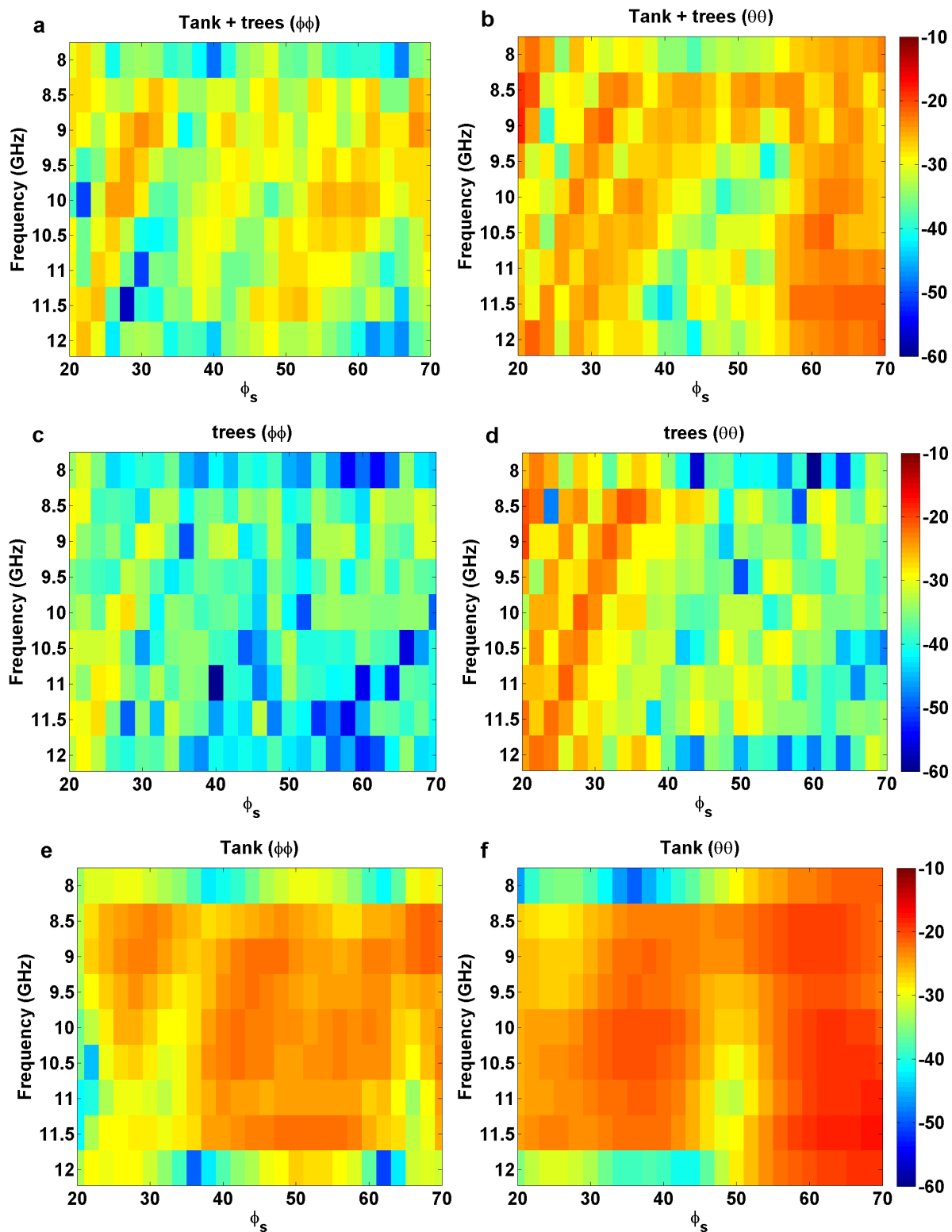


Figure 4.19 amplitude of the fields scattered by the components on the scene. (a) Tank + trees in  $\phi\phi$ . (b) Tank + trees in  $\theta\theta$ . (c) Trees in  $\phi\phi$ . (d) Trees in  $\theta\theta$ . (e) Tank in  $\phi\phi$ . (f) Tank in  $\theta\theta$

## 4.7 CONCLUSION

In this chapter, the microwave analogy was applied to a case of forest scene containing dielectric and metal targets. The real configuration was downscaled by a factor of 25 and the measurements were made in quasi-monostatic configuration, with a quasi-monostatic angle of  $12^\circ$ . We begin the study with same configurations containing a single target, metal or dielectric placed on a metal plate representing the ground. The aim of starting with simple targets was to assess the alignment accuracy in the quasi-monostatic configuration, and also the measurement accuracy. We mention here that the measurements were made in Hardgating at only 9 frequencies between 8 GHz and 12 GHz, and what makes these measurements more challenging than the bistatic measurement is that the drift correction and lowpass filtering post-processing are not used since they are not yet adapted to the quasi-monostatic case. The experimental results with a single target were compared to simulations and quite good agreement was obtained even on the phases of the fields, which indicates a good measurement accuracy. In the next step, a combination of one metal target and one dielectric target was studied. The dielectric here is obtained by filling an empty cylinder with a high permittivity liquid. Unfortunately the knowledge of the high permittivity liquid was not enough precise to be really confident that the simulated scene is really comparable to the measured one. The comparison between experiments and simulations was thus just acceptable here.

We end up this study with a complex scene containing a small forest scaled model containing five trees analogs and a metal tank analog. The tank analog was obtained in additive manufacturing using polymer material and was later fully covered with aluminum tape to make it PEC. The trees analogs were also made in additive manufacturing with an empty structure in order to fill it with the high permittivity liquid. The tank was placed between the trees analogs and the whole scene was measured. It was experimentally observed that in some conditions of the configuration, specifically for monostatic angles above  $45^\circ$ , the presence of the tank is masked by the presence of the trees with high permittivity.

Overall, we noticed that the accuracy of the quasi-monostatic measurements is lower than that of the bistatic measurements. The reason behind is that no post-processing is applied on the quasi-monostatic measurements. The drift correction and the low pass angular filter that had been proposed in the past are dedicated to the case where the transmitting antenna has a fixed position and the receiving antenna is moving. Therefore, it would be interesting in the future to adapt those post-processing techniques to the quasi-monostatic configuration. In addition, the positioning system used for azimuthal bistatic measurement is more accurate than the wagon on the vertical arch that is used for monostatic measurements.

## GENERAL CONCLUSION AND PERSPECTIVES

---

The microwave analogy is a useful approach to experimentally investigate a scattering problem when targets are very large (vehicles, trees, comets, etc.) or very small (nanoparticles, microorganisms, etc.). The experiment is therefore scaled to the microwave range and the target is mimicked by a centimeter-sized analog, while maintaining the same initial wavelength over target dimension ratio and conserving the same initial permittivity and permeability. Microwave analogy fills a special need because it allows high controllability of the experiment parameters. Scaled analogue measurements require the construction of analog targets and require a versatile and accurate measurement device.

This PhD thesis aims at widening the application of the microwave analogy by adopting the appropriate techniques to create objects of controlled shapes and permittivity using additive manufacturing technologies, as well as optimizing the measurement setup and enhancing the measurement accuracy. A special interest is given for low scattering targets with low permittivity contrasts and/or small dimensions compared to the wavelength. The microwave analogy experiments are made in the anechoic chamber of the Centre Commun de Ressources en Microondes. In the past, the measurements were made with an “old” setup having limited features and most of the measured targets were fabricated using classical machining techniques with lack of solutions to control their properties.

I began this work with extensive study on the characterization of the measurement setup, whose devices were previously renewed. The nature and levels of random noise affecting the measured scattered field was characterized from repetition measurements in bistatic azimuthal configuration. From the noise characterization, it was possible to determine associated uncertainty to each value of the experimental scattered field. The study shows that the measurement uncertainties are inversely proportional to the amplitude of the measured field. For the types of targets under study, the measurement accuracy is lower in the backward scattering direction, where the measured amplitudes are the lowest, and it is higher in the forward direction, where the measured amplitude are the highest. This study allowed to conclude that this behavior is most probably related to the measurement uncertainties of the VNA itself. In order to enhance the measurement accuracy while maintaining a linear operation in the receiving devices, I proposed a novel optimization technique which consists on angular zones decompositions with different power profiles. This technique benefits from the flexibility of the measurement devices that allows to adjust separately the levels of the reference ( $a_1$ ) and test ( $b_2$ ) signals at the input of each device in the measurement chain, to obtain the optimal

accuracy while avoiding a non-linear behavior. This technique has allowed to reduce the random noise especially in the backward directions, and it allowed to measure targets that were not measurable in the past, such as spheres with  $\epsilon'$  down to 1.1 and aggregate analogs with dimensions much smaller than the wavelength and complex shape.

The measurement accuracy enhancement was further addressed by investigating the filtering of the stray signals originated from undesired reflections within the anechoic chamber. A Hardgating system utilizing two RF switches and a function generator was installed to the measurement setup and its performance was evaluated with comparison to the traditional Softgating technique. Hardgating systems are most common in monostatic and quasi-monostatic RCS measurements and in quite large chambers but here it was used in both quasi-monostatic and bistatic measurements and in a relatively small chamber (gated width of 8 ns). The system showed good efficiency and provided, over the Softgating that requires high frequency sampling, the advantage of measurements time saving, which can be up to 85%. The employment of this system will be useful in the future in measurements for inverse problem purposes where measurements durations last many days even at a single frequency, so that Softgating cannot be applied. Another advantage is that Hardgating is independent of the antennas bandwidth, which is required to be large enough in soft-gated measurement. The Hardgating system showed more efficiency in quasi-monostatic measurements where the delay between the incident and scattered signals is large enough to clearly isolate the scattered one. In bistatic configuration it is also possible to filter out the scattered signal in the backward direction but not in the forward because the delay between the incident and scattered signals is almost negligible. It is also important to mention here that before choosing between Softgating and Hardgating, the time response of the target should be estimated. Hardgating can only be selected if the response of the target in time is shorter than the duration of the ON state of the receiving switch, which is equal to 8 ns in the studied configuration. For targets with longer duration response, the Softgating should be selected. Hardgating was used in this thesis measurements of the spheroidal microalgae analogs with  $\epsilon'$  down to 1.29, the silicon spheres dimer with high  $\epsilon'$  and the trees analogs. For the soot aggregates analogs, Softgating was selected because high frequency sampling over large bandwidth was already needed for the determination of the Extinction Cross Section with a small frequency step.

Moreover, a new and optimized quasi-monostatic configuration was developed during this thesis. A transmitting and receiving antennas are now fixed on the same wagon on the vertical arch. The transmitting and receiving remote mixers which were more than many meters of cables away from the antennas are now fixed on the same wagon. This has overcome

the problems of power attenuation and phase shifts due to the propagating of the sensitive RF signals in long distances cables. The quasi-monostatic measurements are made in Hardgating mode. The efficiency of the quasi-monostatic configuration was validated through experiments on dielectric and metal cylinders as well as on trees analogs, and good measurement accuracy was obtained. In this configuration, direct coupling between the antennas is high. In addition, reflected signals from the ground of the chamber are also high due to the orientations of the antennas on the vertical arch. Therefore, the use of the Hardgating system has remarkably improved the quality of the measurements and it is recommended to be used in the future quasi-monostatic measurements. Still, the bistatic measurements showed higher accuracy than those in quasi-monostatic ones. The reason behind the difference is that no post-processing is applied on the quasi-monostatic measurements. The drift correction and the low pass angular filter that had been proposed in the past are dedicated to the case where the transmitting antenna has a fixed position and the receiving antenna is moving. Therefore, it would be interesting in the future to adapt the drift correction post-processing technique to the quasi-monostatic case.

The second main achievement of this thesis is the implication of the additive manufacturing stereolithography to control the geometric and electromagnetic properties of analogs. This process was initiated by a collaboration with the Centre de Transfert de Technologie du Mans. Three categories of analogs were investigated in terms of relative permittivity: analogs with low real part of permittivity ( $\epsilon' < 3$ ), objects with high real part of permittivity ( $\epsilon' > 3$ ) and objects with non-null imaginary part of permittivity ( $\epsilon'' \neq 0$ ). All the first tests to verify the actual characteristics of the build targets were made on spheres to determine their complex permittivity from far-field scattering measurements with comparison to Mie. The most interesting progress was made on the analogs with low  $\epsilon'$  by creating porous structures. In order to create and control the porosity, the proposed idea consists on creating the porosity using tetrahedral meshed structure in the volume of the analog. Two parameters are used to govern the porosity: the mesh size and the diameter of the tetrahedrons edges. It is possible to select their convenient values for a demanded value of  $\epsilon'$ . The meshing design is made with the free software "Gmsh" and the thickness of the edges is managed with the CAD commercial software "CATIA". Several spheres samples were manufactured in this technique with values of  $\epsilon'$  between 1 and 3, and their scattering measurements showed satisfactory results with comparison to Mie simulations.

The realized tests reveal that there are of course limits on the choice of the edges diameters and lengths beyond which the structure is not homogenized. The smaller the mesh

size, the more homogenized the object. At the same time, the objects with high number of meshes required long processing time to generate cylinders from the meshes edges. A trade off should be made between these two conditions especially with large volume. The results showed that for a homogenization of the meshed spheres, the common criteria of mesh size  $< \frac{\lambda}{10}$  is not a real limit. With mesh size of  $\frac{\lambda}{3.3}$ , quite satisfactory homogenization was obtained. For the edges diameters, good results were obtained with diameters below and equal to 0.56 mm, and discrepancies begin to appear with diameters equal to 1 mm. The investigation of other spheres with edges diameter 0.56 mm and 1 mm still worth verification.

For analogs with high  $\epsilon'$  and analogs with  $\epsilon'' \neq 0$ , the proposed ideas is to add convenient additive particles to the bulk material of the 3D printer to increase the real or the imaginary part of the permittivity. Tests were performed with alumina and barium titanate ceramics additives with different percentages to investigate  $\epsilon' > 3$  and with carbon and with zinc oxide to investigate  $\epsilon'' > 0$ . Unfortunately, in both cases it was difficult to reach significant changes in permittivity. The highest achieved value  $\epsilon'$  was 3.3 with 20% of alumina. For the control of  $\epsilon''$ , only a percentage of 0.5% of carbon and zinc oxide allowed to manufacture complete spheres, but this low percentage of lossy additives had no impact on  $\epsilon''$ . The main reason behind the failure with the used all type of additives is that when their percentage is increased, they block the complete photopolymerization of the liquid resin and only few layers of the object could be produced. One of the solutions to overcome the encountered difficulties in manufacturing composite materials is to utilize stereolithography printers which are specifically modified to deal with composite resins [81]. It would be also interesting to test other additive manufacturing technologies such as Fused Deposition Modeling. This technology has shown of some researches a capability to print with filaments made out of composite materials [90].

As a result, the use of additive manufacturing has paved the way for the investigation of new analogs whose controlled fabrication was difficult in the past. We were able to manufacture, for the first time, heterogeneous microalgae spheroidal analogs with  $\epsilon'$  down to 1.1 in the aim to answer the needs of our collaborators working in photobioreactors engineering. Scattering experiments on those fabricated heterogeneous targets were made but the results still need to be validated though comparisons to numerical simulations. The optimization of measurement setup has allowed to obtain accurate measurements of analogs such as spheroids, spheres and soot aggregates, all of them are low scattering targets. It became possible to intelligently select, for each measurement case, the most adequate settings of the measurement

setup depending on the working frequencies, used antennas, angular displacement but also according to the objective of the experiment.

This thesis has shown the potential of the microwave analogy to the understanding and solving of several classes of issues in electromagnetic and light scattering. Hopefully this will open the door for many new perspectives to a wide range of research area. The applications are being driven to a higher level: the next step is carrying out microwave analogy experiments on complex shaped and heterogeneous microalgae analogs for photobioreactors engineering, more realistic soot analogs with non-null imaginary part of relative permittivity, large forest scene for radar applications, comet scaled models and dust particles for astrophysics application. In what concerns down-scaling large objects, the use of the microwave analogy on such objects would be promising because those domains containing those targets are quite large compared to the wavelength (may be up to  $50\lambda \times 50\lambda \times 50\lambda$  large) and their numerical modeling would be impractical. In such cases one could refer to the microwave analogy as an “experimental modeling”. In the light of these applications, and since the measurement setup has now become more controlled and optimized, the operation frequency band of the setup of the CCRM will be extended to 40 GHz. This will help making scaling factors almost two times greater than what is possible with the current frequency band in order to keep the plane wave illumination at the far-field conditions. The other important application that can benefit from the progress achieved in this thesis is 3D measurements (spherical measurements) of analogs with particular shapes and permittivities to increase the number of available experimental data sets for inversion purposes.

## PUBLICATIONS

---

### PEER-REVIEWED JOURNALS

1. Barreda, Á. I., Saleh, H., Litman, A., González, F., Geffrin, J. M., & Moreno, F. (2017). Electromagnetic polarization-controlled perfect switching effect with high-refractive-index dimers and the beam-splitter configuration. *Nature communications*, 8, 13910.
2. Saleh, H., Charon, J., Dauchet, J., Tortel, H., & Geffrin, J. M. (2017). Microwave analog experiments on optically soft spheroidal scatterers with weak electromagnetic signature. *Journal of Quantitative Spectroscopy and Radiative Transfer*, 196, 1-9.

### INTERNATIONAL CONFERENCES

1. Saleh, H., Geffrin, J. M., & Tortel, H. (2016, Jun). Bistatic RCS Measurements of Low Scattering Targets: Hard and Soft Time Gating. In *IEEE Antennas and Propagation Society and the United States National Committee of URSI (AP-S/URSI)*, Fajardo, United-states.
2. Saleh, H., Geffrin, J. M., & Tortel, H. (2016, July). Comparison of Software and Hardware Time Gating Techniques on the Measurements of Low RCS Targets in a Bistatic Configuration. In *Advanced Electromagnetics Symposium (AES)*, Malaga, Spain.
3. Saleh, H., Geffrin, J. M., & Tortel, H. (2017, March). Bistatic scattering measurement on low permittivity spheroidal objects. In *European Conference on Antennas and Propagation (EUCAP)*, IEEE, Paris, France.
4. Geffrin, J. M., Saleh, H., Eyraud, C., & Litman, A. (2017, March). On the interest of a bistatic radar cross section setup to measure various scattering quantities. In *European Conference on Antennas and Propagation (EUCAP)*, IEEE, Paris, France.
5. Eyraud, C., Geffrin, J. M., & Saleh, H. (2017, March). Quantitative imaging using scattering matrix: Influence of the polarization. In *European Conference on Antennas and Propagation (EUCAP)*, IEEE, Paris, France.
6. Saleh, H., Eyraud, E., Geffrin, J.M. (2017, September). Optimization of the experimental parameters and of the noise of scattering measurements for inverse scattering applications. In *International Conference on Electromagnetics in Advanced Applications (ICEAA)*, IEEE, Verona, Italy.

### NATIONAL CONFERENCES

1. Saleh, H., Geffrin, J. M., & Tortel, H. (2015, October). Application of microwave analogy to the study of scattering by photosynthetic microalgae. *DGR Ondes*, Lyon, France.
2. Saleh, H., Geffrin, J. M., & Tortel, H. (2016, October). Experimental approach to investigate light interaction with soot aggregates through microwave analogs. *DGR Suie*, Orléans, France.
3. Saleh, H., Geffrin, J. M., Eyraud, C., Tortel, H., & Litman, A. (2016, November). Intérêt de l'analogie microonde pour l'étude des propriétés radiatives de particules et plus. *DGR Accort*, Marseille, France.
4. Saleh, H., Geffrin, J. M., Tortel, H., Eyraud, C., & Litman, A. (2017, May). Détermination de la permittivité d'objets faiblement diffractant à partir de leurs SER. *XXèmes Journées Nationales Microondes (JNM)*, Saint-Malo, France.



## REFERENCES

- [1] N. N. Youssef, "Radar cross section of complex targets," *Proc. IEEE*, vol. 77, no. 5, pp. 722–734, May 1989.
- [2] R. Leitgeb, M. Wojtkowski, A. Kowalczyk, C. K. Hitzenberger, M. Sticker, and A. F. Fercher, "Spectral measurement of absorption by spectroscopic frequency-domain optical coherence tomography," *Opt. Lett.*, vol. 25, no. 11, pp. 820–822, Jun. 2000.
- [3] R. Geise, A. Enders, H. Vahle, and H. Spieker, "Scaled Measurements of Instrument-Landing-System Disturbances Due to Large Taxiing Aircraft," *IEEE Trans. Electromagn. Compat.*, vol. 50, no. 3, pp. 485–490, Aug. 2008.
- [4] G. G. Peixoto, A. L. de Paula, L. A. Andrade, C. M. A. Lopes, and M. C. Rezende, "Electromagnetic signature on scale model of an aircraft," in *SBMO/IEEE MTT-S International Conference on Microwave and Optoelectronics, 2005.*, 2005, pp. 386–388.
- [5] R. Gente *et al.*, "Scaled Bistatic Radar Cross Section Measurements of Aircraft With a Fiber-Coupled THz Time-Domain Spectrometer," *IEEE Trans. Terahertz Sci. Technol.*, vol. 2, no. 4, pp. 424–431, Jul. 2012.
- [6] K. Belkebir and M. Saillard, "Special section: Testing inversion algorithms against experimental data," *Inverse Probl.*, vol. 21, no. 6, p. S1, 2004.
- [7] K. Belkebir and M. Saillard, "Testing inversion algorithms against experimental data: inhomogeneous targets," *Inverse Probl.*, vol. 21, no. 6, p. S1, 2004.
- [8] J. M. Geffrin and P. Sabouroux, "Continuing with the Fresnel database: experimental setup and improvements in 3D scattering measurements," *Inverse Probl.*, vol. 25, no. 2, p. 024001, Feb. 2009.
- [9] R. Vaillon and J.-M. Geffrin, "Recent advances in microwave analog to light scattering experiments," *J. Quant. Spectrosc. Radiat. Transf.*, vol. 146, pp. 100–105, Oct. 2014.
- [10] S. Bellez, H. Roussel, C. Dahon, and J.-M. Geffrin, "A rigorous forest scattering model validation through comparison with indoor bistatic scattering measurements," *Prog. Electromagn. Res. B*, vol. 33, pp. 1–19, 2011.
- [11] J. M. Geffrin *et al.*, "Magnetic and electric coherence in forward- and back-scattered electromagnetic waves by a single dielectric subwavelength sphere," *Nat. Commun.*, vol. 3, p. 1171, 2012.
- [12] C. Geuzaine and J.-F. Remacle, "Gmsh: A 3-D finite element mesh generator with built-in pre- and post-processing facilities," *Int. J. Numer. Methods Eng.*, vol. 79, no. 11, pp. 1309–1331, Sep. 2009.
- [13] "CATIA, <https://www.3ds.com/fr/produits-et-services/catia/>."
- [14] D. W. Burr, K. J. Daun, K. A. Thomson, and G. J. Smallwood, "Optimization of measurement angles for soot aggregate sizing by elastic light scattering, through design-of-experiment theory," *J. Quant. Spectrosc. Radiat. Transf.*, vol. 113, no. 5, pp. 355–365, Mar. 2012.
- [15] N. G. Khlebtsov, V. A. Bogatyrev, L. A. Dykman, and A. G. Melnikov, "Spectral Extinction of Colloidal Gold and Its Biospecific Conjugates," *J. Colloid Interface Sci.*, vol. 180, no. 2, pp. 436–445, Jun. 1996.
- [16] K. Chamailard, S. G. Jennings, C. Kleefeld, D. Ceburnis, and Y. J. Yoon, "Light backscattering and scattering by nonspherical sea-salt aerosols," *J. Quant. Spectrosc. Radiat. Transf.*, vol. 79, pp. 577–597, Jun. 2003.
- [17] B. Weinzierl *et al.*, "Airborne measurements of dust layer properties, particle size distribution and mixing state of Saharan dust during SAMUM 2006," *Tellus B*, vol. 61, no. 1, pp. 96–117, Feb. 2009.
- [18] W. P. Arnott, Y. Y. Dong, J. Hallett, and M. R. Poellot, "Role of small ice crystals in radiative properties of cirrus: A case study, FIRE II, November 22, 1991," *J. Geophys. Res. Atmospheres*, vol. 99, no. D1, pp. 1371–1381, Jan. 1994.

- [19] J. Dauchet, S. Blanco, J.-F. Cornet, and R. Fournier, "Calculation of the radiative properties of photosynthetic microorganisms," *J. Quant. Spectrosc. Radiat. Transf.*, vol. 161, pp. 60–84, août 2015.
- [20] A. J. Baran, "A review of the light scattering properties of cirrus," *J. Quant. Spectrosc. Radiat. Transf.*, vol. 110, no. 14–16, pp. 1239–1260, Sep. 2009.
- [21] P. Yang *et al.*, "Scattering and absorption property database for nonspherical ice particles in the near- through far-infrared spectral region," *Appl. Opt.*, vol. 44, no. 26, p. 5512, Sep. 2005.
- [22] T. Nousiainen, "Optical modeling of mineral dust particles: A review," *J. Quant. Spectrosc. Radiat. Transf.*, vol. 110, no. 14–16, pp. 1261–1279, Sep. 2009.
- [23] S. K. Sharma, "A modified Rayleigh-Gans-Debye formula for small angle X-ray scattering by interstellar dust grains," *Astrophys. Space Sci.*, vol. 357, no. 1, p. 80, Apr. 2015.
- [24] M. I. Mishchenko, *Electromagnetic Scattering by Particles and Particle Groups: An Introduction*. Cambridge University Press, 2014.
- [25] M. I. Mishchenko, L. D. Travis, and A. A. Lacis, *Scattering, Absorption, and Emission of Light by Small Particles*. Cambridge University Press, 2002.
- [26] T. Harmel, M. Hieronimi, W. Slade, R. Röttgers, F. Roullier, and M. Chami, "Laboratory experiments for inter-comparison of three volume scattering meters to measure angular scattering properties of hydrosols," *Opt. Express*, vol. 24, no. 2, p. A234, Jan. 2016.
- [27] H. Berberoglu, L. Pilon, and A. Melis, "Radiation characteristics of *Chlamydomonas reinhardtii* CC125 and its truncated chlorophyll antenna transformants *tlal*, *tlax* and *tlal-CW+*," *Int. J. Hydrog. Energy*, vol. 33, no. 22, pp. 6467–6483, Nov. 2008.
- [28] O. Munoz, F. Moreno, D. Guirado, D. D. Dabrowska, H. Volten, and J. W. Hovenier, "The Amsterdam-Granada Light Scattering Database," *J. Quant. Spectrosc. Radiat. Transf.*, vol. 113, no. 7, pp. 565–574, May 2012.
- [29] B. Å. S. Gustafson, "Scaled analogue experiments in electromagnetic scattering," in *Light Scattering Reviews 4*, D. A. A. Kokhanovsky, Ed. Springer Berlin Heidelberg, 2009, pp. 3–30.
- [30] J. M. Greenberg, N. E. Pedersen, and J. C. Pedersen, "Microwave Analog to the Scattering of Light by Nonspherical Particles," *J. Appl. Phys.*, vol. 32, no. 2, p. 233, 1961.
- [31] D. W. Schuerman, "The Microwave Analog Facility at Sunya: Capabilities and Current Programs," in *Light Scattering by Irregularly Shaped Particles*, D. W. Schuerman, Ed. Springer US, 1980, pp. 227–232.
- [32] Greenberg, J. M., "From interstellar dust to comets to the zodiacal light," *Symposium-International Astronomical Union*, pp. 343–350, 1980.
- [33] R. H. Zerull, "Laboratory Investigations and Optical Properties of Grains," *Int. Astron. Union Colloq.*, vol. 85, pp. 197–206, Jan. 1985.
- [34] K. Weiss-Wrana, R. H. Giese, and R. H. Zerull, "Microwave and Laser Facilities to Determine Scattering and Colour Signatures Related to the Physical Properties of Dust Particles," in *Properties and Interactions of Interplanetary Dust*, R. H. Giese and P. Lamy, Eds. Springer Netherlands, 1985, pp. 219–221.
- [35] R.H. Zerull, R.H. Giese, and K. Weiss, "Scattering functions of nonspherical dielectric and absorbing particles vs Mie theory," *Applied Optics*, Apr-1977.
- [36] R. H. Zerull, B. A. Gustafson, K. Schulz, and E. Thiele-Corbach, "Scattering by aggregates with and without an absorbing mantle: microwave analog experiments," *Appl. Opt.*, vol. 32, no. 21, pp. 4088–4100, Jul. 1993.
- [37] Y. L. Xu and B. A. Gustafson, "Experimental and theoretical results of light scattering by aggregates of spheres," *Appl. Opt.*, vol. 36, no. 30, pp. 8026–8030, Oct. 1997.
- [38] Y. Xu and B. Å. S. Gustafson, "Comparison between Multisphere Light-scattering Calculations: Rigorous Solution and Discrete-Dipole Approximation," *Astrophys. J.*, vol. 513, no. 2, p. 894, 1999.

- [39] K. W. T. Waldemarsson and B. Å. S. Gustafson, "Interference effects in the light scattering by transparent plates," *J. Quant. Spectrosc. Radiat. Transf.*, vol. 79–80, pp. 1111–1119, Sep. 2003.
- [40] L. Kolokolova and B. Å. S. Gustafson, "Scattering by inhomogeneous particles: microwave analog experiments and comparison to effective medium theories," *J. Quant. Spectrosc. Radiat. Transf.*, vol. 70, no. 4–6, pp. 611–625, août 2001.
- [41] J. E. Thomas-Osip, B. Å. S. Gustafson, L. Kolokolova, and Y.-L. Xu, "An investigation of Titan's aerosols using microwave analog measurements and radiative transfer modeling," *Icarus*, vol. 179, no. 2, pp. 511–522, décembre 2005.
- [42] L. Kolokolova, M. S. Hanner, A.-C. Lévassieur-Regourd, and B. Å. S. Gustafson, "Physical properties of cometary dust from light scattering and thermal emission," in *Comets II*, 2004, pp. 577–604.
- [43] Y. Chevalier, P. Minvielle, F. Degery, and P. Bérisset, "Indoor spherical 3D RCS near-field facility," *Annual Meeting of the Antenna Measurement Techniques Association, AMTA*, Nov-2007.
- [44] D. Escot, D. Poyatos, J. A. Aguilar, I. Montiel, I. González, and F. S. de Adana, "Indoor 3D Full Polarimetric Bistatic Spherical Facility for Electromagnetic Tests," *IEEE Antennas Propag. Mag.*, vol. 52, no. 4, pp. 112–118, août 2010.
- [45] D. Escot-Bocanegra, D. Poyatos-Martinez, I. Montiel-Sanchez, F. M. Saez de Adana, and I. Gonzalez-Diego, "Spherical Indoor Facility Applied to Bistatic Radar Cross Section Measurements," *Prog. Electromagn. Res. Lett.*, vol. 26, pp. 181–187, 2011.
- [46] P. López-Rodríguez, O. Hernán-Vega, D. Poyatos-Martínez, and D. Escot-Bocanegra, "BIANCHIA: A spherical indoor facility for bistatic electromagnetic tests," in *AMTA 2016 Proceedings*, 2016, pp. 1–6.
- [47] A. Zeitler *et al.*, "Amplitude and Phase Measurements of Scattered Fields for Quantitative Imaging in the W-band," *IEEE Trans. Antennas Propag.*, vol. 61, no. 7, pp. 3927–3931, Jul. 2013.
- [48] F. Nsengiyumva, "Contribution à la détection d'objets sur pistes d'aéroport (FOD) par tomographie millimétrique en bande W et polarimétrie," phd thesis, Université Nice Sophia Antipolis, 2016.
- [49] S. Bellez, H. Roussel, C. Dahon, J. C. Castelli, and A. Cheraly, "Full Polarimetric Bistatic Radar Imaging Experiments on Sets of Dielectric Cylinders Above a Conductive Circular Plate," *IEEE Trans. Geosci. Remote Sens.*, vol. 51, no. 7, pp. 4164–4176, Jul. 2013.
- [50] J. C. Castelli, "Imagerie par ondelettes multidimensionnelles pour l'analyse de la SER des cibles," *Rev. Electr. Electron.*, no. 4, pp. 77–85, 2001.
- [51] Christelle Eyraud, "Caractérisation et optimisation, dans le domaine des hyperfréquences, des mesures de champs diffractés. Applications aux problèmes directs et inverses tridimensionnels," 2006.
- [52] C. Eyraud, J.-M. Geffrin, and A. Litman, "Drift correction for 3D scattering measurements," in *IEEE Antennas and Propagation Society International Symposium 2006*, 2006, pp. 2003–2006.
- [53] O. Bucci and G. Franceschetti, "On the spatial bandwidth of scattered fields," *IEEE Trans. Antennas Propag.*, vol. 35, no. 12, pp. 1445–1455, Dec. 1987.
- [54] O. Merchiers *et al.*, "Microwave measurements of the full amplitude scattering matrix of a complex aggregate: a database for the assessment of light scattering codes," *Opt. Express*, vol. 18, no. 3, pp. 2056–2075, février 2010.
- [55] M. I. Tribelsky, J.-M. Geffrin, A. Litman, C. Eyraud, and F. Moreno, "Small Dielectric Spheres with High Refractive Index as New Multifunctional Elements for Optical Devices," *Sci. Rep.*, vol. 5, p. 12288, Jul. 2015.
- [56] B. T. Draine and P. J. Flatau, "Discrete-Dipole Approximation For Scattering Calculations," *JOSA A*, vol. 11, no. 4, pp. 1491–1499, Apr. 1994.

- [57] C. Eyraud, A. Litman, A. Hérique, and W. Kofman, "Microwave imaging from experimental data within a Bayesian framework with realistic random noise," *Inverse Probl.*, vol. 25, no. 2, p. 024005, Feb. 2009.
- [58] D. W. Mackowski and M. I. Mishchenko, "Calculation of the T matrix and the scattering matrix for ensembles of spheres," *JOSA A*, vol. 13, no. 11, pp. 2266–2278, Nov. 1996.
- [59] B. Stout, J. C. Auger, and A. Devilez, "Recursive T matrix algorithm for resonant multiple scattering: applications to localized plasmon excitations," *JOSA A*, vol. 25, no. 10, pp. 2549–2557, Oct. 2008.
- [60] M. M. Leibfritz, M. D. Blech, F. M. Landstorfer, and T. F. Eibert, "A comparison of software- and hardware-gating techniques applied to near-field antenna measurements," *Adv. Radio Sci. Kleinheubacher Berichte*, vol. 5, pp. 43–48, Jun. 2007.
- [61] C. Barnett and D. Dunn, *Practical Considerations for Making Pulsed Antenna Measurements*. Long Beach: AMTA, 1994.
- [62] R. Shoulders and C. Chi, "Pulsed Antenna Measurements With the Agilent PNA Microwave Network Analyzer," in *Proceedings of the Meeting and Symposium of Antenna Measurement and Techniques Association, Irvine, CA, USA, 2003*, pp. 86–91.
- [63] Keysight Technologies, "Pulsed-RF S-Parameter Measurements with the PNA Microwave Network Analyzers Using Wideband and Narrowband Detection." .
- [64] Schluper , Bert, "Narrow Pulse Measurements on Vector Network Analyzers."
- [65] J. F. Aubin, J. Caserta, and M. A. Bates, "A NEW GATED-CW RADAR IMPLEMENTATION."
- [66] John Aubin, Christopher Kelly, Andy Humen, Randy Engle, Curtis Hodnefield, and Jeff Platt, "Multi-purpose RCS/Antenna test facility at Nurad Technologies, Inc," *AMTA*, 2004.
- [67] StingRay brochure, "Gated-CW Radar Architecture - A Complete RCS Measurement System." .
- [68] J. Lemanczyk, J. Hartmann, and D. Fasold, "Evaluation of Hard Gating in the ESA/ESTEC CPTR," *AMTA 2004*, 2004.
- [69] D. Fasold, J. Hartmann, and P. Rittsteiger, "Application of Double Reflector Compact Ranges for Time Domain RCS Measurements."
- [70] José Maria Tamayoa, "SHAPE Pilot ENTARES Engineering: Electromagnetic simulation for large model using HPC," Zenodo, Jun. 2014.
- [71] J. C. Castelli *et al.*, "Interlaboratory comparisons of radar cross section measurements by the #x201C;GTi #x201D;; criteria suggestions," in *2017 11th European Conference on Antennas and Propagation (EUCAP)*, 2017, pp. 273–275.
- [72] *NIST/SEMATECH e-Handbook of Statistical Methods*. .
- [73] J. Yi, A. de Lustrac, G. P. Piau, and S. N. Burokur, "Lenses designed by transformation electromagnetics and fabricated by 3D dielectric printing," in *2016 IEEE International Symposium on Antennas and Propagation (APSURSI)*, 2016, pp. 1385–1386.
- [74] H. Saleh, J. Charon, J. Dauchet, H. Tortel, and J.-M. Geffrin, "Microwave analog experiments on optically soft spheroidal scatterers with weak electromagnetic signature," *J. Quant. Spectrosc. Radiat. Transf.*, vol. 196, pp. 1–9, 2017.
- [75] Á. I. Barreda, H. Saleh, A. Litman, F. González, J.-M. Geffrin, and F. Moreno, "Electromagnetic polarization-controlled perfect switching effect with high-refractive-index dimers and the beam-splitter configuration," *Nat. Commun.*, vol. 8, p. 13910, Jan. 2017.
- [76] J. Yon, A. Bescond, and F. Liu, "On the radiative properties of soot aggregates part 1: Necking and overlapping," *J. Quant. Spectrosc. Radiat. Transf.*, vol. 162, pp. 197–206, Sep. 2015.
- [77] ASTM F2792-12a, "Standard Terminology for Additive Manufacturing Technologies (Withdrawn 2015)," vol. 2, 2012.
- [78] P. J. Bártolo, *Stereolithography: materials, processes and applications*. Springer Science & Business Media, 2011.

- [79] C. Saint-Flour, F. Degery, B. Etchessahar, P. Massaloux, G. Mazé-Merceur, and O. Vacus, "RCS of targets with plasmonic coatings: Computation, additive manufacturing and measurement," in *2017 11th European Conference on Antennas and Propagation (EUCAP)*, 2017, pp. 2595–2598.
- [80] Maalouf, A. and Gingat, R., "Réalisation de charges hyperfréquences par technologie additive," *XXèmes Journées Nationales Microondes*, Saint-Malo, 2017.
- [81] N. Delhote, S. Bila, D. Baillargeat, T. Chartier, and S. Verdeyme, "Advanced design and fabrication of microwave components based on shape optimization and 3D ceramic stereolithography process," in *Advances in Ceramics-Synthesis and Characterization, Processing and Specific Applications*, InTech, 2011.
- [82] N. T. Nguyen, N. Delhote, M. Ettore, D. Baillargeat, L. L. Coq, and R. Sauleau, "Design and Characterization of 60-GHz Integrated Lens Antennas Fabricated Through Ceramic Stereolithography," *IEEE Trans. Antennas Propag.*, vol. 58, no. 8, pp. 2757–2762, Aug. 2010.
- [83] N. Delhote, D. Baillargeat, S. Verdeyme, M. Thevenot, C. Delage, and C. Chaput, "Large experimental bandpass waveguide in 3D EBG woodpile manufactured by layer-by-layer ceramic stereolithography," in *2007 IEEE/MTT-S International Microwave Symposium*, 2007, pp. 1431–1434.
- [84] N. Delhote, D. Baillargeat, S. Verdeyme, C. Delage, and C. Chaput, "Narrow Ka Bandpass Filters Made Of High Permittivity Ceramic By Layer-By-Layer Polymer Stereolithography," in *2006 European Microwave Conference*, 2006, pp. 510–513.
- [85] N. Delhote, D. Baillargeat, S. Verdeyme, C. Delage, and C. Chaput, "Innovative Shielded High  $Q$  Dielectric Resonator Made of Alumina by Layer-by-Layer Stereolithography," *IEEE Microw. Wirel. Compon. Lett.*, vol. 17, no. 6, pp. 433–435, Jun. 2007.
- [86] P. I. Deffenbaugh, R. C. Rumpf, and K. H. Church, "Broadband Microwave Frequency Characterization of 3-D Printed Materials," *IEEE Trans. Compon. Packag. Manuf. Technol.*, vol. 3, no. 12, pp. 2147–2155, Dec. 2013.
- [87] R. C. Rumpf, J. Pazos, C. R. Garcia, L. Ochoa, and R. Wicker, "3D Printed Lattices with Spatially Variant Self-Collimation," *Prog. Electromagn. Res.*, vol. 139, pp. 1–14, 2013.
- [88] C. R. Garcia *et al.*, "3D Printing of Anisotropic Metamaterials," *Prog. Electromagn. Res. Lett.*, vol. 34, pp. 75–82, 2012.
- [89] J. H. Sandoval, K. F. Soto, L. E. Murr, and R. B. Wicker, "Nanotailoring photocrosslinkable epoxy resins with multi-walled carbon nanotubes for stereolithography layered manufacturing," *J. Mater. Sci.*, vol. 42, no. 1, pp. 156–165, Jan. 2007.
- [90] F. Castles *et al.*, "Microwave dielectric characterisation of 3D-printed BaTiO<sub>3</sub>/ABS polymer composites," *Sci. Rep.*, vol. 6, p. srep22714, Mar. 2016.
- [91] C. Eyraud, J. M. Geffrin, A. Litman, and H. Tortel, "Complex Permittivity Determination From Far-Field Scattering Patterns," *IEEE Antennas Wirel. Propag. Lett.*, vol. 14, pp. 309–312, 2015.
- [92] C. F. Bohren, D. R. Huffman, and Z. Kam, "Book-Review - Absorption and Scattering of Light by Small Particles," *Nature*, vol. 306, p. 625, Dec. 1983.
- [93] J.-M. Geffrin, C. Eyraud, A. Litman, and P. Sabouroux, "Optimization of a bistatic microwave scattering measurement setup: From high to low scattering targets," *Radio Sci.*, vol. 44, no. 2, p. RS2007, avril 2009.
- [94] K. K. Karkkainen, A. H. Sihvola, and K. I. Nikoskinen, "Effective permittivity of mixtures: numerical validation by the FDTD method," *IEEE Trans. Geosci. Remote Sens.*, vol. 38, no. 3, pp. 1303–1308, May 2000.
- [95] R. Popielarz, C. K. Chiang, R. Nozaki, and J. Obrzut, "Dielectric Properties of Polymer/Ferroelectric Ceramic Composites from 100 Hz to 10 GHz," *Macromolecules*, vol. 34, no. 17, pp. 5910–5915, Aug. 2001.
- [96] J. Dauchet, "Analyse radiative des photobioréacteurs," Theses, Université Blaise Pascal - Clermont-Ferrand II, 2012.

- [97] M. I. Mishchenko, "Vector radiative transfer equation for arbitrarily shaped and arbitrarily oriented particles: a microphysical derivation from statistical electromagnetics," *Appl. Opt.*, vol. 41, no. 33, pp. 7114–7134, Nov. 2002.
- [98] M. I. Mishchenko, "Microphysical approach to polarized radiative transfer: extension to the case of an external observation point," *Appl. Opt.*, vol. 42, no. 24, pp. 4963–4967, Aug. 2003.
- [99] M. I. Mishchenko, "Maxwell's equations, radiative transfer, and coherent backscattering: A general perspective," *J. Quant. Spectrosc. Radiat. Transf.*, vol. 101, no. 3, pp. 540–555, Oct. 2006.
- [100] M. Neuman, "Applied problems and computational methods in radiative transfer," 2013.
- [101] J. Dauchet, J.-F. Cornet, F. Gros, M. Roudet, and C.-G. Dussap, "Chapter One - Photobioreactor Modeling and Radiative Transfer Analysis for Engineering Purposes," in *Advances in Chemical Engineering*, vol. 48, J. Legrand, Ed. Academic Press, 2016, pp. 1–106.
- [102] L. Pilon and R. Kandilian, "Chapter Two - Interaction Between Light and Photosynthetic Microorganisms," in *Advances in Chemical Engineering*, vol. 48, J. Legrand, Ed. Academic Press, 2016, pp. 107–149.
- [103] T. Wriedt, "Light scattering theories and computer codes," *J. Quant. Spectrosc. Radiat. Transf.*, vol. 110, no. 11, pp. 833–843, juillet 2009.
- [104] F. M. Kahnert, "Numerical methods in electromagnetic scattering theory," *J. Quant. Spectrosc. Radiat. Transf.*, vol. 79–80, pp. 775–824, Sep. 2003.
- [105] J. A. Berrie and G. L. Wilson, "Design of target support columns using EPS foam," *IEEE Antennas Propag. Mag.*, vol. 45, no. 1, pp. 198–206, février 2003.
- [106] K. L. Kelly, E. Coronado, L. L. Zhao, and G. C. Schatz, "The Optical Properties of Metal Nanoparticles: The Influence of Size, Shape, and Dielectric Environment," *J. Phys. Chem. B*, vol. 107, no. 3, pp. 668–677, Jan. 2003.
- [107] S. A. Maier, *Plasmonics: Fundamentals and Applications*. Springer Science & Business Media, 2007.
- [108] A. García-Etxarri *et al.*, "Strong magnetic response of submicron Silicon particles in the infrared," *Opt. Express*, vol. 19, no. 6, pp. 4815–4826, Mar. 2011.
- [109] "Monodisperse silicon nanocavities and photonic crystals with magnetic response in the optical region - ProQuest." [Online]. Available: <https://search.proquest.com/openview/e7dc12fca7507a7996164ee8689305d1/1?pq-origsite=gscholar&cbl=546298>. [Accessed: 19-Aug-2017].
- [110] A. B. Evlyukhin, C. Reinhardt, A. Seidel, B. S. Luk'yanchuk, and B. N. Chichkov, "Optical response features of Si-nanoparticle arrays," *Phys. Rev. B*, vol. 82, no. 4, p. 045404, Jul. 2010.
- [111] M. Kerker, D.-S. Wang, and C. L. Giles, "Electromagnetic scattering by magnetic spheres," *JOSA*, vol. 73, no. 6, pp. 765–767, Jun. 1983.
- [112] B. Rolly, B. Bebey, S. Bidault, B. Stout, and N. Bonod, "Promoting magnetic dipolar transition in trivalent lanthanide ions with lossless Mie resonances," *Phys. Rev. B*, vol. 85, no. 24, p. 245432, Jun. 2012.
- [113] W.-S. Chang *et al.*, "A Plasmonic Fano Switch," *Nano Lett.*, vol. 12, no. 9, pp. 4977–4982, Sep. 2012.
- [114] "COMSOL Multiphysics 5.0 (Comsol Inc., 2015)."
- [115] B. García-Cámara, R. Gómez-Medina, J. J. Sáenz, and B. Sepúlveda, "Sensing with magnetic dipolar resonances in semiconductor nanospheres," *Opt. Express*, vol. 21, no. 20, pp. 23007–23020, Oct. 2013.
- [116] A. F. Khalizov, B. Hogan, C. Qiu, E. L. Petersen, and R. Zhang, "Characterization of Soot Aerosol Produced from Combustion of Propane in a Shock Tube," *Aerosol Sci. Technol.*, vol. 46, no. 8, pp. 925–936, Aug. 2012.
- [117] G. Okyay, "Impact of the morphology of soot aggregates on their radiative properties and the subsequent radiative heat transfer through sooty gaseous mixtures," phdthesis, Université Paris-Saclay, 2016.

## References

---

- [118] M. J. Berg, C. M. Sorensen, and A. Chakrabarti, “Extinction and the optical theorem. Part I. Single particles,” *JOSA A*, vol. 25, no. 7, pp. 1504–1513, Jul. 2008.
- [119] R. G. Newton, “Optical theorem and beyond,” *Am. J. Phys.*, vol. 44, no. 7, pp. 639–642, Jul. 1976.
- [120] L. H. H. Roussel, M. Casaletti, C. Dahon, and R. Mittra, “Hybrid formulation for the electromagnetic analysis of metallic objects placed in natural environments,” in *2017 11th European Conference on Antennas and Propagation (EUCAP)*, 2017, pp. 3534–3537.

## ABSTRACT

---

The interaction between an impinging electromagnetic wave and a target results in a scattered wave, which depends upon the frequency, the size, shape and electromagnetic properties of the target. The measurement of a scattered signal can be used to detect or characterize a target, and the applications range from radar systems at large scale to optical tomography at the microscale. When the targets have very large or very small dimensions, the microwave analogy appears as a useful approach to experimentally investigate a scattering problem. The experiment is therefore scaled to the microwave range and the target is mimicked by a centimeter-sized analog, while maintaining the same initial wavelength over target dimension ratio and conserving the same initial permittivity. The microwave scattering experiments are realized in the anechoic chamber of the Centre Commun de Ressources en Microondes at the frequencies between 2 GHz and 18 GHz.

The objective of this thesis is to widen the application of the microwave analogy by adopting the appropriate techniques to create objects of controlled shapes and electromagnetic properties using special manufacturing technologies, as well as by developing a versatile setup providing accurate measurements. A special interest is given on low scattering targets, i.e. with low permittivity contrasts and/or small dimensions compared to the wavelength. An extensive study on the random noise characterization of the measurement setup was made and the undesired reflections within the anechoic chamber were investigated. As a result, a novel optimization technique was proposed which allow having a flexible control of the setup parameters according to the investigated target. It consists on angular zones decompositions of the bistatic region with different power profiles. In addition, A Hardgating system utilizing two RF switches was installed to the measurement setup, allowing to make pulsed signals measurements and to filter out the stray signals.

Thanks the new setup optimization, it became possible to accurately measure low scattering levels down to  $-60$  dBm<sup>2</sup>. Moreover, additive manufacturing technologies were involved in the fabrication of analogs and a novel technique was proposed to obtain targets with “on-demand” value complex permittivity and shape. It became possible manufacture low scattering analogs of the real part of permittivity for any value between 1 and 3 by creating well controlled porous structures.

Three main targets are studied within the scope of this thesis: low permittivity spheroids, analogs of photosynthetic microalgae, soot aggregates analogs with complex shape, and scaled forest scene models composed of tree analogs with some metal vehicle analogs.



## RESUME

---

La diffraction est un phénomène issu de la l'interaction d'une onde électromagnétique incidente avec un objet. En électromagnétisme, le champ diffracté, qui en résulte, est fonction de la fréquence, de la taille de l'objet et de ses caractéristiques diélectriques et magnétiques. La mesure du signal ainsi diffracté peut être mise à profit pour caractériser un objet. On peut citer les radars comme des applications qui concernent les grands objets et la tomographie optique pour les échelles micrométriques. Dans le cadre des études expérimentales, l'analogie microonde peut s'avérer bénéfique autant pour les grands que les petits objets. Son principe est de transposer à l'échelle centimétrique les objets dont nous souhaitons étudier la diffraction. Pour être pertinente, cette translation d'échelle doit être réalisée en créant un analogue respectant le même rapport dimension sur longueur d'onde, tout en conservant la, sur une fréquence donnée, la même permittivité. Toutes les mesures de diffraction de cette thèse ont été réalisées dans la chambre anéchoïque du Centre Commun de Ressources en Microondes avec des fréquences variant entre 2 GHz et 18 GHz.

Les objectifs de cette thèse sont d'élargir le champ des applications de l'analogie microonde en adaptant les techniques de fabrication des analogues pour créer des objets de caractéristiques électromagnétiques et de géométrie contrôlées d'une part, et d'autre part de développer un outil versatile et précis pour réaliser les mesures de diffraction. Un intérêt particulier a été porté aux objets faiblement diffractant, ce qui peut être dû à leurs faibles dimensions aussi bien qu'à leurs faibles permittivités. A la suite de la caractérisation des réflexions parasites et de celle du bruit aléatoire perturbant les mesures, une nouvelle technique d'optimisation du paramétrage des appareils de mesure, qui tient compte des objets étudiés, a pu être proposée. Elle comporte notamment un réglage des puissances de source en fonction des angles de bistatisme et un filtrage temporel, par switch, qui a été mis en place et paramétré pour filtrer les signaux parasites mesurés.

Les bénéfices de ces diverses optimisations des paramètres de mesures ont été démontrés et ils ont permis de mesurer des niveaux de section efficace radar aussi bas que  $-60 \text{ dBm}^2$ . De plus, les avancées sur le contrôle de la permittivité permettent de réaliser des analogues de géométrie maîtrisée avec des permittivités relatives à la carte dans la gamme de 1 à 3 ; la permittivité étant ajustée par contrôle de la porosité.

Les trois principales études présentées concernent : des sphéroïdes de faible permittivité, analogues de microalgues photosynthétiques, des agrégats de suies de forme complexes, et des scènes forestières composées d'analogues d'arbres et de véhicules.